

Charmonium Correlation and Spectral Functions in Quenched Lattice QCD at Finite Temperature

Dissertation

zur Erlangung des Doktorgrades
der Fakultät für Physik
der Universität Bielefeld

vorgelegt von
Heng-Tong Ding

September 2010

Charmonium Correlation and Spectral Functions in Quenched Lattice QCD at Finite Temperature

Heng-Tong Ding

Vollständiger Abdruck der von der Fakultät für Physik der Universität Bielefeld
zur Erlangung des akademischen Grades eines

Doktors der Naturwissenschaften (Dr. rer. nat.)

genehmigten Dissertation.

Prüfer der Dissertation (Gutachter):

Prof. Dr. Edwin Laermann

Prof. Dr. Helmut Satz

Weitere Mitglieder des Prüfungsausschusses:

Prof. Dr. Mikko Laine

Tag der mündlichen Prüfung (Disputation): 12. Oktober 2010

Table of Contents

Introduction	1
1 Lattice QCD - A brief introduction	5
1.1 Gluon fields on the lattice	7
1.2 Matter fields on the lattice	8
1.2.1 Naïve action and fermion doublers	8
1.2.2 Wilson fermions	9
1.3 The continuum limit of lattice QCD	12
1.4 Simulation technique and error estimation	14
1.5 Simulation details	18
1.5.1 Simulation parameters	18
1.5.2 Scale determination	19
1.5.3 J/ψ mass tuning	20
1.6 Renormalization constants	24
2 Mesonic correlation and spectral functions	29
2.1 Mesonic correlation and spectral functions	29
2.1.1 A close look at the integrand kernel	36
2.1.2 The reconstructed correlator	37
2.1.3 Sum rules	38
2.2 Maximum Entropy Method	39
2.2.1 Likelihood function	40
2.2.2 Entropic prior information	41
2.2.3 Posterior probability	42
2.2.4 Distributions and their normalizations	43
2.2.5 MEM algorithm	44
2.2.6 The extended MEM	44
2.2.7 MEM analysis with zero mode contribution suppressed	47
2.2.8 Remarks on MEM	47
2.3 Free temporal correlation and spectral function	48

2.3.1	Free spectral function in the continuum	49
2.3.2	Free spectral function for Wilson fermions on the lattice	53
2.3.3	Comparison of free spectral function and correlator	55
2.4	Linear response theory and Heavy quark diffusion	59
2.5	Charmonium at finite temperature on the lattice: a brief review	67
3	Analysis of charmonium properties at vanishing momentum	71
3.1	Toy model test of spectral function	71
3.2	Mock data test of MEM	75
3.3	Effective mass	81
3.4	Spectral functions below T_c	84
3.5	Reconstructed correlator	88
3.5.1	The pseudo scalar correlators	88
3.5.2	The P wave correlators	89
3.5.3	The vector correlators	90
3.6	Estimate of the zero mode contribution	94
3.6.1	Thermal moments of correlators	96
3.7	Spectral functions above T_c	100
3.7.1	Default model dependences	100
3.7.2	Systematic uncertainties and statistical errors	105
4	Analysis of charmonium properties at non-zero momentum	115
4.1	Screening mass and dispersion relation	115
4.2	Longitudinal and transverse correlation function	117
4.3	The reconstructed correlators	119
	Conclusion and outlook	123
A	The Euclidean Dirac γ matrices and the SU(N) generators λ	127
A.1	Dirac matrices	127
A.2	SU(N) generators	128
B	Memory optimization for the clover term	129
	References	131
	Acknowledgements	145

Introduction

In 1974, an unusual resonance was discovered almost simultaneously at the Brookhaven National Laboratory (BNL) [1] and at the Stanford Linear Accelerator Center (SLAC) [2]. This new resonance, which is called “ J/ψ ”, was the first observed bound state of a charm quark and its antiquark ($c\bar{c}$). By analogy to positronium, the bound state of $c\bar{c}$ in general is then named charmonium. The charmonium system, which is mainly governed by the strong force, should be the simplest object for studying the strong interaction. It was hoped to play the same role in understanding hadronic system as its analog, the hydrogen atom, which is governed by the electromagnetic force, had played in understanding atomic physics. Indeed, this has been the case. The analyses of properties of charmonium and of its higher sibling bottomonium have induced the development of many methods in QCD [3, 4].

Physics thrives on analogies. Since charmonium has been a useful candidate to study hadronic systems at zero temperature, T. Matsui and H. Satz were wondering whether it could also be useful to study some sort of new “medium” at finite temperature. Due to the success of the potential model at zero temperature, in 1986 they proposed the suppression of J/ψ in the medium as a signal of the formation of the Quark Gluon Plasma (QGP) assuming the quark-antiquark potential being color screened [5]. This idea has been triggering intensely studies on the properties of heavy quarkonium states (charmonium and bottomonium) in a hot and dense QCD medium, both experimentally and theoretically [3, 6, 7].

The experiments carried out at the SPS at CERN and the RHIC at BNL have indeed observed J/ψ suppression [3, 6, 7]. The interpretation of experimental data, however, is not as straightforward as the original idea proposed since the observed modification when comparing J/ψ production in nuclei-nuclei (AA) collisions to that in proton-proton (pp) collisions could be caused by two distinct classes of effects. On the one hand there are cold nuclear matter effects, which originate from the presence of cold nuclear matter in target and projectile. These can be studied from pA collisions with respect to pp collisions [8]. On the other hand there are hot medium effects, which are of the primary interest and concern the properties of the QGP we want to study. In

order to disentangle these two effects, it is crucial to have a good understanding of the dynamics of the quarkonium in the QGP and the fate of its possible bound states.

From the theoretical point of view, the charmonium spectral function at finite temperature [9, 10], which contains all the information of the hadron properties in the thermal medium, such as the presence, the location and the width of bound states (and thus about dissociation temperatures) as well as transport properties, is the key quantity to be investigated. Since this is a difficult task, several theoretical approaches to determine the quarkonium properties at finite temperature have been followed.

The most traditional one is the non-relativistic potential model, which assumes the interaction between a heavy quark pair inside the quarkonium can be described by a potential [11]. Due to its success at zero temperature, the potential model is applied to this phenomenon at finite temperature [12–23]. It is based either on models or on finite temperature lattice QCD results [24] for the heavy quark potential in a non-relativistic Schrödinger equation. The resulting dissociation temperatures depend strongly on the potential used. Recently progress has been made in comparing directly to correlators calculated on the lattice with the potential model results in order to clarify certain ambiguities [19–23, 25] or trying to tell from the experimental data which potential is more appropriate [26]. However, the potential model approach at finite temperature is still under scrutiny.

Another potential-like investigation [27–35] is the calculation of the correlation function of a heavy quark pair directly in real time. This renders the long time behavior of the dynamics with the possibility of being described by a Schrödinger like equation with a complex potential. The potential includes both, effects of screening via its real part, and of the interaction with the medium via its imaginary part. However, this approach is only valid in the infinite quark mass limit where the potential can be calculated and is also well defined. More recently a new approach is proposed in Ref. [36]. It is based on a path integral for non-relativistic massive particles with a non-local self-interaction that summarizes the effects of the medium on the heavy quark. However, the effects of the medium on the heavy quark in this approach is modeled with only Coulomb interactions. Thus it needs further research.

First principle calculations in lattice QCD are thus crucially needed to determine the dynamics of heavy quarks in the hot medium. The investigations of charmonium at finite temperature, which has been performed in both quenched and full lattice QCD, have led to the rather surprising result that J/ψ appears to survive up to temperatures well above T_c [37–43]. This is in sharp contrast to the results from the potential model [44]. In this thesis we will try to understand more about the dynamics of heavy quarks in the hot medium within the lattice QCD approach.

The activities carried out in this thesis are summarized in the following paragraphs:

- In the first chapter, we will give a brief introduction to lattice QCD. The standard Wilson gauge action and the non-perturbatively improved Sheikholeslami-Wohlert fermion action are explained. After that, simulation techniques as well as error estimation methods are described. We will present the lattice parameters used in our simulation and how the scale is set. At the end we will show renormalization constants used in our analysis.
- In the second chapter we will first introduce the basics about mesonic correlation and spectral functions. We find that the reconstructed correlators can be directly obtained from the measured lattice correlation function at a certain lower temperature. Next we give a review on the Maximum Entropy Method, which is used to extract the spectral function from the lattice calculated correlation function. We also introduce some variants of the Maximum Entropy Method to suppress possible zero mode contributions. The extended Maximum Entropy Method, which can deal with non-positive spectral functions, is introduced to the lattice QCD field for the first time. Then we have a brief discussion on the general features of free correlation and spectral functions in both the continuum and the Wilson fermion case, where the zero mode contribution is also described. Thereafter we give a brief review on linear response theory and, in addition by using the Langevin equations, we have a brief discussion on the heavy quark diffusion in the medium. At the end a review on the current status of charmonium studies with the lattice QCD approach is given.
- The third chapter includes the main results of this thesis concerning the temperature dependence of charmonium properties. A toy model is employed to study the contribution of different frequency parts of the spectral function to the correlators. Both measured and reconstructed correlators are analyzed. Furthermore the zero mode contributions are discussed. We test the applicability of the Maximum Entropy Method to our specific situation with mock data. We reconstruct the spectral functions in the pseudo scalar and vector spectral channels at $T = 0.73 T_c$, $1.46 T_c$, $2.20 T_c$, and $2.93 T_c$. We also discuss the possible systematic uncertainties, including the dependences on default models and on the number of data points used, as well as the statistical errors.
- In the fourth chapter the properties of the charmonium states moving with respect to the heat bath frame are studied at the correlator level. The screening mass, measured correlator as well as the reconstructed correlator are investigated.
- The last chapter summarizes the results and provides an outlook on possible directions for future investigations.

Chapter 1

Lattice QCD - A brief introduction

Lattice gauge theory, which nowadays serves as a main numerical tool to study the non-perturbative properties of QCD, was suggested by K. G. Wilson already in 1974 [45]. It is based on the path integral formalism and is regularized by introducing a finite lattice spacing. In this way the space-time is discretized and the path integral becomes a finite yet high dimensional integral. The discretization of space and time introduces “errors”, which vanish when the lattice spacing is taken to zero, i.e. continuum limit. The theoretical and technical details can be found in various textbooks [46–48] such that only a brief introduction is given here.

We start by writing down the Lagrangian of QCD in the continuum:

$$\mathcal{L}_{\text{QCD}} = \mathcal{L}_{\text{gluon}} + \mathcal{L}_{\text{fermion}}, \quad (1.1)$$

$$\mathcal{L}_{\text{gluon}} = -\frac{1}{4} \sum_{a=1}^{N_c^2-1} F_a^{\mu\nu}(x) F_{\mu\nu}^a(x), \quad (1.2)$$

$$\mathcal{L}_{\text{fermion}} = \sum_{f=1}^{N_f} \bar{\psi}_f^\alpha(x) (\not{D}_{\alpha\beta} - m_f \delta_{\alpha\beta}) \psi_f^\beta(x), \quad (1.3)$$

where Greek letters are spinor indices, a is the color index, N_c is the number of colors ($N_c = 3$ for QCD) and m_f is the quark mass with flavor f . The covariant derivative \not{D} and the field strength tensor $F_{\mu\nu}^a$ read:

$$\not{D} = i(\partial_\mu - ig \frac{\lambda^a}{2} A_\mu^a) \gamma^\mu, \quad (1.4)$$

$$F_{\mu\nu}^a = \partial_\mu A_\nu^a - \partial_\nu A_\mu^a + gf^{abc} A_\mu^b A_\nu^c, \quad (1.5)$$

where A_μ^a are the gauge fields, ψ_f^α are the quark fields, λ^a are the generators of $\text{SU}(N_c)$, f_{abc} are the corresponding structure constants and g is the bare coupling constant.

The partition function of QCD in the Euclidean path-integral formalism is given by:

$$\mathcal{Z}(T, V) = \int \prod_{\mu} \mathcal{D}A_{\mu} \prod_{f=1}^{N_f} \mathcal{D}\psi_f \mathcal{D}\bar{\psi}_f \exp(-S_E[T, V, A_{\mu}, \psi_f, \bar{\psi}_f, g, m_f]), \quad (1.6)$$

where the Euclidean action S_E reads:

$$S_E[T, V, A_{\mu}, \psi_f, \bar{\psi}_f, g, m_f] = \int_0^{1/T} d\tau \int_V d^3\mathbf{x} \mathcal{L}_{QCD}^E[A_{\mu}, \psi_f, \bar{\psi}_f, g, m_f], \quad (1.7)$$

where the Euclidean Lagrangian \mathcal{L}_{QCD}^E is obtained from Eq. (1.1) by going from Minkowski to Euclidean space, i.e. substituting $t \rightarrow -i\tau$ with $\tau \in \mathbb{R}$ and reads as follows

$$\begin{aligned} \mathcal{L}_{QCD}^E &= \mathcal{L}_{gluon}^E + \mathcal{L}_{fermion}^E \\ &= \frac{1}{4} F_a^{\mu\nu}(x) F_{\mu\nu}^a + \sum_{f=1}^{N_f} \bar{\psi}_f^{\alpha}(x) \left(\not{D}_{\alpha\beta}^E + m_f \delta_{\alpha\beta} \right) \psi_f^{\beta}(x). \end{aligned} \quad (1.8)$$

Now the Euclidean covariant derivative turns into

$$\not{D}^E = \gamma_{\mu}^E D_{\mu}^E = \left(\partial_{\mu} + ig \frac{\lambda_a}{2} A_{\mu}^a \right) \gamma_{\mu}^E, \quad (1.9)$$

where the γ_{μ}^E and λ_a are the Euclidean Dirac matrices and $SU(N_c)$ generators given in the appendices A.1 and A.2. The thermal expectation value of physical observables can be obtained through:

$$\langle \mathcal{O} \rangle = \frac{\int \prod_{\mu} \mathcal{D}A_{\mu} \prod_{f=1}^{N_f} \mathcal{D}\psi_f \mathcal{D}\bar{\psi}_f \mathcal{O} \exp(-S_E)}{\int \prod_{\mu} \mathcal{D}A_{\mu} \prod_{f=1}^{N_f} \mathcal{D}\psi_f \mathcal{D}\bar{\psi}_f \exp(-S_E)}. \quad (1.10)$$

In practice there are basically two ways to evaluate Eq. (1.10). One way is to use perturbative methods but then the magnitude of the momenta is limited by a finite cut-off Λ . The other way is lattice gauge theory as mentioned before. It is a theory regularized on a four-dimensional discretized Euclidean space-time. After introducing a hyper-cubic lattice of size $N_{\sigma}^3 \times N_{\tau}$ with a small but finite lattice spacing a and defining the fields on the lattice sites, Eq. (1.10) becomes multiple integrations and can be computed via e.g. Monte Carlo simulations. The volume V as well as the the temperature T on the lattice are related to its spatial and temporal extents

$$V = (aN_{\sigma})^3, \quad T = \frac{1}{aN_{\tau}}, \quad (1.11)$$

where N_{σ} and N_{τ} are the number of discretized points in spatial and temporal directions, respectively. A consequence of lattice gauge theory is that some of the symmetries, e.g. the Lorentz symmetry, are lost. Since all the symmetries are restored in the

continuum limit, in order to recover the real physics, we remove the discretization by taking the continuum limit $a \rightarrow 0$ at fixed V and T ($N_\tau \rightarrow \infty$) and the thermodynamic limit $V \rightarrow \infty$ ($N_\sigma \rightarrow \infty$). Consequently the infrared and ultraviolet momentum cut-off $\tilde{\Lambda} = \pi/(aN_\sigma)$, $\Lambda = \pi/a$ goes to zero and infinity, respectively.

At finite a the “errors” of lattice observables mainly include discretization effects and finite volume effects. To make the error small one needs to obey the following inequality

$$a \ll \xi \ll aN_\sigma \quad (1.12)$$

with ξ being the correlation length of the particle to be investigated. For instance ξ is proportional to the inverse of the particle mass m , so the discretization effects should be small if $am \ll 1$ and the finite volume effects should be small if $amN_\sigma \gg 1$.

In the following sections we will briefly review the discretized version of fields we used in our simulation, the simulation techniques and parameters employed as well as the scale determination and the renormalization of quantities on the lattice.

1.1 Gluon fields on the lattice

The gluon fields are represented by the elements of the non-abelian SU(3) group. On the lattice they are defined as the links between lattice sites connecting site na to $(n + \hat{\mu})a$ in the μ direction

$$U_\mu(n) = \mathcal{P} \exp \left(iga \int_{na}^{(n+\hat{\mu})a} dy A_\mu(y) \right), \quad (1.13)$$

where \mathcal{P} denotes path ordering, $A_\mu = \sum_{a=1}^{N_c^2-1} \frac{\lambda^a}{2} A_\mu^a$. The trace of any path ordered gauge field product on a closed loop is gauge invariant. The simplest closed loop is the plaquette

$$U_{\mu\nu}(n) \equiv U_\mu(n)U_\nu(n + \hat{\mu})U_{-\mu}(n + \hat{\mu} + \hat{\nu})U_{-\nu}(n + \hat{\nu}) \quad (1.14)$$

$$= U_\mu(n)U_\nu(n + \hat{\mu})U_\mu^\dagger(n + \hat{\nu})U_\nu^\dagger(n), \quad (1.15)$$

where the property $U_\mu(n) = U_{-\mu}^\dagger(n + \hat{\mu})$ of the gauge links is used.

The Wilson action for the gauge field is given by a sum over plaquette variables $U_{\mu\nu}(n)$:

$$S_G = \beta \sum_{n,\mu<\nu} \left(1 - \frac{1}{N_c} \text{Re Tr } U_{\mu\nu}(n) \right), \quad (1.16)$$

where the gauge coupling β is related with the bare coupling g through $\beta = 2N_c/g^2$.

To reproduce the continuum gauge action an expansion in powers of the lattice spacing a and the coupling g needs to be performed. Using the Baker-Campbell-Hausdorff

formula $e^A e^B = e^{A+B+1/2[A,B]+\dots}$ and expanding the plaquette (1.15) about $n + \frac{\hat{\mu}+\hat{\nu}}{2}$ gives

$$U_{\mu\nu}(n) = \exp \left\{ iga^2 \left(\partial_\mu A_\nu(na) - \partial_\nu A_\mu(na) + ig [A_\mu(na), A_\nu(na)] \right) + \mathcal{O}(a^3) \right\}, \quad (1.17)$$

so that one arrives at the continuum gauge action with corrections starting at $\mathcal{O}(a^2)$ in $\mathcal{O}(g^0)$:

$$\begin{aligned} S_G &= a^4 \sum_{n,\mu<\nu} (\text{Tr } F_{\mu\nu}(n) F^{\mu\nu}(n) + \mathcal{O}(a^2)) + \mathcal{O}(g^2 a^2) \\ &\xrightarrow{a \rightarrow 0} \frac{1}{2} \int_V d^3 \mathbf{x} \int_0^{1/T} d\tau \text{Tr} (F_{\mu\nu}(n) F^{\mu\nu}(n)) + \mathcal{O}(g^2), \end{aligned} \quad (1.18)$$

where $F_{\mu\nu}$ is the field strength tensor

$$F_{\mu\nu}(x) = \partial_\mu A_\nu(n) - \partial_\nu A_\mu(n) + ig [A_\mu(n), A_\nu(n)]. \quad (1.19)$$

One can improve the gauge action to the higher orders of corrections, e.g. by adding further gauge invariant terms. But the further improvement requires a larger computing effort and does not reduce the overall error of the complete action. Since in our work the lattice spacing is already quite small, we used the standard Wilson gauge action (1.16) in our simulation.

1.2 Matter fields on the lattice

1.2.1 Naïve action and fermion doublers

On the lattice the fermion fields $\psi(n)$ are defined on the lattice sites. The naïve discretized form of the continuum action is

$$S_F = \sum_{n,l,\alpha,\beta} \hat{\psi}_\alpha(n) M_{\alpha\beta}(n,l) \hat{\psi}_\beta(l), \quad (1.20)$$

where the fermion matrix reads

$$M_{\alpha\beta}(n,l) = \frac{1}{2} \sum_\mu (\gamma_\mu)_{\alpha\beta} \left[U_\mu(n) \delta_{l,n+\hat{\mu}} - U_\mu^\dagger(n - \hat{\mu}) \delta_{l,n-\hat{\mu}} \right] + \hat{m} \delta_{ln} \delta_{\alpha\beta}, \quad (1.21)$$

here the symbols with hats are dimensionless quantities obtained with the help of transformations, e.g. $\hat{m} = ma$ and $\hat{\psi} = \psi a^{3/2}$. To check to which degree the naïve fermion action (1.20) reproduces the continuum one we need to expand the naïve action in powers of the lattice spacing a . For a gauge link this expansion reads

$$U_\mu(n) = \mathbb{1} + iga \left[A_\mu(na) + \frac{1}{2} a \partial_\mu A_\mu(na) + \frac{1}{6} a^2 \partial_\mu^2 A_\mu(na) + \mathcal{O}(a^3) \right] + \mathcal{O}(a^2 g^2). \quad (1.22)$$

Inserting the above expression into the lattice action (1.20), one arrives at

$$\begin{aligned}
S_F &= a^4 \sum_n \left\{ \sum_\mu \left(\gamma_\mu^{\alpha\beta} \right) \bar{\psi}_\alpha(na) \frac{1}{2a} \left[\psi_\beta((n+\mu)a) - \psi_\beta((n-\mu)a) \right. \right. \\
&\quad \left. \left. + ig a \left(A_\mu(na) \psi_\beta((n+\mu)a) + A_\mu((n-\mu)a) \psi_\beta((n-\mu)a) \right) \right] \right. \\
&\quad \left. + m \psi_\alpha(na) \psi_\beta(na) \delta^{\alpha\beta} \right\} + \mathcal{O}(a^5) \tag{1.23}
\end{aligned}$$

$$\begin{aligned}
&\xrightarrow{a \rightarrow 0} \int_V d^3x \int_0^{1/T} d\tau \bar{\psi}^\alpha(x) (\not{D}_{\alpha\beta} + m \delta_{\alpha\beta}) \psi^\beta(x). \tag{1.24}
\end{aligned}$$

Thus the continuum fermion action is reproduced up to order $\mathcal{O}(a^2)$.

The propagator of a free fermion in the momentum space is obtained by the Fourier transform of the inverse of the fermion matrix

$$\tilde{M}_{\alpha\beta}^{-1} \propto \frac{\left(m - i \sum_\mu \gamma_\mu \tilde{p}_\mu \right)_{\alpha\beta}}{m^2 + \sum_\mu \tilde{p}_\mu^2}, \tag{1.25}$$

where \tilde{p}_μ is given by $\tilde{p}_\mu = \sin(p_\mu a)/a$. For $\tilde{p}_\mu \rightarrow p_\mu$ Eq. (1.25) will give the familiar continuum propagator in the continuum limit. However as the momentum p_μ is restricted to the so called Brillouin zone (BZ) $[-\pi/a, \pi/a]$, the zeros of the sine-function at the edges of the BZ would destroy the correct continuum limit. Thus there exist 16 poles where \tilde{p}_μ takes a finite value in the limit of $a \rightarrow 0$. Only one of them, $p = (0, 0, 0, 0)$, corresponds to the physical single particle propagator and each of the additional 15 ones involving high momentum excitation of the order of π/a (and $-\pi/a$) corresponds to an unwanted particle state which is called a ‘‘doubler’’. Since locality is a mandatory property and because of the no-go theorem [49], all the lattice actions have to be a compromise between breaking chiral symmetry and allowing doublers. There are quite a few different discretized versions of fermion actions, e.g. Staggered fermions [50–52], domain wall fermions [53–55] and Wilson fermions [45]. Here in this work since we focus on the spectroscopy and properties of charmonium states, the number of points in the temporal directions is very important as we will see in the following chapters. Due to this and also due to the available computing resource we will use Wilson fermions as described in the next section.

1.2.2 Wilson fermions

To avoid doublers Wilson proposed to add a new dimension 5 operator, $\frac{1}{2} \bar{\psi} D_\mu^2 \psi$, which vanishes in the continuum limit:

$$\frac{1}{2} \bar{\psi} D_\mu^2 \psi = \hat{\psi}(n) \sum_\mu \left\{ U_\mu(n) \delta_{n+\hat{\mu},l} + U_\mu^\dagger(n-\hat{\mu}) \delta_{n-\hat{\mu},l} - 2\delta_{n,l} \right\} \hat{\psi}(l). \tag{1.26}$$

The new fermion matrix then becomes

$$M_{\alpha\beta}^W(n, l) = (\hat{m}+4)\delta_{n,l}\delta_{\alpha\beta} - \frac{1}{2} \sum_{\mu} \left\{ (\mathbb{1} - \gamma_{\mu})_{\alpha\beta} U_{\mu}(n) \delta_{n+\hat{\mu},l} + (\mathbb{1} + \gamma_{\mu})_{\alpha\beta} U_{\mu}^{\dagger}(n-\hat{\mu}) \delta_{n-\hat{\mu},l} \right\}. \quad (1.27)$$

With a redefinition of the dimensionless fermion fields $\tilde{\psi}(n) = \sqrt{\hat{m}+4} \hat{\psi}(n)$ the matrix changes into:

$$\tilde{M}_{\alpha\beta}^W(n, l) = \delta_{n,l} \delta_{\alpha\beta} - \kappa \sum_{\mu} \left\{ (\mathbb{1} - \gamma_{\mu})_{\alpha\beta} U_{\mu}(n) \delta_{n+\hat{\mu},l} + (\mathbb{1} + \gamma_{\mu})_{\alpha\beta} U_{\mu}^{\dagger}(n-\hat{\mu}) \delta_{n-\hat{\mu},l} \right\}, \quad (1.28)$$

where κ is the hopping parameter: $\kappa = 1/(2\hat{m}+8)$. Consequently the fermion propagator becomes:

$$(M^W(p))_{\alpha\beta}^{-1} \propto \frac{\left(-i \sum_{\mu} \gamma_{\mu} \sin(p_{\mu}a)/a + m(p) \right)_{\alpha\beta}}{\sum_{\mu} \sin^2(p_{\mu}a)/a^2 + m^2(p)}, \quad (1.29)$$

where

$$m(p) = m + \frac{2}{a} \sum_{\mu} \sin^2(p_{\mu}a/2). \quad (1.30)$$

The new propagator indicates that the doubler receives an additional mass, which is proportional to inverse lattice spacing. If the lattice spacing is small enough, the doubler masses would be very heavy and thus their contribution is small and vanishes in the continuum limit.

To reduce the lattice cutoff errors to $\mathcal{O}(a^2)$ Sheikholeslami and Wohlert [56] used the procedure proposed by Symanzik [57]. They added additional counter terms of dimension $d > 4$ to the pure Lagrangian and tuned coefficients such that all contribution of order $\mathcal{O}(a^{d-4})$ could be eliminated. In this way the $\mathcal{O}(a)$ -improved Sheikholeslami-Wohlert action (also called clover action) S_F^{SW} reads

$$S_F^{SW} = \sum_{n,l} \tilde{\psi}(n) \tilde{M}^{SW}(n, l) \tilde{\psi}(l) \quad (1.31)$$

with $\tilde{\psi} = \psi/\sqrt{2\kappa}$ and the fermion matrix

$$\tilde{M}^{SW}(n, l) = A(n)\delta_{n,l} - \kappa \Delta_{n,l}, \quad (1.32)$$

where

$$\Delta_{n,l} = \sum_{\mu} (\mathbb{1} - \gamma_{\mu}) U_{\mu}(n) \delta_{n+\mu,l} + (\mathbb{1} + \gamma_{\mu}) U_{\mu}^{\dagger}(n-\mu) \delta_{n-\mu,l} \quad (1.33)$$

and the correction term

$$A(n) = \mathbb{1} - ig \frac{\kappa c_{SW}}{2} \sigma^{\mu\nu} F_{\mu\nu}, \quad (1.34)$$

where

$$F_{\mu\nu}(n) = -\frac{i}{8g} \sum_j \left(U_{\mu\nu}^j(n) - U_{\mu\nu}^{j\dagger}(n) \right), \quad (1.35)$$

with an additional mass parameter m' . By definition X' vanishes in the continuum limit. Putting X' into Eq. (1.39) one obtains the following relation in the continuum limit

$$\langle \alpha | \partial^\mu (Z_A A_\mu) | \beta \rangle = \langle \alpha | \bar{\psi} \{T_a, m_q\} \gamma_5 \psi | \beta \rangle. \quad (1.42)$$

Hence the axial current is conserved for a vanishing quark mass $m_q = m - m'$.

Using $\langle \alpha | = \langle 0 |$ and $| \beta \rangle = | P \rangle$ (a pion state) in Eq. (1.42) and integrating over space leads to the definition of the AWI quark mass

$$m_{\text{AWI}}(\tau) = \frac{\sum_{\mathbf{x}} \langle \partial_\mu (Z_A A_\mu(\tau, \mathbf{x})) P^\dagger(0) \rangle}{\sum_{\mathbf{x}} \langle P(\tau, \mathbf{x}) P^\dagger(0) \rangle}. \quad (1.43)$$

Since the fourth component of the axial current has the largest overlap with the pion state, we determine m_{AWI} through relation (1.43) by setting $\mu = 4$ in practice. The signal of the AWI quark mass can be improved by using a higher lattice derivative to $\mathcal{O}(a^4)$ following Ref. [60]. The result from (1.43) can be further improved by the redefinition of the currents

$$A_\mu^I = A_\mu + a c_A \tilde{\nabla}_\mu P, \quad (1.44)$$

$$V_\mu^I = V_\mu + a c_V \tilde{\nabla}_\nu T_{\mu\nu}, \quad (1.45)$$

where $\tilde{\nabla} = \frac{1}{2}(\Delta^b + \Delta^f)$, Δ^f (Δ^b) is the forward (backward) derivative on the lattice and $T_{\mu\nu} = \bar{\psi} \sigma_{\mu\nu} \psi$ denotes the tensor current. The coefficient c_A has been determined non-perturbatively [58]

$$c_A = -0.00756 \frac{1 - 0.748g^2}{1 - 0.977g^2} g^2 \quad \text{with} \quad 0 \leq g \leq 1, \quad (1.46)$$

and the coefficient c_V almost vanishes for $\beta > 6.4$ [61].

1.3 The continuum limit of lattice QCD

As addressed before, the lattice regularization introduces a finite momentum cut-off and breaks some symmetries. These consequences should be removed in the thermodynamic limit $V \rightarrow \infty$ and in the continuum limit $a \rightarrow 0$.

The quantities $\mathcal{O}(g(a), a)$ on the lattice are all rescaled through lattice spacing a to be dimensionless quantities $\hat{\mathcal{O}}(g(a), a)$

$$\lim_{a \rightarrow 0} \mathcal{O}(g(a), a) = \lim_{a \rightarrow 0} \left(\frac{1}{a}\right)^{d_O} \hat{\mathcal{O}}(g(a), a) = O_{\text{phys}}, \quad (1.47)$$

where d_O is the dimension of the lattice observable $\mathcal{O}(g(a), a)$ and O_{phys} is the physical continuum observable. The continuum limit is reached when $g \rightarrow 0$ due to asymptotic freedom. When close to the continuum limit, the observable measured on the lattice

should be independent of the lattice spacing a , leading to the renormalization group equation

$$\left[a \frac{\partial}{\partial a} - \beta(g) \frac{\partial}{\partial g} \right] \mathcal{O}(g(a), a) = 0, \quad (1.48)$$

which can be solved in the perturbative regime and leads to the β function defined as

$$\beta(g) = -a \frac{\partial g}{\partial a}, \quad (1.49)$$

which has been computed perturbatively up to fourth order

$$\beta(g) = -\beta_0 g^3 - \beta_1 g^5 - \beta_2 g^7 - \beta_3 g^9 + \mathcal{O}(g^{11}). \quad (1.50)$$

The coefficients for SU(3) in the $\overline{\text{MS}}$ scheme are [62]

$$\beta_0 = \frac{1}{(4\pi)^2} \left(11 - \frac{2}{3} N_f \right), \quad (1.51)$$

$$\beta_1 = \frac{1}{(4\pi)^4} \left(102 - \frac{38}{3} N_f \right), \quad (1.52)$$

$$\beta_2 = \frac{1}{(4\pi)^6} \left(\frac{2857}{2} - \frac{5033}{18} N_f + \frac{325}{54} N_f^2 \right), \quad (1.53)$$

$$\begin{aligned} \beta_3 = \frac{1}{(4\pi)^8} & \left(\frac{149753}{6} + 3564 \zeta_3 + \left(-\frac{1078361}{162} - \frac{6508}{27} \zeta_3 \right) N_f \right. \\ & \left. + \left(\frac{50065}{162} + \frac{6472}{81} \zeta_3 \right) N_f^2 + \frac{1093}{729} N_f^3 \right). \end{aligned} \quad (1.54)$$

ζ is Riemann's zeta function, with $\zeta_3 \approx 1.202057$. N_f is the number of quark flavors. Note the first two coefficients β_0 and β_1 are independent of the renormalization scheme.

Using the two-loop order β function the differential equation (1.49) has the solution

$$g^{-2}(a) = 2\beta_0 \log \left(\frac{1}{a\Lambda} \right) + \frac{\beta_1}{\beta_0} \log \left(2 \log \left(\frac{1}{a\Lambda} \right) \right), \quad (1.55)$$

where Λ is the integration parameter ($a\Lambda \ll 1$) and depends on the renormalization scheme. Inverting Eq. (1.55) gives

$$a\Lambda = R(g^2) \equiv (\beta_0 g^2)^{-\beta_1/2\beta_0^2} \exp \left(-\frac{1}{2\beta_0 g^2} \right). \quad (1.56)$$

The above equation can be used to determine the physical scale of the lattice spacing a for given β at finite temperature by rescaling, e.g. see section 1.5.2. At finite lattice spacing there are corrections on the right hand side of Eq. (1.48), which can be reduced by improving actions and operators.

1.4 Simulation technique and error estimation

In this section we will briefly review the algorithm we used in the simulation and the way we employed to estimate the errors.

To evaluate thermal averages from Eq. (1.10) one has to deal with the multi-dimensional integral over gauge and fermion fields on the lattice. Monte Carlo simulation is suitable to do the job. One normally considers generating the configurations according to the Boltzmann weight $\exp(-S)$ to ensure a high hit efficiency and thus build a Markov chain of configurations. The expectation value of the observable of interest $\langle O \rangle$ is given by

$$\langle O \rangle = \lim_{N \rightarrow \infty} \frac{1}{N} \sum_{i=1}^N O[C_i], \quad (1.57)$$

where N is the number of configurations in the generated ensemble. The configurations generated after some finite number of thermalization steps should be distributed according to the probability $\exp(-S)$. This can be achieved by requiring the transition probability $P(C \rightarrow C')$ between two consecutive configurations to meet the detailed balance condition

$$\exp(-S(C))P(C \rightarrow C') = \exp(-S(C'))P(C' \rightarrow C). \quad (1.58)$$

which ensures the configuration approaches the phase region belonging to the thermal equilibrium of the system. Additionally the probability distribution has to be ergodic, i.e. $P(C \rightarrow C')$ should be finite for every configuration pair C and C' .

The partition function in lattice QCD can be written as

$$\begin{aligned} Z &= \int \mathcal{D}U \mathcal{D}\psi \mathcal{D}\bar{\psi} \exp(-\bar{\psi}M\psi - S_G(U)) \\ &= \int \mathcal{D}U \det M \exp(-S_G(U)) \end{aligned} \quad (1.59)$$

where $\mathcal{D}U$, $\mathcal{D}\psi$ and $\mathcal{D}\bar{\psi}$ are defined as $\mathcal{D}U = \prod_{\mu,n} dU_{\mu}(n)$, $\mathcal{D}\psi = \prod_n d\psi(n)$, $\mathcal{D}\bar{\psi} = \prod_n d\bar{\psi}(n)$, and M is the fermionic matrix. An enormous amount of computing time can be saved by setting $\det M = \text{constant}$, e.g. 1. This approximation is known as *quenched approximation*. Physically it corresponds to neglecting internal quark loops and the presence of gluon and valence quark fields only in the thermal background. Obviously it is not appropriate to implement this approximation for physics where the dynamic quark loop has a significant contribution, e.g. the study of the magnetic QCD equation of state [63]. But it is suitable for the qualitative understanding of the most features of QCD, where the contribution from gluon fields dominates. For instance, the hadron spectrum and decay constant calculations within the quenched approximation agree with the experimental values in an average 10% range [64–66]. Since in this work

our focus is on the spectroscopy of charmonium and also due to available computing resources, we will restrict ourselves to the quenched approximation.

To evaluate the thermal averages in Eq. (1.10) within the quenched approximation, one thus needs to determine the inverse of the fermion matrix $M^{-1}(x, y)$ on every gauge configuration. This can be done by solving the following inhomogeneous equation

$$M(x, y)\psi(y) = \phi(x) \quad (1.60)$$

with point-like sources $\phi(x)$ for every color-spin combination of the quark fields. Since $M(x, y)$ is a huge sparse matrix Eq. (1.60) can only be solved approximately by an iterative method, i.e. restricting the error function of residuals r , $\langle r, r \rangle = \langle M\psi - \phi, M\psi - \phi \rangle$, below some certain value ϵ . The Conjugate Gradient (CG) algorithm [67] requires M to be Hermitian and positive definite, a condition which can be fulfilled by replacing Eq. (1.60) with $M^\dagger M\psi = M^\dagger \phi$. An alternative is the application of algorithms which do not require Hermiticity, e.g. the stabilized bi-conjugate gradients (BiCGStab) algorithm [68]. It has been found that CG is fast for the case of large quark mass or above T_c while the BiCGStab performs better for small quark masses below T_c . The convergence time of both algorithms is governed by the ratio of the largest to the smallest eigenvalues of the matrix, which approaches infinity at vanishing quark mass $m_q \rightarrow 0$ ($\kappa \rightarrow \kappa_c$). Since in the current work we are focusing on the charmonium system, we utilize CG for both cases below and above T_c .

Additionally the even-odd preconditioning technique [69] has been used to accelerate the inversion of the matrix. It decouples the lattice into (e)ven and (o)dd sites. Consequently the equation $M\psi = \phi$ becomes

$$\begin{pmatrix} A_{ee} & -\kappa\Delta_{eo} \\ -\kappa\Delta_{oe} & A_{oo} \end{pmatrix} \begin{pmatrix} \psi_e \\ \psi_o \end{pmatrix} = \begin{pmatrix} \phi_e \\ \phi_o \end{pmatrix}, \quad (1.61)$$

where Δ and A are defined in Eq. (1.33) and (1.34). Multiplying the above relation with

$$\begin{pmatrix} \mathbb{1}_{ee} & \kappa\Delta_{eo}A_{oo}^{-1} \\ 0 & 0 \end{pmatrix} \quad (1.62)$$

one obtains

$$\tilde{M}_{ee}\psi_e = (A_{ee} - \kappa^2\Delta_{eo}A_{oo}^{-1}\Delta_{oe})\psi_e = \phi_e + \kappa\Delta_{eo}A_{oo}^{-1}\phi_o = \tilde{\phi}_e, \quad (1.63)$$

$$\psi_o = A_{oo}^{-1}(\phi_o + \kappa\Delta_{oe}\psi_e), \quad (1.64)$$

with a new source vector $\tilde{\phi}_e$ and a modified fermion matrix \tilde{M}_{ee} . After the inversion is done on the even sites of lattice through Eq. (1.63), the solution for the odd sites can be simply obtained by a back substitution through Eq. (1.64). The preconditioning procedure reduces the number of required iteration steps since the new matrix \tilde{M}_{ee}

contains κ^2 rather than κ . Consequently \tilde{M}_{ee} gets closer to the unity matrix when κ is very small. Further acceleration is achieved in our simulation due to the fact that $\frac{1-\gamma_\mu}{2}$ in Eq. (1.33) are projectors of rank 2 which can be decomposed from the four-spinor ψ into two two-spinors. This is utilized to save computing time in the matrix inversion routine [70].

Another important property we used to save computing time is the γ_5 hermiticity

$$\gamma_5 M^{-1}(x, y) \gamma_5 = (M^{-1})^\dagger(y, x). \quad (1.65)$$

Thus for computing two point relation functions, i.e. Eq. (2.34), one only needs to invert the fermion matrix once.

In our current simulation the typical lattice size is e.g. $128^3 \times 48$. The simulation of such a big lattice is strongly constrained by the available computing resources. Due to the typical size of the propagator, which is $N_\sigma^3 \cdot N_\tau \cdot N_c^2 \cdot 4^2 \cdot 16/1024^3 = 216$ GB, even in the parallel way the I/O could cost the same amount or even more computing time as the inversion of the fermion matrix. Thus we do not write/read the propagators to/from the storage devices and just use them as intermediate variables. To save additional computing time for the inversion of the fermion matrix we measure both the spatial and temporal correlators in one run. In addition we need to take care of the memory consumption due to the limited memory size of each CPU (500 MB) in our available machines. For a relatively small local lattice size of $16 \cdot 16 \cdot 16 \cdot 12^1$, we have to have $8 \cdot 8 \cdot 8 \cdot 8 = 4096$ CPUs in order to simulate our largest lattice size $128^3 \times 96$. The memory for the propagator itself in such a simulation is already around 150 MB and the additional memory required to store the matrix for the clover term is of the same order. We have to reduce the memory consumed by the codes to meet the restriction by the hardware. The only memory we can reduce is the one from the clover term, i.e. rather evaluating them in the real time than allocating space for them on the heaps. The details can be found in the appendix B.

In this work the local pseudo heat bath algorithm [71, 72] has been used to generate a new configuration after one sweep over the lattice. One further step is to reduce the autocorrelation time of the Markov chain, which can be done by using the overrelaxation update algorithm [73, 74]. In our simulation 5 overrelaxation steps have been performed between every heat bath update.

Systematic errors are taken to be the quenched approximation, finite size effects and scaling violations. Their influence will be discussed in the following analysis. The statistical errors due to a limited sample of configurations are unavoidable. Since the configurations as well as the final observable are statistically correlated, the naive error estimate would be suspicious and misleading. Thus the jackknife and bootstrap methods

¹Due to the even-odd preconditioning the local lattice size in each direction has to be even.

are applied for error estimation in the same data set and different data sets, respectively [75].

Given that f is a function of the observable x , in the Jackknife method one first divides the N data sets into N_b blocks with the same number of data sets n : $\{x_i^j\}_{i=1, n}^{j=1, N_b}$. By leaving one block out, one calculates the average over $N_b - 1$ blocks:

$$X_\ell = \frac{1}{n(N_b - 1)} \sum_{j \neq \ell} \sum_{i=1}^n x_i^j, \quad (1.66)$$

and then calculates the standard mean value of x

$$\bar{X} = \frac{1}{N_b} \sum_{\ell}^{N_b} X_\ell. \quad (1.67)$$

With the pseudo Jackknife data sets

$$\tilde{X}_\ell = N_b \bar{X} - (N_b - 1) X_\ell, \quad (1.68)$$

and let $f_\ell = f(\tilde{X}_\ell)$, the mean and variance of $f(x)$ given by Jackknife method is:

$$\bar{f} = \frac{1}{N_b} \sum_{\ell=1}^{N_b} f_\ell \quad \text{and} \quad \sigma^J(\bar{f}) = \sqrt{\frac{1}{N_b(N_b - 1)} \sum_{\ell=1}^{N_b} (f_\ell - \bar{f})^2}. \quad (1.69)$$

Given that F is a function of the distribution g and h , which are related with lattice observables $\{x_i\}_{i=1, N_1}$ and $\{y_i\}_{i=1, N_2}$ respectively, $F = F(g(x), h(y))$. The bootstrap method works as the following:

1. Divide the data sets into Jackknife blocks $\{g_\ell\}_{\ell=1, N_{b1}}$ and $\{h_\ell\}_{\ell=1, N_{b2}}$. The mean value of F is obtained from the Jackknife averages of distribution g and h over measurements of x and y , respectively: $\bar{F} = F(\bar{g}, \bar{h})$.
2. From the Jackknife blocks obtained from the first step, randomly pick up block i and j from distribution g and h , without avoiding double sampling. And then calculate the quantity over the selected data: $F_m = F(g_i, h_j)$.
3. Repeat steps 2 a large number of times, say N_{boot} . The bootstrap error is then given by

$$\sigma^B = \sqrt{\frac{1}{N_{\text{boot}} - 1} \sum_{m=1}^{N_{\text{boot}}} (F_m - \bar{F})^2}. \quad (1.70)$$

The auto correlation length in our data is small and normally we set block length to 10 in the Jackknife error estimation and $N_{\text{boot}} = 5000$ in the bootstrap procedure.

1.5 Simulation details

In this section the scale determination and the simulation parameters for the clover improved Wilson fermions as well as gauge fields are given. The tactics to tune the hopping parameter κ are presented and the discussion on the resulting meson masses is also given.

1.5.1 Simulation parameters

All the simulations are performed on the IBM-JUGENE computer at NIC Jülich and Blue Gene computers at BNL/NewYork with double precision numbers. The simulation parameters are shown in Table 1.1. The gauge field configurations have been generated with the standard Wilson gluon action on an isotropic lattice. All the subsequent configurations are separated by 500 sweeps, each with 5 overrelaxation steps per heat bath. We have simulated at three values of the bare coupling $\beta = 6/g^2 = 6.872, 7.457$ and 7.793 . At these β values the lattice spacing has been determined from the string tension parameterization from formula (1.71) [76].

For the fermion part the $\mathcal{O}(a)$ Symanzik-improved Sheikholeslami-Wohlert action has been implemented in our simulation with c_{SW} listed in Table 1.1. The inversion of the Dirac matrix was carried out by means of Conjugate Gradient algorithm. For the finest lattice, $\beta = 7.793$, we have measured two point correlation functions on $128^3 \times 96$, $128^3 \times 48$, $128^3 \times 32$ and $128^3 \times 24$ at $0.73 T_c$, $1.46 T_c$, $2.20 T_c$ and $2.93 T_c$, respectively. Due to the size of the currently simulated lattice and the correlation function decreasing exponentially with distance, we employed a rather small convergence value of 10^{-24} in the CG algorithm.

β	a [fm]	a^{-1} [GeV]	L_σ [fm]	c_{SW}	κ	$N_\sigma^3 \times N_\tau$	T/ T_c	N_{conf}
6.872	0.031	6.432	3.93	1.412488	0.13035	$128^3 \times 32$	0.74	126
						$128^3 \times 16$	1.49	198
7.457	0.015	12.864	1.96	1.338927	0.13179	$128^3 \times 64$	0.74	179
						$128^3 \times 32$	1.49	250
7.793	0.010	18.974	1.33	1.310381	0.13200	$128^3 \times 96$	0.73	234
						$128^3 \times 48$	1.46	461
						$128^3 \times 32$	2.20	105
						$128^3 \times 24$	2.93	81

Table 1.1. Lattice parameters and number of configurations for the clover improved Wilson fermion action. The non-perturbatively determined c_{SW} are obtained from Eq. (1.37).

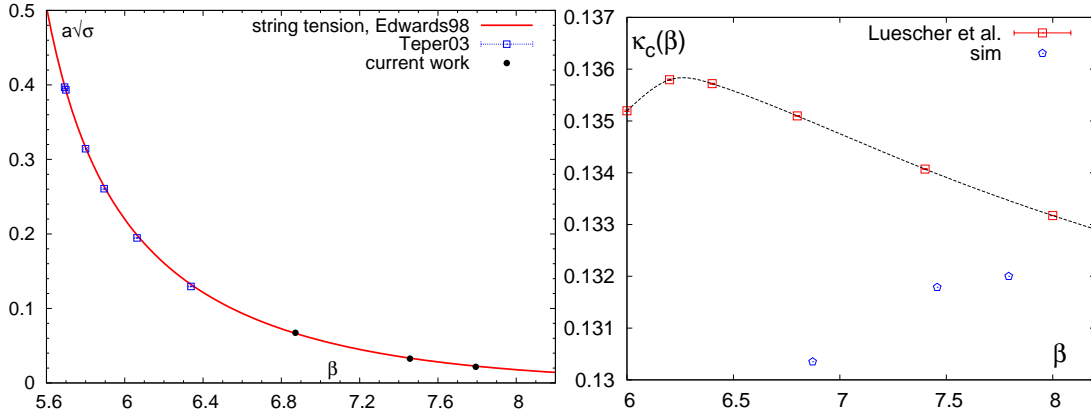


Figure 1.1. Left: The scale determination of $a\sqrt{\sigma}$ versus β . The label “string tension, Edwards98” denotes the results from Eq. (1.71) and “Teper03” labels the data points from Ref. [78]. “current work” means the β and a values we adopted in current work. Right: Critical hopping parameters κ_c versus β values from Ref. [58] by Lüscher et al., “sim” stands for the κ values used in our simulations.

1.5.2 Scale determination

As mentioned before, all the fields and observables defined on the lattice are in terms of the lattice spacing a such that only dimensionless quantities appear during the lattice simulation. The physical scale is then set by comparing lattice results with physical quantities, e.g. experiment results. There are several ways to fix the scale. Here we adopt the way using the square root of the string tension, $\sqrt{\sigma}$, which characterizes the long distance behavior of the static quarkonium potential $V_{q\bar{q}} = -\alpha/r + \sigma r$ at $T = 0$. For the Wilson gauge action Edwards et al. [76] parameterized the string tension in the range of $5.6 \leq \beta \leq 6.5$ using [77]

$$(a\sqrt{\sigma})(g) = R(g^2) \frac{1 + c_2 r^2(g) + c_4 r^4(g) + c_6 r^6(g)}{\lambda/\sqrt{\sigma}}, \quad (1.71)$$

$$r(g) \equiv \frac{R(g^2)}{R(g^2(\beta = 6.0))}, \quad (1.72)$$

where the constants $c_2 = 0.2731$, $c_4 = -0.01545$, $c_6 = 0.01975$, $\lambda/\sqrt{\sigma} = 0.01364$ and the function $R(g^2)$ is the universal two-loop scaling function of SU(3) gauge theory given in Eq. (1.56). The lattice spacing multiplied by the square root of the string tension $a\sqrt{\sigma}$ versus β is shown in the left plot of Fig. 1.1.

In order to obtain the physical temperature of the lattice in units of the critical one, for definiteness we have consistently chosen the string tension to set the scale by

$$T/T_c = (T/\sqrt{\sigma}) \cdot (\sqrt{\sigma}/T_c), \quad (1.73)$$

where $T_c/\sqrt{\sigma} = 0.630(5)$ is taken from [79]. Whenever converting to physical units we use a value for the string tension of $\sqrt{\sigma} = 428$ MeV. Thus T_c is 270 MeV. The lattice spacing $a(\beta)$ as well as the estimated T/T_c are listed in Table 1.1.

1.5.3 J/ψ mass tuning

Since the isotropic clover improved Wilson fermions are implemented in our simulation, in addition to the lattice spacing, i.e. the gauge coupling β , only one parameter, the hopping parameter κ needs to be tuned to reproduce the physical mass of the charmonia. Here we restrict ourselves to tune the κ value to reproduce the mass of charmonium in the vector channel, i.e. J/ψ . To hit the correct region of κ values in our simulation, we utilize the empirical relation between the Renormalization Group Invariant (RGI) quark mass and the meson mass in the vector channel of the lowest state.

The RGI quark mass is a physical quantity and does not depend on the scheme or the scale. The non-perturbative $\mathcal{O}(a)$ improved definition of the RGI quark mass is based on the bare quark mass m_q

$$m_{\text{RGI}} = Z_m Z [1 + b_m am_q] m_q \quad , \quad (1.74)$$

where the renormalization factor Z_m has been determined very precisely in the range of $6.0 \leq \beta \leq 6.5$ [80], the renormalization constant Z and the improvement coefficient b_m have been computed non-perturbatively in Ref. [60,81]. The coefficients appearing in the two definitions are all parameterized in terms of the bare coupling g_0 [80,81] and are listed as the following:

$$Z_m(g_0^2) = 1.752 + 0.321(6/g_0^2 - 6) - 0.220(6/g_0^2 - 6)^2, \quad (1.75)$$

$$Z(g_0^2) = (1 + 0.090514 g_0^2) \frac{1 - 0.9678 g_0^2 + 0.04284 g_0^4 - 0.04373 g_0^6}{1 - 0.9678 g_0^2}, \quad (1.76)$$

$$b_m(g_0^2) = -(0.5 + 0.09623 g_0^2) \frac{1 - 0.6905 g_0^2 + 0.0584 g_0^4}{1 - 0.6905 g_0^2}. \quad (1.77)$$

The bare quark mass am_q is related to the critical hopping parameter κ_c through relation (1.38). κ_c has been determined for some β values in Ref. [58] as shown in the right plot of Fig. 1.1. By doing an interpolation one can get the corresponding κ_c , which is also shown in the right plot of Fig. 1.1. Thus together with formula (1.74) the RGI quark mass for our β values can be obtained.

Collecting the data points from Refs. [39,82] and together with the experimental value of ρ mass [83], we plot the relation of meson masses in the vector channel M_{VC} versus the RGI quark mass m_{RGI} in Fig. 1.2. There is an approximately linear relation between M_{VC} and m_{RGI} with some ‘‘correct’’ κ values. Utilizing this empirical relation, we hit the κ values and the corresponding M_{VC} and m_{RGI} are shown as red points in Fig. 1.2.

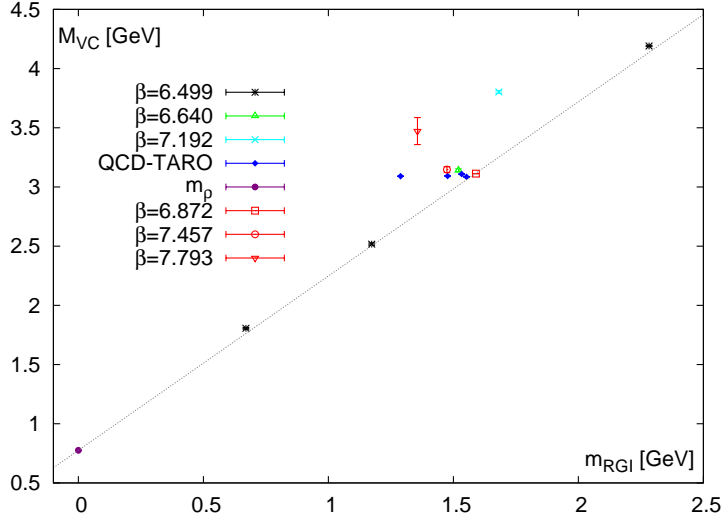


Figure 1.2. Meson mass in vector channel versus the RGI quark mass evaluated from Eq. (1.74). The data points for $\beta = 6.499, 6.640$ and 7.192 are obtained from Ref. [39]. “QCD-TARO” labels the data points from Ref. [82]. The red points of $\beta = 6.872, 7.457$ and 7.793 are from our current simulation.

The calculation of the RGI mass we did from Eq. (1.74) strongly depends on the accurate determination of κ_c since the bare quark mass m_q is used. At temperatures below the critical one, one can determine the bare quark mass m_q by searching for the critical hopping parameter κ_c , where the pion mass vanishes. When going above the critical temperature the chiral symmetry is restored, then the pion is no longer a Goldstone boson and has a non-zero mass. Thus instead one utilizes the AWI quark mass defined in Eq. (1.43) with the $\mathcal{O}(a)$ non-perturbatively improved currents Eq. (1.44). The AWI quark mass should be independent of temperature as well as of the temporal or spatial directions that used to measure the operator (1.44) since it is based on the operator identity and should hold for all distances. We find indeed there is no dependence on direction at both above and below critical temperature. Obviously the distance in the spatial direction is larger and is going to be mainly analyzed in this work.

The AWI quark mass is related to the RGI quark mass through

$$m_{\text{RGI}} = Z_m [1 + (b_A - b_P)am_q] m_{\text{AWI}}, \quad (1.78)$$

where the combination $b_A - b_P$ of the improvement coefficients of the axial current and pseudoscalar density has been non-perturbatively computed in Refs. [60, 81]:

$$(b_A - b_P)(g_0^2) = -0.00093 g_0^2 \frac{1 + 23.3060 g_0^2 - 27.3712 g_0^4}{1 - 0.9833 g_0^2}. \quad (1.79)$$

β	κ	κ_c	am_b	T/T_c	N_τ	am_{AWI}	$m_{\text{RGI}}[\text{GeV}]$	$m_{\overline{\text{MS}}}(m)[\text{GeV}]$
6.872	0.13035	0.13497	0.13130	0.74	32	0.13305(2)	1.592(4)	1.255(2)
				1.49	16	0.13305(2)	1.592(4)	1.255(2)
7.457	0.13179	0.13398	0.06201	0.74	64	0.065430(6)	1.4742(3)	1.1739(2)
				1.49	32	0.065352(4)	1.4734(8)	1.1733(6)
7.793	0.13200	0.13346	0.04143	0.73	96	0.044245(7)	1.358(3)	1.093(2)
				1.46	48	0.044222(2)	1.357(2)	1.094(1)
				2.20	32	0.044280(6)	1.359(3)	1.096(2)
				2.93	24	0.04420(1)	1.357(3)	1.095(2)

Table 1.2. Quark masses on available lattices. m_b stands for bare quark mass, m_{AWI} is obtained from the axial ward identity at the scale of $\mu = 1/a$ and $m_{\overline{\text{MS}}}(m)$ denotes the renormalized quark mass in $\overline{\text{MS}}$ scheme at scale of $\mu = m_{\overline{\text{MS}}}(\mu)$. The errors quoted in am_{AWI} are statistical errors while in m_{RGI} and $m_{\overline{\text{MS}}}(m)$ arise from the two different definitions of m_{RGI} in Eq. (1.74) and Eq. (1.78).

The RGI quark mass can be expressed in terms of running quark mass $m(\mu)$

$$m_{\text{RGI}} = \lim_{\mu \rightarrow \infty} m(\mu) (2b_0 g^2(\mu))^{-d_0/2b_0}, \quad (1.80)$$

where $b_0 = (11 - 2N_f/3)/(4\pi)^2$ and $d_0 = 8/(4\pi)^2$ are the lowest order perturbative coefficients of the renormalization group functions for SU(3) gauge theory. As mentioned before, the RGI quark mass is more a physical quantity, however, it is customary to quote the running quark masses in the $\overline{\text{MS}}$ scheme at some reference scale. In particular, for heavy quarks, e.g. charm quark, the reference scale is chosen to be equivalent to the running quark mass itself: $m_{\overline{\text{MS}}}(\mu) = \mu$. Starting from the scale $\mu_0 = 1/a$, with the coupling constant $g_{\overline{\text{MS}}}^2(\mu_0)$ in $\overline{\text{MS}}$ scheme quoted in Table. 1.4, the evolution of $m_{\overline{\text{MS}}}(\mu)$ to μ can be done using perturbative renormalization group functions which are known with four-loop accuracy [62, 84–86].

The quark masses are listed in Table 1.2. The errors quoted in m_{RGI} are estimated from the two definitions (1.74) and (1.78) since the statistical error arising from am_{AWI} is negligible. One can see that there is only a very small difference brought by the definitions. As we mentioned before, the m_{AWI} is independent of temperature, which consequently makes the RGI quark mass m_{RGI} and running quark mass $m_{\overline{\text{MS}}}(m)$ temperature independent.

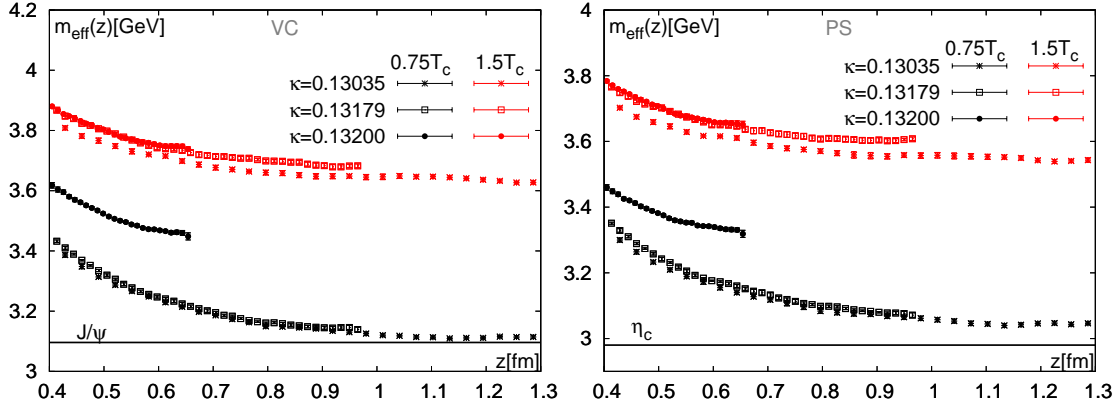
Since we haven't performed simulations on a zero temperature lattice, our estimate of the zero-temperature meson mass is obtained through the screening mass of the spatial correlator at temperatures below the critical temperature T_c ². In fact, the finite

²From the investigation on the dispersion relation in section 4.1, the screening mass is a good

Mass in GeV				
β	J/ψ	η_c	χ_{c1}	χ_{c0}
6.872	3.1127(6)	3.048(2)	3.624(36)	3.540(25)
7.457	3.147(1)(25)	3.082(2)(21)	3.574(8)	3.486(4)
7.793	3.472(2)(114)	3.341(2)(104)	4.02(2)(23)	4.52(2)(37)

Table 1.3. Meson masses.

Masses (in GeV) of the different charmonium states obtained from the screening mass plateau of the spatial correlators below T_c . The errors in the first bracket are the statistical errors and the errors in the second bracket are the errors brought by the limited physical distance.

**Figure 1.3.** The resulting screening masses for vector (left) and pseudo scalar (right) channels from lattice with $\kappa = 0.13035, 0.13179$ and 0.13200 at $T \approx 0.75 T_c$ and $T \approx 1.5 T_c$.

temperature (below confinement) lattice can be considered as a small (in one of the directions) zero temperature lattice. The resulting meson masses from the three κ values used in this work are listed in Table 1.3 and our lattice volumes are summarized in Table. 1.1. For our finest lattice the volume is $(1.33 \text{ fm})^3$. It has been found that even for a size of $(0.75 \text{ fm})^3$ there are no sizable finite volume effects on the quenched lattice [82]. Furthermore, for the light mesons, which have even larger sizes, their spatial correlators calculated on lattices at $0.9 T_c$ ($0.75 T_c$) have produced good estimates for the zero-temperature mass [87] and have a small volume dependence [88,89]. However, as seen from Table. 1.2, e.g. on our finest lattice with $\beta = 7.793$, the running quark mass $m_{\overline{\text{MS}}}(m)$ is smaller than the charm quark mass quoted in Refs. [83,90,91]. At the same time, the J/ψ mass is much larger than 3.097 GeV. Thus there could be finite volume

approximation of the pole mass at temperatures below T_c in our current work.

effects which bring the mass of J/ψ up. In addition, on our finest lattice the physical distance in the spatial direction does not allow us to observe a clear plateau of the screening mass (see Fig. 1.3). But if we focus on the relative change of the properties of charmonium systems at different temperatures, these effects should be under control.

1.6 Renormalization constants

In the current work we consider the local current $J_H^{lat}(\tau, \mathbf{x})$, which has the form of

$$J_H^{lat}(\tau, \mathbf{x}) = \bar{q}(\tau, \mathbf{x}) \Gamma_H q(\tau, \mathbf{x}), \quad (1.81)$$

with Γ_H the γ matrices for different channels. To connect to the continuum case, one has to do the renormalization. Following the transformation in Eq. (1.28), we have

$$J_H^{cont} = 2\kappa Z_H J_H^{lat} a^{-3}. \quad (1.82)$$

The calculation of the renormalization constants Z_H for the currents, which can be defined perturbatively and non-perturbatively, is presented in the following.

The perturbative calculation of Z_H is available at both one-loop and two-loop orders. The one loop calculation of the renormalization constants of some bilinear quark operators for improved Wilson fermions at vanishing quark mass in the quenched approximation [92] has the form of

$$Z_H = 1 - \frac{g^2}{16\pi^2} C_F (\gamma_{\mathcal{O}} \ln(a\mu) + B_{\mathcal{O}}), \quad (1.83)$$

where $C_F = \frac{4}{3}$, $\gamma_{\mathcal{O}}$ is the anomalous dimension and $B_{\mathcal{O}}$ is the finite part of the renormalization constant, which is parameterized as a function of c_{SW} . The values and parameterization form of $\gamma_{\mathcal{O}}$ and $B_{\mathcal{O}}$ can be read off from Ref. [92]. In the lowest order perturbation theory $c_{\text{SW}} = 1$. Thus during the evaluation of Eq. (1.83) c_{SW} needs to be set to 1.

Since the renormalization constants calculated from lattice perturbation theory often deviate far from the non-perturbative ones, tadpole improvement was proposed to enhance the predictive power of lattice perturbation theory [92–94]. The renormalization constants in the Landau gauge with tadpole improvement read [95]:

$$Z_H = u_0(g^2) \left(1 - \frac{g_P^2}{16\pi^2} C_F (\gamma_{\mathcal{O}} \ln(a\mu) + B_{\mathcal{O}} - \pi^2) \right), \quad (1.84)$$

with u_0 approximated by the fourth root of the plaquette expectation value [96]

$$u_0 = 1 - \frac{g^2}{16\pi^2} C_F \pi^2 + \mathcal{O}(g^4) \simeq \left\langle \frac{1}{N_c} \sum_x \text{Re Tr } U_{\mu\nu}(x) \right\rangle^{1/4}, \quad (1.85)$$

which can be calculated non-perturbatively on the lattice. One way to define the tadpole improved coupling is given by $g_P^2 = g^2/u_0^4$ [97]. It is more common to replace g_P^2 with $g_{\overline{\text{MS}}}^2$ to perform the calculation in the $\overline{\text{MS}}$ scheme.

To compute $g_{\overline{\text{MS}}}^2$ one starts with the determination of the coupling g_V in the V scheme, which is defined by the potential $V(\mu) = -C_F g_V^2(\mu)/\mu^2$. The plaquette expectation value can be expanded in terms of g_V^2 in the quenched case as follows [97]

$$-\ln(u_0^4) = \frac{C_F g_V^2(\mu^*)}{4} \left[1 - \frac{g_V^2(\mu^*)}{4\pi} \left(\frac{11N_c}{12\pi} \ln \left(\frac{6.7117}{\mu^*} \right)^2 \right) \right] + \mathcal{O}(g_V^6(\mu^*)), \quad (1.86)$$

whereby the matching should be most accurate at the scale $\mu^* = 3.4018/a$ [97]. With the plaquette expectation value quoted in Table 1.4 the evolution of coupling g to the scale $\mu = 1/a$ can be carried out with the standard two loop renormalization group equation through Eq. (1.55). The relation of scale parameters between the $\overline{\text{MS}}$ scheme and the V scheme is $\Lambda_{\overline{\text{MS}}} = 0.6252\Lambda_V$ [93]. The resulting $g_{\overline{\text{MS}}}^2(\mu = 1/a)$ are listed in Table 1.4.

The two-loop order perturbative calculation is available only since recently [98]. The renormalization constants can be written as:

$$\begin{aligned} Z_H^{\text{bare}}(g^2, a\mu) = & 1 + \frac{g^2}{16\pi^2} (-\gamma_0 \ln(a\mu) + z_1) \\ & + \left(\frac{g^2}{16\pi^2} \right)^2 (l_1 \ln^2(a\mu) + l_2 \ln(a\mu) + z_2). \end{aligned} \quad (1.87)$$

The coefficients l_1, l_2, z_1, z_2 can be read off from Refs. [99, 100] as functions of c_{SW} in terms of the bare coupling constants in the renormalized Feynman gauge.

To set up tadpole improvement we need the expansion [101]

$$\begin{aligned} u_0 &= 1 + r_1 \frac{g^2}{16\pi^2} + r_2 \left(\frac{g^2}{16\pi^2} \right)^2 + \mathcal{O}(g^6) \\ &= 1 + r_1 \frac{g_{\text{LAT}}^2}{16\pi^2} + (r_2 - 16\pi^2 r_1 p_1) \left(\frac{g_{\text{LAT}}^2}{16\pi^2} \right)^2 + \mathcal{O}(g_{\text{LAT}}^6), \end{aligned} \quad (1.88)$$

with the above expansion and Eq. (1.87), we arrive at [101]

$$\begin{aligned} Z_H^{\text{LAT}}(g_{\text{LAT}}^2, a\mu) = & u_0 \left[1 + \frac{g_{\text{LAT}}^2}{16\pi^2} (-\gamma_0 \ln(a\mu) + z_1 + C_F \pi^2) \right. \\ & + \left(\frac{g_{\text{LAT}}^2}{16\pi^2} \right)^2 \left(l_1 \ln^2(a\mu) + (l_2 + 16\pi^2 p_1 \gamma_0 + r_1 \gamma_0) \ln(a\mu) \right. \\ & \left. \left. + z_2 - r_2 - 16\pi^2 p_1 (z_1 - r_1) + r_1^2 - r_1 z_1 \right) + \mathcal{O}(g_{\text{LAT}}^6) \right], \end{aligned} \quad (1.89)$$

where

$$g_{\text{LAT}}^2 = g^2/u_0^4, \quad (1.90)$$

$$p_1 = \frac{1}{3}, \quad p_2 = -\frac{2r_2 + 3r_1^2}{128\pi^4}, \quad (1.91)$$

and r_1, r_2 can be found in Ref. [102]. In a similar way to the one-loop perturbative calculations, g_{LAT}^2 is replaced by $g_{\overline{\text{MS}}}^2$ to perform the calculation in the $\overline{\text{MS}}$ scheme.

More reliable renormalization constants can be obtained by non-perturbative calculations, which have been done for vector and axial vector mesons with nearly vanishing quark mass in the range: $6.0 \leq \beta \leq 24.0$ and $0.0 \leq g_0 \leq 1$ [103]. The fitting parameterization with the data reads:

$$Z_{VC} = \frac{1 - 0.7663 g_0^2 + 0.0488 g_0^4}{1 - 0.6369 g_0^2}, \quad (1.92)$$

$$Z_{AV} = \frac{1 - 0.8496 g_0^2 + 0.0610 g_0^4}{1 - 0.7332 g_0^2}. \quad (1.93)$$

It is worth noting that the one-loop perturbative calculations for the PS (pseudo scalar) and AV (axial vector) channels from more recent Refs. [99, 100] (one-loop part of Eq. (1.89)) differ from the previous calculation done in Ref. [92] (Eq. (1.84)), while for the VC (vector) and SC (scalar) channels the results from these two groups coincide. In Fig. 1.4 we show the renormalization constants at vanishing quark mass obtained from different approaches in the AV, VC, PS and SC channels. The label ‘‘1-loop SP09’’ denotes the calculation from Ref. [99, 100] and the label ‘‘1-loop Gockeler97’’ for the results from Ref. [92]. Non-perturbative calculations are only available for the VC and AV channels and it is hard to tell the convergent behavior of lattice perturbation theory from Fig. 1.4. Thus in the data analysis one should try to study the renormalization independent quantities more, e.g. the ratio of two correlators. As pointed out by the authors of Refs. [99, 100], there are terms missing in the calculation for PS and AV done in Ref. [92]. Thus in what follows, we will quote one-loop perturbative renormalization constants from the one-loop part of Eq. (1.89). The renormalization constants at vanishing quark masses for our simulated β values are summarized in Table 1.5.

For the currents with non-vanishing quark mass the renormalization constants are given by:

$$Z_H(am_q, g_{\overline{\text{MS}}}^2) = Z_H(g_{\overline{\text{MS}}}^2, a\mu = 1) (1 + b_H(g_{\overline{\text{MS}}}^2)am_q), \quad (1.94)$$

where the coefficients $b_H(g_{\overline{\text{MS}}}^2)$ can be expanded in powers of the coupling,

$$b_H(g_{\overline{\text{MS}}}^2) = 1 + C_F b_H g_{\overline{\text{MS}}}^2, \quad (1.95)$$

which has been calculated at one loop level [94, 104]. In particular, b_H for the vector channel has been determined non-perturbatively and is parameterized as follows

$$b_{VC} = \frac{1 - 0.6518 g_0^2 - 0.1226 g_0^4}{1 - 0.8467 g_0^2}. \quad (1.96)$$

But the non-perturbative determination of b_{AV} requires a very sophisticated approach. However, if one is interested in situations where am_q is very small (say less than 0.01), a perturbative estimate of b_{AV} may be perfectly satisfactory [103].

In practice, for the vector channels, the non-perturbatively determined renormalization constants are used; for the axial vector channels, the renormalization constants obtained through relations (1.93) and (1.94) with a perturbatively determined b_{AV} are used; for the scalar and pseudo scalar channels, the renormalization constants obtained through the formula (1.94) and the one-loop part of formula (1.89) are used. These renormalization constants are listed in Table. 1.6.

β	u_0	$g_{\overline{\text{MS}}}^2(1/a)$
6.872	0.902626	1.70310
7.457	0.913450	1.43185
7.793	0.918537	1.31517

Table 1.4. The non-perturbatively determined plaquette values u_0 and the resulting $g_{\overline{\text{MS}}}^2$ at $\mu=1/a$.

β	SC _{TI}	PS _{TI}	VC _{TI}	AV _{TI}	VC _{NP}	AV _{NP}
6.872	0.780093	0.844049	0.831763	0.903624	0.829295	0.846796
7.457	0.809197	0.863611	0.853159	0.914299	0.851246	0.867908
7.793	0.822246	0.872505	0.872505	0.919321	0.861273	0.877244

Table 1.5. Renormalization constants at vanishing quark mass. “TI” stands for the results from one-loop tadpole improved perturbative calculations (one-loop part of Eq. (1.89)) at $\mu = 1/a$ while “NP” denotes the non-perturbative results.

β	κ	κ_c	SC _{TI}	PS _{TI}	VC _{TI}	AV _{TI}	VC _{NP}	AV _{NP}
6.872	0.13035	0.13497	0.916090	0.983772	0.969473	1.053021	0.970641	0.986769
7.457	0.13179	0.13398	0.873207	0.928910	0.917675	0.983354	0.917012	0.933458
7.793	0.13200	0.13346	0.864942	0.915940	0.905811	0.965040	0.904983	0.920882

Table 1.6. Renormalization constants in the massive quark case at the scale of $\mu=1/a$. “TI” stands for the results from 1-loop tadpole improved perturbative calculations while “NP” denotes the non-perturbative results.

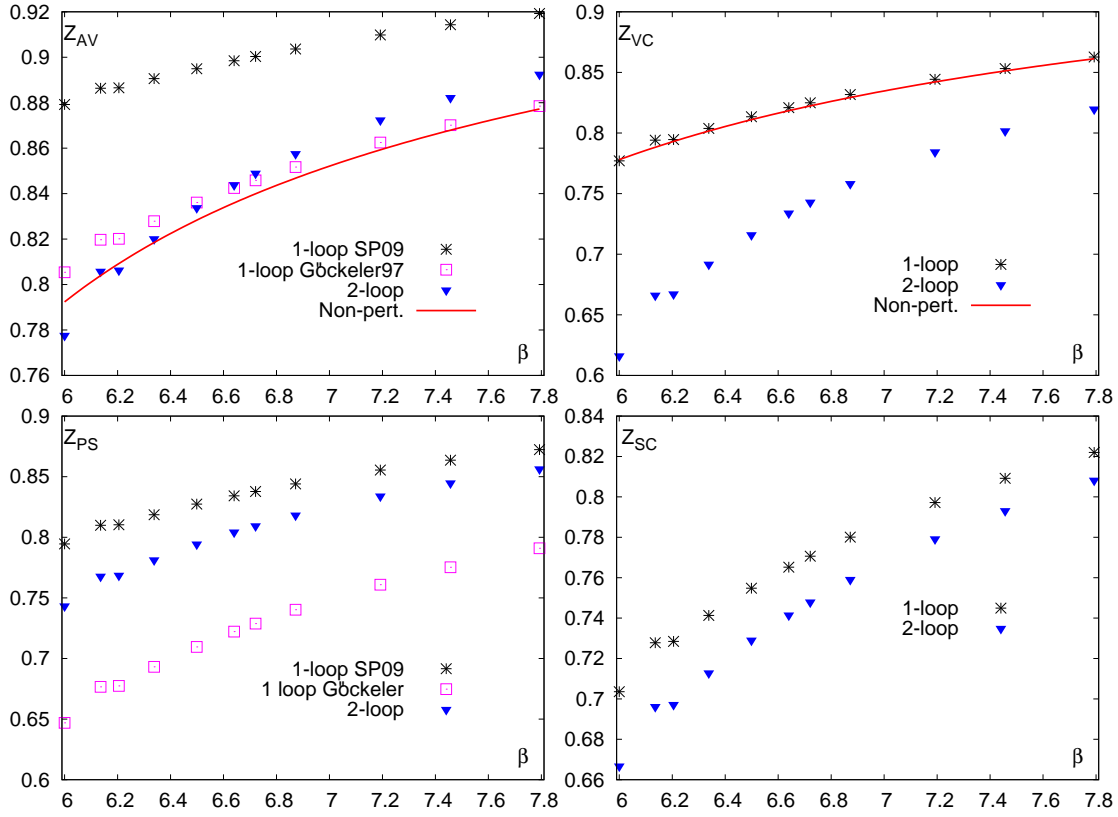


Figure 1.4. Comparisons of renormalization constants at vanishing quark mass from one-loop, two-loop perturbative (with tadpole improvement) and non-perturbative calculations. “1-loop SP09” and “2-loop” are the perturbative results obtained from formula (1.89) while “1-loop Gbckeler” stands for the perturbative results obtained from formula (1.84). “Non-pert.” denotes the non-perturbative results evaluated from formulae (1.92) and (1.93).

Chapter 2

Mesonic correlation and spectral functions

In this chapter we will elaborate the theoretical basics as well as the main techniques used in the charmonium correlation function analysis and also briefly review the current status of the charmonium study. It is organized as follows: In section 2.1 the definition of the correlation function and its relation to the spectral function is given. To study the thermal effects to the charmonia states at the correlator level, we find a very useful relation to calculate the reconstructed correlator directly from the correlation function at the reference temperature. In section 2.2 we will give a brief review on the Maximum Entropy Method, which will be utilized to extract the spectral function from the correlation function. We also introduce variants of the Maximum Entropy Method to suppress the τ independent constant in the correlator. To further enhance the signal of the low frequency part of the spectral function, for the first time, we will introduce the extended Maximum Entropy Method to the lattice QCD field. In section 2.3 we will depict the one-loop calculation of the free correlation and spectral function in the non-interacting case in both the continuum and Wilson discretized lattice case. The main features of the free correlators and spectral functions are discussed. In section 2.4 we will give a brief introduction to linear response theory and heavy quark diffusion. The resulting spectral functions from the Langevin equation are discussed. In section 2.5 we will briefly review the status of the current study on the charmonium system from the lattice QCD approach.

2.1 Mesonic correlation and spectral functions

In this section we will give the definition of the correlation functions in both real and imaginary time and show they can be connected by analytic continuation. More details can be found in various books [9, 10]. Some remarks on the integral kernel and the reconstructed correlator are also presented [105].

We start by the definition of two point correlation functions in the operator formalism in real time:

$$iD^+(t, \mathbf{x}) = \langle \mathcal{O}(t, \mathbf{x}) \mathcal{O}(0, \mathbf{0}) \rangle_\beta, \quad (2.1)$$

$$iD^-(t, \mathbf{x}) = \langle \mathcal{O}(0, \mathbf{0}) \mathcal{O}(t, \mathbf{x}) \rangle_\beta, \quad (2.2)$$

$$(2.3)$$

where $\langle \mathcal{O} \rangle_\beta = 1/Z \sum_n e^{-\beta E_n} \langle n | \mathcal{O} | n \rangle$ stands for thermal average and $\mathcal{O}(t, \mathbf{x})$ is the operator in the Heisenberg picture:

$$e^{-\beta H} \mathcal{O}(t, \mathbf{x}) e^{\beta H} = e^{-\beta H} e^{iHt} \mathcal{O}(0, \mathbf{x}) e^{-iHt} e^{\beta H} = \mathcal{O}(t + i\beta, \mathbf{x}). \quad (2.4)$$

With

$$\langle n | \mathcal{O}(t, \mathbf{x}) | m \rangle = e^{i(k_n - k_m) \cdot x} \langle n | \mathcal{O}(0) | m \rangle \quad (2.5)$$

and inserting a complete set of eigenvectors of H one can express $D^+(t, \mathbf{x})$ as

$$iD^+(t, \mathbf{x}) = \frac{1}{Z(\beta)} \sum_{n,m} e^{-\beta E_n} e^{i(k_n - k_m) \cdot x} |\langle n | \mathcal{O}(0) | m \rangle|^2, \quad (2.6)$$

where $x = (t, \mathbf{x})$ and $k_n = (E_n, \mathbf{k})$. If the convergence in the above equation is controlled by the exponentials, one can see that $D^+(t, \mathbf{x})$ is defined for $-\beta \leq \text{Im } t \leq 0$ and $D^-(t, \mathbf{x})$ is defined for $0 \leq \text{Im } t \leq \beta$.

The Fourier transform of Eq. (2.6)

$$D^+(\omega, \mathbf{p}) = \int \frac{d^4 x}{(2\pi)^4} e^{ip \cdot x} D^+(t, \mathbf{x}) \quad (2.7)$$

can be expressed in terms of the spectral density

$$\sigma^+(\omega, \mathbf{p}) = \frac{1}{Z(\beta)} \sum_{n,m} e^{-\beta E_n} \delta(p + k_n - k_m) |\langle n | \mathcal{O}(0) | m \rangle|^2. \quad (2.8)$$

as $D^+(\omega, \mathbf{p}) = 2\pi\sigma^+(\omega, \mathbf{p})$, where $p = (\omega, \mathbf{p})$.

Inserting relation (2.4) into Eq. (2.7) one has:

$$\begin{aligned} D^+(t, \mathbf{x}) &= D^-(t + i\beta, \mathbf{x}), \\ D^+(\omega, \mathbf{p}) &= e^{\beta\omega} D^-(\omega, \mathbf{p}). \end{aligned} \quad (2.9)$$

The Eq. (2.9) is the Kubo-Martin-Schwinger (KMS) relation.

Similarly we define $D^-(\omega, \mathbf{p}) = 2\pi\sigma^-(\omega, \mathbf{p})$ and using the KMS relation we have

$$\sigma^-(\omega, \mathbf{p}) = \frac{1}{Z(\beta)} \sum_{n,m} e^{-\beta(E_n + \omega)} \delta(p + k_n - k_m) |\langle n | \mathcal{O}(0) | m \rangle|^2. \quad (2.10)$$

The ensemble average of the commutator is

$$D(t, x) = -i \langle [\mathcal{O}(t, \mathbf{x}), \mathcal{O}(0, \mathbf{0})] \rangle = D^+(t, \mathbf{x}) - D^-(t, \mathbf{x}). \quad (2.11)$$

and its spectral density $\sigma(\omega, \mathbf{p})$ can be expressed as

$$\begin{aligned} \sigma(\omega, \mathbf{p}) &= \frac{D^+(\omega, \mathbf{p}) - D^-(\omega, \mathbf{p})}{2\pi} = \sigma^+(\omega, \mathbf{p}) - \sigma^-(\omega, \mathbf{p}) \\ &= \frac{1}{2\pi} \int d^4x e^{i\omega t - i\mathbf{p}\cdot\mathbf{x}} \langle [\mathcal{O}(t, \mathbf{x}), \mathcal{O}(0, \mathbf{0})] \rangle. \end{aligned} \quad (2.12)$$

An explicit expression for $\sigma(\omega, \mathbf{p})$ can be obtained by using (2.8) and (2.10):

$$\begin{aligned} \sigma(\omega, \mathbf{p}) &= \frac{1}{Z(\beta)} \sum_{n,m} e^{-\beta E_n} (1 - e^{-\beta\omega}) \delta(p + k_n - k_m) |\langle n | \mathcal{O}(0) | m \rangle|^2 \\ &= \frac{1}{Z(\beta)} \sum_{n,m} \left(e^{-\beta E_n} - e^{-\beta E_m} \right) \delta(p + k_n - k_m) |\langle n | \mathcal{O}(0) | m \rangle|^2 \\ &= \frac{1}{Z(\beta)} \sum_{n,m} e^{-\beta E_n} \left(\delta(p + k_n - k_m) - \delta(p + k_m - k_n) \right) |\langle n | \mathcal{O}(0) | m \rangle|^2. \end{aligned} \quad (2.13)$$

From the above equation, one can see the spectral function $\sigma(\omega, \mathbf{p})$ has the symmetry of $\sigma(-\omega, -\mathbf{p}) = \sigma(\omega, \mathbf{p})$ and $\omega\sigma(\omega, \mathbf{p}) \geq 0$. If the system is rotationally invariant, which means the state can have same energy ω but opposite momentum \mathbf{p} , the spectral function $\sigma(\omega, \mathbf{p})$ would then be an odd function of ω .

The retarded and advanced propagator are defined as

$$D^R(t, \mathbf{x}) = -\theta(t)D(t, \mathbf{x}), \quad (2.14)$$

$$D^A(t, \mathbf{x}) = \theta(-t)D(t, \mathbf{x}), \quad (2.15)$$

whose Fourier transforms can also be written in terms of the spectral density (2.13) as the following

$$D^R(\omega, \mathbf{p}) = \int_{-\infty}^{+\infty} \frac{dk_0}{k_0 - \omega - i\epsilon} \sigma(k_0, \mathbf{p}), \quad (2.16)$$

$$D^A(\omega, \mathbf{p}) = \int_{-\infty}^{+\infty} \frac{dk_0}{k_0 - \omega + i\epsilon} \sigma(k_0, \mathbf{p}). \quad (2.17)$$

The imaginary parts of these functions are proportional to the spectral density as

$$\text{Im } D^R(\omega, \mathbf{p}) = -\text{Im } D^A(\omega, \mathbf{p}) = \pi \sigma(\omega, \mathbf{p}), \quad (2.18)$$

and the real parts are equivalent

$$\text{Re } D^R(\omega, \mathbf{p}) = \text{Re } D^A(\omega, \mathbf{p}). \quad (2.19)$$

Now we make the connection to the imaginary time picture. The imaginary time propagator in the coordinate space reads

$$G(\tau, \mathbf{x}) = \langle \mathcal{O}(\tau, \mathbf{x}) \mathcal{O}(0, \mathbf{0}) \rangle. \quad (2.20)$$

The time evolution of operator becomes

$$\mathcal{O}(\tau, \mathbf{x}) = e^{H\tau} \mathcal{O}(0, \mathbf{x}) e^{-H\tau}. \quad (2.21)$$

Inserting the complete eigenstates into Eq. (2.20) one arrives at

$$G(\tau, \mathbf{x}) = \frac{1}{Z(\beta)} \sum_{n,m} e^{-\beta E_n} e^{\tau(E_n - E_m)} e^{i(\mathbf{p}_m - \mathbf{p}_n) \cdot \mathbf{x}} |\langle n | \mathcal{O}(0) | m \rangle|^2, \quad (2.22)$$

and its Fourier transform reads

$$\begin{aligned} G(\omega_n, \mathbf{p}) &= \int_0^\beta d\tau \int \frac{d^3 \mathbf{x}}{(2\pi)^3} e^{-i(\mathbf{k} \cdot \mathbf{x} + \omega_n \tau)} G(\tau, \mathbf{x}) \\ &= \frac{1}{Z(\beta)} \sum_{n,m} \frac{e^{-\beta E_n} - e^{-\beta E_m}}{E_m - E_n + i\omega_n} \delta(\mathbf{p} - \mathbf{k}_m + \mathbf{k}_n) |\langle n | \mathcal{O}(0) | m \rangle|^2, \end{aligned} \quad (2.23)$$

where $\omega_n = 2\pi nT$ are called Matsubara frequencies owing to the periodic condition of $G(\tau, \mathbf{x}) = G(\tau + \beta, \mathbf{x})$. The above equation can be related with the spectral density (2.13) as

$$G(\omega_n, \mathbf{p}) = \int_{-\infty}^{+\infty} \frac{dk_0}{k_0 + i\omega_n} \sigma(k_0, \mathbf{p}). \quad (2.24)$$

By comparing the formulae (2.16), (2.17) and (2.24) we find the advanced and retarded propagators can be obtained from the finite temperature imaginary time propagator by analytic continuation as the following

$$D^R(\omega, \mathbf{p}) = G(\omega_n \rightarrow i\omega - \epsilon, \mathbf{p}), \quad (2.25)$$

$$D^A(\omega, \mathbf{p}) = G(\omega_n \rightarrow i\omega + \epsilon, \mathbf{p}). \quad (2.26)$$

The spectral density $\sigma(\omega, \mathbf{p})$ determines both the imaginary and real time propagator and thus is a very important quantity. The analytic continuation from imaginary time propagator to real time propagator serves as a crucial theoretical basis in this work of measuring two-point Euclidean correlation functions.

The Euclidean temporal correlation function $G(\tau, \mathbf{p})$ is defined as

$$G(\tau, \mathbf{p}) = \int d^3 \mathbf{x} e^{-i\mathbf{p} \cdot \mathbf{x}} \langle \mathcal{O}_E(\tau, \mathbf{x}) \mathcal{O}_E(0, \mathbf{0}) \rangle, \quad (2.27)$$

and can be related to the spectral function through

$$\begin{aligned}
G(\tau, \mathbf{p}) &= \int d^3\mathbf{x} e^{-i\mathbf{p}\cdot\mathbf{x}} D^+(-i\tau, \mathbf{x}) \\
&= \int d^3\mathbf{x} \int \frac{d\omega}{2\pi} \int \frac{d^3\mathbf{p}'}{2\pi^3} e^{i(\mathbf{p}'-\mathbf{p})\cdot\mathbf{x}-\omega\tau} D^+(\omega, \mathbf{p}') \\
&= \int \frac{d\omega}{2\pi} \int d^3\mathbf{p}' \delta^3(\mathbf{p}'-\mathbf{p}) e^{-\omega\tau} D^+(\omega, \mathbf{p}') \\
&= \int \frac{d\omega}{2\pi} e^{-\omega\tau} D^+(\omega, \mathbf{p}) \\
&= \int_0^\infty \frac{d\omega}{2\pi} e^{-\omega\tau} D^+(\omega, \mathbf{p}) + \int_{-\infty}^0 \frac{d\omega}{2\pi} e^{-\omega\tau} D^+(\omega, \mathbf{p}) \\
&= \int_0^\infty \frac{d\omega}{2\pi} e^{-\omega\tau} D^+(\omega, \mathbf{p}) + \int_0^\infty \frac{d\omega}{2\pi} e^{\omega\tau} D^-(\omega, \mathbf{p}) \\
&= \int_0^\infty \frac{d\omega}{2\pi} \cdot 2\pi \left((1+n(\omega)) e^{-\omega\tau} + n(\omega) e^{\omega\tau} \right) \sigma(\omega, \mathbf{p}) \\
&= \int_0^\infty d\omega \frac{\cosh\left(\omega\left(\tau - \frac{\beta}{2}\right)\right)}{\sinh\left(\frac{\omega\beta}{2}\right)} \sigma(\omega, \mathbf{p}) \tag{2.28}
\end{aligned}$$

$$= \int_0^\infty d\omega K(\omega, \tau) \sigma(\omega, \mathbf{p}). \tag{2.29}$$

where $K(\omega, \tau)$ is the integration kernel in the continuum limit¹. Since the relation between the temporal correlation function and spectral function is straightforward, it will be utilized to extract the spectral function in the following chapter.

The Euclidean spatial correlation function $G(z, \mathbf{p}_\perp, \omega_n)$ is obtained via an integration over the so called *funny space*, which includes the Euclidean time τ and two spatial directions \mathbf{x}_\perp :

$$G(z, \mathbf{p}_\perp, \omega_n) = \int_0^{1/T} d\tau \int d\mathbf{x}_\perp e^{-i\tilde{\mathbf{p}}\cdot\tilde{\mathbf{x}}} \langle \mathcal{O}_E(\tau, \mathbf{x}) \mathcal{O}_E(0, \mathbf{0}) \rangle, \tag{2.30}$$

where $\mathbf{p}_\perp = (p_x, p_y)$, $\mathbf{x}_\perp = (x, y)$, $\tilde{x} = (\mathbf{x}_\perp, \tau)$ and $\tilde{\mathbf{p}} = (\mathbf{p}_\perp, p_4 = \omega_n)$. The spatial correlation function can again be related with the spectral function through [107]

$$G(z, \mathbf{p}_\perp, \omega_n) = \int_{-\infty}^\infty \frac{dp_z}{2\pi} e^{ip_z z} \int_{-\infty}^\infty dp_0 \frac{\sigma(p_0, \mathbf{p}_\perp, p_z, \omega_n)}{p_0}. \tag{2.31}$$

The above relation is much more complicated than that of the temporal correlation function and thus it is not so straightforward to extract the spectral function from the spatial correlation function. However, one advantage of spatial correlation functions over temporal functions is that the physical extent in the spatial direction is not restricted by the temperature and thus by going to the large distance one can extract the exponentially decayed constant, i.e. screening mass.

¹Although this relation is derived in the continuum limit, it has been shown that this relation also holds in the limit of non-interacting theory [106].

Channel	Γ_H	$^{2S+1}L_J$	J^{PC}	I^G	$c\bar{c}$	$M(c\bar{c})[\text{GeV}]$
PS	γ_5	1S_0	0^{-+}	0^+	η_c	2.980(1)
VC	γ_μ	3S_1	1^{--}	0^-	J/ψ	3.097(1)
SC	1	3P_0	0^{++}	0^+	χ_{c0}	3.415(1)
AV	$\gamma_5\gamma_\mu$	3P_1	1^{++}	0^+	χ_{c1}	3.510(1)

Table 2.1. Charmonium states in different channels from PDG [83].

In this work we consider the local meson operator $J_H(\tau, \mathbf{x})$, which has the form of

$$J_H(\tau, \mathbf{x}) = \bar{\psi}(\tau, \mathbf{x})\Gamma_H\psi(\tau, \mathbf{x}), \quad (2.32)$$

with

$$\Gamma_H = 1, \gamma_5, \gamma_\mu, \gamma_5\gamma_\mu, \quad (2.33)$$

for scalar, pseudo scalar, vector and axial vector channels, respectively. The correspondence of these quantum numbers to different charmonium states is summarized in Table 2.1.

In the path integral formalism the two-point correlation function has the form of

$$\begin{aligned} G_H(x_f, x_i) &= \left\langle J_H(x_f)J_H^\dagger(x_i) \right\rangle \\ &= \frac{1}{Z} \int \mathcal{D}U \mathcal{D}\psi \mathcal{D}\bar{\psi} \left(\bar{\psi}(x_f)\Gamma_H\psi(x_f) \right) \left(\bar{\psi}(x_i)\Gamma_H^\dagger\psi(x_i) \right) e^{-S} \\ &= \frac{1}{Z} \int \mathcal{D}U \left\{ \text{Tr} \left(M^{-1}(x_f, x_i)\Gamma_H M^{-1}(x_i, x_f)\Gamma_H^\dagger \right) \right. \\ &\quad \left. - \text{Tr} \left(\Gamma_H^\dagger M^{-1}(x_i, x_i) \right) \text{Tr} \left(\Gamma_H M^{-1}(x_f, x_f) \right) \right\} e^{-S_G(U)} \quad (2.34) \end{aligned}$$

$$= x_i \begin{array}{c} \curvearrowright \\ \curvearrowleft \end{array} x_f \quad - \quad x_i \begin{array}{c} \curvearrowright \\ \curvearrowright \end{array} \quad \begin{array}{c} \curvearrowleft \\ \curvearrowleft \end{array} x_f. \quad (2.35)$$

where Tr denotes the trace over color and Dirac indices. The second term in Eq. (2.34) describes disconnected diagrams in which each of the quark lines starts and ends at the same point as depicted in Eq. (2.35). The charmonium states we want to study are actually singlet, as seen from Table 2.1. The disconnected diagrams should be small due to OZI suppression and so in our simulation only the connected part, i.e. the first term of Eq. (2.34) is considered. Taking advantage of the γ^5 -Hermiticity of M^{-1} (1.65), the connected part of the two-point function can be computed as

$$G_H(x_f, x_i) = \left\langle \text{Tr} \left(M^{-1}(x_f, x_i)\Gamma_H \gamma^5 (M^{-1})^\dagger(x_f, x_i)\gamma^5 \Gamma_H^\dagger \right) \right\rangle. \quad (2.36)$$

The temporal and spatial correlators can thus be obtained through

$$G_H(\tau, \mathbf{p}) = \sum_{\mathbf{x}} e^{-i\mathbf{p}\cdot\mathbf{x}} G_H(\tau, \mathbf{x}; 0, \mathbf{0}), \quad (2.37)$$

$$G_H(z, \mathbf{p}_\perp, \omega_n) = \sum_{\vec{\mathbf{x}}} e^{-i\vec{\mathbf{p}}\cdot\vec{\mathbf{x}}} G_H(\tau, \mathbf{x}; 0, \mathbf{0}). \quad (2.38)$$

In particular the vector channel can be decomposed into the density-density correlator

$$G_{\text{NN}}(\tau, \mathbf{x}) = \langle J^0(\tau, \mathbf{x}) J^0(0, \mathbf{0}) \rangle \quad (2.39)$$

and the current-current correlator

$$G_{\text{JJ}}^{ij} = \langle J^i(\tau, \mathbf{x}) J^j(0, \mathbf{0}) \rangle. \quad (2.40)$$

These correspond to the real time correlators

$$G_{\text{NN}}(\tau, \mathbf{x}) = -D_{\text{NN}}^+(-i\tau, \mathbf{x}), \quad (2.41)$$

$$G_{\text{JJ}}^{ij}(\tau, \mathbf{x}) = D_{\text{JJ}}^+(-i\tau, \mathbf{x}). \quad (2.42)$$

The corresponding real time retarded correlators $\chi_{\text{NN}}(t, \mathbf{x})$ and $\chi_{\text{JJ}}(t, \mathbf{x})$ can be defined in the same way. The current-current retarded correlator in the momentum-energy space can be decomposed into longitudinal and transverse parts:

$$\chi_{\text{JJ}}^{ij}(\omega, \mathbf{p}) = \left(\frac{\mathbf{p}^i \mathbf{p}^j}{\mathbf{p}^2} - \delta_{ij} \right) \chi_{\text{JJ}}^T(\omega, \mathbf{p}) + \frac{\mathbf{p}^i \mathbf{p}^j}{\mathbf{p}^2} \chi_{\text{JJ}}^L(\omega, \mathbf{p}). \quad (2.43)$$

The density-density correlators can be related to the longitudinal current-current correlators due to current conservation

$$\chi_{\text{NN}}(\omega, \mathbf{p}) = \frac{\mathbf{p}^i \mathbf{p}^j}{\omega^2} \chi_{\text{JJ}}^{ij} = \frac{\mathbf{p}^2}{\omega^2} \chi_{\text{JJ}}^L(\omega, \mathbf{p}). \quad (2.44)$$

The spectral function in the vector channel is related to the experimentally accessible differential cross section for the thermal production of dilepton pairs² [9, 108, 109]

$$\frac{dW}{d\omega d^3\mathbf{p}} = \frac{5\alpha^2}{27\pi^2} \frac{1}{\omega^2 (e^{\omega/T} - 1)} \sigma_V(\omega, \mathbf{p}, T), \quad (2.45)$$

where α is the electromagnetic fine structure constant, σ_V is the spectral function in γ^μ channel. The presence or absence of the bound states of heavy quarkonium can be observed from this quantity. Additionally the spectral function in γ^i channel is related to the heavy quark diffusion constant D [9, 110]

$$D = \frac{\pi}{3\chi_{00}^i} \lim_{\omega \rightarrow 0} \sum_{i=1}^3 \frac{\sigma_V^{ii}(\omega, \vec{p} = 0, T)}{\omega}, \quad (2.46)$$

²Here in this formula the lepton is considered as massless particle.

where χ^{00} is the quark number susceptibility of χ_H with $\gamma_H = \gamma^0$. χ_H is defined as the space-time integral over the Euclidean correlation function,

$$\chi_H = \int_0^{1/T} d\tau G_H(\tau, T, \mathbf{p} = 0), \quad (2.47)$$

which is connected to spectral function directly with the help of relation (2.61)

$$\chi_H = 2 \int_0^\infty d\omega \frac{\sigma_H(\omega, \mathbf{p} = 0)}{\omega}. \quad (2.48)$$

2.1.1 A close look at the integrand kernel

The relation between spectral function and temporal correlation function is:

$$G(\tau, T, \mathbf{p}) = \int_0^\infty d\omega K(\tau, \omega, T) \sigma(\omega, T, \mathbf{p}). \quad (2.49)$$

where the integral kernel reads

$$K(\omega, \tau, T) = \frac{\cosh(\omega(\tau - 1/2T))}{\sinh(\omega/2T)}. \quad (2.50)$$

The kernel has following important properties:

- In the very high frequency region or the case $T \rightarrow 0$,

$$K(\tau, \omega) = e^{-\omega\tau}, \quad (2.51)$$

which indicates that the correlation function is very insensitive to the large ω behavior of the spectral function.

- In the very low frequency region,

$$K(\tau, \omega) = \frac{2T}{\omega} + \left(\frac{1}{6T} - \tau + T\tau^2\right)\omega + \mathcal{O}[\omega]^3, \quad (2.52)$$

which is divergent at $\omega = 0$ and consequently the spectral function at $\omega \approx 0$ should be at the order or higher order of 0.

- $K(\tau, \omega, T)$ has a trivial temperature dependence, which one should remove, if one wants to compare the difference of the spectral function directly at the correlator level.

2.1.2 The reconstructed correlator

To study the difference of the spectral function at temperature T and T' directly from the temporal correlator³, one constructs

$$G_{\text{rec}}(\tau, T; T') = \int_0^\infty d\omega \sigma(\omega, T') \frac{\cosh(\omega(\tau - 1/2T))}{\sinh(\omega/2T)}, \quad (2.53)$$

in order to cancel the trivial temperature dependence of $K(\tau, \omega, T)$. The deviation of $G(\tau, T)$ from $G_{\text{rec}}(\tau, T; T')$ indicates the thermal modification of the spectral function.

One normally needs a technique to obtain the spectral function $\sigma(\omega, T')$ at a reference temperature T' and consequently the evaluation of Eq. (2.53) suffers from the uncertainty of the determination of the spectral function brought by the certain technique.

We find a useful exact relation [105]⁴:

$$\frac{\cosh[\omega(\tau - N_\tau/2)]}{\sinh(\omega N_\tau/2)} \equiv \sum_{\tau'=\tau; \tau'+=N_\tau}^{N'_\tau - N_\tau + \tau} \frac{\cosh[\omega(\tau' - N'_\tau/2)]}{\sinh(\omega N'_\tau/2)}, \quad (2.54)$$

where $T' = (aN'_\tau)^{-1}$, $T = (aN_\tau)^{-1}$, $\tau' \in [0, N'_\tau - 1]$, $\tau \in [0, N_\tau - 1]$, $N'_\tau = m N_\tau$, $m \in \mathbb{Z}^+$. N_τ and N'_τ are the number of time slices in the temporal directions at temperature T and T' , respectively. τ denotes the time slice of the correlation function at temperature T while τ' denotes the time slice of the correlation function at temperature T' . The sum of τ' on the right hand side of Eq. (2.54) starts from $\tau' = \tau$ with a step length N_τ to the upper limit $N'_\tau - N_\tau + \tau$. After putting $\sigma(\omega, T')$ into both sides of the above relation and performing the integration over ω , one immediately arrives at:

$$G_{\text{rec}}(\tau, T; T') = \sum_{\tau'=\tau; \tau'+=N_\tau}^{N'_\tau - N_\tau + \tau} G(\tau', T'), \quad (2.55)$$

which shows the evaluation of $G_{\text{rec}}(\tau, T; T')$ can be done directly from the correlator $G(\tau', T')$ at T' .

For instance when $T = 2T'$,

$$G_{\text{rec}}(\tau, T; T') = G(\tau, T') + G(\tau + N_\tau, T'), \quad (2.56)$$

when $T = 3T'$,

$$G_{\text{rec}}(\tau, T; T') = G(\tau, T') + G(\tau + N_\tau, T') + G(\tau + 2N_\tau, T'), \quad (2.57)$$

³For the spatial correlator the physical distance does not change with temperature and one does not need any reconstruction to compare the spatial correlators at different temperatures.

⁴Our finding covers the special case of $T = 2T'$ (Eq. (2.56)) and $T = 0$ (Eq. (2.56)) which were previously found in Ref. [111].

when $T = 4T'$,

$$G_{\text{rec}}(\tau, T; T') = G(\tau, T') + G(\tau + N_\tau, T') + G(\tau + 2N_\tau, T') + G(\tau + 3N_\tau, T'). \quad (2.58)$$

In particular when $T' = 0$, which means N'_τ goes to infinity (at fixed lattice spacing a):

$$G_{\text{rec}}(\tau, T; 0) = \sum_{\ell \in \mathbb{Z}} G(|\tau + \ell N_\tau|, T' = 0). \quad (2.59)$$

In practice we will utilize Eq. (2.56), (2.57) and (2.58) to reconstruct the correlators in the following chapter.

2.1.3 Sum rules

The kernel obeys two following relations. One is in the sum representation:

$$\sum_{\tau=0}^{N_\tau-1} K(\omega, \tau) = 1/\tanh(\omega/2), \quad (2.60)$$

and the other one is in the integral representation:

$$\int_0^{1/T} d\tau K(\omega, \tau) = \frac{2}{\omega}. \quad (2.61)$$

With relation (2.60) we arrive at the first sum rule:

$$\sum_{\tau=0}^{N_\tau-1} G(\tau) = \int_0^\infty d\omega \coth\left(\frac{\omega}{2}\right) \sigma(\omega, T), \quad (2.62)$$

which sheds some light on the size of the spectral function.

Performing the sum over τ on both sides of Eq. (2.49) and Eq. (2.53), with relation (2.61), one has

$$\sum_{\tau=0}^{N_\tau-1} G(\tau, T) = \int_0^\infty d\omega \coth\left(\frac{\omega}{2}\right) \sigma(\omega, T), \quad (2.63)$$

$$\sum_{\tau=0}^{N_\tau-1} G_{\text{rec}}(\tau, T; T') = \int_0^\infty d\omega \coth\left(\frac{\omega}{2}\right) \sigma(\omega, T'). \quad (2.64)$$

With the above two relations, one obtains the second sum rule of the spectral function:

$$\int_0^\infty d\omega \coth\left(\frac{\omega}{2}\right) \Delta\sigma(\omega) = \sum_{\tau=0}^{N_\tau-1} (G(\tau, T) - G_{\text{rec}}(\tau, T; T')), \quad (2.65)$$

where $\Delta\sigma(\omega) = \sigma(\omega, T) - \sigma(\omega, T')$. The second sum rule can give us some hints on the gross features of the thermal modification to the spectral function.

Similarly we have in the integral representation

$$2 \int_0^\infty d\omega \frac{\Delta\sigma(\omega)}{\omega} = \int_0^{1/T} d\tau (G(\tau, T) - G_{\text{rec}}(\tau, T; T')). \quad (2.66)$$

2.2 Maximum Entropy Method

The Maximum Entropy Method (MEM) is currently the best tool on the market for extracting the spectral function from the correlation data. Since the 70s it has been widely implemented in various fields [112–117], e.g. condensed matter physics, nuclear physics and image reconstruction in astrophysics. Around 2000 MEM was introduced to lattice QCD by Asakawa et al. [118]. It has been successfully applied to the lattice QCD data at zero temperature to extract the parameters of the ground and excited states of hadrons [119–124]. The application to finite temperature lattice QCD has also been made recently [37–41, 105, 109, 125, 126].

In this section we will first review the standard Maximum Entropy Method. More details can be found from the reviews and textbooks [117, 118, 127, 128]. The standard MEM can only be used for the analysis of non-negative spectral functions. We will then introduce the extended Maximum Entropy Method [105], which is also applicable for the analysis on negative spectral functions⁵.

The imaginary two point static temporal correlation functions can be obtained from lattice QCD simulations, while the dynamic spectral function can be extracted by inverting:

$$G(\tau, T, \mathbf{p}) = \int_0^\infty d\omega \frac{\cosh(\tau(\omega - \frac{1}{2T}))}{\sinh(\frac{\omega}{2T})} \sigma(\omega, T, \mathbf{p}). \quad (2.67)$$

Inverting Eq. (2.67) to extract the spectral function is a typical ill-posed problem. At finite temperature the inversion is more complicated, since the temporal extent is always restricted by the temperature, $a\tau \leq 1/T$. The spectral functions we want to have should be continuous and have an approximate degree of freedom of $\mathcal{O}(1000)$, while the correlators are calculated in the discretized time slices with limited numbers, typically $\mathcal{O}(10)$. So an infinite number of solutions exist. The task then is to select the best one from the solutions by some criterion. The best one could be the most probable one or the “average” spectrum. Due to the non-negativity and the normalizability of the spectral function it can be interpreted as a probability function, thus the guiding principle for the selection could be the Bayesian statistical inference [132], which is the root of the Maximum Entropy Method.

According to Bayes’s theorem the joint probability $P[X, Y]$ of two given events X and Y can be written as:

$$P[X, Y] = P[X|Y]P[Y] = P[Y|X]P[X], \quad (2.68)$$

⁵For the two-point correlation function with non-equal operators, its corresponding spectral function is not necessarily positive semi-definite. Typical examples are the meson and baryon mixing, e.g. $\rho - \omega$, $\Lambda - \Omega^0$ [129–131].

where $P[Y]$ is the probability of Y and $P[X|Y]$ is the conditional probability of X given Y . From probability theory the condition for the marginalization of a variable reads:

$$P[X] = \int dY P[X, Y], \quad (2.69)$$

and the condition for normalization is:

$$\int dX P[X] = 1, \quad \int dX P[X|Y] = 1. \quad (2.70)$$

From (2.68) and (2.69) one obtains:

$$P[X] = \int dY P[X|Y]P[Y] \quad (2.71)$$

Applied to our specific problem the probability of spectral function $\sigma(\omega, \mathbf{p})$ given data $G(\tau, \mathbf{p})$ and prior knowledge parameterized in H can be expressed as:

$$P[\sigma|GH] = P[G|\sigma H]P[\sigma|H]/P[G|H], \quad (2.72)$$

where $P[\sigma|GH]$ is called the posterior probability, $P[G|\sigma H]$, the likelihood function, $P[\sigma|H]$, the prior probability, and $P[G|H]$, the evidence. Eq. (2.72) is very meaningful since it transfers the problem of specifying the posterior probability into the problem of specifying the likelihood function and the prior probability. The latter ones can be more easily accessible by making reasonable assumptions (for the likelihood function) and having specific knowledge (for the prior probability).

2.2.1 Likelihood function

The likelihood function is a probability distribution for the data given in terms of its dependences on a set of parameters. Following the central limit theorem, the functional form of $P[G|\sigma H]$ can be expressed via the usual χ^2 when the number of measurements M becomes large:

$$P[G|\sigma H] \propto \exp(-L) = \exp\left(-\frac{\chi^2}{2}\right), \quad (2.73)$$

with

$$\chi^2 = \sum_{i,j}^{N_\tau/2} (\bar{G}(\tau_i) - F(\tau_i)) C_{ij}^{-1} (\bar{G}(\tau_j) - F(\tau_j)), \quad (2.74)$$

where $\bar{G}(\tau_i)$ is the average over all measurements

$$\bar{G}(\tau_i) = \frac{1}{M} \sum_{m=1}^M G^m(\tau_i), \quad (2.75)$$

C is the covariance matrix,

$$C_{ij} = \frac{1}{M(M-1)} \sum_{m=1}^M (G^m(\tau_i) - \bar{G}(\tau_i)) (G^m(\tau_j) - \bar{G}(\tau_j)), \quad (2.76)$$

and the fitting function

$$F(\tau_i) = \int_0^\infty d\omega K(\tau_i, \omega) \sigma(\omega) \simeq \sum_j K_{ij} \sigma_j \quad (2.77)$$

is obtained in the discretized version through a predefined kernel $K_{ij} \equiv K(\tau_i, \omega_j)$ and the spectral function $\sigma_j = \sigma(\omega_j) \Delta\omega$.

Using the data to find an appropriate spectral function cannot be done solely with a least-squares fitting procedure by maximizing the likelihood function (2.73) or minimizing χ^2 (2.74), since too many parameters for the spectral function $\sigma(\omega)$ have to be used during the fitting procedure, which unfortunately leads to overfitting ($\chi^2 \approx 0$) and non-unique results. Thus some sort of regularization methods is required. An entropic prior is one of the best regulators in the literature⁶, which will be described in the following section.

2.2.2 Entropic prior information

The prior probability

$$P[\sigma|H] \propto \exp(\alpha S), \quad (2.78)$$

with the Shannon-Jaynes entropy [133–135]

$$\begin{aligned} S[\sigma] &= \int_0^\infty d\omega \left[\sigma(\omega) - m(\omega) - \sigma(\omega) \ln \left(\frac{\sigma(\omega)}{m(\omega)} \right) \right] \\ &\simeq \sum_i S_i = \sum_i \left[\sigma_i - m_i - \sigma_i \ln \left(\frac{\sigma_i}{m_i} \right) \right], \end{aligned} \quad (2.79)$$

where $m(\omega)$ is a real and positive function called default model and it needs the prior information of the spectral function $\sigma(\omega)$ as input. In the discretized version $\sigma_i = \sigma(\omega_i) \Delta\omega$ and $m_i = m(\omega_i) \Delta\omega$. From Eq. (2.79), one can see the entropy is a non-positive number and reaches the maximum value zero when $\sigma_i = m_i$. Consequently how negative the entropy is can be a measure of how much σ_i differs from m_i . One can expand the entropy about $\sigma(\omega) = m(\omega)$:

$$S[\sigma] \approx -\frac{1}{2} \int_0^\infty d\omega [\sigma(\omega) - m(\omega)]^2 / m(\omega). \quad (2.80)$$

⁶There are also some other regularization methods in the literature, such as Tikhonov [136] and L-curved regularization [137].

One has to note that the functional form of the entropy has been chosen to satisfy certain requirements: the entropy should not depend on the type of data being analyzed and the units of σ , the extra knowledge about σ in one part of frequency space should not affect σ elsewhere and the independent data should combine multiplicatively [117]⁷.

2.2.3 Posterior probability

Together with Eq. (2.72), (2.73) and (2.78), the posterior probability reads

$$P[\sigma|GH] \propto \exp(\alpha S - L) \equiv \exp(Q). \quad (2.81)$$

Thus the most probable spectral function can be obtained by maximizing $P[\sigma|GH]$ or by maximizing Q as a function of σ :

$$\alpha \nabla S - \nabla L = 0. \quad (2.82)$$

We expand Q about the maximum for a fixed value of α in a coordinate system which is described by the variable X_i [117]

$$\begin{aligned} Q(\sigma, \alpha) &\approx Q(\hat{\sigma}_\alpha) + \sum_i \delta X_i \left[\frac{\partial Q}{\partial X_i} \right]_{\sigma=\hat{\sigma}_\alpha} + \frac{1}{2} \sum_{i,j} \delta X_i \delta X_j \left[\frac{\partial^2 Q}{\partial X_i \partial X_j} \right]_{\sigma=\hat{\sigma}_\alpha} \\ &= Q(\hat{\sigma}_\alpha) + \frac{1}{2} \sum_{i,j,k,l} \delta X_i \delta X_j \left[\frac{\partial \sigma_k}{\partial X_i} \frac{\partial \sigma_l}{\partial X_j} \frac{\partial^2 Q}{\partial \sigma_k \partial \sigma_l} \right]_{\sigma=\hat{\sigma}_\alpha}, \end{aligned} \quad (2.83)$$

where $\delta X_i = X_i - \hat{X}_i$ and

$$\frac{\partial^2 Q}{\partial \sigma_k \partial \sigma_l} = \alpha \frac{\partial^2 S}{\partial \sigma_k \partial \sigma_l} - \frac{\partial^2 L}{\partial \sigma_k \partial \sigma_l} = -\frac{\alpha \delta_{kl}}{\sqrt{\sigma_k \sigma_l}} - \frac{\partial^2 L}{\partial \sigma_k \partial \sigma_l}. \quad (2.84)$$

With a new coordinate system

$$\frac{\partial \sigma_k}{\partial X_l} = \sqrt{\sigma_k} \delta_{kl} \quad (2.85)$$

we can further write

$$Q(\sigma, \alpha) \approx Q(\hat{\sigma}_\alpha) - \frac{1}{2} \sum_{ij} \delta X_i \Gamma_{ij} \delta X_j, \quad (2.86)$$

where Γ is a positive-definite matrix $\Gamma_{ij} = \alpha \delta_{ij} + \Lambda_{ij}$ with

$$\Lambda_{ij} = \left[\sqrt{\sigma_i} \frac{\partial^2 L}{\partial \sigma_i \partial \sigma_j} \sqrt{\sigma_j} \right]_{\sigma=\hat{\sigma}_\alpha}, \quad (2.87)$$

and

$$\frac{\partial^2 L}{\partial \sigma_i \partial \sigma_j} = [K^T \cdot C^{-1} \cdot K]_{ij}. \quad (2.88)$$

⁷The proof of these properties can be found in Ref. [118].

2.2.4 Distributions and their normalizations

The likelihood function in a specific form can be expressed as

$$P[G|\sigma] = e^{-\chi^2/2}/Z_L, \quad (2.89)$$

where

$$Z_L = \int DG e^{-\chi^2} = \int \prod_i dG_i e^{-\chi^2} = (2\pi)^{N/2} \sqrt{\det C}. \quad (2.90)$$

The prior probability of the spectral function given α in a specific form can be expressed as

$$P[\sigma|\alpha] = e^{\alpha S}/Z_S(\alpha), \quad (2.91)$$

where

$$Z_S(\alpha) = \int D\sigma e^{\alpha S} = \prod_i \int \frac{d\sigma_i}{\sqrt{\sigma_i}} e^{\alpha S_i}. \quad (2.92)$$

S_i as a function of $\sqrt{\sigma_i}$ can be expanded about $\sqrt{m_i}$:

$$S_i \approx -2(\sqrt{\sigma_i} - \sqrt{m_i})^2, \quad (2.93)$$

which leads to

$$Z_S(\alpha) \approx \left(\frac{\pi}{2\alpha}\right)^{N/2} = \frac{(\pi/2)^{N/2}}{\sqrt{\det \alpha I}}. \quad (2.94)$$

The posterior probability of α given the data

$$P[\alpha|G] = P[\alpha] \int \mathcal{D}A \frac{e^Q}{Z_L Z_S(\alpha)}, \quad (2.95)$$

where the value of $P[\alpha]$ is set to be $1/\alpha$ following Jeffrey's argument [138]. Inserting Eq. (2.86) into Eq. (2.95) and with relations (2.90) and (2.94), we have:

$$\begin{aligned} P[\alpha|G] &\approx \frac{1}{\alpha} \frac{e^{Q(\hat{\sigma}_\alpha)}}{Z_L Z_S(\alpha)} \int \mathcal{D}X e^{-\frac{1}{2}\delta X \cdot (\alpha I + \Lambda) \cdot \delta X} \\ &= \frac{1}{\alpha} \frac{e^{Q(\hat{\sigma}_\alpha)}}{(\pi/2)^{N/2} \sqrt{\det C}} \sqrt{\frac{\det \alpha I}{\det [\alpha I + \Lambda(\hat{\sigma}_\alpha)]}}. \end{aligned} \quad (2.96)$$

Then the final spectral function we want is:

$$\begin{aligned} \sigma(\omega) &\approx \frac{\int d\alpha \hat{\sigma}_\alpha P[\alpha|G]}{\int d\alpha P[\alpha|G]} \\ &\approx \frac{\sum_{\alpha_{min}}^{\alpha_{max}} \hat{\sigma}_\alpha(\omega) e^{\frac{1}{2}\sum_i \log\left(\frac{\alpha}{\alpha+\lambda_i}\right)+Q} \Delta \log(\alpha)}{\sum_{\alpha_{min}}^{\alpha_{max}} e^{\frac{1}{2}\sum_i \log\left(\frac{\alpha}{\alpha+\lambda_i}\right)+Q} \Delta \log(\alpha)}, \end{aligned} \quad (2.97)$$

where λ is the eigenvalue of Λ .

2.2.5 MEM algorithm

The basic idea of the commonly used MEM algorithm is to get the most probable spectral function from given data by maximizing the conditional probability or solving

$$\alpha \nabla S - \nabla L = 0. \quad (2.98)$$

with

$$\nabla S = - \sum_i \log(\sigma_i/m_i), \quad \nabla L = \frac{\partial F}{\partial \sigma} \frac{\partial L}{\partial F} = K^T \frac{\partial L}{\partial F}. \quad (2.99)$$

Eq. (2.98) can be further written as

$$-\alpha \log(\sigma_i/m_i) = \sum_j K_{ji} \frac{\partial L}{\partial F_j}. \quad (2.100)$$

With the implementation of the singular value decomposition⁸, the $N_\tau \times N_\omega$ kernel K can be written as a product $K = V \Xi U^T$, where V and U are orthogonal matrices while Ξ is a diagonal matrix with ordered singular values ξ_i . Since some ξ_i are very small and rounding errors maybe introduced, the space should be reduced to the singular space with dimension $N_s \leq N_\tau$ by a criterion, e.g. $\xi_{min} > 10^{-10} \xi_{max}$.

Then from Eq. (2.100) it is convenient to parameterize σ with some N_s -dimensional vector \mathbf{u} ,

$$\sigma_i = m_i \exp \left(\sum_{j=1}^{N_s} U_{ij} u_j \right), \quad \frac{\partial \sigma}{\partial \mathbf{u}} = \text{diag}\{\sigma\} U, \quad (2.101)$$

which automatically fulfills the requirement that the spectral function should be non-negative. Inserting the parameterization of the spectral function into Eq. (2.100) the most probable image of the spectral function $\hat{\sigma}_\alpha$ at given α , can be obtained by solving

$$\alpha \mathbf{u} + \Xi V^T \frac{\partial L}{\partial \mathbf{F}} = 0 \quad (2.102)$$

with a standard Newton search algorithm [139, 140]. Then with Eq. (2.97) the final output image of the spectral function can thus be determined.

2.2.6 The extended MEM

As we have seen from the previous description of MEM, the spectral function can only be non-negative in the MEM analysis since it is interpreted as the probability. In some cases, we are also interested in the MEM analysis on the reconstruction of negative distributions, e.g. the spectral function difference $\Delta\sigma(\omega)$ from the difference of the correlators $G(\tau, T)$ and $G_{\text{rec}}(\tau, T)$ (see Eq. (2.65)) might be negative somewhere.

⁸The algorithm without singular value decomposition can be found in Ref. [40].

In condensed matter physics MEM has already been extended to reconstruct distributions which can be either positive or negative [113, 116, 128]. Here for the first time we introduce this extended version of MEM to lattice QCD [105]⁹ and complete the details missed in the previous references.

The idea is straightforward, say \mathbf{g} is the difference between two subsidiary positive distributions \mathbf{f} and \mathbf{h} :

$$\mathbf{g} = \mathbf{f} - \mathbf{h}. \quad (2.103)$$

The total entropy with respect to a common default model \mathbf{m} can then be written as the additive of two Shannon-Jaynes entropies for distributions \mathbf{f} and \mathbf{h} :

$$\tilde{S}(\mathbf{f}, \mathbf{h}) = \sum_i \left(f_i - m_i - f_i \log(f_i/m_i) \right) + \sum_i \left(h_i - m_i - h_i \log(h_i/m_i) \right). \quad (2.104)$$

Generally,

$$\frac{\partial \tilde{S}}{\partial \mathbf{f}} = \frac{\partial \tilde{S}}{\partial \mathbf{g}} \frac{\partial \mathbf{g}}{\partial \mathbf{f}} = - \frac{\partial \tilde{S}}{\partial \mathbf{g}} \frac{\partial \mathbf{g}}{\partial \mathbf{h}} = - \frac{\partial \tilde{S}}{\partial \mathbf{h}} \quad (2.105)$$

with Eq. (2.104) and Eq. (2.105), one obtains:

$$f_i h_i = m_i^2. \quad (2.106)$$

Thus with Eq. (2.103) and Eq. (2.106), the total entropy can be written as a function of \mathbf{g} alone:

$$\tilde{S}(\mathbf{g}) = \sum_i \left(\psi_i - 2m_i - g_i \log [(\psi_i + g_i)/2m_i] \right), \quad (2.107)$$

where

$$\psi_i = (g_i^2 + 4m_i^2)^{1/2}. \quad (2.108)$$

The entropy $\tilde{S}(\mathbf{g})$ has a maximum value when $\mathbf{g} = 0$.

Following the procedures in the previous sections with

$$\frac{\partial \tilde{S}}{\partial g_i} = - \log \left(\frac{\psi_i + g_i}{2m_i} \right), \quad (2.109)$$

$$\frac{\partial^2 \tilde{S}}{\partial g_i \partial g_j} = - \frac{\delta_{ij}}{\sqrt{\psi_i} \sqrt{\psi_j}}, \quad (2.110)$$

we expand $\tilde{Q} = \alpha \tilde{S} - L$ about the maximum for a fixed value of α in a coordinate system which is described by the variable Y_i :

$$\begin{aligned} \tilde{Q}(g, \alpha) &\approx \tilde{Q}(\hat{g}_\alpha) + \sum_i \delta Y_i \left[\frac{\partial \tilde{Q}}{\partial Y_i} \right]_{g=\hat{g}_\alpha} + \frac{1}{2} \sum_{i,j} \delta Y_i \delta Y_j \left[\frac{\partial^2 \tilde{Q}}{\partial Y_i \partial Y_j} \right]_{g=\hat{g}_\alpha} \\ &= \tilde{Q}(\hat{g}_\alpha) + \frac{1}{2} \sum_{i,j,k,l} \delta Y_i \delta Y_j \left[\frac{\partial g_k}{\partial Y_i} \frac{\partial g_l}{\partial Y_j} \frac{\partial^2 \tilde{Q}}{\partial g_k \partial g_l} \right]_{g=\hat{g}_\alpha}, \end{aligned} \quad (2.111)$$

⁹We note that MEM has been used to deal with negative spectral functions by Langfeld et al. in Ref. [121], but their entropy terms (formula (46) and (47)) obviously do not fulfill with the requirements we mentioned in Section 2.2.2.

where $\delta Y_i = Y_i - \hat{Y}_i$ and

$$\frac{\partial^2 \tilde{Q}}{\partial g_k \partial g_l} = \alpha \frac{\partial^2 \tilde{S}}{\partial g_k \partial g_l} - \frac{\partial^2 L}{\partial g_k \partial g_l} = -\frac{\alpha \delta_{kl}}{\sqrt{\psi_k} \sqrt{\psi_l}} - \frac{\partial^2 L}{\partial g_k \partial g_l}. \quad (2.112)$$

With a new coordinate system

$$\frac{\partial g_k}{\partial Y_l} = \sqrt{\psi_k} \delta_{kl} \quad (2.113)$$

we can further write

$$\tilde{Q}(g, \alpha) \approx \tilde{Q}(\hat{g}_\alpha) - \frac{1}{2} \sum_{ij} \delta Y_i \tilde{\Gamma}_{ij} \delta Y_j, \quad (2.114)$$

where $\tilde{\Gamma}$ is the positive-definite matrix $\tilde{\Gamma}_{ij} = \alpha \delta_{ij} + \tilde{\Lambda}_{ij}$ with

$$\tilde{\Lambda}_{ij} = \left[\sqrt{\psi_i} \frac{\partial^2 L}{\partial g_i \partial g_j} \sqrt{\psi_j} \right]_{g=\hat{g}_\alpha}, \quad (2.115)$$

where $\frac{\partial^2 L}{\partial g_i \partial g_j}$ has the following form

$$\frac{\partial^2 L}{\partial g_i \partial g_j} = \left[K^T \cdot \tilde{C}^{-1} \cdot K \right]_{ij}, \quad (2.116)$$

with \tilde{C} the covariance matrix of the correlation data for the distribution g .

The corresponding normalization function

$$\tilde{Z}_S = \prod_i \int \frac{dg_i}{\sqrt{\psi_i}} e^{\alpha \tilde{S}_i}, \quad (2.117)$$

is maximized at $g_i = 0$ and can be approximated by:

$$\tilde{Z}_S \approx \prod_i \int \frac{dg_i}{2m_i} e^{-\alpha g_i^2/4/m_i} \approx \left(\frac{\pi}{\alpha} \right)^{N/2} = \frac{\pi^{N/2}}{\sqrt{\det \alpha I}}. \quad (2.118)$$

which together with Eq. (2.114) give us the final output image:

$$g(\omega) \approx \frac{\sum_{\alpha_{min}}^{\alpha_{max}} \hat{g}_\alpha(\omega) e^{\frac{1}{2} \sum_i \log \left(\frac{\alpha}{\alpha + \lambda_i} \right) + \tilde{Q}} \Delta \log(\alpha)}{\sum_{\alpha_{min}}^{\alpha_{max}} e^{\frac{1}{2} \sum_i \log \left(\frac{\alpha}{\alpha + \lambda_i} \right) + \tilde{Q}} \Delta \log(\alpha)} \quad (2.119)$$

which is similar to Eq. (2.97). Then we can use the same algorithm that we used in the standard MEM only replacing the entropy term and the parameterization of the spectral function, that is to

- replace Eq. (2.79) with Eq. (2.107),
- replace Eq. (2.101) with

$$g_i = 2m_i \sinh \left(\sum_j U_{ij} u_j \right), \quad \frac{\partial g}{\partial u} = 2m U \cosh \left(\sum U u \right). \quad (2.120)$$

2.2.7 MEM analysis with zero mode contribution suppressed

To suppress the τ independent constant in the correlator¹⁰ in the MEM analysis one way is to look into the difference of neighboring correlators, $G(\tau) - G(\tau + 1)$ [126], which gives

$$G(\tau) - G(\tau + 1) = \int_0^\infty d\omega \sigma(\omega, T) K_{\text{diff}}(\tau, \omega), \quad (2.121)$$

where K_{diff} is given by

$$K_{\text{diff}}(\tau, \omega) = 2 \sinh\left(\frac{\omega}{2}\right) \frac{\sinh[\omega(N_\tau - 2\tau - 1)/2]}{\sinh(\omega N_\tau/2)}. \quad (2.122)$$

The relation (2.121) is exact and without any approximation. Consequently the spectral function obtained from the inversion of the relation (2.121) should be the same as that in the relation (2.67) except the constant contribution is suppressed. The new kernel K_{diff} goes smoothly to zero when the energy goes to zero as

$$\lim_{\omega \rightarrow 0} K_{\text{diff}}(\omega, \tau) = \frac{N_\tau - 2\tau - 1}{N_\tau} \omega + \mathcal{O}(\omega^3). \quad (2.123)$$

This avoids the divergence problem of the standard kernel at $\omega = 0$ as pointed out by Aarts et al. [41] and opens the possibility to explore the information of spectral functions in the very low frequency region.

The other way is to look into midpoint subtracted correlators [141]

$$G(\tau) - G\left(\frac{N_\tau}{2}\right) = \int_0^\infty d\omega \sigma(\omega, T) K_{\text{sub}}(\tau, \omega), \quad (2.124)$$

with

$$K_{\text{sub}}(\tau, \omega) = \frac{2 \sinh^2[\omega(N_\tau/2 - \tau)/2]}{\sinh(\omega N_\tau/2)}. \quad (2.125)$$

$K_{\text{sub}}(\tau, \omega)$ has the following limiting behavior at $\omega \rightarrow 0$

$$K_{\text{sub}}(\tau, \omega) = \left(\frac{N_\tau}{4} - \tau + \frac{\tau^2}{N_\tau}\right) \omega + \mathcal{O}(\omega^3). \quad (2.126)$$

Thus one also does not need to worry about the instability of the kernel at $\omega \approx 0$ and we can also explore the behavior of the spectral function in the very low frequency region.

2.2.8 Remarks on MEM

One very important parameter in the MEM analysis is the default model. The default model is important, extremely when the data is not good enough. Since the correlators are not sensitive to the high frequency part of the spectral function, one direct choice is

¹⁰The description of the τ independent constant can be found in section 2.3.1, see e.g. Eq. (2.146).

to supply the correct high frequency information to the default model. Due to asymptotic freedom the large ω part corresponds to the free non-interacting case, which we will discuss in the next session. The default model dependence of a mock data test as well as of the real data is investigated in detail in the next chapter.

Actually one is free to redefine the kernel and the spectral function with a factor and its inverse such that $G(\tau)$ remains unchanged. Rather than putting a prefactor of $\omega/2$ [41] in the kernel to circumvent the singularity of the kernel, here we adopt the following modified kernel [126, 142]

$$\tilde{K}(\tau, \omega) = \tanh\left(\frac{\omega}{2}\right) K(\omega, \tau), \quad (2.127)$$

$$\tilde{\sigma}(\omega) = \coth\left(\frac{\omega}{2}\right) \sigma(\omega), \quad (2.128)$$

which has several advantages:

- the large ω behavior of the kernel $K(\tau, \omega)$ and the spectral function $\sigma(\omega)$ are not changed
- the limits of $\tilde{K}(\tau, \omega)$ for $T \rightarrow 0$ and $\omega \rightarrow 0$ are finite and commutable.
- the size of $\tilde{\sigma}(\omega)$ can be estimated from the sum rule Eq. (2.62).

2.3 Free temporal correlation and spectral function

In this section we will briefly review the derivation of free temporal correlation and spectral functions in the non-interacting case at the lowest order in the loop expansion. More details can be found in the Refs. [106, 143]. A discussion of the general features of the free correlation and spectral functions is also presented.

We rewrite the definition of the spectral function with quantum numbers H in the coordinate space (Fourier transform of Eq. (2.12)):

$$\sigma_H(\tau, \mathbf{x}) = \langle [J_H(\tau, \mathbf{x}), J_H(0, \mathbf{0})] \rangle, \quad (2.129)$$

where the local meson operator $J_H(\tau, \mathbf{x})$ has the form of

$$J_H(\tau, \mathbf{x}) = \bar{q}(\tau, \mathbf{x}) \Gamma_H q(\tau, \mathbf{x}), \quad (2.130)$$

with

$$\Gamma_H = 1, \gamma_5, \gamma_\mu, \gamma_5 \gamma_\mu, \quad (2.131)$$

for scalar, pseudo scalar, vector and axial vector channels, respectively. The spectral function is related to the correlation function,

$$G_H(\tau, \mathbf{x}) = \langle J_H(\tau, \mathbf{x}) J_H(0, \mathbf{0}) \rangle, \quad (2.132)$$

via the standard integral relation

$$G_H(\tau, \mathbf{p}) = \int_0^\infty d\omega \sigma_H(\omega, \mathbf{p}) K(\tau, \omega). \quad (2.133)$$

2.3.1 Free spectral function in the continuum

At the lowest order in the loop expansion the Euclidean correlators in momentum space read:

$$G_H(\bar{P}) = -T \sum_n \int \frac{d^3k}{2\pi^3} \text{Tr} (S(K) \Gamma_H S(P + K) \gamma^0 \Gamma_H \gamma^0), \quad (2.134)$$

where $\bar{P} = (i\omega_n, \mathbf{p})$ with $\omega_n = 2\pi nT$ ($n \in \mathbb{Z}$) the Matsubara frequency in the imaginary time formalism. The fermion propagators are given by

$$S(\tilde{K}) = -\frac{1}{i\tilde{\omega}_n \gamma^0 - \gamma \mathbf{k} - m} = -\int_{-\infty}^{\infty} \frac{d\omega}{2\pi} \frac{\sigma_F(\omega, \mathbf{k})}{i\tilde{\omega}_n - \omega}, \quad (2.135)$$

with $\tilde{K} = (i\tilde{\omega}_n, \mathbf{k})$, $\tilde{\omega}_n = (2n+1)\pi T$ ($n \in \mathbb{Z}$) the fermionic Matsubara frequency and $\sigma_F(\omega, \mathbf{k})$ the spectral density of the fermion,

$$\sigma_F(K) = (\not{K} + m) \sigma(K) = 2\pi(\not{K} + m) \text{sgn}(k^0) \delta(k_0^2 - \omega_{\mathbf{k}}^2), \quad (2.136)$$

with $K = (k^0, \mathbf{k})$ and $\omega_{\mathbf{k}} = \sqrt{\mathbf{k}^2 + m^2}$. In the spectral representation of the fermion propagators the spectral function has the form as follows

$$\begin{aligned} \sigma_H(P) &= \frac{1}{\pi} \text{Im} G_H(i\omega_n \rightarrow \omega + i0^+, \mathbf{p}) \\ &= \frac{N_c}{\pi} \int \frac{d^4k}{(2\pi)^4} \text{Tr} \left((\not{K} + m) \Gamma_H (\not{K} + m) \gamma^0 \Gamma_H^\dagger \gamma^0 \sigma(K) \sigma(R) [n_F(k^0) - n_F(r^0)] \right), \end{aligned} \quad (2.137)$$

where $P = (\omega, \mathbf{p})$, $R = P + K = (\omega + k^0, \mathbf{p} + \mathbf{k})$ and $n_F(\omega) = (e^{\omega/T} + 1)^{-1}$ is the Fermi distribution.

After performing the momentum integral in the above relation one arrives at the

final expression of the free continuum spectral function [143]

$$\begin{aligned}
\sigma_H(P) = & \Theta(s - 4m^2) \frac{N_c T^2}{2\pi^2} \left\{ \right. \\
& \frac{\beta(P)}{24T^2} \left[(3\omega^2 - \mathbf{p}^2 \beta^2(P)) a_H^{(1)} + (3\mathbf{p}^2 - (3\omega^2 - 2\mathbf{p}^2) \beta^2(P)) a_H^{(2)} - 12m^2 a_H^{(3)} \right] \\
& + \frac{1}{4|\mathbf{p}|T} \left[(\omega^2 - \mathbf{p}^2 \beta^2(P)) a_H^{(1)} + (\mathbf{p}^2 - \omega^2 \beta^2(P)) a_H^{(2)} - 4m^2 a_H^{(3)} \right] \ln \frac{1 + e^{-\bar{p}+/T}}{1 + e^{-\bar{p}-/T}} \\
& + \left(a_H^{(1)} + a_H^{(2)} \right) \left(\beta(P) \left[\text{Li}_2(-e^{-\bar{p}+/T}) + \text{Li}_2(-e^{-\bar{p}-/T}) \right] \right. \\
& \quad \left. + \frac{2T}{|\mathbf{p}|} \left[\text{Li}_3(-e^{-\bar{p}+/T}) - \text{Li}_3(-e^{-\bar{p}-/T}) \right] \right) \left. \right\} \\
& + \Theta(-s) \frac{N_c T^2}{2\pi^2} \left\{ \frac{1}{4|\mathbf{p}|T} \left[(\omega^2 - \mathbf{p}^2 \beta^2(P)) a_H^{(1)} + (\mathbf{p}^2 - \omega^2 \beta^2(P)) a_H^{(2)} - 4m^2 a_H^{(3)} \right] \right. \\
& \ln \frac{1 + e^{-\bar{p}+/T}}{1 + e^{\bar{p}-/T}} + \left(a_H^{(1)} + a_H^{(2)} \right) \left(\beta(P) \left[\text{Li}_2(-e^{-\bar{p}+/T}) - \text{Li}_2(-e^{\bar{p}-/T}) \right] \right. \\
& \quad \left. \left. + \frac{2T}{|\mathbf{p}|} \left[\text{Li}_3(-e^{-\bar{p}+/T}) - \text{Li}_3(-e^{\bar{p}-/T}) \right] \right) \right\}. \quad (2.138)
\end{aligned}$$

where

$$\bar{p}_\pm = \frac{1}{2} [\omega \pm |\mathbf{p}| \beta(P)], \quad \beta(P) = \sqrt{1 - \frac{4m^2}{s}}, \quad s = \omega^2 - \mathbf{p}^2, \quad (2.139)$$

and the polylogarithm function Li_s is defined as $\text{Li}_s(z) = \sum_{k=1}^{\infty} \frac{z^k}{k^s}$. The coefficients $a_H^{(i)}$ for different channels can be read off from Table 2.2. It is not so straightforward to read off the physics from the above equation, so we consider several limits in the following paragraphs.

In the large frequency limit the spectral functions of channels $\Gamma_H = 1, \gamma^i, \gamma^5, \gamma^i \gamma^5$ increase with ω^2

$$\lim_{\omega \rightarrow \infty} \sigma_H(\omega, \mathbf{p}) = \Theta(s - 4m^2) \frac{N_c}{16\pi^2} \omega^2 (a_H^{(1)} - a_H^{(2)}). \quad (2.140)$$

while the spectral functions in the other two channels $\Gamma_H = \gamma^0, \gamma^5 \gamma^0$ increase with \mathbf{p}^2

$$\lim_{\omega \rightarrow \infty} \sigma_{VC}^{00}(\omega, \mathbf{p}) = \Theta(s - 4m^2) \frac{N_c}{12\pi^2} \mathbf{p}^2, \quad (2.141)$$

$$\lim_{\omega \rightarrow \infty} \sigma_{AV}^{00}(\omega, \mathbf{p}) = \Theta(s - 4m^2) \frac{N_c}{12\pi^2} (\mathbf{p}^2 + 6m^2). \quad (2.142)$$

Since the correlation function is given as the integral of the spectral function in the frequency space, the low frequency information in γ^0 and $\gamma^0 \gamma^5$ should be more pronounced than in the other channels as indicated from the formulae (2.140), (2.141) and (2.142).

	Γ_H	$a_H^{(1)}$	$a_H^{(2)}$	$a_H^{(3)}$
σ_{SC}	$\mathbb{1}$	1	-1	1
σ_{PS}	γ_5	1	-1	-1
σ_{VC}^{00}	γ^0	1	1	1
σ_{VC}^{ii}	γ^i	3	-1	-3
σ_{VC}	γ^μ	2	-2	-4
σ_{AV}^{00}	$\gamma^0 \gamma_5$	1	1	-1
σ_{AV}^{ii}	$\gamma^i \gamma_5$	3	-1	3
σ_{AV}	$\gamma^\mu \gamma_5$	2	-2	4

Table 2.2. Coefficients $a_H^{(i)}$ for free spectral functions in different channels H [143]. The index i is summed over $i = 1, 2, 3$ in γ^i and $\gamma^i \gamma_5$ channels. $\sigma_{\text{VC}} = \sigma_{\text{VC}}^{ii} - \sigma_{\text{VC}}^{00}$ and $\sigma_{\text{AV}} = \sigma_{\text{AV}}^{ii} - \sigma_{\text{AV}}^{00}$.

In the zero momentum limit the spectral functions (2.149) reduce to [143]¹¹

$$\begin{aligned} \sigma_H(\omega, \mathbf{0}) &= \frac{N_c}{16\pi^2} \Theta(\omega^2 - 4m^2) \omega^2 \tanh\left(\frac{\omega}{4T}\right) \sqrt{1 - \left(\frac{2m}{\omega}\right)^2} \\ &\quad \times \left[\left(a_H^{(1)} - a_H^{(2)}\right) + \left(\frac{2m}{\omega}\right)^2 \left(a_H^{(2)} - a_H^{(3)}\right) \right] \\ &\quad + N_c \left[\left(a_H^{(1)} + a_H^{(3)}\right) I_1 + \left(a_H^{(2)} - a_H^{(3)}\right) I_2 \right] \omega \delta(\omega), \end{aligned} \quad (2.143)$$

with

$$I_1 = -2 \int \frac{d^3\mathbf{k}}{(2\pi)^3} \frac{\partial n_F(\omega_{\mathbf{k}})}{\partial \omega_{\mathbf{k}}}, \quad I_2 = -2 \int \frac{d^3\mathbf{k}}{(2\pi)^3} \frac{\mathbf{k}^2}{\omega_{\mathbf{k}}^2} \frac{\partial n_F(\omega_{\mathbf{k}})}{\partial \omega_{\mathbf{k}}}. \quad (2.144)$$

There appears a $\omega\delta\omega$ term in the above spectral function. As indicated from relation (2.52), when the frequency approaches zero the integrand kernel $K(\tau, \omega)$ behaves as $2T/\omega$, thus the $\omega\delta\omega$ term will give a τ independent constant term to the correlator. Furthermore in the case of vanishing quark mass $I_1 = I_2 = T^2/6$ and the correlation function can be given analytically [143]

$$G_H(\tau, \mathbf{p} = 0) = \frac{N_c T^3}{6} \left(\left(a_H^{(1)} + a_H^{(2)}\right) + \frac{3}{2} \left(a_H^{(1)} - a_H^{(2)}\right) \frac{3u + u \cos(2u) - 2 \sin(2u)}{\sin^3(u)} \right), \quad (2.145)$$

with $u = 2\pi T(\tau - 1/(2T))$. If one evaluates $a_H^{(1)} + a_H^{(2)}$ from Table 2.2, one can see that there are non-zero τ independent constants in the correlation functions in γ^0 , γ^i ,

¹¹There is a typo in the last term of Eq. (2.143), i.e. Eq. (19) in Ref. [143]. $(a_H^{(1)} + a_H^{(2)})I_1$ should be $(a_H^{(1)} + a_H^{(3)})I_1$.

$\gamma^0\gamma^5$ and $\gamma^i\gamma^5$ channels. Specially due to charge conservation, the correlation function in the γ^0 channel G_{VC}^{00} and its spectral function σ_{VC}^{00} are related to the quark number susceptibility χ through

$$G_{VC}^{00}(T, \mathbf{p} = 0) = T\chi, \quad (2.146)$$

$$\sigma_{VC}^{00}(\omega, \mathbf{p} = 0) = \omega\delta(\omega)\chi, \quad (2.147)$$

and in this case $\chi = N_c T^2/3$. In the non-zero quark mass case I_1 and I_2 are not equal any more and consequently there will be a non-zero τ independent constant contribution to the correlator in all the channels except the pseudo scalar channel. This can be seen from the quark number susceptibility in general

$$\chi(m, \mathbf{p} = 0) = -2N_c \int \frac{d^3\mathbf{k}}{(2\pi)^3} \frac{\left(a_H^{(1)} + a_H^{(2)}\right) \mathbf{k}^2 + \left(a_H^{(1)} + a_H^{(3)}\right) m^2}{\omega_{\mathbf{k}}^2} \frac{\partial n_F(\omega_{\mathbf{k}})}{\partial \omega_{\mathbf{k}}}. \quad (2.148)$$

In the zero mass limit, the spectral functions reduce to

$$\begin{aligned} \sigma_H(P) = & \Theta(\omega^2 - \mathbf{p}^2) \frac{N_c T^2}{2\pi^2} \left\{ \right. \\ & \frac{1}{4|\mathbf{p}|T} (\omega^2 - \mathbf{p}^2) \left(a_H^{(1)} - a_H^{(2)} \right) \ln \left(\frac{\cosh \left(\frac{\omega + \mathbf{p}}{4T} \right)}{\cosh \left(\frac{\omega - \mathbf{p}}{4T} \right)} \right) + \frac{1}{12T^2} \left(a_H^{(1)} + a_H^{(2)} \right) \mathbf{p}^2 \\ & + \left(a_H^{(1)} + a_H^{(2)} \right) \left(\text{Li}_2(-e^{-(\omega + |\mathbf{p}|)/2T}) + \text{Li}_2(-e^{-(\omega - |\mathbf{p}|)/2T}) \right) \\ & \left. + \frac{2T}{|\mathbf{p}|} \left[\text{Li}_3(-e^{-(\omega + |\mathbf{p}|)/2T}) - \text{Li}_3(-e^{-(\omega - |\mathbf{p}|)/2T}) \right] \right\} \\ & + \Theta(\mathbf{p}^2 - \omega^2) \frac{N_c T^2}{2\pi^2} \left\{ \right. \\ & \frac{1}{4|\mathbf{p}|T} (\omega^2 - \mathbf{p}^2) \left(a_H^{(1)} - a_H^{(2)} \right) \left[\ln \left(\frac{\cosh \left(\frac{\omega + \mathbf{p}}{4T} \right)}{\cosh \left(\frac{\omega - \mathbf{p}}{4T} \right)} \right) - \frac{\omega}{2T} \right] \\ & + \left(a_H^{(1)} + a_H^{(2)} \right) \left(\text{Li}_2(-e^{-(\omega + |\mathbf{p}|)/2T}) - \text{Li}_2(-e^{-(\omega - |\mathbf{p}|)/2T}) \right) \\ & \left. + \frac{2T}{|\mathbf{p}|} \left[\text{Li}_3(-e^{-(\omega + |\mathbf{p}|)/2T}) - \text{Li}_3(-e^{-(\omega - |\mathbf{p}|)/2T}) \right] \right\}. \quad (2.149) \end{aligned}$$

As one can see obviously from the above equation the spectral function depends on the coefficients $a_H^{(1)}$ and $a_H^{(2)}$ but not $a_H^{(3)}$. In other words, as expected, in the chiral limit (vanishing quark mass) scalar and pseudo scalar (vector and axial vector) degenerate.

In the limit of $\mathbf{p} \ll T$ and the non-relativistic limit, i.e. $n_F = \exp(-\mathbf{p}^2/(2MT))$, one can get the low energy part of spectral functions of the density-density correlator

and of the longitudinal current-current correlator as follows [144]

$$\sigma^{\text{NN}}(\omega, \mathbf{p}) \Big|_{\text{low}} = \chi_s \omega \frac{1}{\sqrt{2\pi \mathbf{p}^2 \langle \frac{v^2}{3} \rangle}} \exp\left(-\frac{\omega^2}{2\mathbf{p}^2 \langle \frac{v^2}{3} \rangle}\right), \quad (2.150)$$

$$\sigma^{\text{JJ}}(\omega, \mathbf{p}) \Big|_{\text{low}} = \chi_s \frac{\omega^3}{\mathbf{p}^2} \frac{1}{\sqrt{2\pi \mathbf{p}^2 \langle \frac{v^2}{3} \rangle}} \exp\left(-\frac{\omega^2}{2\mathbf{p}^2 \langle \frac{v^2}{3} \rangle}\right), \quad (2.151)$$

where χ_s is the static quark number susceptibility, $\langle \frac{v^2}{3} \rangle$ is the thermal average of the squared velocity of quarks. For the massive quark case $\langle \frac{v^2}{3} \rangle = T/M$ while for the massless quark case $\langle \frac{v^2}{3} \rangle = 1/3$.

2.3.2 Free spectral function for Wilson fermions on the lattice

The meson spectral functions on a $N_\sigma^3 \times N_\tau$ lattice are derived as follows. The discretized version of Eq. (2.134) reads:

$$G_H(\tau, \mathbf{p}) = -\frac{N_c}{L^3} \sum_{\mathbf{k}} \text{Tr} \left(S(\tau, \mathbf{k}) \Gamma_H S(-\tau, \mathbf{r}) \Gamma_H \right), \quad (2.152)$$

with $\mathbf{p} = \mathbf{k} + \mathbf{r}$, and the Wilson fermion propagator is

$$S(K) = \frac{-i\gamma_4 \sin k_4 - i\mathcal{K}_{\mathbf{k}} + 1 - \cos k_4 + \mathcal{M}_{\mathbf{k}}}{\sin^2 k_4 + \mathcal{K}_{\mathbf{k}}^2 + (1 - \cos k_4 + \mathcal{M}_{\mathbf{k}})^2}, \quad (2.153)$$

with

$$\mathcal{K}_{\mathbf{k}} = \sum_{i=1}^3 \gamma_i \sin k_i, \quad \mathcal{M}_{\mathbf{k}} = \sum_{i=1}^3 (1 - \cos k_i) + m \quad (2.154)$$

where for spatial directions ($i=1,2,3$), periodic boundary conditions are used: $k_i = 2\pi n_i / N_\sigma$ with $n_i \in \mathbb{Z}, n_i \in [-N_\sigma/2 + 1, N_\sigma/2]$; for the temporal direction anti-periodic boundary conditions are employed: $k_4 = \pi(2n_4 + 1)/N_\tau$ with $n_4 \in \mathbb{Z}, n_4 \in [-N_\tau/2 + 1, N_\tau/2]$.

Using the mixed representation in Ref. [145]

$$S(\tau, \mathbf{k}) = \gamma_4 S_4(\tau, \mathbf{k}) + \sum_{i=1}^3 \gamma_i S_i(\tau, \mathbf{k}) + \mathbb{1} S_u(\tau, \mathbf{k}), \quad (2.155)$$

where

$$\begin{aligned} S_4(\tau, \mathbf{k}) &= S_4(\mathbf{k}) \cosh(\tilde{\tau} E_{\mathbf{k}}), \\ S_i(\tau, \mathbf{k}) &= S_i(\mathbf{k}) \sinh(\tilde{\tau} E_{\mathbf{k}}), \\ S_u(\tau, \mathbf{k}) &= S_u(\mathbf{k}) \sinh(\tilde{\tau} E_{\mathbf{k}}) - \frac{\delta_{\tau 0}}{2(1 + \mathcal{M}_{\mathbf{k}})}. \end{aligned} \quad (2.156)$$

Here $\tilde{\tau} = \tau - 1/2T$ and

$$\begin{aligned} S_4(\mathbf{k}) &= \frac{\sinh(E_{\mathbf{k}})}{2\mathcal{E}_{\mathbf{k}} \cosh(E_{\mathbf{k}}/2T)}, \\ S_i(\mathbf{k}) &= \frac{i \sin k_i}{2\mathcal{E}_{\mathbf{k}} \cosh(E_{\mathbf{k}}/2T)}, \\ S_u(\mathbf{k}) &= -\frac{1 - \cosh(E_{\mathbf{k}}) + \mathcal{M}_{\mathbf{k}}}{2\mathcal{E}_{\mathbf{k}} \cosh(E_{\mathbf{k}}/2T)}, \end{aligned} \quad (2.157)$$

with $\mathcal{E}_{\mathbf{k}} = (1 + \mathcal{M}_{\mathbf{k}}) \sinh(E_{\mathbf{k}})$. The single particle energy $E_{\mathbf{k}}$ is determined by

$$\cosh(E_{\mathbf{k}}) = 1 + \frac{\mathcal{K}_{\mathbf{k}}^2 + \mathcal{M}_{\mathbf{k}}^2}{2(1 + \mathcal{M}_{\mathbf{k}})}. \quad (2.158)$$

The final term in $S_u(\tau, \mathbf{k})$ is the sole remnant of the nonpropagating time doubler and in the following we consider $0 < \tau < 1/T$. The propagator satisfies $S(-\tau, \mathbf{k}) = \gamma_5 S^\dagger(\tau, \mathbf{k}) \gamma_5$. Thus correlators are given by [143]

$$\begin{aligned} G_H(\tau, \mathbf{p}) &= \frac{4N_c}{L^3} \sum_{\mathbf{k}} \left[a_H^{(1)} S_4(\tau, \mathbf{k}) S_4^\dagger(\tau, \mathbf{r}) - a_H^{(2)} \sum_i S_i(\tau, \mathbf{k}) S_i^\dagger(\tau, \mathbf{r}) \right. \\ &\quad \left. - a_H^{(3)} S_u(\tau, \mathbf{k}) S_u^\dagger(\tau, \mathbf{r}) \right], \end{aligned} \quad (2.159)$$

and the spectral functions can be obtained from the integral relation (2.133) [143]

$$\begin{aligned} \sigma_H^{\text{Wilson}}(P) &= \frac{2N_c}{L^3} \sum_{\mathbf{k}} \sinh\left(\frac{\omega}{2T}\right) \left\{ \right. \\ &\quad \left[a_H^{(1)} S_4(\mathbf{k}) S_4^\dagger(\mathbf{r}) + a_H^{(2)} \sum_i S_i(\mathbf{k}) S_i^\dagger(\mathbf{r}) + a_H^{(3)} S_u(\mathbf{k}) S_u^\dagger(\mathbf{r}) \right] \delta(\omega + E_{\mathbf{k}} - E_{\mathbf{r}}) \\ &\quad + \left[a_H^{(1)} S_4(\mathbf{k}) S_4^\dagger(\mathbf{r}) - a_H^{(2)} \sum_i S_i(\mathbf{k}) S_i^\dagger(\mathbf{r}) - a_H^{(3)} S_u(\mathbf{k}) S_u^\dagger(\mathbf{r}) \right] \delta(\omega - E_{\mathbf{k}} - E_{\mathbf{r}}) \\ &\quad \left. + (\omega \rightarrow -\omega) \right\}, \end{aligned} \quad (2.160)$$

where the coefficients $a_H^{(i)}$ are same as before (see Table 2.2).

At the symmetry point $\tau = 1/(2T)$ ($\tilde{\tau} = 0$) the form of the fermion propagator (2.156) in the mixed representation becomes simpler and one can easily obtain

$$G_H(\tau = 1/2T, \mathbf{p}) = \frac{4N_c}{L^3} \sum_{\mathbf{k}} a_H^{(1)} S_4(\mathbf{k}) S_4^\dagger(\mathbf{r}). \quad (2.161)$$

From Table. 2.2 one concludes the midpoint of the scalar and pseudo scalar (vector and axial vector) channel overlaps

$$G_{\text{SC}}(\tau = 1/2T, \mathbf{p}) = G_{\text{PS}}(\tau = 1/2T, \mathbf{p}), \quad (2.162)$$

$$G_{\text{VC}}(\tau = 1/2T, \mathbf{p}) = G_{\text{AV}}(\tau = 1/2T, \mathbf{p}). \quad (2.163)$$

It is worth noting that the above relations hold for both massive and massless quark cases.

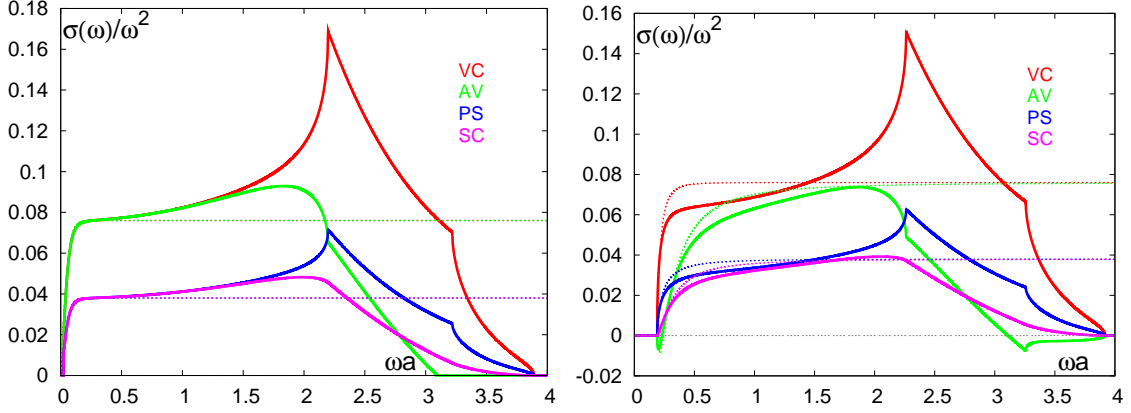


Figure 2.1. Free spectral functions $\sigma(\omega, \mathbf{p} = 0)/\omega^2$ as a function of ωa on $N_\tau = 64$ lattices. The solid lines are free lattice spectral functions while the dotted lines correspond to free continuum spectral functions. The left plot is for zero quark mass case and the right one is with non-zero quark mass $ma = 0.01$. VC, AV, PS and SC denote vector (γ^μ), axial vector ($\gamma^5\gamma^\mu$), pseudo scalar and scalar channel, respectively. Note in the right plot the $\delta(\omega)/\omega$ behavior at $\omega = 0$ is not shown for VC, AV and SC channels.

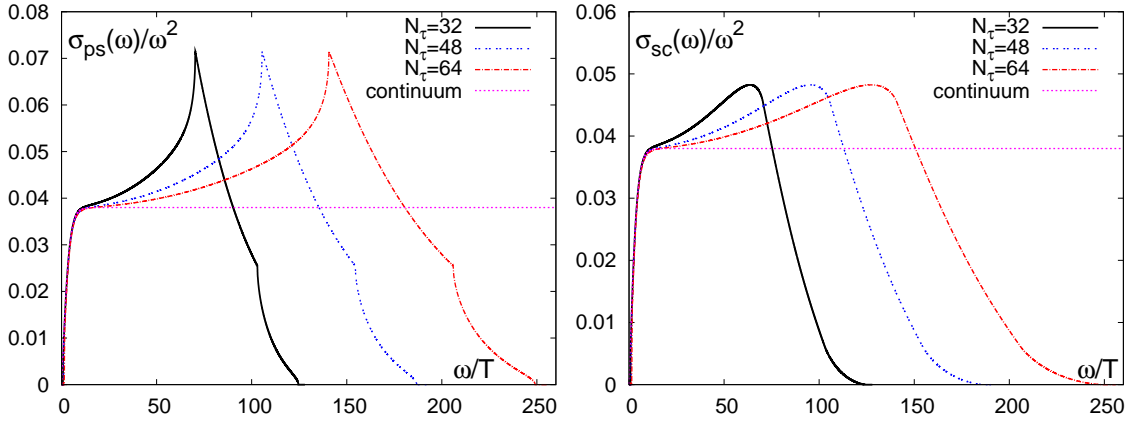


Figure 2.2. Massless pseudo scalar (left) and scalar (right) spectral functions $\sigma(\omega, \mathbf{p} = 0)/\omega^2$ as a function of ω/T with $N_\tau = 32, 48, 64$ at fixed T .

2.3.3 Comparison of free spectral function and correlator

Based on the calculation in the previous two sections, we now study the properties of free lattice and continuum spectral functions from different aspects. The lattice spectral function can be evaluated with different N_σ and N_τ . Here we focus on the effects of N_τ and take the thermodynamic limit $N_\sigma \rightarrow \infty$. Technically we take $N_\sigma = 4000$, $N_\omega = 2000$ with a bin width $\Delta\omega \approx 4/N_\omega$.

We plot the free spectral function for different channels at zero momentum in Fig. 2.1. The left plot is for zero quark mass case and the right one is with non-zero quark mass $ma = 0.01$. To suppress the large ω rise we divide the spectral function by ω^2 . In the massless case (chiral limit) we can see that the continuum spectral functions of the vector (VC) and axial vector (AV), pseudo scalar (PS) and scalar (SC) coincide. They reach a constant value of $3/(4\pi^2)$ and $3/(8\pi^2)$, respectively, as indicated from Eq. (2.140). When the quark mass is non-zero the chiral symmetry is explicitly broken and consequently the continuum vector and axial vector, pseudo scalar and scalar start to differ in the low frequency region and coincide only in the high frequency region where the quark mass is negligible. Let's now look at free lattice spectral functions. Due to the Wilson discretization the chiral symmetry is explicitly broken. Thus the free lattice spectral functions of vector and axial vector (scalar and pseudo scalar) only coincide in the low frequency region in the massless case and do not overlap at all in the non-zero quark mass case where the chiral symmetry is broken more severely. The deviation of the lattice spectral functions from the continuum ones, especially in the high frequency region, is mainly due to lattice discretization effects. Rather than approaching a constant value like the free continuum spectral function the free lattice spectral function goes to zero at a certain ω value. This can be understood from the single particle dispersion relation (2.158), where the single particle energy can be expressed as

$$E(\mathbf{k}) = \log \left(1 + \frac{\mathcal{K}_{\mathbf{k}}^2 + \mathcal{M}_{\mathbf{k}}^2}{2(1 + \mathcal{M}_{\mathbf{k}})} + \frac{\sqrt{(\mathcal{K}_{\mathbf{k}}^2 + \mathcal{M}_{\mathbf{k}}^2)(\mathcal{K}_{\mathbf{k}}^2 + (\mathcal{M}_{\mathbf{k}} + 2)^2)}}{2(1 + \mathcal{M}_{\mathbf{k}})} \right). \quad (2.164)$$

When the fermion momentum \mathbf{k} hits the edge of the Brillouin zone the doublers contribute at the frequency value of

$$\omega \equiv 2E(\mathbf{k}) = 2 \log(1 + \mathcal{M}_{\mathbf{k}}). \quad (2.165)$$

The highest frequency value on the lattice is thus determined when the fermion momentum $\mathbf{k} = (\pi/a, \pi/a, \pi/a)$:

$$a\omega_{max} = 2 \log(1 + (6 + am)), \quad (2.166)$$

and the lowest frequency value on the lattice is

$$a\omega_{min} = 2 \log(1 + am), \quad \mathbf{k} = (0, 0, 0). \quad (2.167)$$

The other two cusps seen from Fig. 2.1 are located at

$$a\omega_1 = 2 \log(1 + (2 + am)), \quad \mathbf{k} = \left(\frac{\pi}{a}, 0, 0\right), \left(0, \frac{\pi}{a}, 0\right), \left(0, 0, \frac{\pi}{a}\right), \quad (2.168)$$

$$a\omega_2 = 2 \log(1 + (4 + am)), \quad \mathbf{k} = \left(\frac{\pi}{a}, \frac{\pi}{a}, 0\right), \left(0, \frac{\pi}{a}, \frac{\pi}{a}\right), \left(\frac{\pi}{a}, 0, \frac{\pi}{a}\right). \quad (2.169)$$

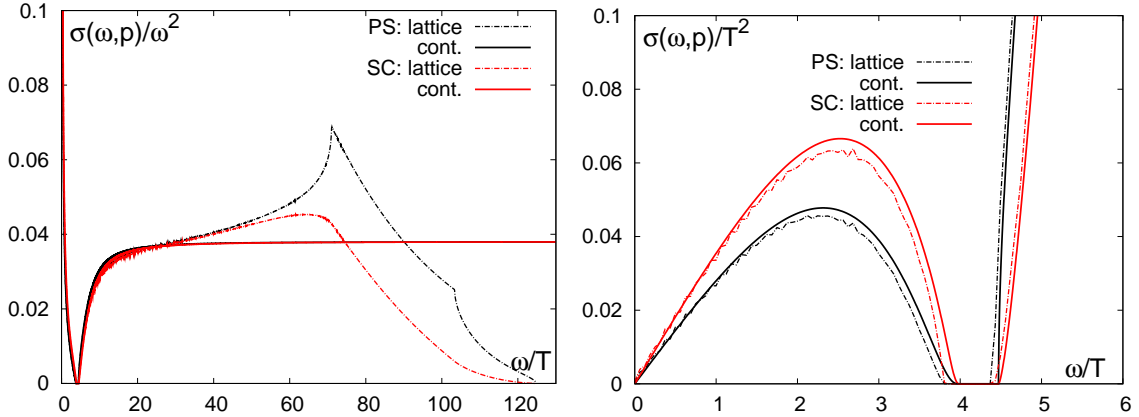


Figure 2.3. Pseudo scalar and scalar spectral functions $\sigma_{PS,SC}(\omega, \mathbf{p})/\omega^2$ (left) and $\sigma_{PS,SC}(\omega, \mathbf{p})/T^2$ (right) as a function of ω/T with $N_\tau = 32$, $|\mathbf{p}|/T = 4$ and $m/T = 1$. The dotted lines are free lattice spectral functions while the solid lines correspond to free continuum spectral functions.

In particular, spectral functions in P wave channels (scalar and axial vector) suffer much larger lattice cut-off effects. This is more notable in the massive quark case, as one can see from the right panel of Fig. 2.1 that there are even some energy regions where the spectral function are negative.

To check lattice cut-off effects we plot the pseudo scalar (left) and scalar (right) spectral function as a function of ω/T at zero momentum and vanishing quark mass with different N_τ at fixed T in Fig. 2.2. ω_{max}/T as well as the peak locations of the two doublers ($a\omega_1$ and $a\omega_2$) increases with increasing N_τ . Recalling the relation $T = 1/(aN_\tau)$ as expected from relation (2.166), this behavior means lattice artifacts (doublers) are shifted to the larger energy region and thus are separated further from the region of the physics interests when the lattice spacing is decreased. As expected the lattice spectral functions reproduce the continuum ones better at larger N_τ .

So far we have looked at zero momentum spectral functions. When momentum is switched on there will be an additional contribution from the frequency region of $\omega^2 < \mathbf{p}^2$, as indicated from Eq. (2.149). In Fig. 2.3 the free pseudo scalar and scalar spectral functions with $|\mathbf{p}|/T = 4$ and $m/T = 1$ are shown. The left plot is for the whole frequency region and shows $\sigma(\omega, \mathbf{p})/\omega^2$ versus ω/T while the right plot shows $\sigma(\omega, \mathbf{p})/T^2$ versus ω/T in the low frequency region. The spectral functions vanish in the energy region of $\mathbf{p}^2 < \omega^2 < \mathbf{p}^2 + 4m^2$. Due to the non-zero quark mass the pseudo scalar and scalar are physically distinct. The mismatch even in such a low frequency region between lattice and continuum is due to the dispersion relations and they will move closer with increasing N_τ .

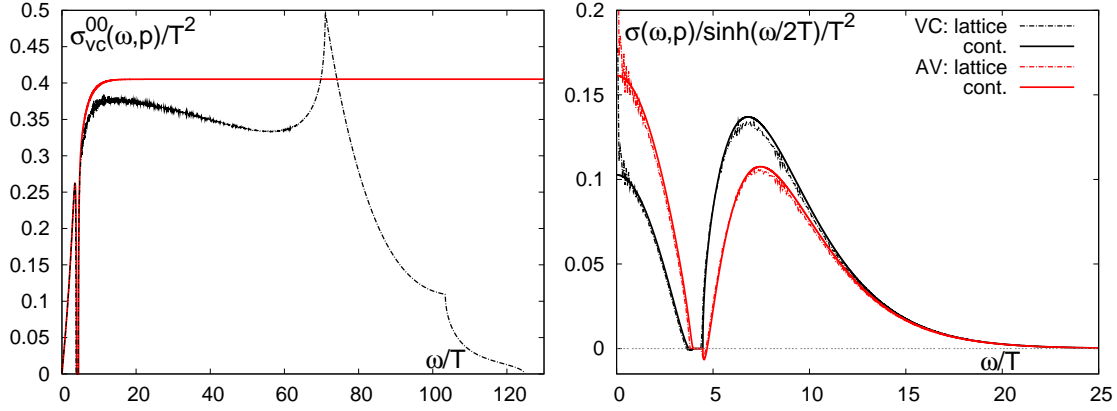


Figure 2.4. Left: Free vector (γ^0 channel) spectral functions $\sigma_{VC}^{00}(\omega, \mathbf{p})/T^2$ as a function of ω/T with $N_\tau = 32$, $|\mathbf{p}|/T = 4$ and $m/T = 1$. The red solid line is the lattice spectral function while the black dash-dotted line denotes the free continuum one. Right: Free spectral function $\sigma(\omega, \mathbf{p})/\sinh(\omega/2T)$ in vector and axial vector channel as a function of ω/T with $N_\tau = 32$, $|\mathbf{p}|/T = 4$ and $m/T = 1$. The dotted lines are free lattice spectral function while the solid lines correspond to free continuum spectral function.

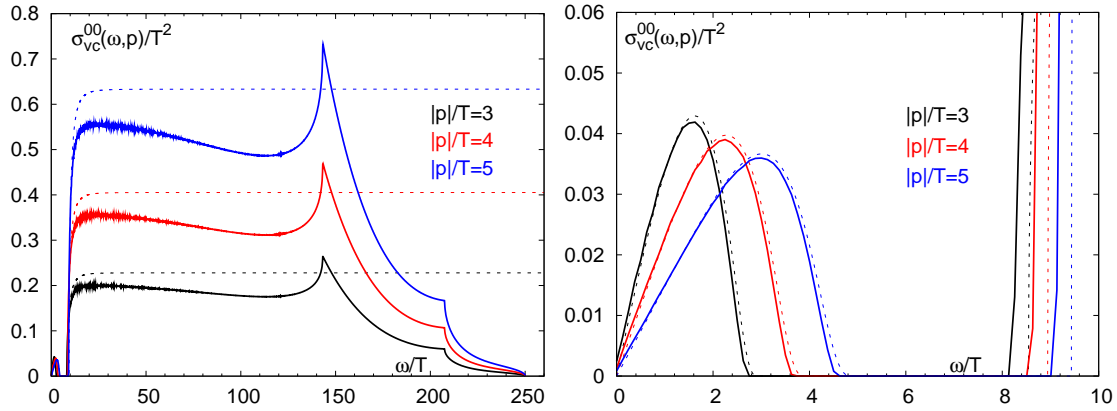


Figure 2.5. Momentum dependences of the spectral functions $\sigma_V^{00}(\omega, \mathbf{p})/T^2$ with $N_\tau = 64$ and $m/T = 1$. Solid lines are free lattice spectral functions while the dotted lines correspond to free continuum spectral functions. The right plot is a blowup of the low frequency region of the left plot.

We have observed τ independent constants in the vanishing momentum correlator from Eq. (2.145) and in particular σ_{VC}^{00} relates with the quark number susceptibility through relation (2.147). The change of this phenomenon is also interesting when going to finite momenta. We show the $\sigma_{VC}^{00}(\omega, \mathbf{p})/T^2$ at $|\mathbf{p}|/T = 4$ and $m/T = 1$ in the left panel of Fig. 2.4. $\sigma_{VC}^{00}(\omega, \mathbf{p})$ does not behave like $\omega\delta\omega$ anymore and now has a

sophisticated structure. The additional interesting feature of this spectral function is that it does not have a ω^2 rise like the other spectral functions, e.g. σ_{VC}^{ii} , as one can read from relations (2.140), (2.141), and (2.142). Thus we show σ_{VC}^{00}/T^2 in the left plot of Fig. 2.4. The small cusps which appear in the very low frequency region are mainly due to momentum effects and the higher frequency region as usual is distorted by the lattice discretization effects. On the right hand side of Fig. 2.4, the vector and axial vector spectral functions multiplied by the integrand kernel at the symmetry point is shown. As we have seen before the midpoint contribution to the correlator from these two channels are the same and thus the area under the spectral functions should be the same: the larger spectral function weight of σ_{VC} above the threshold is compensated by its smaller spectral weight below the lightcone.

We further look into the momentum dependence of the spectral function in the γ_0 channel shown in Fig. 2.5. The spectral functions $\sigma_{VC}^{00}(\omega, \mathbf{p})$ are obtained with $N_\tau = 64$ and $m/T = 4$. We vary the value of $|\mathbf{p}|/T$ to be 3, 4 and 5. One can see from the left plot of Fig. 2.5, the large ω behavior of the continuum spectral functions (labeled by the dashed lines) increases with increasing $|\mathbf{p}|/T$ and scales with \mathbf{p}^2 as indicated from Eq. (2.141). The large free lattice spectral function as usual is distorted by the discretization effects and its amplitude follows the free continuum one and approximately scales with \mathbf{p}^2 . For the very low frequency part of the spectral function, seen in the right panel of the Fig. 2.5, the lattice free spectral function, which appears as a bump, can reproduce the continuum one quite well. The amplitudes in this region do not increase as \mathbf{p}^2 and only the peak location moves to larger frequency when increasing the momentum.

In the following chapter we will take advantage of the above features of the free spectral function in the data analysis.

2.4 Linear response theory and Heavy quark diffusion

One useful (and normally adopted) way to investigate the properties of some certain system is to apply some sort of weak external force to the system and look what happens and then infer from that the properties of the system itself. Linear response theory is the quantitative formalism for dealing with such situations. The beauty of the theory is that the response of the system can be expressed as a product of the external source causing the disturbance with a retarded correlator that is computable using the correlation functions in the thermal equilibrium not dependent on the external source. In other words, the details of the internal dynamic properties can be studied from the static equilibrium features of the system with proper weak external probes. Introductions to this theory and its various applications can be found in many textbooks [10, 110, 146].

In our particular subject, for instance, the heavy quark diffusion constant can be expressed as the low frequency limit of the vector spectral function obtained from the static two point correlation function (Eq. 2.46) via Kubo relation from linear response theory [10]. Phenomenologically the two point correlation function of a charm and anticharm quark pair describes the response of the medium to the presence of two quarks c and \bar{c} traveling to each other from two separated space time points with the temporal separation being the inverse temperature of the medium¹². It concerns the propagation of the single quark and its interaction with the medium, e.g. diffusion properties.

In this section we will restrict ourself to give a brief introduction to linear response theory and together with the Langevin equation we will briefly discuss the resulting spectral functions. More details can be found in the textbooks mentioned above and also in Refs. [144, 147, 148].

The goal of linear response theory is to describe how the ensemble average of any operator $\mathcal{O}(\mathbf{x}, t)$ changes with a weakly external perturbation H_{ext} . The total Hamiltonian of the weakly perturbed system is

$$H = H_0 + H_{ext} . \quad (2.170)$$

The expectation value of $\mathcal{O}(\mathbf{x}, t)$ is modified according to

$$\langle j | \mathcal{O}(\mathbf{x}, t) | j \rangle \rightarrow \langle j | U^{-1}(t) \mathcal{O}(\mathbf{x}, t) U(t) | j \rangle , \quad (2.171)$$

where $U(t)$ is the evolution operator in the interaction representation of H and has the form of

$$U(t) = \exp \left(-i \int_{-\infty}^t dt' H_{ext}(t') \right) . \quad (2.172)$$

Since we are interested in the case where the external field is very weak, we expand the expectation value of $\mathcal{O}(\mathbf{x}, t)$ to the lowest (linear) order of $H_{ext}(t)$

$$\delta \langle j | \mathcal{O}(\mathbf{x}, t) | j \rangle = i \int_{-\infty}^t dt' \langle j | [H_{ext}(t'), \mathcal{O}(\mathbf{x}, t)] | j \rangle . \quad (2.173)$$

Consider an external source $h(\mathbf{x}, t)$ that is coupled to $\mathcal{O}(\mathbf{x}, t)$ via

$$H_{ext} = \int d^3 \mathbf{x} h(\mathbf{x}, t) \mathcal{O}(\mathbf{x}, t) . \quad (2.174)$$

Inserting (2.174) into relation (2.173) gives

$$\delta \langle \mathcal{O}(\mathbf{x}, t) \rangle = -i \int_{-\infty}^t dt' \int d^3 \mathbf{x}' h(\mathbf{x}', t') \langle [\mathcal{O}(\mathbf{x}, t), \mathcal{O}(\mathbf{x}', t')] \rangle . \quad (2.175)$$

¹²One can also interpret the correlation function as describing the response of the charm quark pair to the presence of the medium. It concerns more the fate of the charmonium states in the medium, e.g. dissociation temperatures.

Recall the definition of the retarded correlator (2.14), formula (2.175) becomes

$$\delta\langle\mathcal{O}(\mathbf{x}, t)\rangle = \int_{-\infty}^t dt' \int d^3\mathbf{x}' h(\mathbf{x}', t') D^R(\mathbf{x}, t; \mathbf{x}', t'). \quad (2.176)$$

By using the Fourier transform

$$h(\mathbf{x}', t') = \int \frac{d\omega d^3\mathbf{p}}{(2\pi)^4} e^{i(\mathbf{p}\cdot\mathbf{x}' - \omega t')} h(\omega, \mathbf{p}), \quad (2.177)$$

$$D^R(t - t', \mathbf{x} - \mathbf{x}') = \int \frac{d\alpha d^3\mathbf{k}}{(2\pi)^4} e^{i(\mathbf{k}\cdot(\mathbf{x} - \mathbf{x}') - \alpha(t - t'))} D^R(\alpha, \mathbf{k}). \quad (2.178)$$

and the translation invariance of the retarded correlator we obtain Eq. (2.176) in momentum-time space

$$\delta\langle\mathcal{O}(\mathbf{p}, t)\rangle = \int_{-\infty}^t dt' h(\mathbf{p}, t') D^R(\mathbf{p}, t - t'), \quad (2.179)$$

and in frequency-momentum space

$$\delta\langle\mathcal{O}(\omega, \mathbf{p})\rangle = h(\omega, \mathbf{p}) D^R(\omega, \mathbf{p}). \quad (2.180)$$

Eq. (2.180) means the change in the ensemble average of the field can be expressed as the product of the external source and the retarded Green's function! This is the main result of linear response theory. As we have shown before, the retarded Green's function can be obtained by analytic continuation of the two point correlation function, which in practice is computable from lattice simulation.

One can further assume the external source obeys

$$h(\mathbf{x}, t) = e^{\epsilon t} \theta(-t) h^0(\mathbf{x}), \quad (2.181)$$

which means the external source is slowly ($\epsilon \ll 1$) turned on in the past and abruptly turned off at $t=0$. Inserting relation (2.181) into (2.179) gives the time dependence of the modifications of the ensemble average of \mathcal{O}

$$\delta\langle\mathcal{O}(\mathbf{p}, t)\rangle = \int_{-\infty}^t dt' e^{\epsilon t'} \theta(-t') h^0(\mathbf{p}) D^R(\mathbf{p}, t - t'), \quad (2.182)$$

At $t=0$ this external force has induced the change of the ensemble average of \mathcal{O} ,

$$\delta\langle\mathcal{O}(\mathbf{p}, t = 0)\rangle = \chi_s(\mathbf{p}) h^0(\mathbf{p}), \quad (2.183)$$

where $\chi_s(\mathbf{p})$ is the static susceptibility

$$\chi_s(\mathbf{p}) = \int_0^{\infty} dt e^{-\epsilon t} h^0(\mathbf{p}) D^R(\mathbf{p}, t). \quad (2.184)$$

With the translation invariance of the retarded correlator and ignoring the contribution in terms of ϵ one obtains the time derivative of (2.182) as the following

$$\frac{\partial}{\partial t} (\delta \langle \mathcal{O}(\mathbf{p}, t) \rangle) = -D^R(\mathbf{p}, t) h^0(\mathbf{p}). \quad (2.185)$$

Combining relations (2.183) and (2.185) one can get rid of the external source $h^0(\mathbf{p})$ and express the formula as

$$\chi_s(\mathbf{p}) \frac{\partial}{\partial t} (\delta \langle \mathcal{O}(\mathbf{p}, t) \rangle) = -D^R(\mathbf{p}, t) \delta \langle \mathcal{O}(\mathbf{p}, 0) \rangle. \quad (2.186)$$

Following the framework of linear response theory we assume the system is perturbed by a small excess of heavy quarks [144]

$$\mu(\mathbf{x}, t) = e^{ct} \theta(-t) \mu_0(\mathbf{x}). \quad (2.187)$$

The initial distribution of heavy quarks in the phase according to Boltzmann distribution is [144]

$$f(\mathbf{x}, \mathbf{p}, t = 0) = \exp \left(-\frac{p^2/(2M) + M - \mu(\mathbf{x})}{T} \right). \quad (2.188)$$

Performing the momentum integration and summing over colors and spins the initial net number density of heavy quarks is

$$N(\mathbf{x}, t = 0) = 4N_c \left(\frac{MT}{2\pi} \right)^{3/2} \exp \left(-\frac{M}{T} \right) \sinh \left(\frac{\mu(\mathbf{x})}{T} \right). \quad (2.189)$$

The net heavy quark number density at a later time can be expressed as

$$N(\mathbf{x}, t) = \int d^3\mathbf{x}' P(\mathbf{x} - \mathbf{x}', t) N(\mathbf{x}', 0), \quad (2.190)$$

where $P(\mathbf{x} - \mathbf{x}', t)$ stands for the probability of a heavy quark moving from position \mathbf{x}' at $t = 0$ to position \mathbf{x} at time t . The Fourier transform of $N(\mathbf{x}, t)$ reads

$$N(\mathbf{p}, t) = P(\mathbf{p}, t) N(\mathbf{p}, 0). \quad (2.191)$$

In this case the $D^R(\mathbf{p}, t)$ is just the density-density retarded correlator $\chi_{\text{NN}}(\mathbf{p}, t)$. Comparing the above relation with Eq. (2.186) from linear response theory, one can express the density-density retarded correlator as [144]

$$\chi_{\text{NN}}(\mathbf{p}, t) = -\chi_s(\mathbf{p}) \frac{\partial P(\mathbf{p}, t)}{\partial t}. \quad (2.192)$$

Fortunately, we can get the transition probability $P(\mathbf{p}, t)$ from effective Langevin theory. Due to the time scale for the heavy quark transport M/T^2 being much larger

than the typical time scale for the light quarks in the medium, the macroscopical properties of charm quarks can be described by the Langevin equations [147]

$$\frac{dx^i}{dt} = \frac{p^i}{M}, \quad (2.193)$$

$$\frac{dp^i}{dt} = \xi^i(t) - \eta p^i, \quad (2.194)$$

$$\langle \xi^i(t) \xi^j(t') \rangle = \kappa \delta^{ij} \delta(t - t'), \quad (2.195)$$

where η is the momentum drag coefficient, $\xi^i(t)$ delivers random momentum kicks that are uncorrelated in time and 3κ is the mean squared momentum transfer per unit time. The drag coefficient η and fluctuation coefficient κ are related through the fluctuation-dissipation relation [147, 148]

$$\eta = \frac{\kappa}{2MT}. \quad (2.196)$$

For a time scale which is much larger than $1/\eta$ the heavy quark number density obeys the ordinary diffusion equation

$$\partial_t N + D \nabla^2 N = 0. \quad (2.197)$$

The drag coefficient η can be connected to the diffusion coefficient D by the Einstein relation [147, 148]

$$D = \frac{T}{M\eta} = \frac{2T^2}{\kappa}. \quad (2.198)$$

To get $P(\mathbf{x}, t)$ one would rather consider the discretized Langevin equation as the following

$$\mathbf{x}_{t+1} - \mathbf{x}_t = \mathbf{p}_t/M, \quad (2.199)$$

$$\mathbf{p}_{t+1} - \mathbf{p}_t = \eta \mathbf{p}_t \Delta t + \xi_t \Delta t, \quad (2.200)$$

$$\langle \xi_t^i \xi_{t'}^j \rangle = \frac{\kappa}{\Delta t} \delta^{ij} \delta_{tt'}. \quad (2.201)$$

The initial probability of having momenta \mathbf{p}_0 can be given by

$$P(\mathbf{p}_0) = \frac{1}{(2\pi MT)^{3/2}} \exp\left(-\frac{p_0^2}{2MT}\right), \quad (2.202)$$

and according to Eq. (2.200) and (2.201) the probability of a heavy quark changing momentum from \mathbf{p}_i to \mathbf{p}_{i+1} can be expressed as

$$\begin{aligned} P(\mathbf{p}_{i+1}|\mathbf{p}_i) &= \int d^3\xi \delta^3(\mathbf{p}_{i+1} - (\mathbf{p}_i - \eta \mathbf{p}_i \Delta t + \xi \Delta t)) \\ &\times \left(\frac{\Delta t}{2\pi\kappa}\right)^{3/2} \exp\left(-\frac{\xi^2}{2\kappa/\Delta t}\right). \end{aligned} \quad (2.203)$$

Thus the probability for heavy quark to have momenta \mathbf{p}_n is

$$P(\mathbf{p}_n) = P(\mathbf{p}_n|\mathbf{p}_{n-1}) \cdot P(\mathbf{p}_{n-1}|\mathbf{p}_{n-2}) \cdots P(\mathbf{p}_2|\mathbf{p}_1)P(\mathbf{p}_1|\mathbf{p}_0) \cdot P(\mathbf{p}_0), \quad (2.204)$$

$$= (2\pi\kappa\Delta t)^{-\frac{3}{2}N} P(\mathbf{p}_0) \exp\left(-\sum_{i=0}^{N-1} \frac{\Delta t}{2\kappa} \left(\frac{\mathbf{p}_{i+1} - \mathbf{p}_i}{\Delta t} + \eta \mathbf{p}_i\right)^2\right), \quad (2.205)$$

which together with Eq. (2.199) give the probability of a heavy quark moving a distance $\Delta \mathbf{x}$ over a time Δt

$$P(\Delta \mathbf{x}, \Delta t) = \int \prod_{j=0}^N d^3 \mathbf{p}_j P(\mathbf{p}_n) \delta^3\left(\Delta \mathbf{x} - \sum_{i=0}^{N-1} \frac{\mathbf{p}_i}{M} \Delta t\right). \quad (2.206)$$

Inserting the Fourier integral of the delta function

$$\delta^3\left(\Delta \mathbf{x} - \sum_{i=0}^{N-1} \frac{\mathbf{p}_i}{M} \Delta t\right) = \int \frac{d^3 \mathbf{k}}{(2\pi)^3} \exp\left(i\mathbf{k} \cdot \Delta \mathbf{x} - i \sum_{i=0}^{N-1} \frac{\Delta t}{M} \mathbf{k} \cdot \mathbf{p}_i\right) \quad (2.207)$$

into Eq. (2.206), one obtains

$$P(\Delta \mathbf{x}, \Delta t) = (2\pi\kappa\Delta t)^{-\frac{3}{2}N} \int \prod_{j=0}^N d^3 \mathbf{p}_j \int \frac{d^3 \mathbf{k}}{(2\pi)^3} e^{i\mathbf{k} \cdot \Delta \mathbf{x}} P(\mathbf{p}_0) \\ \times \exp\left(-\sum_{i=0}^{N-1} \frac{\Delta t}{2\kappa} \left(\frac{\mathbf{p}_{i+1} - \mathbf{p}_i}{\Delta t} + \eta \mathbf{p}_i\right)^2 - i \sum_{i=0}^{N-1} \frac{\Delta t}{M} \mathbf{k} \cdot \mathbf{p}_i\right). \quad (2.208)$$

To perform the integration of Eq. (2.208) we first integrate out the \mathbf{p} 's in the order of \mathbf{p}_n to \mathbf{p}_0

$$P(\Delta \mathbf{x}, \Delta t) = \int \frac{d^3 \mathbf{k}}{(2\pi)^3} \exp\left(-\frac{\mathbf{k}^2}{2(b_1 + b_2)} + i\mathbf{k} \Delta \mathbf{x}\right), \quad (2.209)$$

then after performing the \mathbf{k} integration we have a Gauss form

$$P(\Delta \mathbf{x}, t) = \frac{1}{(2\pi\sigma^2)^{3/2}} \exp\left(-\frac{(\Delta \mathbf{x})^2}{2\sigma^2}\right), \quad (2.210)$$

with $t = N\Delta t$ and the width

$$\sigma^2 = b_1 + b_2, \quad (2.211)$$

where the coefficients read as follows

$$b_1 = \frac{\kappa(\Delta t)^3}{M^2} \sum_{m=1}^{N-1} \left(\sum_{\ell=0}^{m-1} (1 - \eta \Delta t)^\ell\right)^2, \quad (2.212)$$

$$b_2 = \frac{T(\Delta t)^2}{M} \left(\sum_{\ell=1}^{N-1} (1 - \eta \Delta t)^\ell\right)^2. \quad (2.213)$$

Taking $N \rightarrow \infty$ and making use of $\exp(x) = \lim_{n \rightarrow \infty} (1 + \frac{x}{n})^n$ we can get

$$b_1 = \frac{\kappa}{M^2} \frac{-e^{-2\eta t} + 4e^{-\eta t} + 2\eta t - 3}{2\eta^3}, \quad (2.214)$$

$$b_2 = \frac{T}{M} \frac{e^{-2\eta t} - 2e^{-\eta t} + 1}{\eta^2}. \quad (2.215)$$

By using the fluctuation-dissipation and Einstein relation (2.196) and (2.198) the width σ^2 in the Gauss form (2.210) finally reads [144]

$$\sigma^2 = \frac{2D}{\eta} (\eta t - (1 - e^{-\eta t})). \quad (2.216)$$

For large times $t \gg 1/\eta$, one has $\sigma^2 \approx 2Dt$ as expected from the ordinary diffusion equation; for small times $t \ll 1/\eta$, one has $\sigma^2 \approx (T/M)t^2$, which reflects the initial thermal velocity distribution of heavy quarks, $\langle v^2/3 \rangle = T/M$ [144].

With relation (2.192) from linear response theory and the probability (2.210) from Langevin effective theory, one finally gets the density-density retarded correlator [144]

$$\begin{aligned} \chi_{\text{NN}}(\omega, \mathbf{p}) = \chi_s(\mathbf{p}) D \mathbf{p}^2 \int_0^\infty dt e^{i\omega t} (1 - e^{-\eta t}) \\ \times \exp\left(-\frac{D\mathbf{p}^2}{\eta} (\eta t - (1 - e^{-\eta t}))\right). \end{aligned} \quad (2.217)$$

Eq. (2.217) summarizes the contribution from the Langevin equation with linear response theory under the assumptions (2.187) and (2.188).

We first look into the behavior of the above equation under the assumption of $D\mathbf{p}^2 \ll \eta$, that is $(D\mathbf{p})^2 \ll T/M$. In this case the integrand of Equation (2.217) can be approximated to

$$\begin{aligned} \chi_{\text{NN}}(\omega, \mathbf{p}) = \chi_s(\mathbf{p}) D \mathbf{p}^2 \int_0^\infty dt e^{i\omega t} (\exp(-D\mathbf{p}^2 t) - \exp(-\eta t)) \\ = \chi_s(\mathbf{p}) D \mathbf{p}^2 \left(\frac{1}{D\mathbf{p}^2 - i\omega} - \frac{1}{\eta - i\omega} \right). \end{aligned} \quad (2.218)$$

For small frequencies $\omega \sim D\mathbf{p}^2 \ll \eta$, the first term dominates and resembles the diffusion equation $(\partial_t + D\nabla^2)^{-1}$; for the large frequency case $\omega \sim \eta \gg D\mathbf{p}^2$, the second term dominates and resembles the drag term of the Langevin equations $(\partial_t + \eta)^{-1}$. The corresponding spectral function is thus given through the relation (2.18)

$$\sigma_{\text{NN}}(\omega, \mathbf{p}) = \frac{1}{\pi} \text{Im} \chi_{\text{NN}}(\omega, \mathbf{p}) = \frac{\chi_s(\mathbf{p})}{\pi} \frac{\omega (\eta^2 - (D\mathbf{p}^2)^2) D \mathbf{p}^2}{((D\mathbf{p}^2)^2 + \omega^2) (\eta^2 + \omega^2)} \quad (2.219)$$

and the spectral function in the current-current channel is obtained through the relation (2.44)

$$\sigma_{\text{JJ}}(\omega, \mathbf{p}) = \frac{\omega^2}{\mathbf{p}^2} \sigma_{\text{NN}}(\omega, \mathbf{p}) = \frac{\chi_s(\mathbf{p})}{\pi} \frac{\omega^3 (\eta^2 - (D\mathbf{p}^2)^2) D}{((D\mathbf{p}^2)^2 + \omega^2) (\eta^2 + \omega^2)}. \quad (2.220)$$

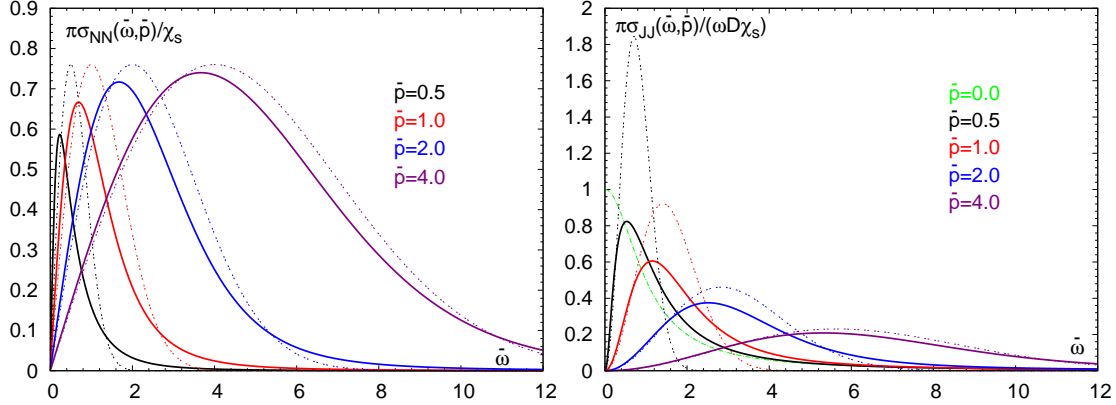


Figure 2.6. Left: The spectral density of the density-density correlator $\sigma_{\text{NN}}(\bar{\omega}, \bar{\mathbf{p}})$ multiplied by $\pi/\chi_s(\bar{\mathbf{p}})$ as a function of a scaled frequency $\bar{\omega}$ for various values of a scaled momentum $\bar{\mathbf{p}} = 0.5, 1.0, 2.0$ and 4.0 . Right: The spectral function of the current-current correlator $\sigma_{\text{JJ}}(\bar{\omega}, \bar{\mathbf{p}})$ multiplied by $\pi/(\omega D\chi_s(\bar{\mathbf{p}}))$ as a function of a scaled frequency $\bar{\omega}$ for various values of a scaled momentum $\bar{\mathbf{p}} = 0, 0.5, 1.0, 2.0$ and 4.0 . In both plots, the solid lines denote the spectral functions from the Langevin equations for non-zero $\bar{\mathbf{p}}$. The dotted lines show the spectral functions in the free theory. The dash-dotted line shows the $\bar{\mathbf{p}} = 0$ result of the Langevin equations (Eq. (2.221)). This plot is an analog of Fig.1 in Ref. [144].

One particularly interesting case in the current-current channel is the one at vanishing momentum $\mathbf{p} = 0$ [144]

$$\sigma_{\text{JJ}}(\omega, \mathbf{0}) = \lim_{\mathbf{p} \rightarrow \mathbf{0}} \frac{\omega^2}{\mathbf{p}^2} \sigma_{\text{NN}}(\omega, \mathbf{p}) = \chi_s(0) \frac{T}{M} \frac{1}{\pi} \frac{\omega\eta}{\omega^2 + \eta^2}. \quad (2.221)$$

In the limit of $\eta \rightarrow 0$,

$$\sigma_{\text{JJ}}(\omega, \mathbf{0}) = \chi_s(0) \frac{T}{M} \omega \delta(\omega). \quad (2.222)$$

It is similar to the spectral function in the free case, i.e. Eq. (2.147) as described in section 2.3.1.

Then we perform the time integration in Eq. (2.217) directly without any assumptions. Due to the typical relaxation time being $1/\eta$, one can redefine

$$\bar{t} = t\eta, \quad \bar{\omega} = \frac{\omega}{\eta} \quad \text{and} \quad \bar{\mathbf{p}}^2 = \frac{D\mathbf{p}^2}{\eta}. \quad (2.223)$$

The density-density retarded correlator Eq. (2.217) thus becomes

$$\chi_{\text{NN}}(\bar{\omega}, \bar{\mathbf{p}}) = \chi_s(\bar{\mathbf{p}}) \bar{\mathbf{p}}^2 \int_0^\infty d\bar{t} e^{i\bar{\omega}\bar{t}} (1 - e^{-\bar{\eta}\bar{t}}) \exp\left(-\bar{\mathbf{p}}^2 \left(\bar{t} - (1 - e^{-\bar{t}})\right)\right) \quad (2.224)$$

$$= \chi_s(\bar{\mathbf{p}}) \bar{\mathbf{p}}^2 \left(1 + i\bar{\omega} e^{\bar{\mathbf{p}}^2} \bar{\mathbf{p}}^{-2(\bar{\mathbf{p}}^2 + i\bar{\omega})} \left(\Gamma(\bar{\mathbf{p}}^2 - i\bar{\omega}) - \Gamma(\bar{\mathbf{p}}^2 - i\bar{\omega}, \bar{\mathbf{p}}^2)\right)\right). \quad (2.225)$$

The calculation from Eq. (2.224) to Eq. (2.225) is exact. The Γ s appearing in the above equation are the Euler gamma function $\Gamma(z)$ and the incomplete gamma function $\Gamma(a, z)$. Consequently the current-current correlator is of the form

$$\chi_{JJ}(\bar{\omega}, \bar{\mathbf{p}}) = \chi_s(\mathbf{p}) D\omega \bar{\omega} \left(1 + i\bar{\omega} e^{\bar{\mathbf{p}}^2} \bar{\mathbf{p}}^{-2(\bar{\mathbf{p}}^2 + i\bar{\omega})} \left(\Gamma(\bar{\mathbf{p}}^2 - i\bar{\omega}) - \Gamma(\bar{\mathbf{p}}^2 - i\bar{\omega}, \bar{\mathbf{p}}^2) \right) \right). \quad (2.226)$$

As one can see from Eq. (2.225) and Eq. (2.226), both the density-density correlator $\chi_{NN}(\bar{\omega}, \bar{\mathbf{p}})$ multiplied by $\pi/\chi_s(\bar{\mathbf{p}})$ and the longitudinal current-current correlator¹³ $\chi_{JJ}(\bar{\omega}, \bar{\mathbf{p}})$ multiplied by $\pi/(\omega D\chi_s(\bar{\mathbf{p}}))$ scale with the rescaled frequency $\bar{\omega}$ and momentum $\bar{\mathbf{p}}$. We thus show the corresponding spectral functions in Fig. 2.6 as functions of $\bar{\omega}$ with $\bar{\mathbf{p}} = 0.5, 1.0, 2.0$ and 4.0 . As expected, as the $\bar{\mathbf{p}}$ increases, the widths of the both spectral functions increase with the increasing frequency $\bar{\omega}$ and momentum $\bar{\mathbf{p}}$. For comparison the spectral function from the free theory (Eq. (2.150) and Eq. (2.151)) are also shown as dotted lines in Fig. 2.6. It is worth noting that at $\bar{\omega} = 0$ the longitudinal current-current spectral function goes to zero when $\bar{\mathbf{p}} \neq 0$ and has a finite value when $\bar{\mathbf{p}} = 0$.

2.5 Charmonium at finite temperature on the lattice: a brief review

The properties of charmonium states at finite temperature have been investigated on the lattice by several groups. Iida et al. tried, by changing the boundary conditions of the simulation, to check the response from the charmonium states [42], Ohno et al. focused on the wave functions [43] with variational analysis and the other groups mainly tried to understand the temperature dependence of the charmonium properties armed with MEM. In this section we will briefly summarize the status from the last approach and a brief list of the lattice parameters of the finest lattices of these groups is given in the Table 2.3. The details can be found in Refs. [37–41].

Datta et al. [39] implemented the Wilson gauge action and clover improved Wilson fermions on isotropic quenched lattices. They measured at four different temperatures of $0.9 T_c$, $1.5 T_c$, $2.25 T_c$ and $3 T_c$ on their finest lattice ($a_\sigma = 0.02$ fm) with $N_\tau = 40, 24, 16$ and 12 , respectively. They utilized the ratio of the measured correlator to the reconstructed correlator for the first time to study thermal modifications of spectral functions. Based on the analysis of the temporal correlators and the reconstructed spectral functions, they found that, *J/ψ and η_c survive up to quite high temperatures, with little observable change up to 1.5 T_c, and then gradually weaken and disappear by*

¹³Here we only mentioned the longitudinal current current spectral function. There is a notable difference between the longitudinal current current spectral function and the transverse one as indicated from Ref. [149]. We will show this difference on the correlator level from our lattice data in section 4.2.

$3 T_c$. For the scalar and axial vector channels, serious modifications are induced by the hot medium already close to T_c , possibly dissociating the mesons by $1.1 T_c$ ¹⁴ [39].

All the other groups are using anisotropic lattices. Asakawa et al. [38] took the simple plaquette gauge action and standard Wilson quark action on quenched anisotropic lattices in their simulation. The renormalized anisotropy is $\zeta = a_\sigma/a_\tau = 4$ with $a_\sigma = 0.039$ fm. They simulated the correlation functions with relatively large number of points in the temporal direction having $N_\tau = 96, 54, 46, 40$ and 32 at $0.78 T_c, 1.38 T_c, 1.62 T_c, 1.87 T_c$ and $2.33 T_c$, respectively. They concentrated on the study of J/ψ and η_c , and found that J/ψ and η_c survive as distinct resonances in the plasma even up to $T \approx 1.6 T_c$ and that they eventually dissociate between $1.6 T_c$ and $1.9 T_c$ [38].

Umeda et al. [37] adopt the standard Wilson plaquette action for the gauge field and the $\mathcal{O}(a)$ improved Wilson type action for the quark field. They measured the correlation functions at only two temperatures ($0.9 T_c$ and $1.1 T_c$) on quenched lattices and concentrated more on smeared correlators. From the analysis of the smeared correlators, they found that at $T \approx 0.9 T_c$, the spectral function exhibits a strong peak, well approximated by a delta function corresponding to the ground state with almost the same mass as at $T = 0$, and at $T \approx 1.1 T_c$, the strong peak structure still persists at almost the same place as below T_c , but with a finite width of a few hundred MeV [37].

Jakovác et al. [40] measured heavy squark correlation functions with the Fermilab action for the heavy quark sector and the standard Wilson action for the gauge sector on quenched anisotropic lattices. They developed a new MEM algorithm without singular value decomposition of the integrand kernel, which can accelerate the running time of the MEM analysis. They also extended the simulation to the bottomonium correlation function. On their finest lattice ($a_\sigma = 0.056$ fm, $\zeta = 4$), they measured charmonium correlation function at $1.09 T_c, 1.20 T_c, 1.50 T_c, 1.99 T_c, 2.39 T_c$ and $2.99 T_c$ with $N_\tau = 44, 40, 32, 24, 20$ and 16 , respectively. They detected the transport contribution in the vector correlators for the first time. From their analysis, they found that the spectral functions in the pseudo scalar channel do not change up to $1.5 T_c$ within systematic and statistical errors of the calculations, the results of $1P$ states suggest the melting of the $1P$ charmonium states at temperature $T = 1.1 - 1.2 T_c$, and the spectral functions in the vector channel at finite temperature always differ from the zero temperature spectral functions and extend to significantly smaller ω values [40].

The most recent published paper is by Aarts et al. [41]. They carried out two-flavor-dynamic simulations on anisotropic lattices and utilized the two-plaquette Symanzik improved gauge action and the fine-Wilson, coarse-Hamber-Wu fermion action with stout-link smearing. The finest lattice they simulated has $a_\sigma = 0.163$ fm with $\zeta = 6$ and the temporal lattice extend being $N_\tau = 80, 32, 24$ and 16 at $0.42 T_c, 1.05 T_c,$

¹⁴In this section, all the texts with Italian style are quoted from the corresponding references.

	$N_\sigma^3 \times N_\tau$	T/T_c	#conf	$a_\sigma[10^{-3}\text{fm}]$	a_σ/a_τ
Umeda02 [37]	$20^3 \times 32$	0.88	1000		
	$20^3 \times 26$	1.08	1000	96	4
Asakawa03 [38]	$32^3 \times 96$	0.78	194		
	$32^3 \times 54$	1.38	150	39	4
	$32^3 \times 46$	1.62	182		
	$32^3 \times 40$	1.87	181		
Datta03 [39]	$40^3 \times 40$	0.9	85		
	$64^3 \times 24$	1.5	80	20	1
	$48^3 \times 16$	2.25	100		
	$48^3 \times 12$	3	90		
Jakováč06 [40]	$24^3 \times 44$	1.09	110		
	$24^3 \times 40$	1.20	1680	56	4
	$24 \cdot 32 \times 32$	1.50	1000		
	$24^3 \times 24$	1.99	300		
	$24^3 \times 20$	2.39	640		
	$24^3 \times 16$	2.99	310		
Aarts07 [41]	$12^3 \times 80$	0.42	250		
	$8^3 \times 32$	1.05	1000	162	6
	$8^3 \times 24$	1.40	1000		
	$8^3 \times 16$	2.09	1000		

Table 2.3. A brief summary of parameters of the finest lattices used by several groups to study charmonium via the MEM approach. The details can be found in Refs. [37–41].

1.40 T_c and 2.09 T_c , respectively. As pointed out in Ref. [125], at finite temperature the commonly used Maximum Entropy Method is inherently unstable at small energies due to the divergence of the integrand kernel at $\omega = 0$ (see e.g. Eq. (2.52)). Thus the MEM analysis done in Ref. [37–40] might be unstable in the very small ω region. Using the improved integrand kernel proposed in Ref. [125] to avoid the instability of MEM at $\omega \approx 0$, Aarts et al. found their results indicate that *the S-waves (J/ψ and η_c) survive up to temperatures close to 2 T_c , while the P waves (χ_{c0} and χ_{c1}) melt away below 1.2 T_c* ¹⁵ [41].

In addition to the instability of MEM found in Ref. [125], Umeda [141] recently discussed a constant contribution to meson correlators at finite temperature (see e.g. in section 2.3.1), which should be removed in the MEM analysis to get the correct spectral function shape of the bound state. Later on Datta and Petreczky implemented the time

¹⁵Note the pseudo critical temperature T_c in 2 flavor QCD is different from that in quenched QCD. T_c in Ref. [41] is around 205 – 210 MeV.

derivative of the ratio of the measured correlator to the reconstructed correlator and found the temperature dependence of this ratio in the vector and P waves channels can be understood mainly from the zero mode contribution [150], which is also confirmed by our MEM analysis of the vector channel at $T \approx 1.5T_c$ [126].

Besides the information on the bound states, due to the Kubo relation, the transport properties of the medium can in principle also be read from the spectral function in the appropriate mesonic channel. Recent progress to obtain the heavy quark diffusion constant on the lattice has been made in Ref. [144,151], however, it is quite hard to get precise values due the quality of the correlator data.

Recently, it is realized that it could be also interesting to look into the correlation functions at non-zero momentum: first the dispersion relation might be changed and also the bound state could be melted when moving in the heatbath, second the spectral function could also give some hints on the transport properties of the medium [149]. Progress on the lattice has been reported in various contributions [40, 152–156].

In the following chapter, we will analyze the correlator data from different aspects and try to develop further understanding of the dynamics of charm quarks in the medium and the fate of its possible bound states at finite temperature.

Chapter 3

Analysis of charmonium properties at vanishing momentum

3.1 Toy model test of spectral function

In this section we will employ a toy model to address the in-medium charmonium behavior [157]. We start from a single Breit-Wigner resonance and study its effect on the correlator under different conditions. Then we include continuum contributions and identify their effect. In general there are three distinct features of the spectral function which determine the behavior of the correlator: the width of the resonance, its relative strength to the continuum and the onset point of the continuum. All three parameters are presumably coupled through the temperature. By varying the three parameters separately we study the effect of the different contributions of the spectral function to the correlator. In addition, we also consider the transport contribution in the very low frequency region to the correlator.

We analyze the sensitivity of the correlators to the spectral function by using the two following reference correlators:

$$G_0(\tau, T) = \int_0^\infty d\omega \sigma(\omega, T=0) K(\tau, T), \quad (3.1)$$

$$G_{free}(\tau, T) = \int_0^\infty d\omega \sigma_{free}(\omega, T) K(\tau, T), \quad (3.2)$$

where $G_0(\tau, T)$ is the so called “reconstructed” correlator and $G_{free}(\tau, T)$ is the free correlator at finite T . Comparing to $G_0(\tau, T)$ or $G_{free}(\tau, T)$ we can analyze if the correlator or the corresponding spectral function behaves more like the zero temperature one or is closer to the free one. The ratios of the finite T correlators to these two

references are:

$$R_0(\tau, T) = \frac{G(\tau, T)}{G_0(\tau, T)}, \quad (3.3)$$

$$R_{free}(\tau, T) = \frac{G(\tau, T)}{G_{free}(\tau, T)}. \quad (3.4)$$

then $R_0 \approx 1$ and $R_{free} \approx 1$ could serve as an indication for the presence or dissolution of the bound state, respectively.

We consider the spectral function as a combination of the resonance and the continuum: $\sigma = \sigma_{res} + \sigma_{cont} + \sigma_{trans}$. For the spectral function of the resonance the following form is taken at $T = 0$:

$$\sigma_{res}(\omega, T = 0) = |\Phi(0)|^2 \delta(\omega - M) = |\Phi(0)|^2 2M \delta(\omega^2 - M^2), \quad (3.5)$$

where M denotes the mass of J/ψ and $\Phi(0)$ is the wave function of the J/ψ at the origin and determines the relative strength of the resonance contribution¹. Using the vacuum spectral function in Eq. (3.5), we obtain a correlator at temperature T ,

$$G_0^{res}(\tau, T) = |\Phi(0)|^2 \frac{\cosh[M(\tau - 1/(2T))]}{\sinh(M/(2T))}, \quad (3.6)$$

where in current study $|\Phi(0)|^2$ is set to 1 GeV^3 [19].

At finite temperature T we take the spectral function of the resonance to have the relativistic Breit-Wigner like form

$$\sigma_{res}(\omega, \gamma) = N(\gamma) |\Phi(0)|^2 \frac{M}{\pi} \frac{2\omega\gamma}{\omega^2\gamma^2 + (\omega^2 - M^2)^2}, \quad (3.7)$$

where γ is the width of the resonance at half-maximum. We allow this width to have a (so far unspecified) temperature dependence, $\gamma = \gamma(T)$. Note that

$$\lim_{\epsilon \rightarrow 0} \frac{1}{\pi} \frac{\epsilon}{x^2 + \epsilon^2} = \delta(x). \quad (3.8)$$

So that for $\gamma(T) \rightarrow 0$ when $T \rightarrow 0$ we recover the correct $T = 0$ behavior. The normalization factor $N(\gamma)$ is introduced to maintain the normalization to unity given by the δ -function for the Breit-Wigner form: when $\gamma \rightarrow 0$, $N(\gamma) \rightarrow 1$. In other words, we want to assure that the resonance contribution always is of the same strength, no matter what the width is.

One should note that the *Ansatz* for the spectral resonance we are using here behaves linearly in ω in the vicinity of $\omega = 0$. Thus we introduce an additional lower bound $\omega_0 = 2m_c$, with m_c as the charm quark mass, in order to remove this segment. $N(\gamma, \omega_0)$ is now defined such as to retain the same strength as at $T = 0$ for $\sigma_{res}(\omega, \gamma)$

¹In this section, only J/ψ is concerned.

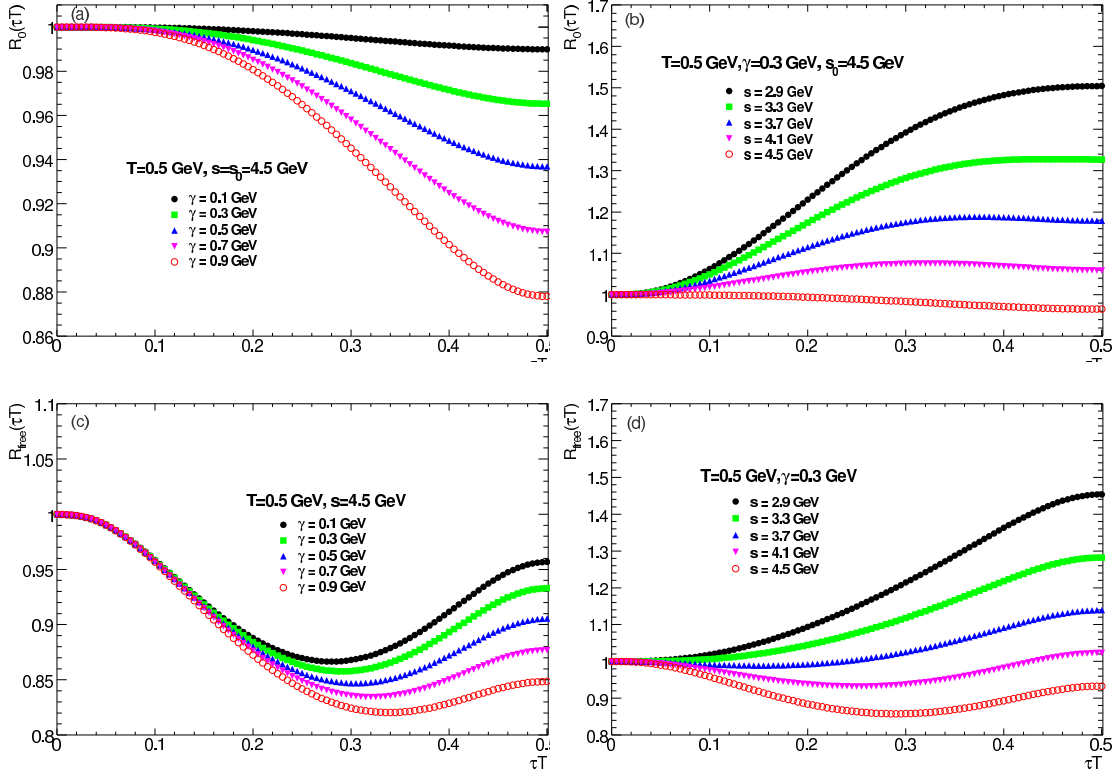


Figure 3.1. Ratios without the transport contribution. $R_0(\tau T)$ and $R_{free}(\tau T)$ versus τT . (a) γ dependence of $R_0(\tau T)$, (b) s dependence of $R_0(\tau T)$, (c) γ dependence of $R_{free}(\tau T)$, (d) s dependence of $R_{free}(\tau T)$.

with a finite width resonance and a threshold cut-off ω_0 . A straightforward calculation gives

$$\frac{1}{N(\gamma, \omega_0)} = \frac{2M}{\pi\sqrt{4M^2 - \gamma^2}} \left[\frac{\pi}{2} - \arctan \left(\frac{2\omega_0^2 + \gamma^2 - 2M^2}{\gamma\sqrt{4M^2 - \gamma^2}} \right) \right]. \quad (3.9)$$

For the continuum part of the spectral function we take the formula of

$$\sigma_{cont} = \frac{3}{8\pi^2} \omega^2 \tanh \left(\frac{\omega}{4T} \right) \sqrt{1 - \left(\frac{s}{\omega} \right)^2} \left(2 + \left(\frac{s}{\omega} \right)^2 \right), \quad (3.10)$$

where s is the threshold of the continuum, for $T = 0$, $s = s_0$, for the free case, $s = 2m_c$ and for finite T , s is T dependent. At zero temperature s_0 and m_c are set to be 4.5 GeV and 1.32 GeV, respectively [19].

Concerning the transport peak, here we use the *Ansatz* as mentioned in section 2.4

$$\sigma_{trans}(\omega) = A \frac{\omega\eta}{\omega^2 + \eta^2}, \quad (3.11)$$

where A is a normalization constant to maintain the area under $\sigma_{trans}(\omega)/\omega$ to be a constant [158].

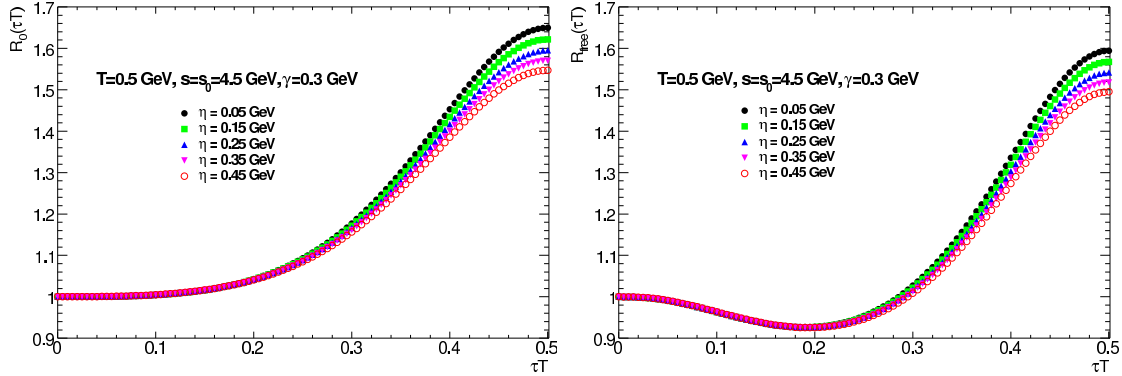


Figure 3.2. Ratios with transport contribution included. Left: R_0 versus τT varying the width of the transport peak $\eta=0.05, 0.15, 0.25, 0.35$ and 0.45 . Right: the same setting as the left plot but for R_{free} .

Having the spectral functions in hand we can construct $R_0(\tau, T)$ and $R_{free}(\tau, T)$,

$$R_0(\tau, T) = \frac{G^{res}(\tau, T, \gamma) + G^{cont}(\tau, T, s) + G^{trans}(\tau, T, \eta)}{G_0^{res}(\tau, T) + G^{cont}(\tau, T, s = s_0)}, \quad (3.12)$$

$$R_{free}(\tau, T) = \frac{G^{res}(\tau, T, \gamma) + G^{cont}(\tau, T, s) + G^{trans}(\tau, T, \eta)}{G^{cont}(\tau, T, s = 2m_c)}. \quad (3.13)$$

We first check the effects brought by the resonance part and the continuum part to the ratios $R_0(\tau, T)$ and $R_{free}(\tau, T)$. In this case we don't include the contribution from the transport peak in the calculation of R_0 and R_{free} in Eq. (3.12) and Eq. (3.13). The ratios R_0 (plots (a) and (b) in upper panel) and R_{free} (plots (c) and (d)) are shown in Fig. 3.1. Plot (a) shows different values of the resonance's width at fixed threshold $s = s_0 = 4.5$ GeV and plot (b) is for different values of the continuum's threshold at fixed width $\gamma = 0.3$ GeV. We can see that both increasing the resonance's width and decreasing the continuum's threshold can make R_0 deviate further away from unity but in the opposite direction. With the width of 0.9 GeV only making a deviation of 12% at the symmetry point, the influence of the resonance is smaller than that of the continuum, with the threshold being 0.8 GeV smaller than $s_0=4.5$ GeV making a difference of 20% . The corresponding pictures for the ratio R_{free} are shown in plots (c) and (d) in Fig. 3.1. Similar to R_0 the influence of the resonance is smaller than that of the continuum.

We further include the transport peak part into the evaluation of R_0 and R_{free} . We set the width of the resonance peak to $\gamma = 0.3$ GeV, the threshold of the continuum to $s = s_0 = 4.5$ GeV. We then vary the width of the transport peak η to be $0.05, 0.15, 0.25, 0.35$ and 0.45 GeV. The ratio R_0 (left) and R_{free} (right) are shown in Fig. 3.2. After the transport peak contribution is included, we find the temperature dependence of $R_0(\tau T)$ changes strongly in the large distances. $R_0(\tau, T)$ becomes larger than unity at

distances $\tau T \gtrsim 0.1$ and reaches around 1.6 at the largest distance. The small distances behavior of R_0 shown in Fig. 3.2 is similar with that in Fig. 3.1. We also observe that the widths of the transport peak varying from 0.05 GeV to 0.45 have a relative small effects on R_0 . Similar effects are found on R_{free} .

Within the current scenario of the spectral function the correlator is more sensitive to the change of the continuum part than of the resonance and the transport parts, which makes the exploration of properties of the resonance and transport peaks difficult.

3.2 Mock data test of MEM

A common technique to extract the spectral functions from the correlator is the Maximum Entropy Method as we described in the last chapter. Since the default model (DM) is a very important parameter in the MEM analysis, we will make a mock data test of the Maximum Entropy method to check the dependence on the default models in this section.

The mock spectral function we use here is a relativistic Breit-Wigner peak with a continuum part

$$\sigma(\omega, T) = \sigma_{\text{rbw}}(\omega, T) + \sigma_{\text{cont}}(\omega, T), \quad (3.14)$$

where $\sigma_{\text{rbw}}(\omega, T)$ is of the form

$$\sigma_{\text{rbw}}(\omega, T) = \frac{M\gamma}{(\omega^2 - M^2)^2 + M^2\gamma^2} \frac{\omega^2}{\pi}. \quad (3.15)$$

To let $\sigma_{\text{rbw}}(\omega, T)/\omega^2$ go to zero smoothly, we let the width γ vary with ω [159]

$$\gamma(\omega) = \theta(\omega - \omega_0) \left(1 - \frac{\omega_0^2}{\omega^2}\right)^5 \gamma_0. \quad (3.16)$$

The continuum spectral function $\sigma_{\text{cont}}(\omega, T)$ is chosen as the free lattice spectral function.

In the real situation the correlation function data generated on the lattice is correlated and consequently its covariance matrix is not diagonal. To mimic the noise better we adopt the following covariance matrix in our mock data [40]

$$C_{ij}^{\text{mock}} = \frac{C_{ij}}{\bar{G}(\tau_i)\bar{G}(\tau_j)} G^{\text{mock}}(\tau_i)G^{\text{mock}}(\tau_j), \quad (3.17)$$

where C_{ij} is the covariance matrix from the real data and is of the form of Eq. (2.76), $\bar{G}(\tau)$ denotes the mean value of the correlation function from the real data and takes the form of Eq. (2.75), and $G^{\text{mock}}(\tau)$ are evaluated from the spectral function in Eq. (3.14). In the following test the real lattice data are obtained from data sets of $128^3 \times 48$ at $1.46 T_c$ with $\beta = 7.793$ and from $128^3 \times 64$ at $0.74 T_c$ with $\beta = 7.457$.

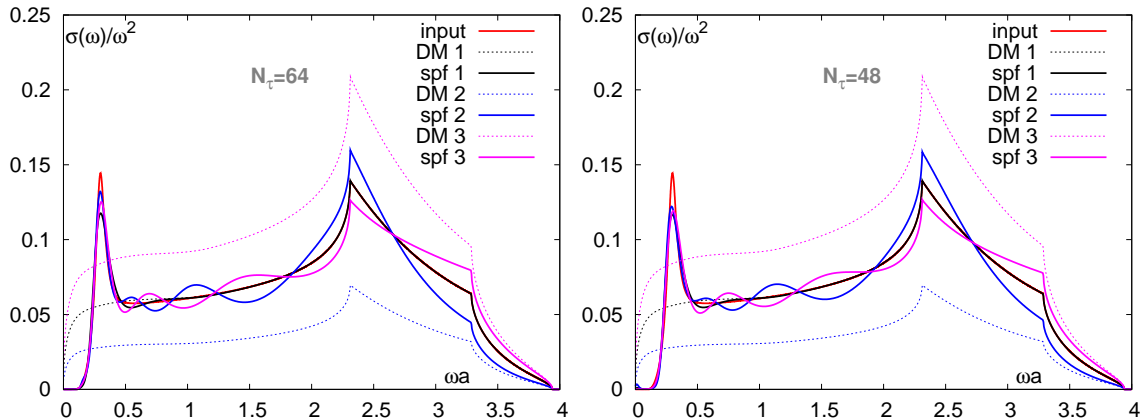


Figure 3.3. The DM dependence (varying the large ω part) of spectral function extracted from mock data with $N_\tau = 64$ (left) and $N_\tau = 48$ (right). “DM”s are the default models and “spf”s are the corresponding output spectral functions. “input” labels the input spectral function of the mock data. “DM 1”, “DM 2” and “DM 3” have the same shape and only differ in amplitudes as described in the text.

The default model is very important as it strongly affects the output of the MEM when the quality of the data is not sufficient to fully constrain the spectral function. As we are focusing on the modification of the ground state of the spectral function, it is natural to choose a DM which reproduces the behavior of the spectral function in the very large ω region. To investigate the effects brought by the very large ω prior information, in Fig. 3.3, we show the outputs of MEM using different default models

$$m(\omega) = F \cdot \sigma_{\text{cont}}(\omega), \quad (3.18)$$

where F is a constant. We first focus on the left panel of Fig. 3.3, where the test is done with $N_\tau = 64$. The red solid line denotes the input spectral function $\sigma(\omega)$ of Eq. (3.14). All the dotted lines stand for different DMs and the solid lines in the same color are the corresponding output spectral functions from MEM. For “DM 1”, we set $F=1$, which means the DM reproduces the high frequency behavior of the input spectral function. For “DM 2” and “DM 3”, F is set to be 0.5 and 1.5, respectively. At first glance, in the high frequency region ($a\omega \gtrsim 2.3$) the output spectral functions from MEM are trying to follow the shape or the trend of the default model; in the low frequency region ($a\omega \lesssim 0.5$) the output spectral functions have an important universality that is not present in the default model and might be present in the real spectral function (physics). The bias of the output spectral function to the default model in the large ω region is mainly due to the insensitivity of the correlator to the details of the spectral function in this region. If the exact large ω behavior is provided, for instance, here “DM 1” with $F=1$, MEM simply does nothing but reproduces it. In the small ω region,

impressingly enough, all three output spectral functions from different default models reproduce the correct peak location and the qualitatively correct shape of the resonance part of the input spectral function. In particular the output spectral function “spf 1” with correct large ω information in the DM gives the most reliable image. “spf 2” and “spf 3” with incorrect large ω prior information produce some wiggles in the frequency regions higher than the resonance part. These are normally considered to be “lattice artifacts” but could also be the “MEM artifacts”. From this study we see that it is important to include the “correct” high frequency behavior of the spectral function in the default model.

We also checked the MEM output dependence on the temporal lattice extent N_τ . We did the same exercise with the number of points $N_\tau = 48$. As one can see from the right panel of Fig. 3.3, with a smaller number of data points $N_\tau = 48$, the spectral function is also well reproduced. This indicates that in the real case at $1.46 T_c$, i.e. $128^3 \times 48$ on our finest lattice, the spectral function extracted from MEM should be reliable. Nevertheless, the “correct” large ω behavior in the default model is still favorable when the quality of data is not sufficient as we emphasized before.

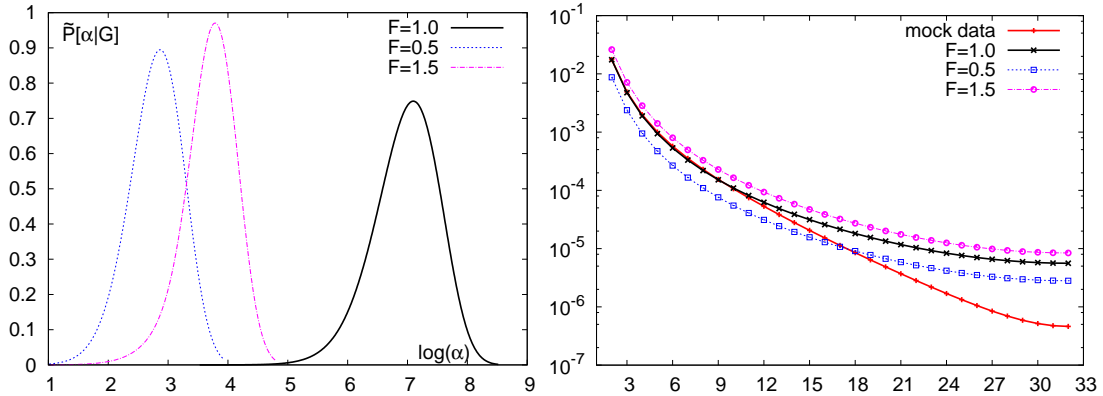


Figure 3.4. Weight factor distribution (left) and correlators calculated from the DM (right) according to the left plot of Fig. 3.3.

Thanks to asymptotic freedom the high frequency part should resemble the free spectral function. It could be helpful to compare the correlators calculated from the default models to the real lattice data (shown in the right plot of Fig. 3.4). If similar behavior of the real correlator data and the correlator calculated from the default model exists at some small distances, it could indicate the default model has the correct large frequency information of the spectral function, consequently the normalized weight function $\tilde{P}[\alpha|G]$ may have a peak location at larger α (shown in the left panel of Fig. 3.4). However, one cannot judge from the comparisons of quantities in Fig. 3.4 which output spectral function from MEM is definitely better, since α itself as a param-

eter just reflects the relative weight of the entropy S and the likelihood function L . If $\tilde{P}[\alpha|G]$ has a large peak location, it just means MEM tends to fit the spectral function to the default model while if the peak location is small it tells us that MEM tends to fit the spectral function to the lattice data. One also has to keep in mind that, no matter what kind of default model is used, the correlators, that are calculated from the output spectral functions obtained from MEM, always reproduce the lattice correlator data within the errors. This essentially accents the importance of the prior knowledge of the spectral function and a careful analysis of the default model dependence. In practice what we will do in the real data analysis is to choose the free lattice spectral function as a default model at large ω and change its amplitude to reproduce the small distance behavior of the correlation function to circumvent the issue of differences between the free lattice correlator and the renormalized lattice data.

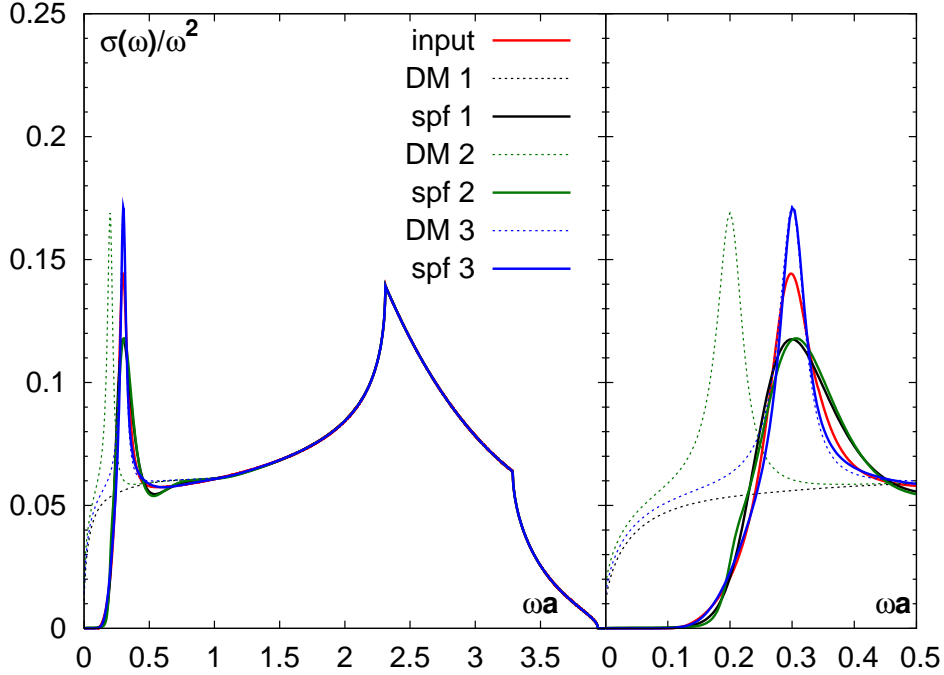


Figure 3.5. The DM dependence (varying the resonance peak) of the spectral function extracted from mock data with $N_\tau = 64$. The resonance peak in the input mock spectral function has a width $a\gamma = 0.15$ and peak location $a\omega = 0.3$. The right panel is a blowup of the left plot in the low frequency region. “input” is the input mock spectral function. “DM”s are default models while “spf”s are corresponding output spectral functions.

We now provide the correct large ω ($a\omega \gtrsim 1$) information and vary the low frequency information (resonance part $0 \leq \omega \lesssim 0.8$) in the default model. This can help us to know how many details of the resonance part of the spectral function we can explore from MEM with the current quality of the mock data. In Fig. 3.5, we show the output

spectral functions extracted from mock data with $N_\tau = 64$. Again the red solid line denotes the input spectral function. The peak location and the width of the resonance part of the input mock spectral function are $a\omega = 0.3$ and $a\gamma = 0.15$, respectively. “DM”s are default models and “spf”s are corresponding output spectral functions. “DM 1” is the free spectral function. “DM 2” is the free spectral function plus a resonance peak whose peak location is $a\omega = 0.2$ and width is $a\gamma = 0.05$. The corresponding output spectral functions “spf 1” and “spf 2”, corresponding to “DM 1” and “DM 2”, are quite independent of the default models. They reproduce the peak location correctly and the width of the peak with a precision of 20%, even with the prior information “incorrectly” provided in $0 \leq a\omega \lesssim 0.55$ in “DM2”! We now put “partly” correct information into “DM 3” to test whether we can get more details of the resonance peak, e.g. the width. “DM 3” is also a combination of a free spectral function and a resonance peak, but the resonance peak in “DM 3” has a same peak location as that in the input mock spectral function ($a\omega = 0.3$) and a relatively smaller width $a\gamma = 0.05$ compared to that in the input mock spectral function ($a\gamma = 0.15$). Unfortunately, probably due to the quality of the data, the output “spf 3” from MEM simply reproduces the “DM 3”. Thus it is hard to get a precise determination of the absolute width of the resonance peak but still by comparing the width of the resonance peak from MEM at different temperatures one can get a qualitative feeling of the thermal modification of the resonance due to the change of the width.

In addition we add a transport peak at $\omega \approx 0$ using

$$\sigma_{trans}(\omega) \propto \frac{1}{\pi} \frac{\omega\eta}{\omega^2 + \eta^2} \quad (3.19)$$

and try to find out to what extent MEM can explore it under the current circumstances. In this case $\sigma_{trans}(\omega)/\omega^2$ is divergent at $\omega = 0$. As in the previous test we adopt the default model that reproduces the large ω ($a\omega \gtrsim 2.3$) behavior of the input spectral function. For the very low frequency region ($a\omega \lesssim 0.12$) in the default model, we utilize a form like formula (3.19) varying the width η and the amplitude. We tried with three default models, all with the same widths but different amplitudes of the transport peak. In the left panel of Fig. 3.6 we show the spectral function divided by ω^2 , $\sigma(\omega)/\omega^2$, to cancel the large ω rise. We observe that the resonance parts of the output spectral functions are quite independent of the three default models provided. In the right panel of Fig. 3.6 we plot $\sigma(\omega)a/\omega$ in the very low frequency region to show the transport peak in more detail. For the very low frequency parts of the default models we keep the widths of the transport peaks unchanged and vary the amplitudes. Surprisingly there are only minor changes of the output spectral functions even if the amplitude of the transport peak is amplified four times.

As we found in the test done in Fig. 3.6 the output transport peak from MEM is

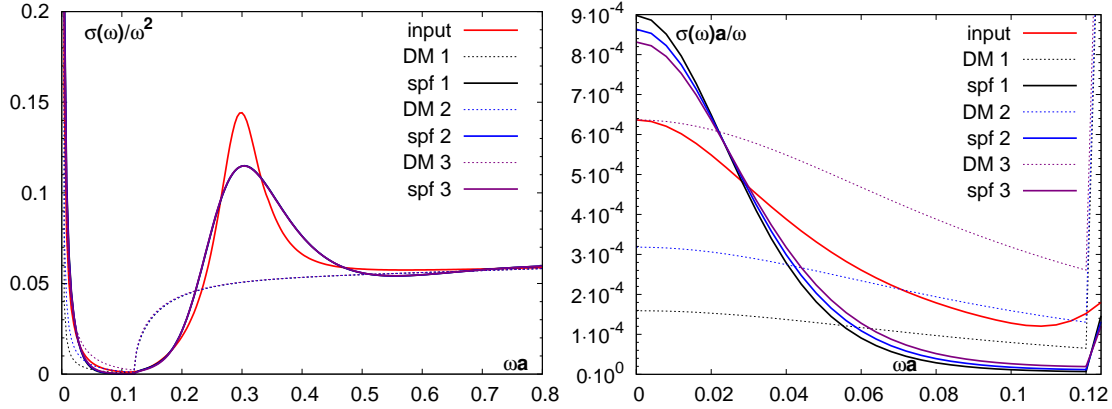


Figure 3.6. The DM dependence (varying the amplitudes of the transport peak) of the spectral function extracted from mock data with $N_\tau = 64$. The left plot shows $\sigma(\omega)/\omega^2$ as a function of ωa while the right plot shows $\sigma(\omega)a/\omega$ as a function of ωa . The very high frequency ($a\omega \gtrsim 2.3$) behavior of all the DMs is the same as that of the input spectral functions. The very low frequency ($a\omega \lesssim 0.12$) information in the DMs is the transport peak like, with fixed width but different amplitudes. The resonance width of the input spectral function $a\gamma$ is set to be 0.15 and the transport width $a\eta$ is set to be 0.05. The width of the transport peak in the default model is fixed to be 0.1.

quite independent of the default model when the large ω ($a\omega \gtrsim 0.12$) information and the width of the transport peak in the default model are not changed. We also checked the case when the width of the transport peak in the default model is changed. This is done with the amplitudes of the transport peak and the large ω information are fixed in the default model. As seen from the left plot of Fig. 3.7 the resonance part of the spectral function again shows only small default model dependence. In the right plot of Fig. 3.7 the low frequency part of the output spectral function depends on the default model a lot. This can be understood to be the same situation as with the width of the resonance peak, due to the intrinsic insensitivity of the correlators to these quantities. We also find an empirical rule: when one provides a peak (transport or resonance) which is much narrower than the real input, MEM will be “fooled” by the prior information provided in the default model and just follows the trend of the default model not only in the high frequency region but also in the low frequency region; on the other side, if one provides a relatively broad peak into the default mode, MEM can reproduce the input spectral function qualitatively. It is sure that one cannot set a reference scale to say which is broad and which is narrow, or in other words, it is a compromise between the prior information provided into default models and the quality of the correlator data.

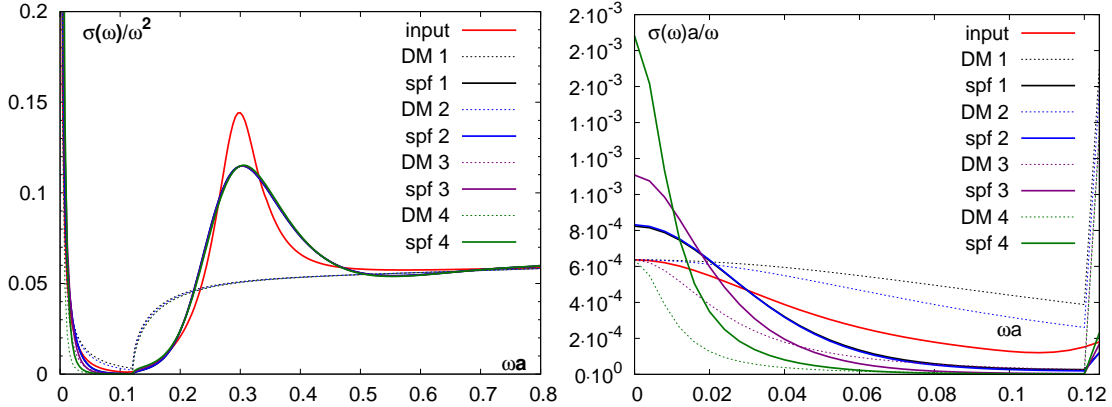


Figure 3.7. The DM dependence (varying the width of the transport peak) of the spectral function extracted from mock data with $N_\tau = 64$. The left plot shows $\sigma(\omega)/\omega^2$ as a function of ωa while the right plot shows $\sigma(\omega)a/\omega$ as a function of ωa . The high frequency behavior ($a\omega \gtrsim 2.3$) of all the DMs are the same to the input spectral functions. The very low frequency ($a\omega \lesssim 0.12$) information in the DMs are the transport peak like and with fixed amplitudes but different widths. Both the resonance width $a\gamma$ and the transport peak width $a\eta$ of the input spectral function are set to be 0.1. “DM 1”, “DM 2”, “DM 3” and “DM 4” are the default models with $a\eta$ to be 0.1, 0.15, 0.025 and 0.01, respectively.

3.3 Effective mass

Now we start to do analysis on the real lattice data. Since our correlation function is precisely measured on the lattice, we first investigate the charmonium properties at the correlator level. At this level one can look into the effective mass $m_{\text{eff}}^{\text{cosh}}(\tau)$ obtained from the ratios of the neighboring correlators

$$\frac{G(\tau)}{G(\tau+1)} = \frac{\cosh \left[m_{\text{eff}}^{\text{cosh}}(\tau) \left(\frac{N_\tau}{2} - \tau \right) \right]}{\cosh \left[m_{\text{eff}}^{\text{cosh}}(\tau) \left(\frac{N_\tau}{2} - \tau - 1 \right) \right]}. \quad (3.20)$$

The effective mass $m_{\text{eff}}^{\text{cosh}}(\tau)$ should give the lowest energy states of the corresponding channel at very large distance. As we already saw, even in the free continuum case, there are constant (zero mode) contributions in the correlators. To focus on the peak structure of the lowest energy states it is useful to suppress or remove the constant contribution from the correlators by using appropriate techniques. Since the constant contribution is τ independent one straightforward idea is to check the derivative of the correlator with respect to Euclidean time τ , practically by using differences of the neighboring correlators

$$G_{\text{diff}}(\tau) = G(\tau) - G(\tau+1), \quad (3.21)$$

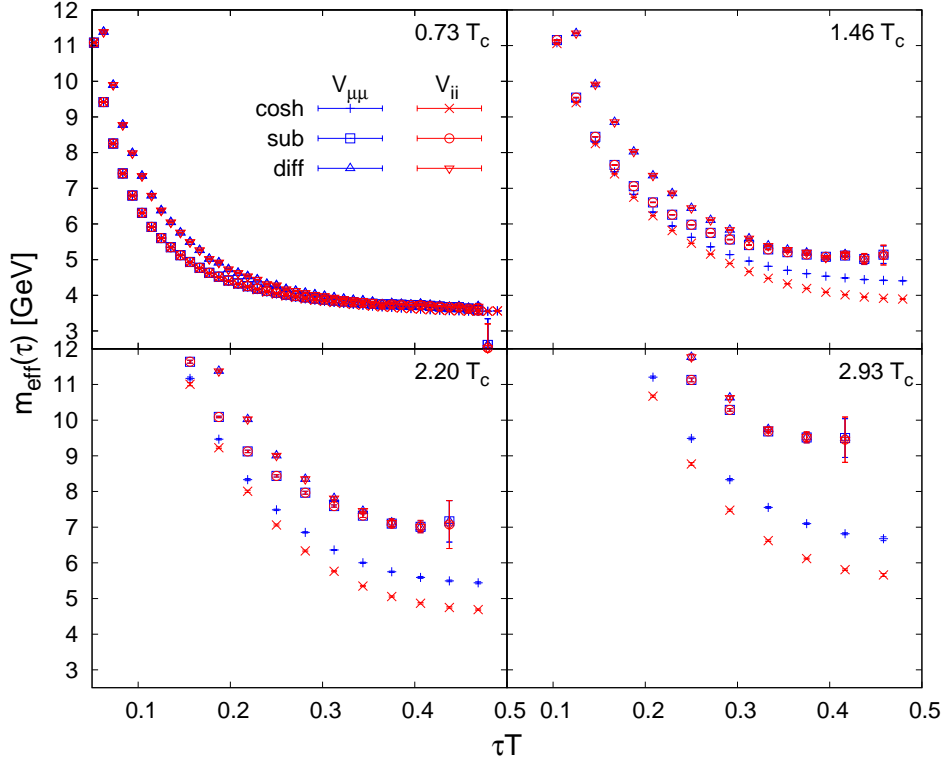


Figure 3.8. The effective mass $m_{\text{eff}}(\tau)$ as a function of τT obtained from the standard correlators $m_{\text{eff}}^{\text{cosh}}(\tau)$ (Eq. (3.20)), the differential correlator $m_{\text{eff}}^{\text{diff}}(\tau)$ (Eq. (3.22)) and the midpoint subtracted correlator $m_{\text{eff}}^{\text{sub}}(\tau)$ (Eq. (3.24)) at temperatures $0.73 T_c$, $1.46 T_c$, $2.20 T_c$ and $2.93 T_c$ calculated on the lattice with $\beta = 7.793$.

where $G_{\text{diff}}(\tau)$ is equal to the symmetric derivative at $\tau + 1/2$. The corresponding effective mass can be defined as [141]²

$$\frac{G_{\text{diff}}(\tau)}{G_{\text{diff}}(\tau + 1)} = \frac{\sinh \left[m_{\text{eff}}^{\text{diff}}(\tau) \left(\frac{N_\tau}{2} - \tau - 1/2 \right) \right]}{\sinh \left[m_{\text{eff}}^{\text{diff}}(\tau) \left(\frac{N_\tau}{2} - \tau - 3/2 \right) \right]}. \quad (3.22)$$

Since among all the correlator data points the symmetry point of correlation function has the largest contribution from the zero mode contribution, an alternative way to suppress the zero mode contribution is to look into the midpoint subtracted correlator

$$G_{\text{sub}}(\tau) = G(\tau) - G(N_\tau/2). \quad (3.23)$$

The corresponding effective mass can be defined as [141]

$$\frac{G_{\text{sub}}(\tau)}{G_{\text{sub}}(\tau + 1)} = \frac{\sinh^2 \left[\frac{1}{2} m_{\text{eff}}^{\text{sub}}(\tau) \left(\frac{N_\tau}{2} - \tau \right) \right]}{\sinh^2 \left[\frac{1}{2} m_{\text{eff}}^{\text{sub}}(\tau) \left(\frac{N_\tau}{2} - \tau - 1 \right) \right]}. \quad (3.24)$$

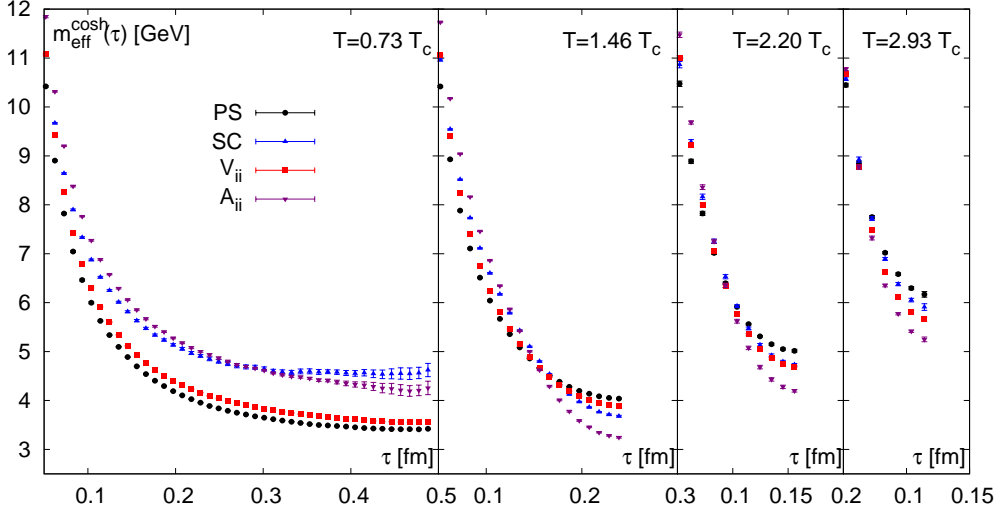


Figure 3.9. Temperature dependence of effective mass obtained from the standard correlator $m_{\text{eff}}^{\text{cosh}}(\tau)$ (Eq. (3.20)) calculated on our finest lattice with $\beta = 7.793$.

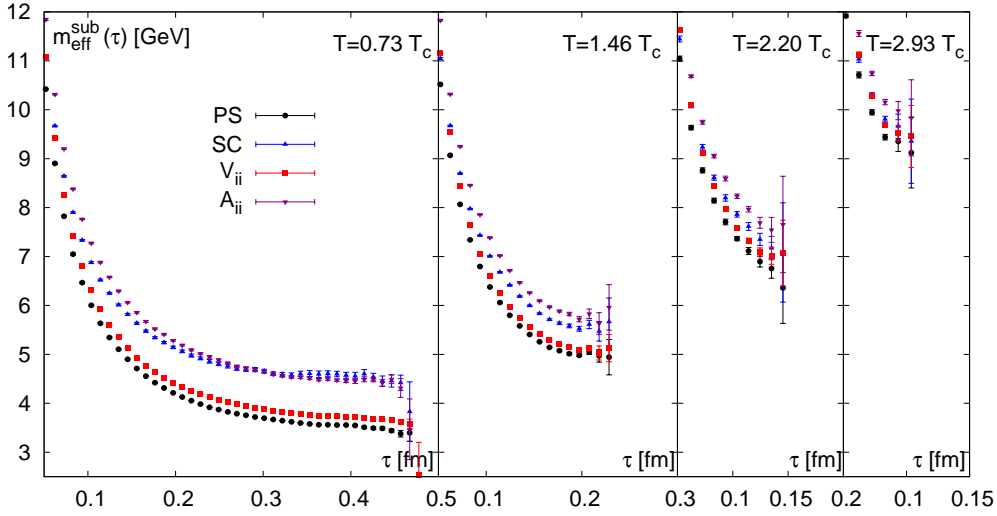


Figure 3.10. Temperature dependence of effective mass obtained from the midpoint subtracted correlator $m_{\text{eff}}^{\text{sub}}(\tau)$ (Eq. (3.24)) calculated on our finest lattice with $\beta = 7.793$.

Since there is only a τ independent constant difference between V_{ii} and $V_{\mu\mu}$ channels, thus V_{ii} and $V_{\mu\mu}$ channels can be a good platform to test behaviors of $m_{\text{eff}}^{\text{diff}}$ and $m_{\text{eff}}^{\text{sub}}$. In Fig. 3.8 we plot $m_{\text{eff}}^{\text{cosh}}(\tau)$, $m_{\text{eff}}^{\text{diff}}(\tau)$ and $m_{\text{eff}}^{\text{sub}}(\tau)$ of these two channels at four different temperatures available on our finest lattice. At temperatures below T_c $m_{\text{eff}}^{\text{cosh}}$ should be the same in the V_{ii} and $V_{\mu\mu}$ channels since the constant difference from these

²There is a typo of the corresponding formula (Eq.(8)) in Ref. [141].

two channels is nearly zero. When going to higher temperatures above T_c one can see clearly that at large distances there is a difference of $m_{\text{eff}}^{\text{cosh}}$ in the V_{ii} and $V_{\mu\mu}$ channels due to the finite τ independent constant. At small distance $m_{\text{eff}}^{\text{cosh}}$ in these two channels coincides, since the constant contribution becomes negligible. The effective masses obtained from the differential correlators in the $V_{\mu\mu}$ and V_{ii} channels overlap with each other at all distances. When going to higher temperature, as expected from section 2.3.1, the discrepancy between $m_{\text{eff}}^{\text{cosh}}$ in the $V_{\mu\mu}$ and V_{ii} channels becomes larger at larger distance, but $m_{\text{eff}}^{\text{diff}}$ is always the same in these two channels at all distances. The third quantity, $m_{\text{eff}}^{\text{sub}}$, gives similar results as $m_{\text{eff}}^{\text{diff}}$ at all temperatures. $m_{\text{eff}}^{\text{sub}}$ and $m_{\text{eff}}^{\text{diff}}$ overlap with each other at very large distances and start to differ only at small distances, in particular $m_{\text{eff}}^{\text{sub}}$ reproduces $m_{\text{eff}}^{\text{cosh}}$ at small distances. The results shown in Fig. 3.8 indicate both methods work well for this obvious case. Since $m_{\text{eff}}^{\text{sub}}$ works better we will utilize it to investigate the other channels at finite temperature.

As a reference we first plot the standard effective mass $m_{\text{eff}}^{\text{cosh}}(\tau)$ for PS, SC, V_{ii} and A_{ii} at all temperatures available from our simulation in Fig. 3.9. In the same physical distance, the S wave states i.e. the pseudo scalar and vector channels show small changes up to $1.46 T_c$, while the P waves states show large changes even at $1.46 T_c$. The corresponding effective mass from the midpoint subtracted correlator is shown in Fig. 3.10. We find that both P wave states and S waves states change dramatically already at $1.46 T_c$. This indicates there might be thermal modifications beyond the zero mode contributions. To really get a clear understanding, one has to investigate on the spectral functions in these channels.

3.4 Spectral functions below T_c

In this section we will discuss the spectral function obtained from MEM at temperatures below T_c . We will mainly focus on results from our finest lattice $128^3 \times 96$ with $\beta = 7.793$. When we analyze the correlation function using MEM, we always set the number of points in the frequency space to $N_\omega = 8000$, with the minimum $a\omega_{\text{min}} = 0.000001^3$ and the step length $a\Delta\omega = 0.0005$, i.e. we fix $a\omega_{\text{max}} \approx 4$. As we discussed in the mock data test, it would be better to provide the prior information into the default model, which describes the very high frequency part of the real spectral function. The direct choice here is the free lattice spectral function which has an automatic cut-off at $a\omega \approx 4$. If there is no additional description, we implicitly use the free lattice spectral functions obtained with quark mass $am \approx 0.06$ in our MEM analyses. The value $am \approx 0.06$ corresponds to the value of $m_{\overline{\text{MS}}}(m)$ listed in Table 1.2. In Fig. 3.11 we show the ratio

³One actually can set $a\omega = 0$ numerically. Since the $a\omega_{\text{min}}$ (0.000001) we used is already a very small number and N_ω is very large, there are no effects brought by this issue.

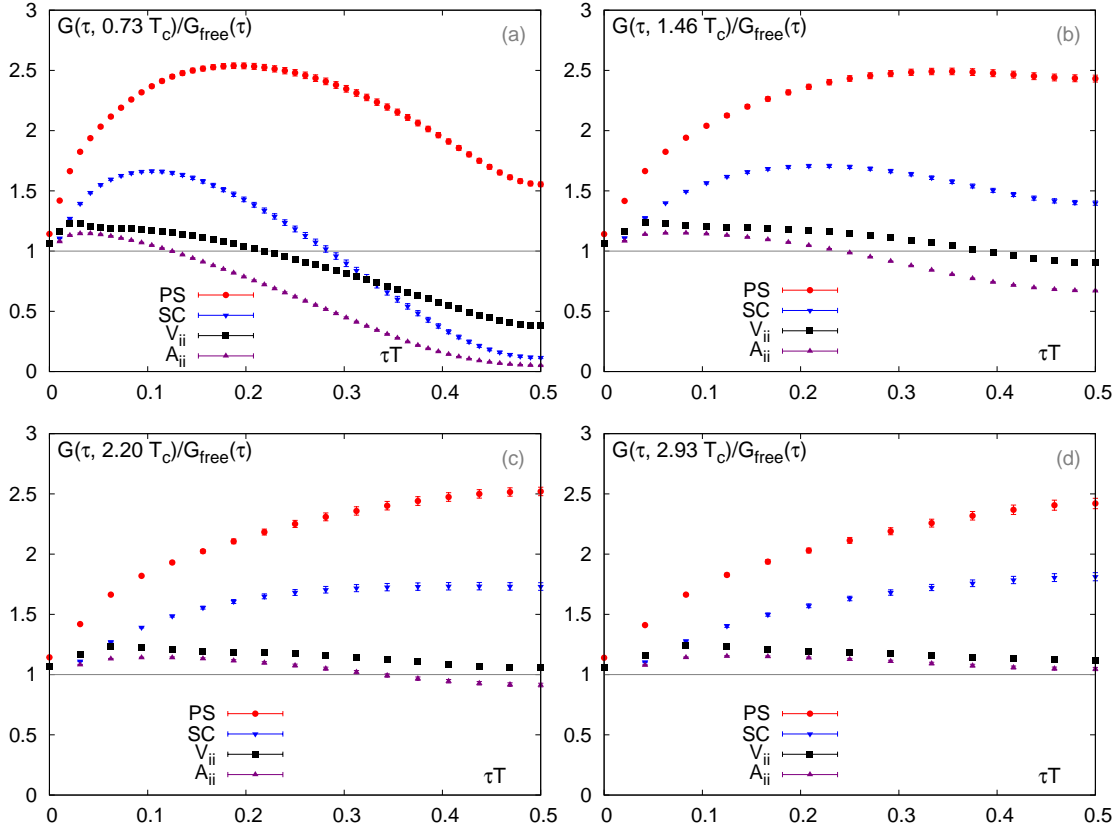


Figure 3.11. Ratios of $G(\tau, T)$ to $G_{\text{free}}(\tau)$ at $0.73 T_c$ (a), $1.46 T_c$ (b), $2.20 T_c$ (c) and $2.93 T_c$ (d) from our finest lattice with $\beta = 7.793$. Quark mass used in the calculation of free correlators is obtained from Table 1.2.

of the correlator data to the free lattice correlator with $am \approx 0.06$. There are still quite some differences of the ratio $G(\tau, T)/G_{\text{free}}(\tau)$ from unity at small distances, at $0.73 T_c$ (a), $1.46 T_c$ (b), $2.20 T_c$ (c) and $2.93 T_c$ (d), even after the renormalization to the correlator data mentioned in section 1.6. This difference might be partly due to the inaccuracy of the renormalization constants. To reduce discretization effects, we omit some correlation data points at very small distances, i.e. we use $\tau/a = 4, 5, 6, \dots, N_\tau/2$. To reduce the difference between the free lattice correlation function and the correlation data, we normalize the free spectral function to make the free spectral function roughly equal to the real spectral function in the large frequency region. In practice, we set $G(\tau/a = 4, T)/G_{\text{free}}(\tau/a = 4, T) = 1$. To explore the very low frequency behavior of the spectral function and avoid the instability of the kernel at $\omega \approx 0$, we use the modified kernel given in Eq. (2.127).

Due to large lattice cut-off effect in the scalar and axial vector channels, which is seen already in the free case (see e.g. the right panel of Fig. 2.1), at the spectral function

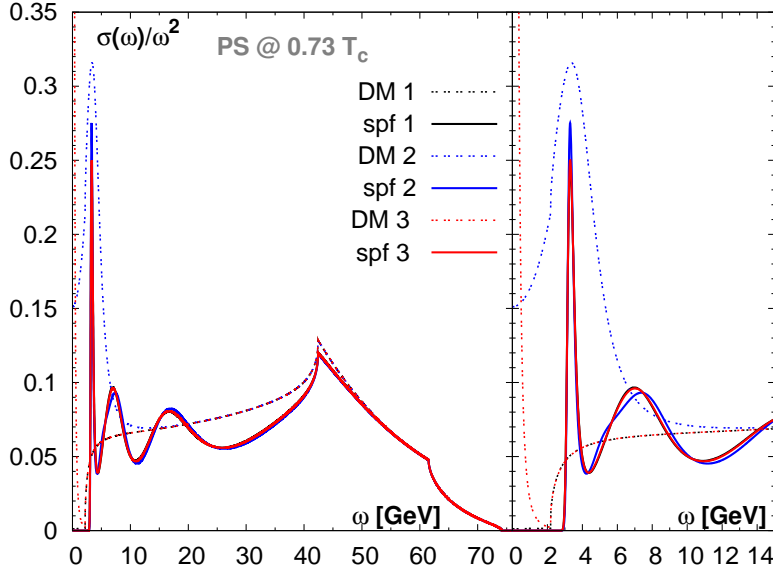


Figure 3.12. Default model dependences of the output spectral functions in the PS channel at $0.73 T_c$ on the $128^3 \times 96$ lattice. The plot in the right panel is a blowup of the low energy region of the left panel. “DM”s are the input default models while “spf”s are the corresponding MEM outputs.

level we restrict ourselves to study the S wave states only.

We first look at the spectral function in the PS channel. We show the default model dependence of the PS spectral function in Fig. 3.12. The left panel of Fig. 3.12 shows the default models and the output spectral function from MEM in the whole energy region while the right panel of Fig. 3.12 is a blowup in the low frequency region ($\omega \leq 14$ GeV). To suppress the large ω rise, we plot the spectral function divided by ω^2 as a function of ω . The default models are all represented by the dotted lines and the output spectral functions are the corresponding solid lines with the same colors. We test three different default models, “DM 1” is the normalized free lattice spectral function, “DM 2” is the normalized free lattice spectral function supplemented with a resonance peak located in the low frequency region and “DM 3” is the normalized free lattice spectral function with a transport peak, i.e. Eq. (3.19) in the very low frequency region. In the very high frequency region ($\omega \gtrsim 55$ GeV), as we can see from the left panel of Fig. 3.12, the MEM outputs just resemble the behavior of the input default models as we already saw from the mock data test. In the low frequency region, as seen from the right panel of Fig. 3.12, the spectral functions from MEM have a uniform behavior that is different from the input default models, which should be physics. The default model dependence of the first peak is very weak, though there are some differences in the amplitudes of the output spectral functions. The peak locations of the first peak

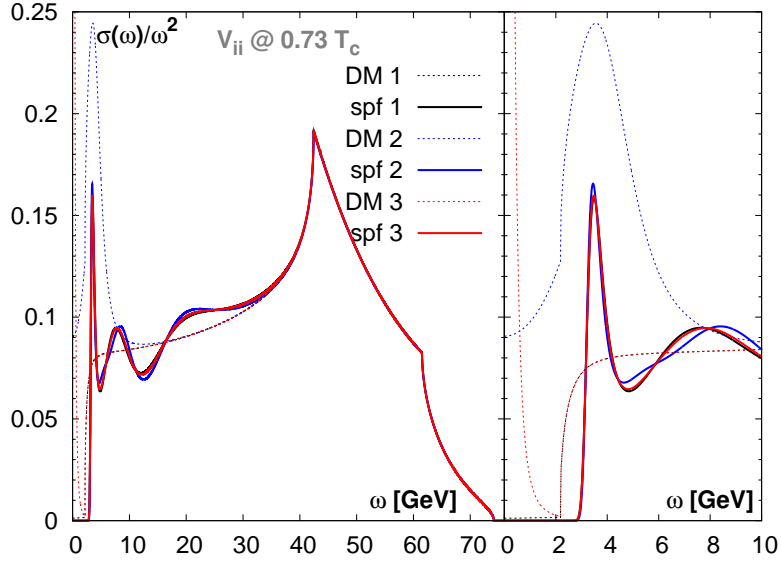


Figure 3.13. Default model dependences of the output spectral functions in the V_{ii} channel at $0.73 T_c$ on the $128^3 \times 96$ lattice. The plot in the right panel is a blowup of the low energy region of the left panel. “DM”s are the input default models while “spf”s are the corresponding MEM outputs.

are always the same, at around $\omega \approx 3.31$ GeV, which in turn is close to the value of the screening mass obtained from the spatial correlator quoted in Table 1.3. Thus this peak can be interpreted as the bound state peak of η_c and remains quite stable and robust from MEM with quite different prior information. However, the width of this peak cannot be directly interpreted as the width of η_c due to the statistics and number of data points. The second and third peak in the Fig. 3.12 could be a mixture of higher excited states or MEM artifacts due to the finite lattice spacing and limited number of correlator points.

Since there is no zero mode contribution in the PS channel in the high temperature limit as we have learned from section 2.3.1, it would be interesting to check whether it has a zero mode contribution at the temperature below T_c . We thus put transport prior information into the default model (“DM 3”). It turns out there is no transport peak in “spf 3”. As in the infinite temperature limit there is also no zero mode contribution in this channel we thus conclude there is no zero mode contribution in the pseudo scalar channel at temperatures above T_c . Then the PS spectral function would be a good candidate to look into the change of the bound states.

We did the same exercise for the vector channel V_{ii} (summing over the spatial components only). The results are shown in Fig. 3.13. Again the MEM outputs are quite independent of the default models. The ground peak stays stable and robust, and

its peak location is approximately $\omega \approx 3.48$ GeV, which is comparable to the value we obtained in Table 1.3. As for the pseudo scalar channel, the width of the ground peak is affected by the quality of the data and cannot be interpreted as the width of J/ψ . The second peak could be again a mixture of higher excited states and the artifacts of MEM. We also put a transport peak into the default model (“DM 3”), and like the case in pseudo scalar channel, we find there is no transport peak in “spf 3” as well. We thus conclude at this temperature there is also no zero mode contribution in the vector channel.

3.5 Reconstructed correlator

As seen in the previous section we have successfully reconstructed spectral functions in the PS and V_{ii} channel. We are confident that there are ground state peaks in each channel locating at the correct meson masses at $T < T_c$. At temperatures above T_c , the temporal extent becomes shorter and the number of data points available for the analysis becomes smaller. Thus the reconstruction of the spectral function will become difficult. To analyze thermal modifications of spectral functions, we will first investigate the ratio of the measured correlator to the reconstructed correlator, which can remove the trivial temperature dependence of the kernel $K(\omega, T, \tau)$.

$$\frac{G(\tau, T)}{G_{\text{rec}}(\tau, T)} = \frac{\int_0^\infty d\omega K(\tau, T, \omega) \sigma(\omega, T)}{\int_0^\infty d\omega K(\tau, T, \omega) \sigma(\omega, T')}. \quad (3.25)$$

With relation (2.55) we calculate $G_{\text{rec}}(\tau, T)$ directly from the correlator data at temperature T' and thus the systematic error is more under control.

3.5.1 The pseudo scalar correlators

We first investigate the temperature dependence of the pseudo scalar correlators. We show the numerical results for $G(\tau, T)/G_{\text{rec}}(\tau, T)$ at $1.46 T_c$, $2.20 T_c$ and $2.93 T_c$ on our finest lattice in Fig. 3.14. $G_{\text{rec}}(\tau, T)$ are evaluated from correlator data at $T' = 0.73 T_c$. The ratio of $G(\tau, T)/G_{\text{rec}}(\tau, T)$ shows very little deviation from unity at $1.46 T_c$. As seen from Fig. 3.14, the temperature effects start to set in at around 0.06 fm at $1.46 T_c$ and make the ratio deviate from unity around 5% at the largest distance. The very small temperature dependence of the pseudo scalar correlator might indicate that the corresponding ground state $\eta_c(1S)$ survives up to the temperature as high as $1.46 T_c$. When going to the higher temperature, $2.20 T_c$, the temperature effects set in at a much smaller distance (≈ 0.02 fm). The deviation slope is larger and the deviation from unity ($\approx 8\%$) is much larger at the largest available distance. At the highest temperature we have, $2.93 T_c$, the deviation of the ratio from unity becomes about 12% at the largest

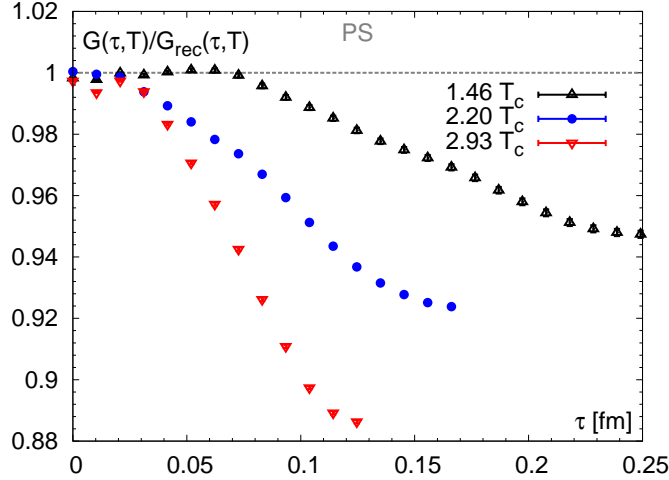


Figure 3.14. The ratio $G(\tau, T)/G_{\text{rec}}(\tau, T)$ for the PS channel as function of the Euclidean distance τ on our finest lattice with $\beta = 7.793$ ($a^{-1} = 18.974$ GeV) at $T = 1.46, 2.20$ and $2.93 T_c$. The reconstructed correlator G_{rec} is reconstructed from correlator data at $0.73 T_c$.

distance. This may suggest considerable modifications in the lowest state of pseudo scalar channel at this temperature.

The qualitative temperature dependence is found to be similar to the previous findings of Ref. [40]. The differences of G/G_{rec} in Ref. [40] are smaller. This might be due to first, we are calculating the G/G_{rec} exactly without evaluating the spectral functions from MEM, and second, an anisotropic lattice is used in Ref. [40]. In favor of saving computing power anisotropic lattices are always employed to get a relatively large number of points in the temporal directions, but decreasing the temporal lattice spacing a_τ at fixed spatial lattice spacing a_σ , i.e. increasing the anisotropy $\zeta = a_\sigma/a_\tau$, will not reduce cut-off effects. Unfortunately the mass of J/ψ is not tuned accurately on our finest lattice ($\beta = 7.793$, $a^{-1} = 18.974$ GeV) but lattice cut-off effects should be very small.

3.5.2 The P wave correlators

In this subsection we will discuss the temperature dependence of the scalar and axial vector (summing over spatial components only) correlators corresponding to P wave states.

The numerical results for these two channels are shown in Fig. 3.15 on our finest lattice. In the left panel of Fig. 3.15 the ratio G/G_{rec} for the scalar channel is shown while in the right panel the ratio for the axial vector is shown. We find already at $1.46 T_c$ that a significant thermal modification of the mesons is manifest in G/G_{rec} at all

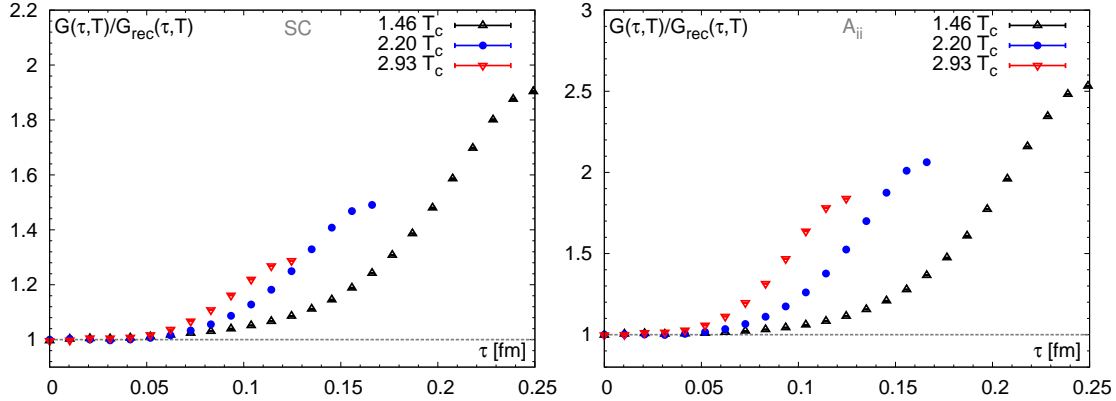


Figure 3.15. The ratio $G(\tau, T)/G_{\text{rec}}(\tau, T)$ of P wave states as a function of the Euclidean distance τ on our finest lattice with $\beta = 7.793$ ($a^{-1} = 18.974$ GeV) at $T = 1.46, 2.20$ and $2.93 T_c$. The reconstructed correlator G_{rec} is reconstructed from correlator data at $0.73 T_c$. The left plot is for the SC channel and the right one is for the A_{ii} channel.

distances. G/G_{rec} reach around 1.9 in the SC channel and around 2.5 in the A_{ii} channel at the largest available distance. Such a magnitude of the deviation from unity is much larger compared to the case of the PS channel. This indicates a strong modification of the properties of the low frequency region of the spectral function (maybe the frequency region including the lowest states) and the possible dissolution of 1P charmonium states already at $1.46 T_c$. We also observe the deviation of $G(\tau, T)/G_{\text{rec}}(\tau, T)$ from unity at the largest distances decreases with increasing temperature, which is in contradiction to the case of the PS channel.

3.5.3 The vector correlators

We show the ratio $G(\tau, T)/G_{\text{rec}}(\tau, T)$ for vector correlator V_{ii} (summing over spatial components only) on our finest lattice in Fig. 3.16. As one can see from this figure the temperature dependence of $G(\tau, T)/G_{\text{rec}}(\tau, T)$ is different from the pseudo scalar case and this ratio is larger than unity at large distance⁴. The deviation of $G(\tau, T)/G_{\text{rec}}(\tau, T)$ from unity starts from smaller distances at higher temperatures. Unlike in the PS, SC and A_{ii} channels the magnitudes of $G(\tau, T)/G_{\text{rec}}(\tau, T)$ at the largest available distance at different temperatures do not differ that much.

To study lattice spacing effects on the ratio of measured correlators to reconstructed correlators, we show the ratios on our two coarse lattices in Fig. 3.17. The two plots

⁴The ratio $G(\tau, T)/G_{\text{rec}}(\tau, T)$ in the $V_{\mu\mu}$ channel (summing over both the temporal and spatial components) is smaller than unity at large distance due to the presence of the τ independent constant G_V^{00} .

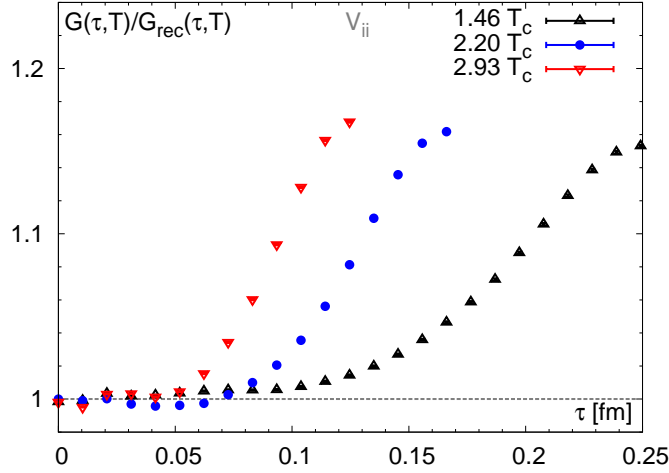


Figure 3.16. The ratio $G(\tau, T)/G_{\text{rec}}(\tau, T)$ for the V_{ii} channel as a function of the Euclidean distance τ on our finest lattice with $\beta = 7.793$ ($a^{-1} = 18.974$ GeV) at $T = 1.46, 2.20$ and $2.93 T_c$. The reconstructed correlator G_{rec} is reconstructed from $0.73 T_c$ correlator data.

in the upper panel of Fig. 3.17 are the results from the lattice with $\beta = 6.872$, $a^{-1} = 6.432$ GeV while the two plots in the lower panel are the results from the lattice with $\beta = 7.457$, $a^{-1} = 12.864$ GeV. The plots on the left hand side are for P wave states and the plots on the right hand side are for S wave states. By comparing the results from $\beta = 6.872$ and $\beta = 7.457$ with that from our finest lattice $\beta = 7.793$, it is clear that the temperature dependence of the correlator is not affected significantly by the finite lattice spacing. The difference we see from the two coarser lattices and the finest lattice could originate from the different masses of the mesons due to the κ tuning.

The big rise of the ratio G/G_{rec} at large distances in the vector channel seen from Fig. 3.16 indicates the thermal change of the spectral function in the low frequency region. Initially, the deviation of the ratio in the vector channel was interpreted as to indicate a considerable thermal change of the bound states. Recently it is found that the temperature dependence of the vector correlator can be also explained by the diffusion contribution [40, 126, 141].

To illustrate this point we take a look at the ratio of the differences of the neighboring correlators to the difference of the corresponding reconstructed correlators

$$\frac{G^{\text{diff}}(\tau, T)}{G_{\text{rec}}^{\text{diff}}(\tau, T)} \equiv \frac{G(\tau, T) - G(\tau + 1, T)}{G_{\text{rec}}(\tau, T) - G_{\text{rec}}(\tau + 1, T)}, \quad (3.26)$$

which equals the ratio of the time derivative of the correlators to the time derivative of the reconstructed correlators at $\tau + 1/2$. If the diffusion contribution is just a τ independent constant it will be canceled in this ratio. One can also check the ratio of

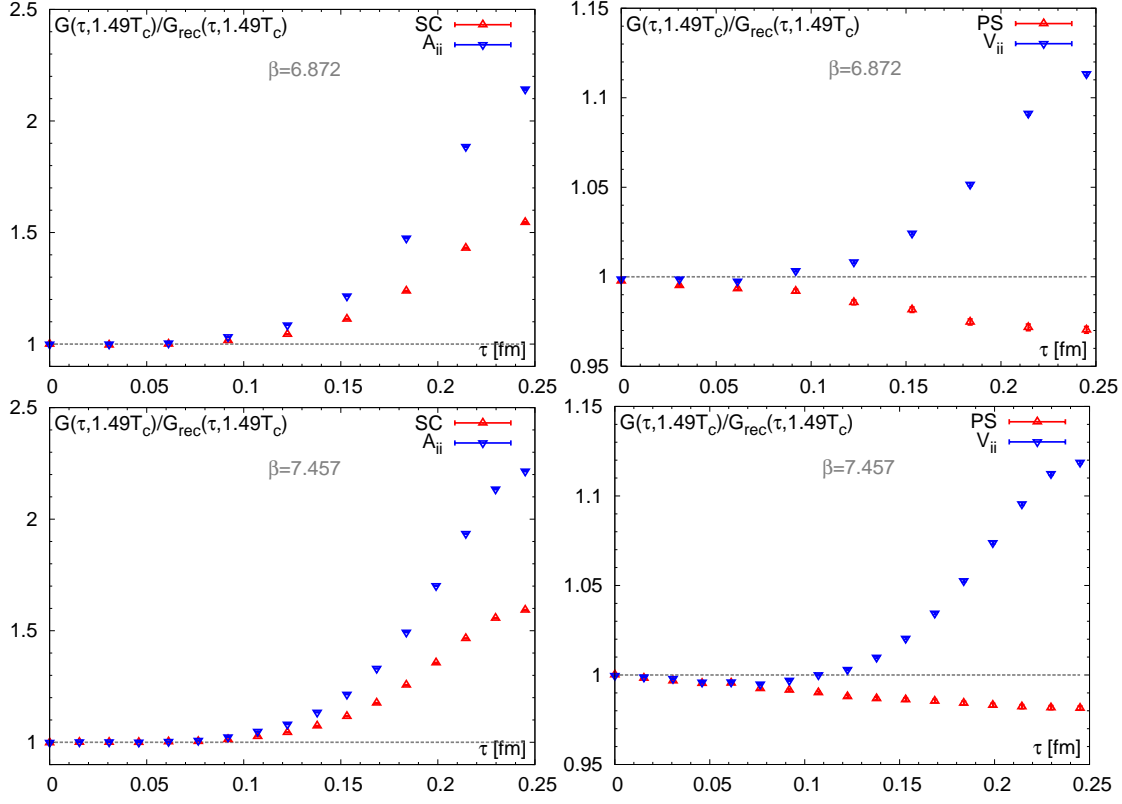


Figure 3.17. The ratio $G(\tau, T)/G_{\text{rec}}(\tau, T)$ as a function of the Euclidean distance τ at $1.49 T_c$ on two coarse lattices. The reconstructed correlator G_{rec} is reconstructed from correlator data at $0.74 T_c$. The plots on the top show the results from lattice data sets with $\beta = 6.872$ ($a^{-1} = 6.432$ GeV) while the lower plots show the results from lattice data sets with $\beta = 7.457$ ($a^{-1} = 12.864$ GeV).

midpoint subtracted correlators

$$\frac{G^{\text{sub}}(\tau, T)}{G_{\text{rec}}^{\text{sub}}(\tau, T)} \equiv \frac{G(\tau, T) - G(N_\tau/2, T)}{G_{\text{rec}}(\tau, T) - G_{\text{rec}}(N_\tau/2, T)}. \quad (3.27)$$

One expects that this ratio has only a very small temperature dependence, if the diffusion contribution is dominated at the largest distance and at the same time is a almost τ independent constant.

In Fig. 3.18, we show the results for $G^{\text{sub}}/G_{\text{rec}}^{\text{sub}}$ and $G^{\text{diff}}/G_{\text{rec}}^{\text{diff}}$ in the V_{ii} (left) and also in the PS channel (right). The filled symbols denote the ratio $G^{\text{sub}}/G_{\text{rec}}^{\text{sub}}$ while open symbols label the ratio $G^{\text{diff}}/G_{\text{rec}}^{\text{diff}}$. The ratios $G^{\text{sub}}/G_{\text{rec}}^{\text{sub}}$ and $G^{\text{diff}}/G_{\text{rec}}^{\text{diff}}$ give similar results at all the distances. Seen from the left panel of Fig. 3.18 the magnitude of the measured correlator to the reconstructed correlator reduces dramatically after the implementation of the difference of neighboring correlators (Eq. (3.26)) and mid-point

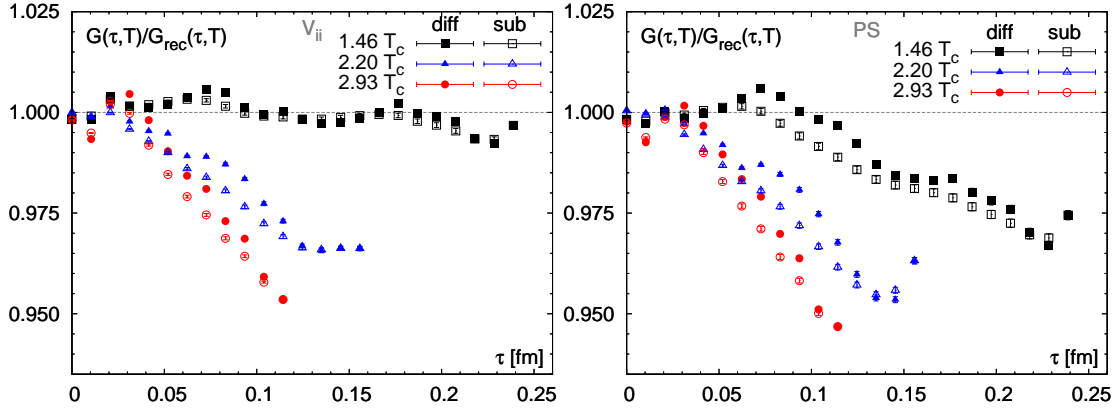


Figure 3.18. The ratio $G^{\text{sub}}(\tau, T)/G_{\text{rec}}^{\text{sub}}(\tau, T)$ ($G^{\text{diff}}(\tau, T)/G_{\text{rec}}^{\text{diff}}(\tau, T)$) of S wave states as a function of the Euclidean distance τ on our finest lattice with $\beta = 7.793$ at $T = 1.46, 2.20$ and $2.93 T_c$. The “diff” and “sub” stand for the results of the ratio $G^{\text{diff}}/G_{\text{rec}}^{\text{diff}}$ and $G^{\text{sub}}/G_{\text{rec}}^{\text{sub}}$, respectively. The left plot is for the V_{ii} channel and the right one is for the PS channel.

subtracted correlators (Eq. (3.27)). At $1.46 T_c$ the ratio is more or less unity at all distances, at $2.20 T_c$ and $2.93 T_c$ the ratio becomes even smaller than unity at large distances. This could be understood by the zero mode contribution as mentioned in section 2.3.1. The zero mode contribution gives the most temperature dependence of the ratio G/G_{rec} at least at $1.46 T_c$ seen in Fig. 3.16. The deviations of the ratios from unity in the PS channel shown in the right panel of Fig. 3.18 are also reduced. However, the effect is not as strong as that in the V_{ii} channel and the values at the largest distance are shifted up only about 3% at both $1.46 T_c$ and $2.20 T_c$ and about 6% at $2.93 T_c$ compared with the results in Fig. 3.14. Comparing the results for the vector channel (V_{ii}) with those for the pseudo scalar one in Fig. 3.18, we find the ratios $G^{\text{sub}}/G_{\text{rec}}^{\text{sub}}$ ($G^{\text{diff}}/G_{\text{rec}}^{\text{diff}}$) in these two channels have similar behavior at all distances at the two higher temperatures $2.20 T_c$ and $2.93 T_c$. However, they differ at $1.46 T_c$. The phenomenon we observe here might suggest J/ψ could survive up to $1.46 T_c$ and start to melt at $2.20 T_c$. For PS it might be melted already at $1.46 T_c$.

For completeness we also show the results of $G^{\text{sub}}/G_{\text{rec}}^{\text{sub}}$ and $G^{\text{diff}}/G_{\text{rec}}^{\text{diff}}$ in the P wave states on our finest lattice. The left panel of Fig. 3.19 shows the ratios for the A_{ii} channel while the right panel shows the ratio for the SC channel. The magnitudes of the ratios for both A_{ii} and SC are greatly reduced when compared to the ratios shown in Fig. 3.15. This behavior is quite similar to the ratios in the V_{ii} channel and it indicates the big rise seen in G/G_{rec} in Fig. 3.15 could mainly originate from the zero mode contributions.

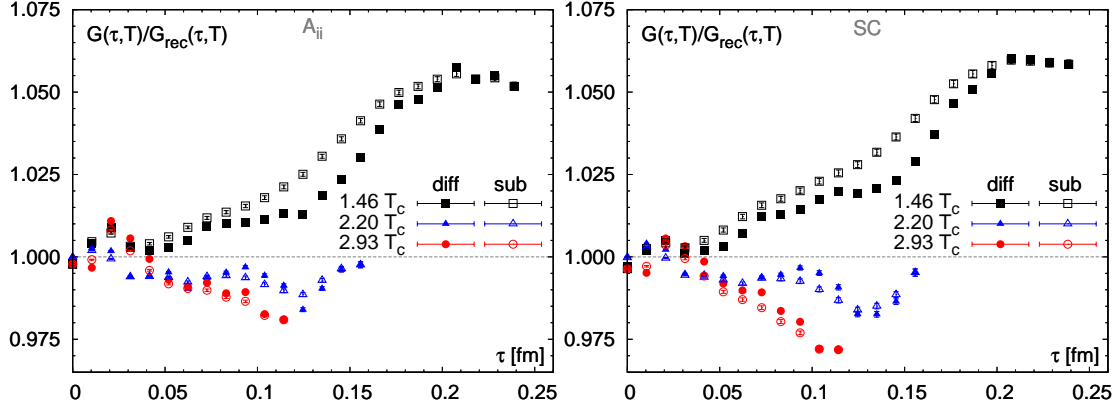


Figure 3.19. The ratio $G^{\text{sub}}(\tau, T)/G_{\text{rec}}^{\text{sub}}(\tau, T)$ ($G^{\text{diff}}(\tau, T)/G_{\text{rec}}^{\text{diff}}(\tau, T)$) of P wave states as a function of the Euclidean distance τ on our finest lattice with $\beta = 7.793$ at $T = 1.46, 2.20$ and $2.93 T_c$. The “diff” and “sub” stand for the results of the ratio $G^{\text{diff}}/G_{\text{rec}}^{\text{diff}}$ and $G^{\text{sub}}/G_{\text{rec}}^{\text{sub}}$, respectively. The left plot is for the A_{ii} channel and the right one is for the SC channel.

3.6 Estimate of the zero mode contribution

Since at higher temperatures the number of data points available becomes smaller, it could be better to provide some physical prior information into the default model. In this section we attempt to estimate the transport contribution in the vector channel at $1.46 T_c$ and put it into the default model in the MEM analysis.

From the above analysis, the ratio of G/G_{rec} for the vector correlator (V_{ii}) at $T = 1.46 T_c$ remains unity up to a distance of ≈ 0.06 fm and its temperature dependence at large distances can be understood by the diffusion contribution. Thus we can assume that the spectral function from the current-current correlator⁵ can be separated into a low frequency part σ_{JJ}^{low} and a high frequency part $\sigma_{JJ}^{\text{high}}$, correspondingly

$$G_{JJ}(\tau, T) = G_{JJ}^{\text{low}}(\tau, T) + G_{JJ}^{\text{high}}(\tau, T). \quad (3.28)$$

In the high frequency region, the lowest vector state J/ψ could, at least at $1.46 T_c$, remain unmodified or suffer from minor thermal changes. So we assume the high frequency behavior can be parameterized as the following

$$G_{JJ}^{\text{high}}(\tau, T) = (1 + k(T)) G_{JJ}^{\text{rec}}(\tau, T), \quad (3.29)$$

where the modification from the temperature below T_c at small distances is parameterized by the coefficient k and $G_{JJ}^{\text{rec}}(\tau, T)$ is the reconstructed correlator at temperature T

⁵The vector channel, as mentioned in the section 2.1, at $T = 1.46 T_c$, can be decomposed into density-density (time-like) part G_{NN} and current-current (space-like) part G_{JJ} .

reconstructed from the correlator at temperature $0.73 T_c$. For the low frequency region, as derived in Eq. (2.221), we make the spectral *Ansatz* as

$$\sigma_{JJ}(\omega) = \frac{3 T \chi_{00}}{\pi M} \frac{\omega \eta}{\omega^2 + \eta^2}, \quad \eta = \frac{T}{MD}, \quad (3.30)$$

where η is the drag coefficient, D denotes the heavy quark diffusion constant and χ_{00} is the quark number susceptibility. Consequently,

$$G_{JJ}^{\text{low}}(\tau, T) = \int_0^\infty d\omega \frac{\cosh(\omega(\tau - 1/2T))}{\sinh(\omega/2T)} \frac{3 T \chi_{00}}{\pi M} \frac{\omega \eta}{\omega^2 + \eta^2}. \quad (3.31)$$

One can fit the following renormalization independent quantity

$$R(\tau, T) \equiv \frac{G(\tau, T)}{G_{JJ}^{\text{rec}}(\tau, T)} = \frac{G_{JJ}^{\text{low}}(\tau, T)}{G_{JJ}^{\text{rec}}(\tau, T)} + 1 + k(T) \quad (3.32)$$

to get four parameters χ_{00} , k , η and M .

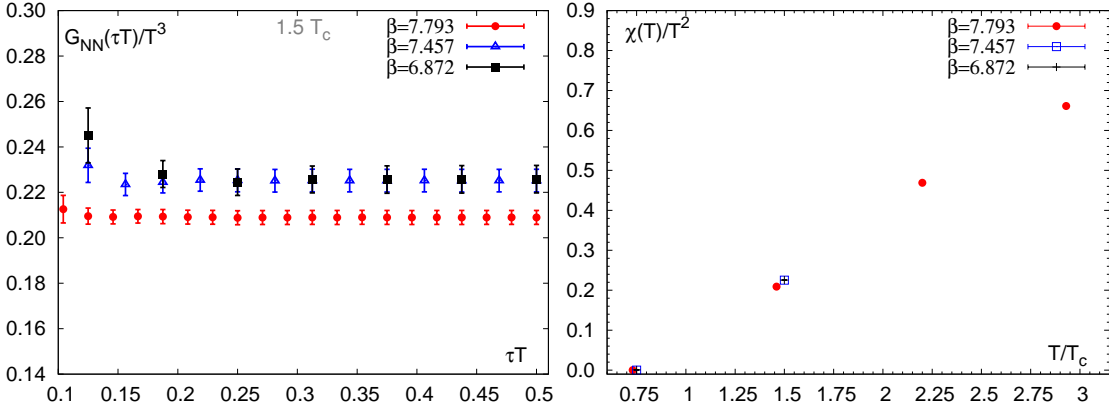


Figure 3.20. Left: the temporal component of the vector correlator $G_{NN}(\tau T)/T^3$ versus τT at $T \approx 1.5 T_c$. Right: the temperature dependence of the quark number susceptibility χ_{00} obtained from available lattice data sets.

Actually we obtain χ_{00} from the density-density correlator through the relation $G_{NN}(T) = T\chi_{00}(T)$. Due to the current we are using in our simulation being a non-conserved current, we need to check to what degree $G_{NN}(T)$ is independent of Euclidean time τ . We show the $G_{NN}(T)$ as a function of Euclidean time τ obtained from our available lattices in the left plot of Fig. 3.20 at $T \approx 1.5 T_c$. It is obvious that the results are very τ independent even at small distances. We also show the temperature dependence of the quark number susceptibility χ_{00} obtained from the available lattice data sets in the right plot of Fig. 3.20. χ_{00}/T^2 increases monotonically with increasing temperature up to $2.93 T_c$. It is hard to explore any quantitative relation between χ_{00}/T^2 and T/T_c due to our limited number of available data points.

In practice, we rewrite Eq. (3.31) as follows

$$G_{JJ}^{\text{low}}(\tau, T) = \int_0^\infty d\omega \frac{\cosh(\omega(\tau - 1/2T))}{\sinh(\omega/2T)} \frac{3\chi_{00}}{\pi} DT \frac{\omega}{\omega^2(MD)^2 + 1}. \quad (3.33)$$

and thus do a χ^2 fit to get parameters DT , MD and k . The resulting fit parameters are listed in Table. 3.1. One has to note the numbers shown in Table 3.1 are obtained under the assumption that J/ψ at $1.46 T_c$ remains almost unchanged.

β	N_τ	$\tau_{\min} : \tau_{\max}$	DT	MD	k
7.793	48	6:24	0.49 ± 0.12	2.22 ± 1.79	0.00016 ± 0.0002
		8:24	0.48 ± 0.12	2.17 ± 1.77	-0.0012 ± 0.0002
		10:24	0.47 ± 0.12	2.06 ± 1.70	-0.0021 ± 0.0004

Table 3.1. Fitting parameters DT , MD and k at $1.46 T_c$ on the lattice of $128^3 \times 48$ with $\beta = 7.793$.

Since the two parameters DT and MD are correlated, we get the parameters but with relatively large uncertainty even with 19 points. We need further information to constrain the spectral function which will be discussed in the following section.

3.6.1 Thermal moments of correlators

As we mentioned before the low frequency part of the spectral function corresponds to the large distance behavior of the correlation spectral function. By doing the Taylor expansion of the correlators at the largest distance accessible at finite temperature

$$\begin{aligned} G_H(\tau T) &= \int_0^\infty d\omega \sigma_H(\omega) \frac{\cosh(\omega(\tau - 1/2T))}{\sinh(\omega/2T)} \\ &= \int_0^\infty d\omega \frac{\sigma_H(\omega)}{\sinh(\omega/2T)} \left[1 + \frac{1}{2!} \left(\frac{\omega}{T}\right)^2 (\tau T - \frac{1}{2})^2 + \frac{1}{4!} \left(\frac{\omega}{T}\right)^4 (\tau T - \frac{1}{2})^4 + \dots \right], \end{aligned} \quad (3.34)$$

one might be able to explore the properties of the low frequency behavior of the spectral function. Here we define the Taylor expansion coefficients and also the time derivatives of the Euclidean correlation function

$$G_H^{(n)} = \frac{1}{n!} \left. \frac{d^n G_H(\tau, T)}{d(\tau T)^n} \right|_{\tau T=1/2} = \frac{1}{n!} \int_0^\infty d\omega \left(\frac{\omega}{T}\right)^n \frac{\sigma_H(\omega)}{\sinh(\omega/2T)}, \quad (3.35)$$

as *thermal moments* [88]. In particular the value of the zeroth moment $G_H^{(0)}$ is the same as the symmetry point $G_H(\tau T = 1/2)$.

As discussed in section 1.6 the renormalization constants of the non-conserved vector current in our lattice calculations is imprecisely determined. To avoid this issue we

consider the ratios of the thermal moments

$$R_H^{n,m} \equiv \frac{G_H^{(n)}}{G_H^{(m)}} \quad (3.36)$$

in which the multiplicative renormalization constants drop out. With this we rewrite the Taylor expansion of the Euclidean correlator (3.34) as follows

$$G_H(\tau T) = G_H^{(0)} \sum_{n=0}^{\infty} R_H^{2n,0} \left(\tau T - \frac{1}{2} \right)^{2n}. \quad (3.37)$$

Before we move to the lattice data analysis, we first have a look at the free continuum spectral function. In the massless case, as discussed in section 2.3.1, the correlator is obtained analytically in Eq. (2.145). Its thermal moments can thus be calculated analytically

$$G_{H,\text{free}}^{(0)}/T^3 = a_H^{(1)}, \quad (3.38)$$

$$G_{H,\text{free}}^{(2)}/T^3 = \frac{7}{5}(a_H^{(1)} - a_H^{(2)})\pi^2, \quad (3.39)$$

$$G_{H,\text{free}}^{(4)}/T^3 = \frac{31}{21}(a_H^{(1)} - a_H^{(2)})\pi^4. \quad (3.40)$$

The coefficients a_H are listed in Table. 2.2. As expected, the moments for the scalar and pseudo scalar (vector and axial vector) are the same. For the comparison to the lattice data we also give the ratio of the moments

$$R_{H,\text{free}}^{2,0} = \frac{7}{5} \left(1 - \frac{a_H^{(2)}}{a_H^{(1)}} \right) \pi^2, \quad (3.41)$$

$$R_{H,\text{free}}^{4,2} = \frac{155}{147} \pi^2. \quad (3.42)$$

The value of $R_{\text{free}}^{2,0}$ remains the same in the vector and axial vector (scalar and pseudo scalar) channels. It is worth noting that the values of $R_{\text{free}}^{4,2}$ are the same in all the channels.

For the lattice data analysis, in practice, we first calculate the curvature of the vector correlation function at $\tau T = 1/2$ from the subsequent differences of the vector correlator at τT and $\tau T = 1/2$

$$\Delta_H(\tau T) = \frac{G_H(\tau T) - G_H(1/2)}{(\tau T - 1/2)^2}. \quad (3.43)$$

To get a renormalization independent quantity, with relation (3.37), the above equation can be further written as follows

$$\frac{\Delta_H(\tau T)}{G_H(1/2)} = R_H^{2,0} \left(1 + \sum_{n=1}^{\infty} R_H^{2n+2,2n} (\tau T - 1/2)^{2n} \right) \quad (3.44)$$

$$= R_H^{2,0} \left(1 + R_H^{4,2} (\tau T - 1/2)^2 + \dots \right). \quad (3.45)$$

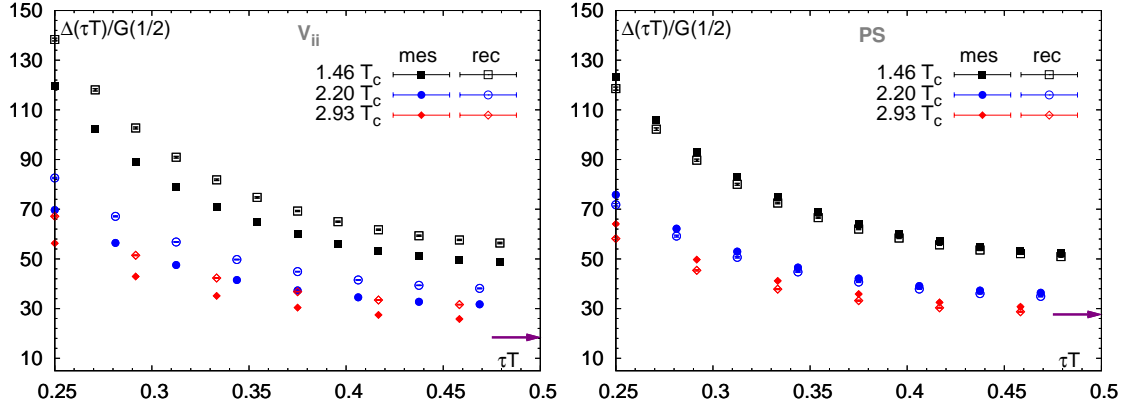


Figure 3.21. The curvatures of the correlation function in the V_{ii} channel (left) and the PS channel (right) versus τT at $1.46 T_c$, $2.20 T_c$ and $2.93 T_c$ on our finest lattice with $\beta = 7.793$. The filled symbols stand for curvatures of the measured correlators (“mes”) while the open symbols denote the curvatures of the reconstructed correlators (“rec”, reconstructed from the data at $0.73 T_c$). The arrows label the values from massless free continuum theory at $\tau T = 1/2$.

We show the results of $\Delta_H(\tau T)/G_H(1/2)$ for the V_{ii} channel in the left plot of Fig. 3.21. For comparison we also show the results for the PS channel in the right plot of Fig. 3.21. In both plots the filled symbols stand for the values obtained from measured correlators at different temperatures while the open symbols denote the values of the correlators at $T > T_c$ reconstructed from the correlation function at $0.73 T_c$. The arrows label the value of $\Delta_H(\tau T)/G_H(1/2)$ from the massless free continuum theory (Eq. (3.41)). The value of $\Delta_H(\tau T)/G_H(1/2)$ at $\tau T = 1/2$ gets closer to the free case with increasing temperature in both V_{ii} and PS channels. At $2.93 T_c$ this value in the PS channel is closer to the free massless limit value than that in the V_{ii} channel. This might be due to the presence of a zero mode contribution at this temperature in the V_{ii} channel, which in turn can also be seen from the comparison of $\Delta_H(\tau T)/G_H(1/2)$ in Fig. 3.21 with $G^{\text{sub}}/G_{\text{rec}}^{\text{sub}}$ in Fig. 3.18.

In what follows we will concentrate on the V_{ii} channel and suppress the label H . We thus use the quadratic *Ansatz*, $R^{2,0} (1 + R^{4,2} (\tau T - 1/2)^2)$, in the interval $[(\tau T)_{\text{min}}, 1/2]$ to fit the data of $\Delta(\tau T)/G(1/2)$ shown in the left plot of Fig. 3.21. Increasing the lower limit of the fit range we eliminate the influence of higher order corrections in a Taylor expansion of $G(\tau T)$ and get better estimates for the ratio of thermal moments defined in Eq. (3.36). Results of these fits for $R^{2,0}$ and $R^{4,2}$ as a function of $(\tau T)_{\text{min}}$ are shown in the left and right plot of Fig. 3.22, respectively. Since

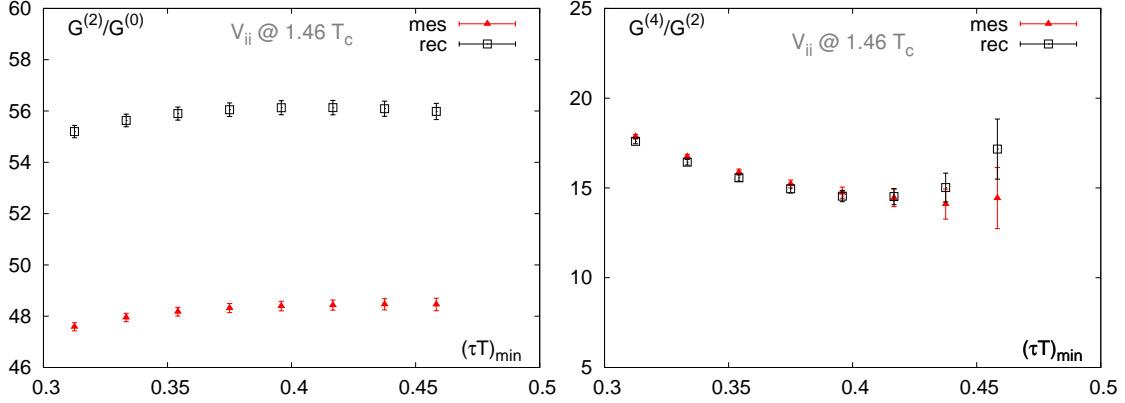


Figure 3.22. Ratios of the thermal moments in the V_{ii} channel from $128^3 \times 48$ lattice at $1.46 T_c$. The left plot shows $G^{(2)}/G^{(0)}$ and the right one shows $G^{(4)}/G^{(2)}$. “mes” denotes the values from the measured correlators at $1.46 T_c$ while “rec” labels the values from the reconstructed correlators at $1.46 T_c$ obtained from the correlation function at $0.73 T_c$.

$G(\tau T)/G_{\text{rec}}(\tau T)$ shown in Fig. 3.16 can be expanded as

$$\frac{G(\tau T)}{G_{\text{rec}}(\tau T)} = \frac{G^{(0)}}{G_{\text{rec}}^{(0)}} \left(1 + (R^{2,0} - R_{\text{rec}}^{2,0}) \left(\tau T - \frac{1}{2} \right)^2 + \dots \right), \quad (3.46)$$

and $G^{\text{sub}}(\tau T)/G_{\text{rec}}^{\text{sub}}(\tau T)$ shown in Fig. 3.18 can be written as

$$\frac{G^{\text{sub}}(\tau T)}{G_{\text{rec}}^{\text{sub}}(\tau T)} = \frac{G^{(2)}}{G_{\text{rec}}^{(2)}} \left(1 + (R^{4,2} - R_{\text{rec}}^{4,2}) \left(\tau T - \frac{1}{2} \right)^2 + \dots \right), \quad (3.47)$$

then the relative magnitude of $G^{(2)}/G^{(0)}$ ($G^{(4)}/G^{(2)}$) from the measured correlator and the reconstructed correlator shown in Fig. 3.22 can be easily understood from Fig. 3.16 and Fig. 3.18.

A linear extrapolation of the results shown in Fig. 3.22 to $\tau T = 1/2$ can give the best estimate for the ratio of the thermal moments. However, due to the statistical errors on $G^{(4)}/G^{(2)}$ being relatively large, it is impossible to further constrain the fitting parameters shown in Table 3.1. Actually one could use a “cleaner” reference correlator, i.e. the free correlator G_{free} rather than the reconstructed correlator G_{rec} . As we have better knowledge of the free correlator G_{free} and its thermal moments it could be more practical to employ it at $2.93 T_c$ where presumably all the bound states are gone and the spectral function is close to the non-interacting case. However, there is still a big uncertainty of the quark mass to be used in the free theory. Thus it is more stable to utilize this way for investigating spectral properties of the light mesons where quark masses can be ignored [88, 89]. Nevertheless, we will provide the parameter we

have obtained in Table 3.1 into the default models for the MEM analysis of the vector channel at $1.46 T_c$.

3.7 Spectral functions above T_c

One has to note that the comparison of the measured correlator with the reconstructed correlator can only give a rough idea of the magnitude of any medium effects at a certain temperature. To really explore the properties of the charmonium states, one has to go to the spectral function level. Thus it is crucial to reconstruct the spectral function from the correlators using MEM. In this section we will study the spectral function at $T > T_c$. The basic settings of MEM are the same as what we mentioned at the beginning of section 3.4, if without additional description.

3.7.1 Default model dependences

At temperatures above T_c , the MEM analysis becomes harder, due to the limited number of points in the temporal direction. As has been done at temperatures below T_c , the default model dependence test is always the first thing we need to do. In principle one should put as much physical information into default models as possible. This rule leads to a very straightforward default model dependence test for the spectral functions above T_c . That is to fully benefit from the two limits which we already know quite well: the free lattice spectral function at very high temperature and the spectral function obtained from MEM at a temperature below T_c . To put these pieces of information into the default model, one might be able to check to which limit, free or confinement limit, the output spectral function is closer. However, due to the fact that below T_c the spectral function has a very sharp ground state peak and the quality of correlator data at temperature above T_c is not sufficient, the MEM output basically reproduces the below T_c spectral function with negligible changes. This inability of MEM is already known from mock data test shown in Fig. 3.5. Thus in the following default model dependence test we will not use the spectral function from below T_c as the default model but the free lattice spectral functions with some additional resonance peaks and/or transport peaks.

We first investigate the PS channel. The feature that there should not exist a zero mode contribution at all temperatures in this channel restricts the choices of default models. Hereby the policy to choose default models is: for the high frequency part, use the large ω part of the free lattice spectral function normalized to the small distance behavior of the correlation data; for the low frequency part, use the resonance peaks with peak locations smaller, equal or larger to the peak location of the spectral functions at temperatures below T_c . We show the default model dependence of the output spectral

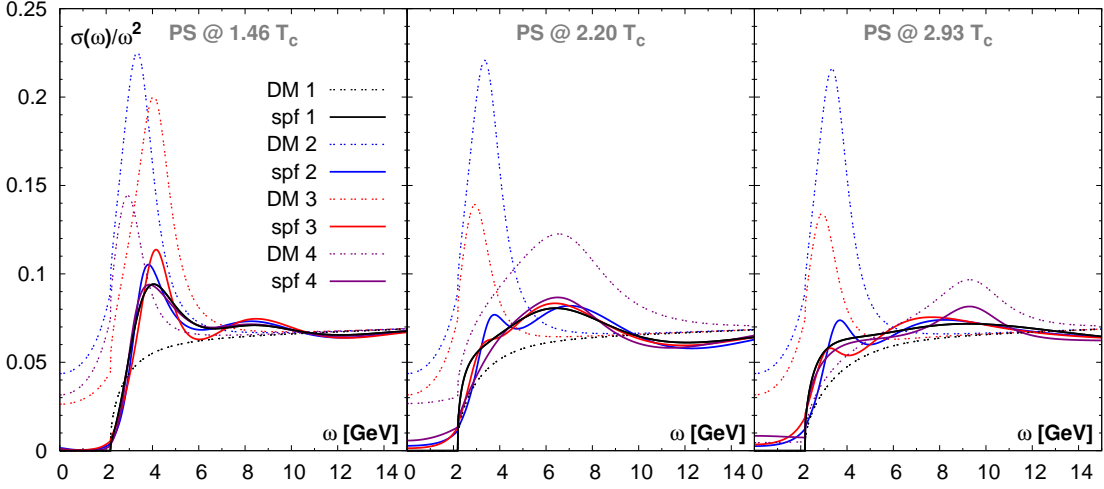


Figure 3.23. Default model dependences of spectral functions in the PS channel at temperatures above T_c . “DM”s are the input default models (dotted lines) while “spf”s are the corresponding MEM outputs (solid lines).

functions from MEM in Fig. 3.23 at the temperatures above T_c , i.e. $1.46 T_c$ (left), $2.20 T_c$ (middle) and $2.93 T_c$ (right). As before all the solid lines correspond to the output spectral functions and their corresponding input default models are dashed lines with the same colors. For all the three temperature analyses, “DM 1” is provided by the normalized free lattice spectral function, “DM 2” is provided by the normalized free lattice spectral function supplemented with a resonance peak with the same peak location as the spectral function at $T < T_c$, “DM 3” is provided by the normalized free lattice spectral function supplemented with a resonance peak whose peak location is smaller than that of the spectral function at $T < T_c$ and “DM 4” is the same as “DM 3” but with a resonance peak whose peak location is larger than that of the below T_c spectral function. “DM 3” and “DM 4” may vary from different temperatures with a relatively larger or smaller peak location/amplitude but the general feature mentioned above does not change. “spf”s are the corresponding MEM outputs. At all the three temperatures we find the output spectral functions are independent of the input default models, considering how big the difference is between the output spectral function and the input default model. At $1.46 T_c$ the location of the ground peak is shifted to higher energy and the width becomes larger compared to the case at $0.73 T_c$. We cannot make a conclusive statement about the dissolution of η_c here since the broadening of the peak and also the shift of the peak location might also be due to the melting of higher states or the enhancement of the continuum, which cannot be identified by using current techniques. When going to higher temperatures at $2.20 T_c$ the ground peak becomes

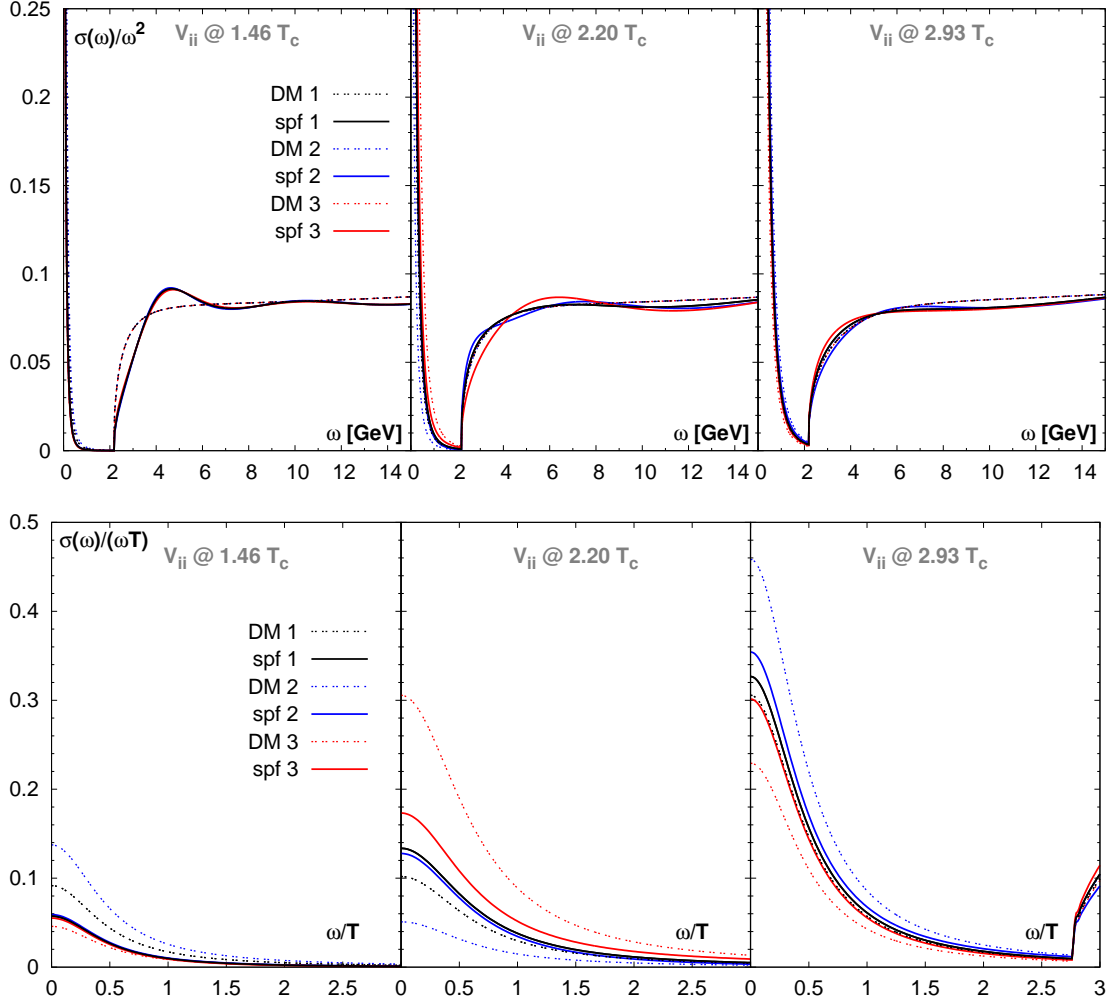


Figure 3.24. Default model dependences (varying the transport peak) of spectral functions in the V_{ii} channel at temperatures above T_c . At each temperature the very large ω part of the default model is fixed to the behavior of the free lattice spectral function. Upper panel: $\sigma(\omega, T)/\omega^2$ as a function of ω , Lower Panel: a blowup of plots in the upper panel in the very low frequency region and plotted as $\sigma(\omega, T)/(\omega T)$ versus ω/T . “DM”s are the input default models while “spf”s are the corresponding MEM outputs.

much broader and its location shifts to even higher energy, which indicates a larger thermal modification. At $2.93 T_c$ we cannot really see a peak and the output spectral functions are quite close to the free case. This could indicate all the PS states are melted at this temperature.

Let’s now move to the vector channel. Here we do the MEM analysis on the correlation function in the V_{ii} (spatial components summed only) channel. It is more complicated than the PS channel due to the presence of the zero mode contribution. In

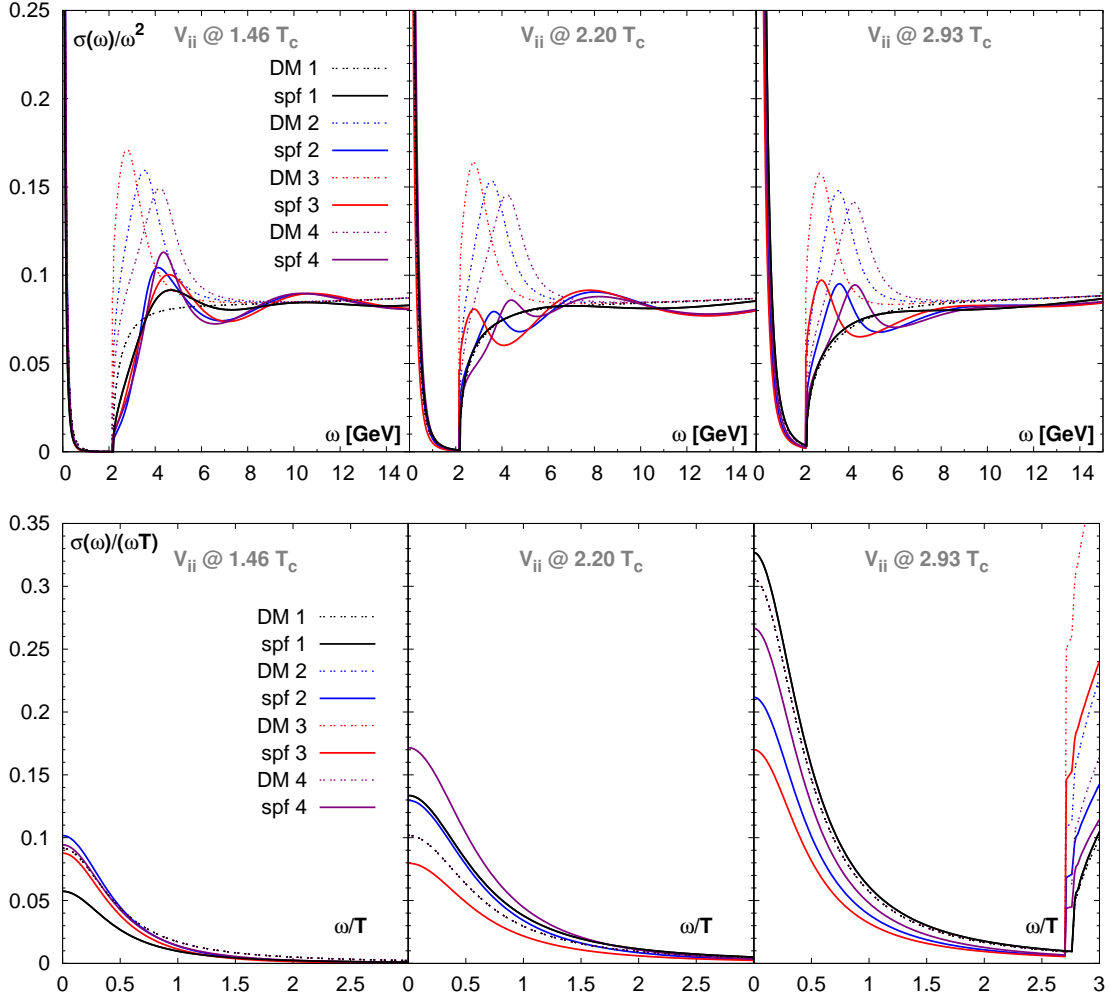


Figure 3.25. Default model dependences (varying the resonance part) of spectral functions in the V_{ii} channel at temperatures above T_c . The transport part of the default model is fixed in each temperature same as that of “DM 1”s in Fig. 3.24. Upper panel: $\sigma(\omega, T)/\omega^2$ as a function of ω , Lower Panel: a blowup of plots in the upper panel in the very low frequency region but plotted as $\sigma(\omega, T)/(\omega T)$ versus ω/T . “DM”s are the input default models while “spf”s are the corresponding MEM outputs.

other words, the physical information concerned with a single quark and one quark pair is all enclosed in the correlation function. Thus for the default model dependence test we first fix the large ω behavior of the default model by using the normalized free lattice spectral function and vary the information on the very low ω part, i.e. the transport peak in Eq. (3.19). We show the result in Fig. 3.24. The upper panel of Fig. 3.24 shows $\sigma(\omega, T)/\omega^2$ as a function of ω in a large ω region while the lower panel of Fig. 3.24 shows $\sigma(\omega, T)/(\omega T)$ as a function of ω/T in the low frequency region. “DM”s are the

input default models while “spf”s are the corresponding MEM outputs. At each temperature the width of the transport peak of the default models are fixed. In particular, the transport parts of “DM 1” in the MEM analysis at $1.46 T_c$ are parameterized as $DT = 0.49$ and $MD = 2.2$ obtained from Table 3.1. Looking at the output spectral functions at each temperature, we find the variation of the lower ω part of the default model gives negligible effects to the intermediate ω part (resonance part) of the output spectral functions. Concerning the temperature dependence of the resonance peak, the upper panel of Fig. 3.24 shows that, already at $1.46 T_c$, the ground state peak compared to that at $0.73 T_c$ (see Fig. 3.13) becomes much broader and is shifted to higher energy. When going to the higher temperature of $2.20 T_c$ one can hardly see a bump in the interesting ω region. At our highest temperature available, i.e. $2.93 T_c$, we find the large ω part more or less resembles the free lattice spectral function and no peak structure is observed. For the transport peak shown in the lower panel of Fig. 3.24, the output is strongly independent on the input default models. Note only the amplitudes of the transport peaks in the default models are changed in the current MEM analyses.

After studying the effects of variation of the transport peak in the default model on the output spectral function in the intermediate ω (resonance peak) region in Fig. 3.24, we now fix the very low frequency (transport peak) part of the default model and vary the intermediate ω (resonance part) behavior of the default models. The default models in the low frequency part are fixed to have the same low frequency behavior as “DM 1” in Fig. 3.24 at each temperature. For the intermediate frequency part we use the same policy as we did in the analysis of the PS channel. We test four different default models. “DM 1” is the normalized free spectral function with a transport peak, “DM 2” is the normalized free spectral function with a transport peak supplemented with a resonance peak whose peak location is same as that of the spectral function at $0.73 T_c$, “DM 3” and “DM 4” are basically the same as “DM 2” but with a resonance peak whose peak location is smaller and larger than that of the below T_c spectral function peak location, respectively. We show the default models and their corresponding output spectral functions (“spf”s) divided by ω^2 as functions of ω in the upper panel of Fig. 3.25. At $T = 1.46 T_c$ there is a minor default model dependence of the output spectral functions, but the trend is similar: the peak location is shifted to a location larger than the peak location of the spectral function at $0.73 T_c$ and also the width becomes larger. At $2.20 T_c$ the default model dependence is a little larger which should be due to the smaller number of data points in the temporal direction and lower statistics. But still, the outputs from MEM have unique differences from the input default models and they all have a trend to resemble the free spectral functions. At $2.93 T_c$ we have only 9 points in the analysis and together with the issue of the transport peak, the default model dependence is considerably larger than that in the analysis at the other temperatures.

Based on the results from 1.46 and $2.20 T_c$ we do not expect the peak location of the resonance peak at $2.93 T_c$ shifted to smaller energies compared to the case at $0.73 T_c$ and would rather expect that the spectral function at this temperature is much closer to the spectral function in the non-interacting case. In the lower panel of Fig. 3.25 we enlarge the very low frequency part of the upper panel in Fig. 3.25 and show $\sigma(\omega)/(\omega T)$ as a function of ω/T . Unlike the case in the lower panel of Fig. 3.24, the change of the default model in the intermediate ω part (resonance part) has a relatively large effect on the output in the low frequency region. Without the quantitative description of the transport peak we can observe a trend that the width of the transport peak becomes smaller with increasing temperature.

3.7.2 Systematic uncertainties and statistical errors

The systematic error includes the uncertainty from different lattice settings and also the number of points as well as the default models used in the MEM analysis.

First we will study the lattice spacing dependence of the output spectral function on our available lattices. We show the spectral function in the PS channel (left) and the V_{ii} channel (right) at temperatures below T_c from the lattices with $a^{-1} = 18.974$ GeV ($\beta = 7.793$, $128^3 \times 96$), $a^{-1} = 12.864$ GeV ($\beta = 7.457$, $128^3 \times 64$) and $a^{-1} = 6.432$ GeV ($\beta = 6.872$, $128^3 \times 32$) in Fig. 3.26. The improvement of output spectral functions can be truly seen with smaller lattice spacing. One can observe that with smaller lattice spacing the lattice cutoff effects can be well separated from the physically interesting frequency region. We find the width of the ground state peak becomes narrower with decreasing lattice spacing. We also find that the second peak should be lattice or MEM artifacts.

We always have to compare the spectral functions at $T > T_c$ to those at $T < T_c$ to check the thermal modification. As the number of points at higher temperatures is reduced, we need to study the dependence on the number of points used in the MEM analysis at $T < T_c$, i.e. use the same number of points below and above T_c to check whether there are deviations. We have studied the default model dependence before, so here we restrict the default model to have the behavior of the free lattice spectral function. At $T = 0.73 T_c$ we select the data points in the temporal direction as to start at $\tau_{min} = 4$ and be separated by a step length of $\Delta\tau$. For instance when $\Delta\tau = 2$ we select data points of $\tau = 4, 6, 8, \dots, 48$, in total 13 points. So the number of points used with $\Delta\tau = 2, 3, 4$ at $0.73 T_c$ correspond to the number points used at $1.46 T_c$, $2.20 T_c$ and $2.93 T_c$, respectively. We show the results in Fig. 3.27. ‘‘DM’’ labels the input default model and the other lines are the output spectral functions with different values of $\Delta\tau$. For both the PS spectral function (left) and the V_{ii} spectral function (right), in the interesting frequency region we observe negligible dependences on the

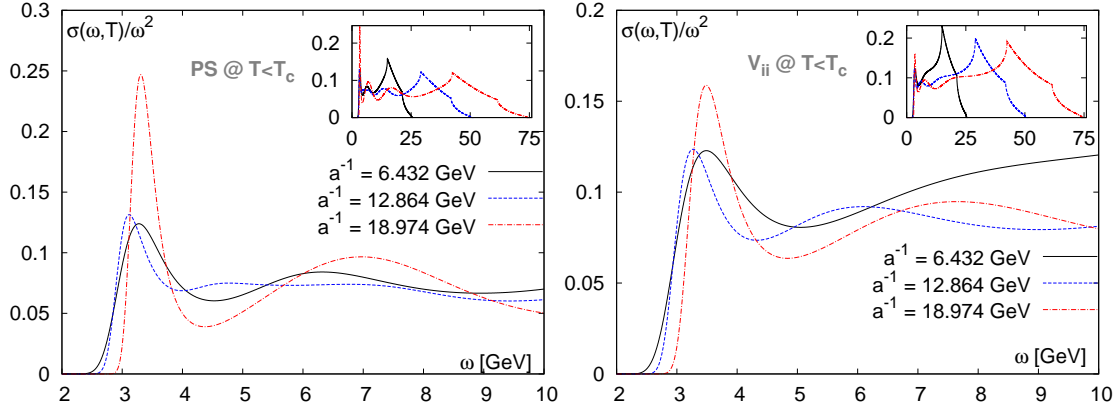


Figure 3.26. Output spectral functions from MEM in the PS (left) and the V_{ii} (right) channels at temperatures below T_c from three different lattices: $128^3 \times 32$ with $\beta = 6.872$ ($a^{-1} = 6.432$ GeV) at $0.74 T_c$, $128^3 \times 64$ with $\beta = 7.457$ ($a^{-1} = 12.864$ GeV) at $0.74 T_c$ and $128^3 \times 96$ with $\beta = 7.793$ ($a^{-1} = 18.974$ GeV) at $0.73 T_c$.

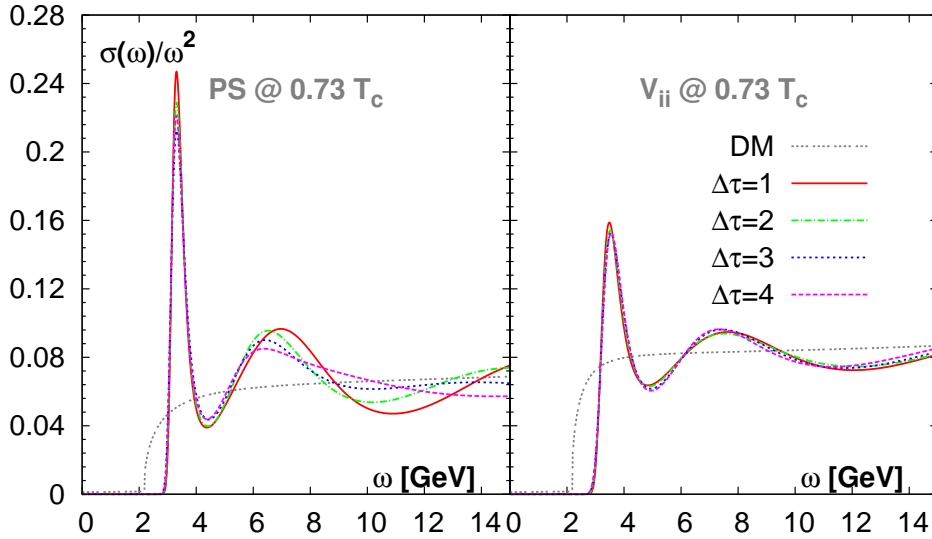


Figure 3.27. Dependence of the output spectral function on the number of points used in the MEM analysis at $T = 0.73 T_c$. The left plot is for the PS channel and the right one is for the V_{ii} channel. All the points included start at $\tau_{min} = 4$. $\Delta\tau$ is the step size between the neighboring data points selected. For instance, $\Delta\tau = 4$ means $\tau = 4, 8, 12, \dots, 48$ are used. “DM” labels the input default model and the other lines are the output spectral functions with different values of $\Delta\tau$.

number of data points used.

To remove the discretization effects, we normally omit some data points at very

small distances. However, it is not very certain that how many data points should be omitted. Thus we check the dependence on τ_{min} of the output spectral function. We vary τ_{min} to be 4, 7, 16, 24 and 36 at $0.73 T_c$ in the PS and V_{ii} channels to see the effects. The default models are fixed in each channel. They are free lattice spectral functions such that $G(\tau = 4)/G_{free}(\tau = 4) = 1$. The upper plot of Fig. 3.28 shows the results for the PS channel while the lower one shows the results for the V_{ii} channel. “DM” denotes default model used. “spf 1”, “spf 2”, “spf 3”, “spf 4” and “spf 5” are the output spectral functions from MEM corresponding to the analyses with $\tau_{min} = 4, 7, 16, 24$ and 36 . For both the PS and V_{ii} channels we observe that the large ω ($\omega \gtrsim 5$ GeV) behavior of the output spectral functions changes with τ_{min} and in the low ω region ($\omega \lesssim 5$ GeV) the peak location of the ground state peak stays unchanged even with $\tau_{min} = 36$. Thus the τ_{min} dependence of the spectral function in the PS and V_{ii} channels in the interesting frequency region is very small at $T < T_c$ on our finest lattice.

We also investigate the default model (induced by the quark mass in the free lattice spectral function) and the τ_{min} dependence of the output spectral function in the PS and V_{ii} channels at $T > T_c$. At higher temperatures the number of points available in the analysis is reduced and we have in total 32, 24 and 12 points at $1.46 T_c$, $2.20 T_c$ and $2.93 T_c$, respectively. Thus we test the value of $\tau_{min} = 4, 7$, and 10 at $1.46 T_c$ and $\tau_{min} = 4, 6$, and 7 at both $2.20 T_c$ and $2.93 T_c$.

We first show τ_{min} dependence of the output spectral function in the PS channel at $T = 1.46, 2.20$ and $2.93 T_c$. The results are shown in the upper plot of Fig 3.29. As in the case of Fig. 3.28 the default models at each temperature are fixed such that $G(\tau = 4, T)/G_{free}(\tau = 4) = 1$. “spf”s are the output spectral functions from MEM with different values of τ_{min} . For the three temperatures above T_c the outputs have a minor dependence on the value of τ_{min} .

Due to the insensitivity of MEM on the very large ω behavior of the spectral function, as we observed from, e.g. the left panel of Fig. 3.13, the outputs always reproduce the very large ω behavior of the input default models, which in our case normally is the free lattice spectral function multiplied by a certain constant to reproduce the value of $G(\tau_{min})$. However, we don’t really know the exact behavior of the large ω part. We thus check the effects caused by using the free lattice spectral functions with different quark masses in the default models. The different quark masses am have an effect on the threshold and the structure of the free spectral function as discussed in section 2.3.2. The results for the PS channel at $T > T_c$ are shown in the lower panel of Fig. 3.29. Here we test with free lattice spectral functions having $am = 0.06^6$ (“DM 1”), $am = 0.04$ (“DM 2”) and $am = 0.02$ (“DM 3”) such that $G(\tau = 4, T)/G_{free}(\tau = 4) = 1$. At $1.46 T_c$ the ground state peak structure is quite independent of the default models. At both

⁶ $am = 0.06$ is the quark mass obtained from the running quark mass on the lattice (see Table 1.2).

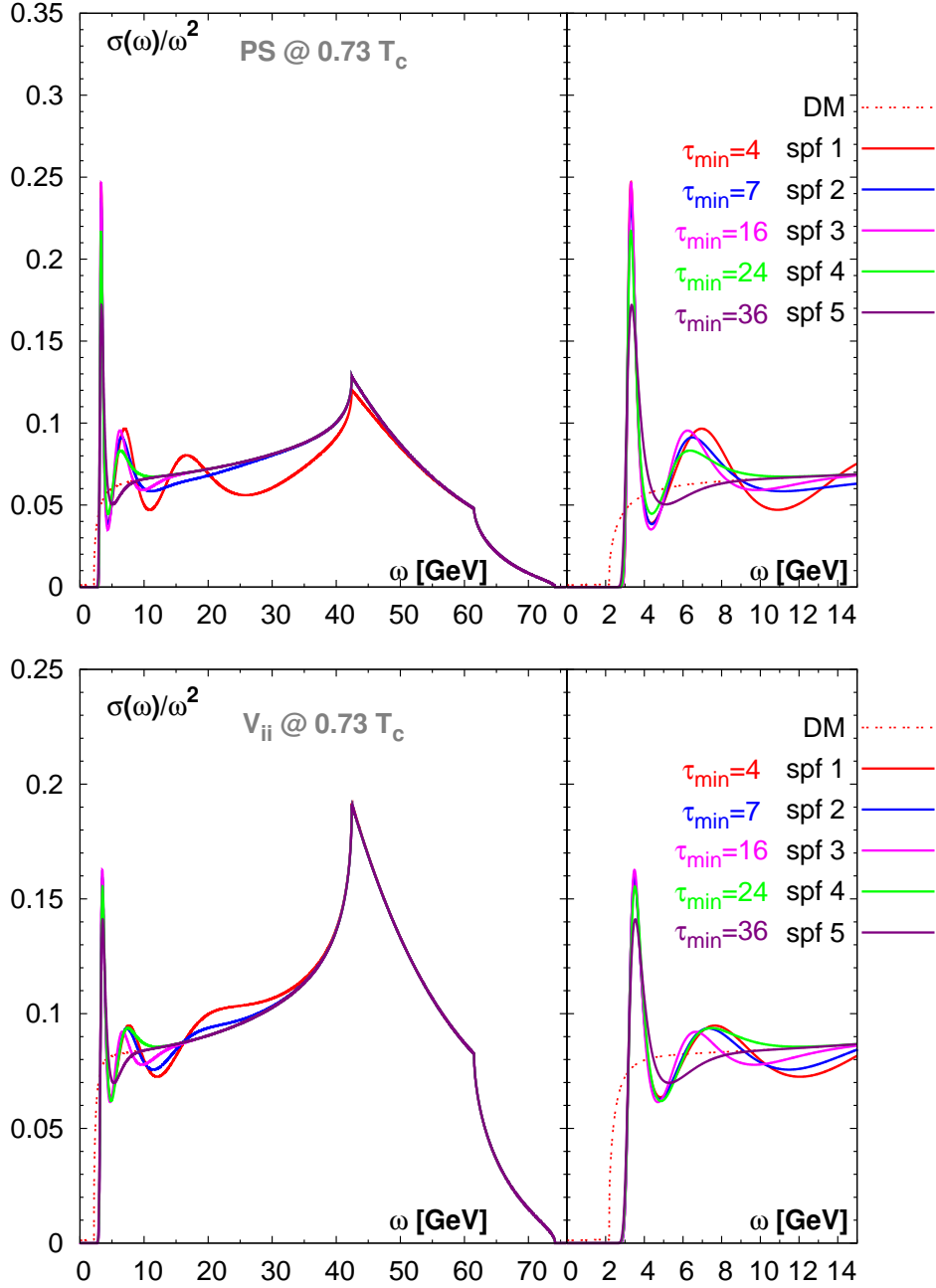


Figure 3.28. The τ_{min} dependence of the output spectral functions at $T = 0.73 T_c$ on our finest lattice of $128^3 \times 96$. The upper plot shows the results in the PS channel while the lower one shows the result in the V_{ii} channel. In each plot, the right panel is a blowup of the left panel. The default models are the same in each plot, which is labeled by “DM”. “spf 1”, “spf 2”, “spf 3”, “spf 4” and “spf 5” are the output spectral functions from MEM with $\tau_{min} = 4, 7, 16, 24$ and 36 , respectively.

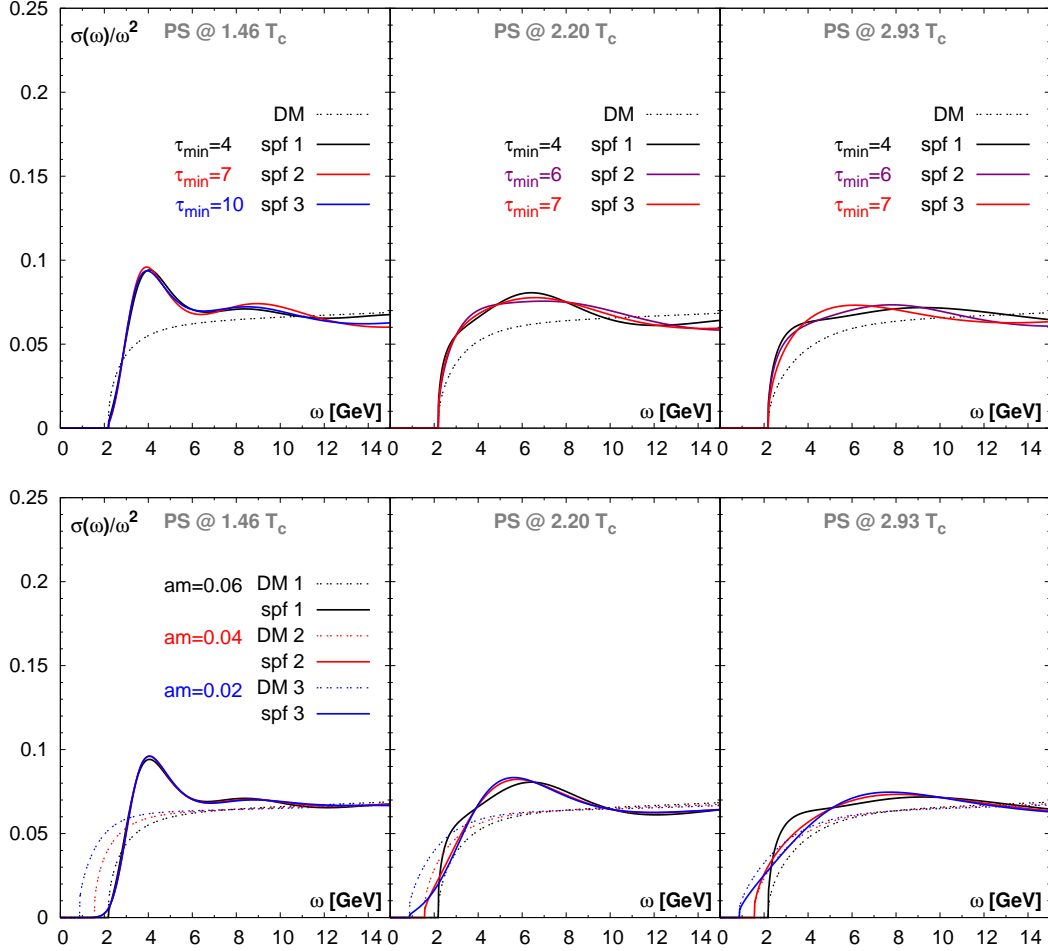


Figure 3.29. The τ_{min} (upper plot) and am (lower plot) dependences of the output spectral functions in the PS channel at $T > T_c$.

At $2.20 T_c$ and $2.93 T_c$ the output spectral function starts to be non-vanishing at the point where the default model starts to be non-zero, i.e. the rising side of the first bump of the output spectral function changes with the default model while the decreasing side has minor changes. Together with the default model test done in Fig. 3.23, the lower panel of Fig. 3.29 indicates a small dependence of the output spectral function in the PS channel at $T > T_c$ on the am parameter of the free lattice spectral function.

We did the same exercise in the analysis for the V_{ii} channel to check the effects of τ_{min} and am . The case of the V_{ii} channel becomes more complicated due to the presence of the transport contributions. We show the results for the dependence of the output spectral function on τ_{min} in Fig. 3.30. The upper panel shows $\sigma(\omega)/\omega^2$ as a function of ω at three available temperatures above T_c while the lower panel focuses on the transport behavior of the spectral function in the low frequency region and

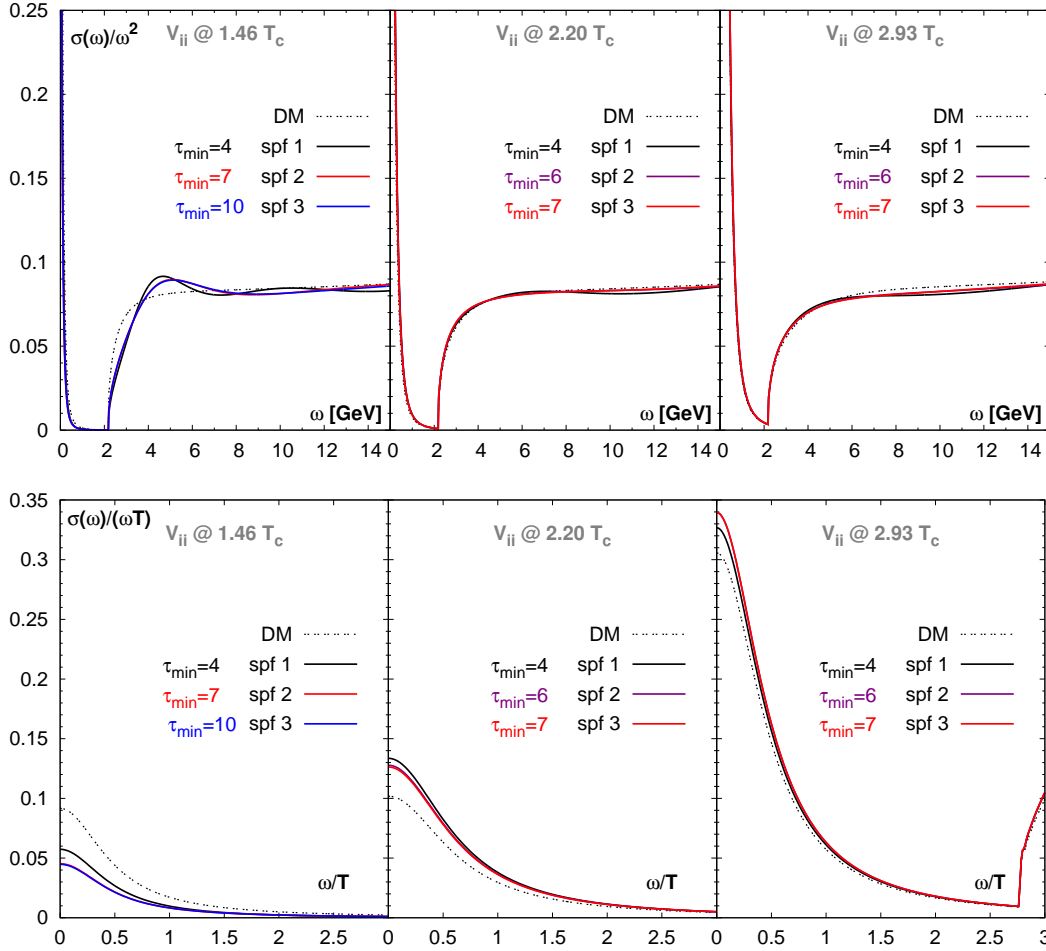


Figure 3.30. The τ_{min} dependence of the output spectral functions in the V_{ii} channel at $T > T_c$. The upper plot shows the behavior of $\sigma(\omega)/\omega^2$ as a function of ω while the lower plot shows the transport behavior of $\sigma(\omega)/(\omega T)$ as a function of ω/T which corresponds to the divergent parts in the upper plot at the corresponding temperatures.

has $\sigma(\omega)/(\omega T)$ as function of ω/T . The default models (“DM”) are the same in the whole frequency region at each temperature. “DM” is provided by the normalized free lattice spectral function and an additional transport peak. “DM” is also the same as “DM 1” in Fig. 3.24 at each temperature. As seen from the upper plot of Fig. 3.30, at $1.46 T_c$, from $\tau_{min} = 4$ to $\tau_{min} = 7$ and 10 , the peak location of the ground peak seems to move a little further to larger energy, however at both $2.20 T_c$ and $2.93 T_c$ the output spectral functions show negligible changes due to the variation of $\tau_{min} = 4, 6$, and 7 . In the lower panel of Fig. 3.30 the very low frequency behavior of the spectral function is shown. Note “DM” in the current frequency region are also the same at each temperature. At all three temperatures the output transport peaks show minor

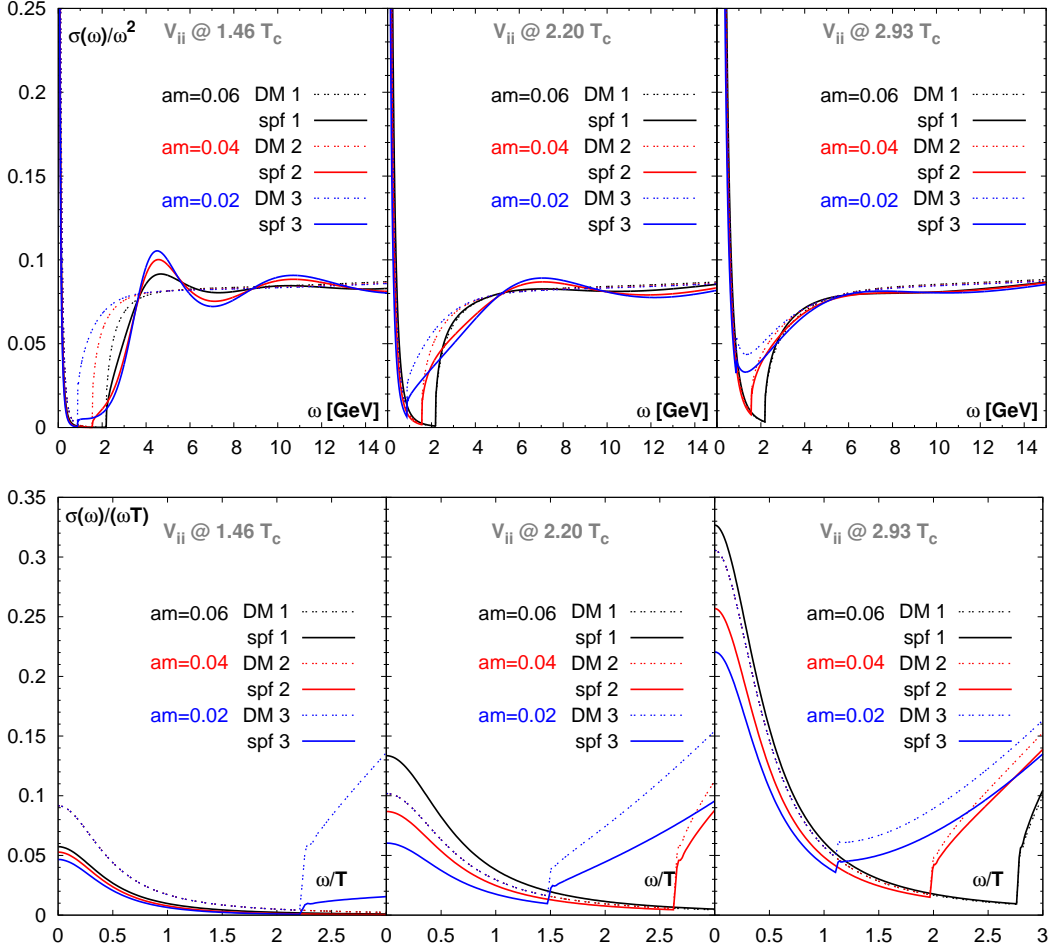


Figure 3.31. The am dependence of the output spectral functions in the V_{ii} channel at $T > T_c$. The upper plot shows the behavior of $\sigma(\omega)/\omega^2$ as a function of ω while the lower plot shows the transport behavior of $\sigma(\omega)/(\omega T)$ as function of ω/T which corresponds to the divergent parts in the upper plot at the corresponding temperatures.

dependences on τ_{min} .

In Fig. 3.31 we show the dependence of the output spectral function in the V_{ii} channel on am at $T > T_c$. The upper panel of Fig. 3.31 shows the large ω behavior of the spectral function and the lower panel highlights the transport peak. “DM 1” here is the same as “DM 1” in Fig. 3.30. Unlike the case in the PS channel, the rising side of the ground state peak starts to be non-zero following the trend the default model already at $1.46 T_c$ and the amplitude of the ground state peak also changes with different values of am . However, the peak location of the ground peak remains almost the same. At $2.20 T_c$, the output spectral functions “spf 2” and “spf 3” from the default models “DM 2” ($am = 0.04$) and “DM 3” ($am = 0.02$) have a small bump structure other than “spf

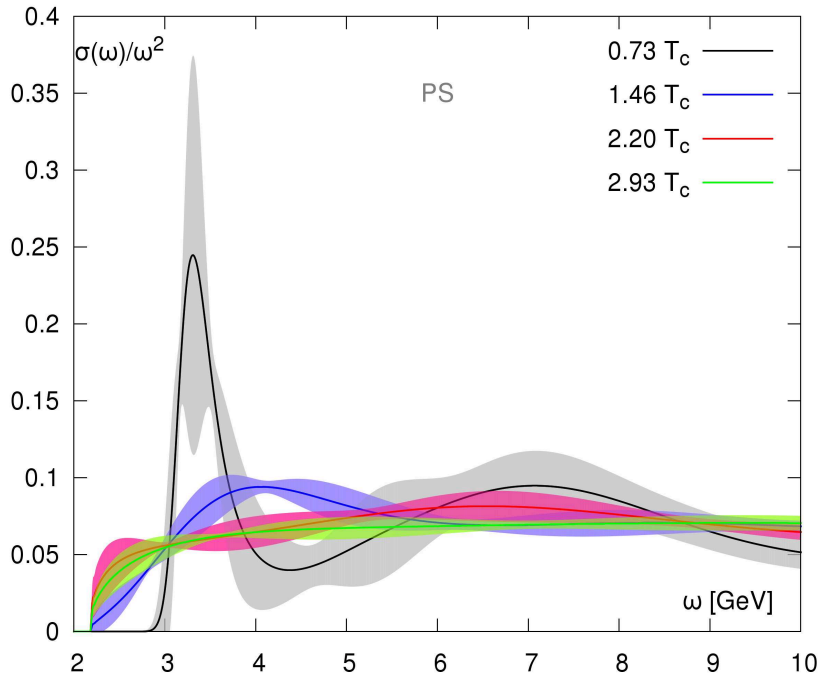


Figure 3.32. The statistical errors for the output spectral functions in the PS channel at all available temperatures on our finest lattice with $\beta = 7.793$. The shaded areas are the errors of the output spectral function. The mean values are the solid lines inside the shaded areas.

1”. At $2.93 T_c$, “spf 1”, “spf 2” and “spf 3” have negligible differences when $\omega \gtrsim 3$ GeV. As seen from the lower panel of Fig. 3.31, with decreasing am , the transport peak’s amplitude becomes smaller and its width becomes larger at all the three temperatures. At $1.46 T_c$ the change of the transport peak of “spf 1” is very small, and when going to higher temperatures the deviations become larger, probably as a consequence of the bigger differences of “spf”s in the frequency region of $1 \lesssim \omega \lesssim 7$ GeV.

After checking the systematic uncertainties we now analyze the statistical errors. The statistical error is obtained from the Jackknife method. In this analysis we fix the default model as “DM 1” in the PS and V_{ii} channels at each temperature shown in the above figures. Quite often statistical errors are given on $\sigma(\omega)$ over a certain ω region in the spectral function plot [37–41], but it is not so straightforward to get a feeling of how big the error is on the spectral function itself. Here we rather calculate the Jackknife error on each point of the spectral function and show them in Fig. 3.32 for the PS channel and in Fig. 3.33 for the V_{ii} channel.

From Fig. 3.32 one can see that at $0.73 T_c$ the spectral function in the PS channel has large uncertainties in the amplitude at the point which corresponds to the ground state peak location in the mean spectral function. However, even at the lower end of the error

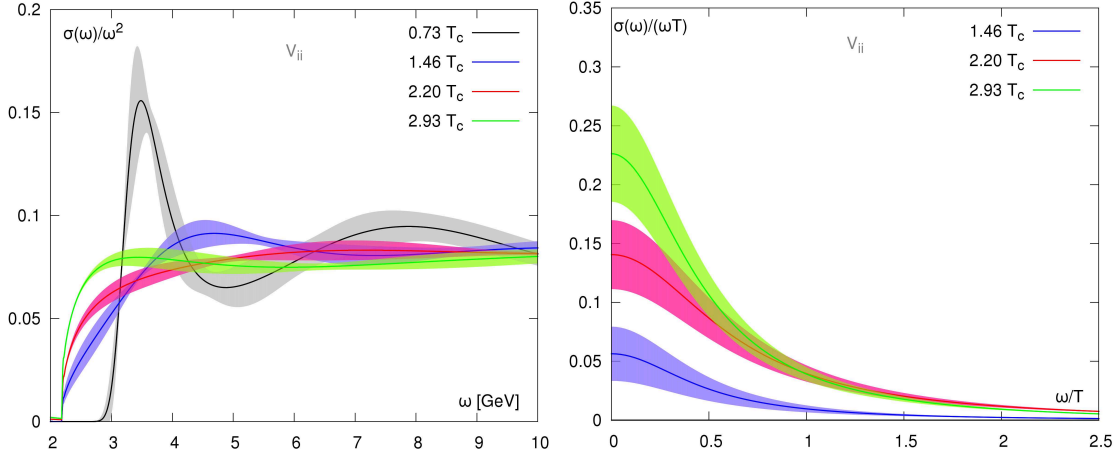


Figure 3.33. The statistical errors for the output spectral functions in the V_{ii} channel at all available temperatures on our finest lattice with $\beta = 7.793$. The left plot is for the large ω region and shows $\sigma(\omega)/\omega^2$ as a function of ω , while the right plot is for the low frequency region and shows $\sigma(\omega)/(\omega T)$ as a function of ω/T . The shaded areas are the errors of the output spectral function. The mean values are the solid lines inside the shaded areas.

bar, the amplitude is still larger than the peak amplitudes at the higher temperatures within the errors. The peak location of the ground state peak at $0.73 T_c$ might be shifted to a lower energy of $\omega \approx 3$ GeV or to a higher energy at $\omega \approx 3.6$ GeV. In the latter case, the peak location would have the same peak location as the spectral function at $1.46 T_c$ but with a much larger amplitude and smaller width. At $2.23 T_c$ there is hardly a peak structure within the statistical errors. At $2.93 T_c$ the spectral function flattens. Thus this picture and together with the systematic uncertainties studied suggest η_c is “partly” melted at $1.46 T_c$ and dissolves at higher temperatures.

In the left plot of Fig. 3.33, we focus on the resonance part of the spectral function in the V_{ii} channel. One sees that the peak location of the spectral function at $0.73 T_c$ does not have an overlap with the peak location of the spectral function at $1.46 T_c$. The amplitudes between these two differs a lot. At both $2.20 T_c$ and $2.93 T_c$ there are hardly any peak structures and at $2.93 T_c$ the spectral function is flattened. Together with the systematic uncertainty study we have done before, this picture indicates J/ψ is already melted at $1.46 T_c$.

The statistical uncertainties of the transport peaks are shown in the right plot of Fig. 3.33. The amplitude of the transport peak at $\omega = 0$ gives the value of the heavy quark diffusion constant. The uncertainties of both, amplitudes and widths of the peak, are relatively small. Recall Eq. (2.46) and with the quark number susceptibility from Fig. 3.20, we get DT of 0.28 ± 0.12 , 0.314 ± 0.065 and 0.358 ± 0.065 at $1.46 T_c$, $2.20 T_c$

and $2.93 T_c$, respectively. The result at $1.46 T_c$ is slightly smaller than the estimation in Table 3.1. This indicates that the *Ansatz* used in section 3.6 might be too simple.

For a short summary of the spectral analysis on the fate of the bound states in the PS and V_{ii} channels, our results suggest that η_c starts to dissolve at $1.46 T_c$ and does not exist when going to higher temperature at $T = 2.20 T_c$, and that J/ψ is already melted at $1.46 T_c$.

Chapter 4

Analysis of charmonium properties at non-zero momentum

4.1 Screening mass and dispersion relation

Since at finite temperature the temporal extent is always restricted by $1/2T$ we also compute the spatial correlation functions in the z direction. Here we plot the effective mass $m_{\text{eff}}(z)$ from the relation

$$\frac{G(z, T)}{G(z + 1, T)} = \frac{\cosh [m_{\text{eff}}(z)(\frac{N_z}{2} - z)]}{\cosh [m_{\text{eff}}(z)(\frac{N_z}{2} - z - 1)]} \quad (4.1)$$

At finite temperature the Lorentz symmetry is lost due to the temporal direction being distinguished as the direction of the four-velocity of the heat bath. Consequently, unlike the zero temperature case where it depends on the Lorentz invariant scalar p^2 , at finite temperature the spectral density will depend on temporal and spatial components of p separately. At temperatures below T_c , however, the spectrum will still consist of particle excitations, their dispersion relations might be more complicated and reflect the breaking of Lorentzian invariance. The spectral density is assumed to have the form

$$\sigma(p_0, \mathbf{p}) = 2\pi \theta(p_0) \delta(p_0^2 - \omega^2(\mathbf{p}, T)), \quad (4.2)$$

with

$$\omega^2(\mathbf{p}, T) = m^2 + \mathbf{p}^2 + \Pi(\mathbf{p}, T), \quad (4.3)$$

containing the temperature dependent vacuum polarization tensor $\Pi(\mathbf{p}, T)$. Assuming the temperature effects can be absorbed into a temperature dependent mass $m(T)$ and a coefficient $A(T)$ which might also be temperature dependent and different from unity, the dispersion relation can be written as

$$\omega^2(\mathbf{p}, T) \simeq m^2(T) + A^2(T) \mathbf{p}^2. \quad (4.4)$$

Such an approximation might hold at least at small temperatures. Evaluating correlation functions from the spectral function (4.2) at zero momentum and together with relation (4.4) one finds the temporal correlator exponentially decays with the so-called pole mass $m(T)$

$$G(\tau, \mathbf{p} = 0) \sim \exp(-m(T) \tau), \quad (4.5)$$

while the spatial correlator exponentially decays with the screening mass $m_{sc}(T)$

$$G(z, \mathbf{p}_\perp, p_4 = 0) \sim \exp(-m_{sc}(T) z). \quad (4.6)$$

with $m_{sc}(T) = m(T)/A(T)$. At zero temperature $A(T=0)=1$ and the screening mass is the same as the pole mass; temperature effects come into play and the screening mass will differ from the pole mass when $A(T) \neq 1$. At non-zero “momentum” ($\mathbf{p}_\perp \parallel p_4 \neq 0$), the spatial correlator is described by E_{sc}

$$G(z, \mathbf{p}_\perp, \omega_n) \sim \exp(-E_{sc} z), \quad (4.7)$$

following the assumption made in relation (4.4) E_{sc} reads

$$E_{sc}^2 = \mathbf{p}_\perp^2 + \frac{\omega_n^2}{A^2} + m_{sc}^2, \quad (4.8)$$

where $\omega_n = 2\pi nT$ are the Matsubara frequencies. It is worth noting that the above relation is the continuum dispersion relation.

In the free limit the decay of the spatial correlator at large distances is dominated by two times the lowest quark Matsubara frequency $\tilde{\omega}_n = (2n+1)\pi T$ [], thus the screening mass of a meson at non-vanishing momentum \mathbf{p}_\perp m_H^{free} in the free limit can be written as

$$m_H = \sqrt{m_q^2 + \tilde{\omega}_0^2} + \sqrt{m_q^2 + \tilde{\omega}_0^2 + \mathbf{p}_\perp^2}, \quad (4.9)$$

By showing the dispersion relation at $T < T_c$ compared with the relation (4.8) one may be able to get a feeling of how large the pole mass differs from the screening mass. Comparing the dispersion relation with the relation (4.9) could also shed some light on to which degree the interacting system is close to a system of free quarks at $T > T_c$.

We first show the dispersion relation of the screening mass in the PS channel in Fig. 4.1. The results are obtained from $128^3 \times N_\tau$ lattices at $0.74 T_c$ ($N_\tau = 64$) and at $1.49 T_c$ ($N_\tau = 32$) with $a^{-1} = 12.864$ GeV. “dir” denotes whether spatial (“dir x”) or temporal (“dir τ ”) directions are used. The lines denote the dispersion relation obtained by fitting with an *Ansatz* of $E_{sc}^2(p) = ap^2 + b$. At $0.75 T_c$, for the results from the spatial directions, we have a good fit with parameters $a=1.02 \pm 0.01$ and $b=9.530 \pm 0.013$. The applicability of the *Ansatz* $ap^2 + b$ indicates our lattice is very close to the continuum limit; for the results from the temporal direction, even though we only have 3 data points, at this temperature, the data points have the same behavior as that

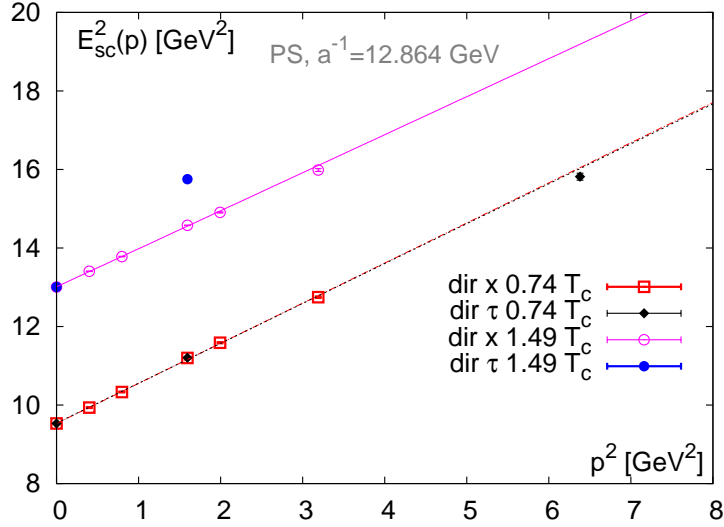


Figure 4.1. The dispersion relation of the screening mass in the PS channel obtained from lattice with $\beta = 7.457$. In the figure, “dir” labels whether spatial (“dir x”) or temporal components (“dir τ ”) of (p_x, p_y, p_t) were chosen. The lines denote the dispersion relation obtained by fitting with the form of Eq. (4.8).

from the spatial direction. We also performed a χ^2 fit and obtained $a=1.01\pm 0.03$ and $b=9.539\pm 0.033$. The slope parameter a here is an analogy of A^{-2} in Eq. (4.8). The proximity of a to 1 indicates the screening mass is a good approximation of the pole mass at $0.74 T_c$. When going to the higher temperature of $1.49 T_c$, the data point from the temporal direction jumps out of the fitting line of the results from spatial directions. Thus, the temporal direction is distinguished from the spatial direction and the breaking of Lorentz symmetry is clearly observed at this temperature.

We then show the dispersion relation of the screening mass in the PS channel on our finest lattice in the left plot of Fig. 4.2. The “momenta” here are chosen to be non-vanishing in the spatial components. With increasing temperature the value of E_{sc}^2 also increases as expected. In the very high temperature limit, $E_{sc}^2(\mathbf{p}_\perp)$ should behave according to Eq. (4.9). However, as shown in the right plot of Fig. 4.2, the curvature of the free case is quite similar to that of the $T=0$ case. Thus it is hardly possible to tell at which temperature the correlator is closer to free from the investigation of the dispersion relation.

4.2 Longitudinal and transverse correlation function

In Table 4.1, we list all the available momenta of the temporal correlation function simulated on our lattice. As indicated in section 2.4, one expects distinct differences

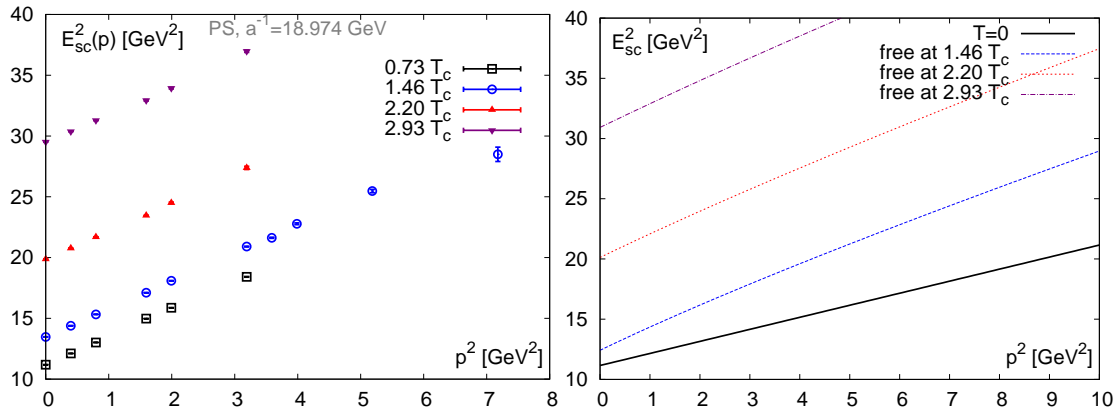


Figure 4.2. Left: The dispersion relation of the screening mass in the PS channel at $0.73 T_c$, $1.46 T_c$, $2.20 T_c$ and $2.93 T_c$ with lattice spacing $a^{-1} = 18.974$ GeV. The momenta are chosen only from spatial directions. Right: The dispersion relation of the screening mass in the PS channel in the free theory (Eq. 4.9) together with the case of $T = 0$.

$\mathbf{p}L/(2\pi)$	$ \mathbf{p} L/(2\pi)$	Longitudinal	Transverse
(0,0,0)	0	-	-
(0,0,1)	1	V_{33}	V_{11} & V_{22}
(0,0,2)	2	V_{33}	V_{11} & V_{22}
(0,0,3)	3	V_{33}	V_{11} & V_{22}
(1,0,0)	1	V_{11}	V_{22} & V_{33}
(1,1,0)	$\sqrt{2}$	-	V_{33}
(2,0,0)	2	V_{11}	V_{22} & V_{33}
(2,1,0)	$\sqrt{5}$	-	V_{33}
(2,2,0)	$2\sqrt{2}$	-	V_{33}

Table 4.1. A list of the momenta $\mathbf{p} = (p_x, p_y, p_z)$ of the temporal correlation function simulated on our lattices. L is the spatial size of the lattice and can be read from Table 1.1. The longitudinal and transverse components of the vector current, $V_{ii} = \bar{q}\gamma^i q$, are also listed in the third and the fourth column, respectively.

between the longitudinal and the transverse correlation functions. In Fig. 4.3, we show both the longitudinal and transverse correlators $G_{L,T}$ normalized by the averaged correlation function $G_{AVE} = (G_L + 2G_T)/3$ for momenta $\tilde{p} = |\mathbf{p}|L/(2\pi) = 1, 2, 3$. The data are obtained from the lattice of $128^3 \times 48$ with $\beta = 7.793$ at $1.46 T_c$. We find clear differences between the longitudinal and transverse correlators: the longitudinal correlator is always larger than the transverse one. Both, the longitudinal and the trans-

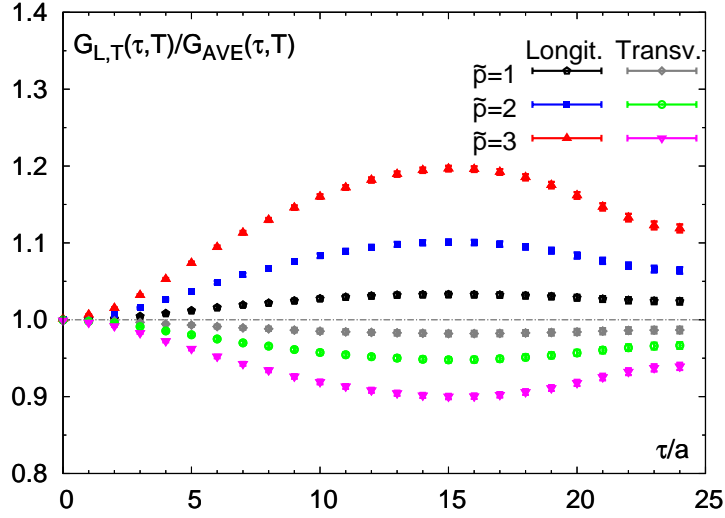


Figure 4.3. Longitudinal and transverse vector correlation functions normalized by the average correlation function, $G_{AVE}(\tau, T, \mathbf{p}) = (G_L(\tau, T, \mathbf{p}) + 2G_T(\tau, T, \mathbf{p}))/3$. The momenta are chosen as $\tilde{p} = |\mathbf{p}|L/(2\pi) = 1, 2, 3$. The grey dot-dashed line labels unity in order to guide eye. The data are obtained from a lattice of size $128^3 \times 48$ with $\beta = 7.793$ at $1.46 T_c$.

verse correlator, deviate from unity further with increasing momenta but in opposite directions.

At the spectral function level, as predicted in Ref. [149] with non-vanishing momenta the longitudinal vector spectral function $\sigma_L(\omega, \mathbf{p})/\omega$ goes to zero at $\omega = 0$ while the transverse vector spectral function $\sigma_T(\omega, \mathbf{p})/\omega$ has a non-zero value at $\omega = 0$. It would be very interesting to understand this feature at the spectral function level, which connects to the transport properties of the heavy quark. The longitudinal and transverse vector spectral function have been investigated very recently in Ref. [156], whose authors found a contradiction between the small ω behavior of the transverse vector spectral function from their lattice data and the prediction made in Ref. [149]. This controversial finding is still under scrutiny and requires further study.

4.3 The reconstructed correlators

Like the case in the zero momentum, we also construct the reconstructed correlator at finite momentum through relation (2.53).

In Fig. 4.4, we show ratios of measured correlators to reconstructed correlators in the PS channel at $T > T_c$ on our finest lattice with spatial extent $L = 1.33$ fm. The momenta are chosen from spatial direction only and $\tilde{p} = |\mathbf{p}|L/(2\pi) = 1, 2$, and 3 . We find G/G_{rec} increases with increasing momentum at all temperatures. This finding

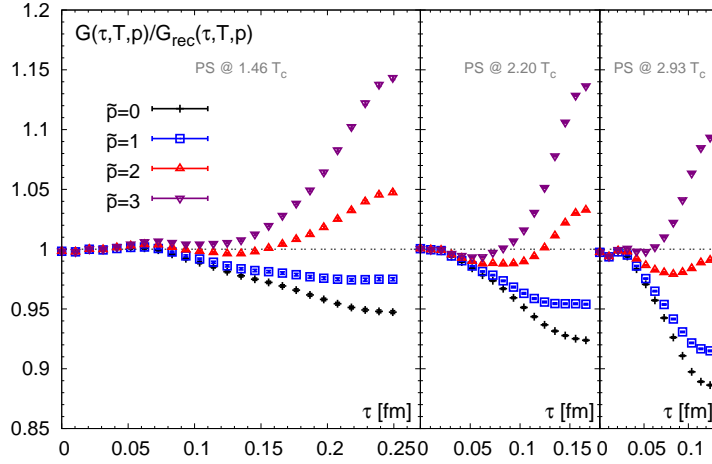


Figure 4.4. The ratios of $G(\tau, T, \mathbf{p})/G_{\text{rec}}(\tau, T, \mathbf{p})$ versus τ at $T > T_c$ varying $\tilde{p} = |\mathbf{p}|L/(2\pi) = 1, 2$ and 3 on our finest lattice with spatial extent $L = 1.33$ fm. The reconstructed correlators G_{rec} are evaluated from the measured lattice correlators at $0.73 T_c$. The grey short-dashed line labels unity in order to guide eye.

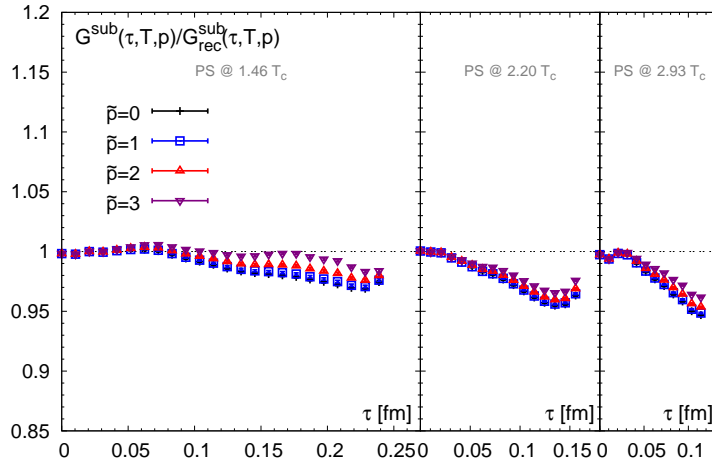


Figure 4.5. The ratios of $G^{\text{sub}}(\tau, T, \mathbf{p})/G_{\text{rec}}^{\text{sub}}(\tau, T, \mathbf{p})$ versus τ at $T > T_c$ varying $\tilde{p} = |\mathbf{p}|L/(2\pi) = 1, 2,$ and 3 on our finest lattice with spatial extent $L = 1.33$ fm. The reconstructed correlators G_{rec} are evaluated from the measured lattice correlators at $0.73 T_c$. The grey short-dashed line labels unity in order to guide eye.

is qualitatively comparable to the results in Ref. [40, 152]. The different temperature dependence of G/G_{rec} in the zero momentum and non-zero momenta cases might be due to different temperature dependent contributions from the frequency part below the light cone in the spectral function. As these low frequency contributions lead to

contributions to the correlator which are nearly constant or have a small curvature, thus we plot midpoint subtracted ratios $G^{\text{sub}}/G_{\text{rec}}^{\text{sub}}$ in the PS channel in Fig. 4.5 to suppress these contributions. We find that the momentum dependences of $G^{\text{sub}}/G_{\text{rec}}^{\text{sub}}$ at each temperature above T_c are very similar. At $T = 2.20$ and $2.93 T_c$, since the bound states may already dissolve, it is more likely that different momentum dependences of G/G_{rec} seen in Fig. 4.4 are due to the contribution of the very low frequency part of the spectral function. To make conclusive statements of this, one has to go to the spectral function level, which needs further research.

Conclusion and outlook

In this thesis, we have investigated the properties of charmonium states at finite temperature in quenched QCD on isotropic lattices. The standard Wilson plaquette action for the gauge field and the non-perturbatively $\mathcal{O}(a)$ improved clover fermion action for charm quarks are implemented in the simulation. In our investigations we used a variety of different lattice spacings to control cut-off effects in the charmonium correlators and spectral functions. In particular, our finest lattices have a very small lattice spacing, i.e. $a = 0.01$ fm. Using the Maximum Entropy Method we have reconstructed the spectral functions both at $T < T_c$ and $T > T_c$. Since the temporal extent is a very important ingredient in the spectral analysis, we measured charmonium correlators on our finest lattices with a relative large size of $128^3 \times 96$, $128^3 \times 48$, $128^3 \times 32$ and $128^3 \times 24$ at $0.73 T_c$, $1.46 T_c$, $2.20 T_c$ and $2.93 T_c$, respectively.

The MEM analyses of charmonium spectral functions have been done very carefully. We utilized the improved integrand kernel to avoid the instability of MEM at very low frequency. The number of points in the accessible frequency interval is set to 8000 in order to give a relative continuous picture of the spectral function. We studied the changes of the output spectral functions when using various default models both below and above T_c . We also checked the dependence of the output spectral functions on the number of data points used in the MEM analysis, in particular we compared the spectral functions at $T > T_c$ and $T < T_c$ reconstructed by using the same number of data points. We estimated statistical errors of the spectral functions as well. The statistical errors are obtained using the Jackknife method and are calculated on every point of the extracted spectral function.

The main physics results of this thesis are summarized as follows:

- At $T < T_c$, we found stable and reliable ground state peaks of both J/ψ and η_c , whose peak locations correspond to their physical masses. At temperatures below T_c , there are no zero mode contributions found in these two channels.
- At $T > T_c$ in the pseudo scalar channel, we observed that the spectral function in this channel at $T = 1.46 T_c$ might have a small overlap with the one at $T < T_c$ within the statistical uncertainties. At both $T = 2.20 T_c$ and $T = 2.93 T_c$, the

spectral functions are distinct from that at $T < T_c$. Our analysis suggests that η_c starts to dissolve at $1.46 T_c$ and does not exist when going to higher temperatures.

- At $T > T_c$ in the vector channel, we observed that vector spectral functions at $T > T_c$ are always distinct from that at $T < T_c$. Our analysis suggests that J/ψ is melted already at $1.46 T_c$. We also identified the transport peak in the vector channel at the spectral function level for the first time. As estimations for the diffusion constant, we obtained DT to be 0.28 ± 0.12 , 0.314 ± 0.065 and 0.358 ± 0.065 at $1.46 T_c$, $2.20 T_c$ and $2.93 T_c$, respectively.

Beside the main results we mentioned before, we found a very useful relation to calculate the reconstructed correlator at T directly from the measured correlator at lower temperature T' without knowing the spectral function at T' . We introduced variants of the Maximum Entropy Method to suppress the zero mode contribution. We also introduced the extended Maximum Entropy Method, which is able to deal with negative spectral functions, to the lattice QCD field for the first time.

There are also quite a lot of interesting things related to this work worth to do in the near future. Some of them are listed as follows

1. Since the correlator data in the scalar and axial vector channels are relatively noisier than that in the pseudo scalar and vector, we didn't include the analysis of these two channels in the current work. It is necessary to study them in details.
2. The ratios G/G_{rec} are found to be close to unity at very small distances in all channels, which indicates spectral functions at $T > T_c$ and $T < T_c$ are similar in the very high frequency region. Thus, in the spectral function $\Delta\sigma$ extracted from the difference $G - G_{\text{rec}}$ the high frequency part should be suppressed. $\Delta\sigma$ then has a pronounced low frequency part and a high frequency part which is close to zero (and might be negative). It would be interesting to apply the extended Maximum Entropy method to the analysis of $G - G_{\text{rec}}$.
3. The detailed study of the properties of charmonium moving with respect to the heat bath frame is promising. It can provide hints on the transport properties of the charm quark as well as the modification of the bound state due to the change of the dispersion relation. The implementation of twisted boundary conditions would be helpful to get arbitrary momenta in each direction.
4. Since the transport peak as well as the resonance peak is enclosed in the vector correlator, it is not easy to disentangle these two contributions. The evaluation of the heavy quark transport properties following a recent proposal [161, 162] itself is very interesting and it can also help us to identify the transport peaks in our MEM analysis.

5. With the advent of the LHC, one has in prospect to measure bottomonium states. Working out the properties of bottomonium at finite temperature from the theoretical side is thus becoming of particular interest. However, to study this topic on the lattice, it needs new sophisticated techniques or large computing time to control the lattice cut-off effects due to the large mass of the bottom quark.

Appendix A

The Euclidean Dirac γ matrices and the $SU(N)$ generators λ

A.1 Dirac matrices

In the Euclidean metric, the γ matrices are defined in terms of the Pauli matrices σ as

$$\gamma_i = \begin{pmatrix} 0 & i\sigma_i \\ -i\sigma_i & 0 \end{pmatrix} \quad \gamma_0 = \begin{pmatrix} \mathbf{1}_2 & 0 \\ 0 & -\mathbf{1}_2 \end{pmatrix}$$

where the Pauli matrices are given by

$$\sigma_1 = \begin{pmatrix} 0 & 1 \\ 1 & 0 \end{pmatrix} \quad \sigma_2 = \begin{pmatrix} 0 & -i \\ i & 0 \end{pmatrix} \quad \sigma_3 = \begin{pmatrix} 1 & 0 \\ 0 & -1 \end{pmatrix}$$

The γ matrices read explicitly

$$\gamma_1 = \begin{pmatrix} 0 & 0 & 0 & i \\ 0 & 0 & i & 0 \\ 0 & -i & 0 & 0 \\ -i & 0 & 0 & 0 \end{pmatrix} \quad \gamma_2 = \begin{pmatrix} 0 & 0 & 0 & 1 \\ 0 & 0 & -1 & 0 \\ 0 & -1 & 0 & 0 \\ 1 & 0 & 0 & 0 \end{pmatrix} \quad \gamma_3 = \begin{pmatrix} 0 & 0 & i & 0 \\ 0 & 0 & 0 & -i \\ -i & 0 & 0 & 0 \\ 0 & i & 0 & 0 \end{pmatrix}$$

$$\gamma_0 = \begin{pmatrix} 1 & 0 & 0 & 0 \\ 0 & 1 & 0 & 0 \\ 0 & 0 & -1 & 0 \\ 0 & 0 & 0 & -1 \end{pmatrix} \quad \gamma_5 = \begin{pmatrix} 0 & 0 & 1 & 0 \\ 0 & 0 & 0 & 1 \\ 1 & 0 & 0 & 0 \\ 0 & 1 & 0 & 0 \end{pmatrix} = \gamma_1\gamma_2\gamma_3\gamma_0$$

with $\{\gamma_\mu, \gamma_\nu\} = 2\delta_{\mu\nu}$ and $\gamma_\mu^\dagger = \gamma_\mu$.

The σ -matrix defined through $\sigma_{\mu\nu} = \frac{1}{2} [\gamma_\mu, \gamma_\nu]$ are listed in the following

$$\begin{aligned} \sigma_{12} &= \begin{pmatrix} i & 0 & 0 & 0 \\ 0 & -i & 0 & 0 \\ 0 & 0 & i & 0 \\ 0 & 0 & 0 & -i \end{pmatrix} & \sigma_{13} &= \begin{pmatrix} 0 & -1 & 0 & 0 \\ 1 & 0 & 0 & 0 \\ 0 & 0 & 0 & -1 \\ 0 & 0 & 1 & 0 \end{pmatrix} & \sigma_{10} &= \begin{pmatrix} 0 & 0 & 0 & -i \\ 0 & 0 & -i & 0 \\ 0 & -i & 0 & 0 \\ -i & 0 & 0 & 0 \end{pmatrix} \\ \sigma_{23} &= \begin{pmatrix} 0 & i & 0 & 0 \\ i & 0 & 0 & 0 \\ 0 & 0 & 0 & i \\ 0 & 0 & i & 0 \end{pmatrix} & \sigma_{20} &= \begin{pmatrix} 0 & 0 & 0 & -1 \\ 0 & 0 & 1 & 0 \\ 0 & -1 & 0 & 0 \\ 1 & 0 & 0 & 0 \end{pmatrix} & \sigma_{30} &= \begin{pmatrix} 0 & 0 & -i & 0 \\ 0 & 0 & 0 & i \\ -i & 0 & 0 & 0 \\ 0 & i & 0 & 0 \end{pmatrix} \end{aligned}$$

with $\sigma_{\mu\mu} = 0$ and $\sigma_{\mu\nu} = -\sigma_{\nu\mu}$.

A.2 $SU(N)$ generators

The elements of Λ of the group $SU(N)$ can be written as

$$\Lambda = \exp \left(\sum_{a=1}^{N^2-1} i T_a \omega^a \right), \quad (\text{A.1})$$

where $\omega^a \in \mathbb{R}$. T_a are the traceless, hermitian generators, which are normalized as the following,

$$\text{Tr}(T_a T_b) = \frac{1}{2} \delta_{ab} \quad (\text{A.2})$$

The generators are defined through the commutation relations and the corresponding total anti-symmetric structure constants $f_{abc} \in \mathbb{R}$ of $SU(N)$

$$[T_a, T_b] = i f_{abc} T_c, \quad a, b, c \in [1, N^2 - 1] \quad (\text{A.3})$$

For $SU(3)$ the generators T_a can be expressed in terms of Gell-Mann matrices λ_a : $T_a = \lambda_a/2$. The Gell-Mann matrices have the following representation

$$\begin{aligned} \lambda_1 &= \begin{pmatrix} 0 & 1 & 0 \\ 1 & 0 & 0 \\ 0 & 0 & 0 \end{pmatrix} & \lambda_2 &= \begin{pmatrix} 0 & -i & 0 \\ i & 0 & 0 \\ 0 & 0 & 0 \end{pmatrix} & \lambda_3 &= \begin{pmatrix} 1 & 0 & 0 \\ 0 & -1 & 0 \\ 0 & 0 & 0 \end{pmatrix} & \lambda_4 &= \begin{pmatrix} 0 & 0 & 1 \\ 0 & 0 & 0 \\ 1 & 0 & 0 \end{pmatrix} \\ \lambda_5 &= \begin{pmatrix} 0 & 0 & -i \\ 0 & 0 & 0 \\ i & 0 & 0 \end{pmatrix} & \lambda_6 &= \begin{pmatrix} 0 & 0 & 0 \\ 0 & 0 & 1 \\ 0 & 1 & 0 \end{pmatrix} & \lambda_7 &= \begin{pmatrix} 0 & 0 & 0 \\ 0 & 0 & -i \\ 0 & i & 0 \end{pmatrix} & \lambda_8 &= \frac{1}{\sqrt{3}} \begin{pmatrix} 1 & 0 & 0 \\ 0 & 1 & 0 \\ 0 & 0 & -2 \end{pmatrix} \end{aligned}$$

Appendix B

Memory optimization for the clover term

We rewrite the clover term A from Eq. (1.34)

$$A(n) = \mathbb{1} - ig \frac{\kappa_{\text{CSW}}}{2} \sigma^{\mu\nu} F_{\mu\nu}, \quad (\text{B.1})$$

with

$$\sigma_{\mu\nu} = \frac{1}{2} [\gamma_\mu, \gamma_\nu], \quad (\text{B.2})$$

$$gF_{\mu\nu}(n) = -\frac{i}{8} \sum_j \left(U_{\mu\nu}^j(n) - U_{\mu\nu}^{j\dagger}(n) \right). \quad (\text{B.3})$$

$\frac{1}{2}\sigma_{\mu\nu}F_{\mu\nu}$ can be further written as

$$\frac{1}{2}\sigma_{\mu\nu}F_{\mu\nu} = \begin{pmatrix} W_0 & W_1 & W_2 & W_3 \\ W_1^\dagger & -W_0 & W_3^\dagger & -W_2 \\ W_2 & W_3 & W_0 & W_1 \\ W_3^\dagger & -W_2 & W_1^\dagger & -W_0 \end{pmatrix} \quad (\text{B.4})$$

with

$$W_0 = -i F_{21}, \quad (\text{B.5})$$

$$W_1 = -i F_{32} + F_{31}, \quad (\text{B.6})$$

$$W_2 = -i F_{34}, \quad (\text{B.7})$$

$$W_3 = -i F_{14} + F_{42}. \quad (\text{B.8})$$

The clover term A can be decomposed as

$$A(n) = L^\dagger(n)D(n)L(n) \quad (\text{B.9})$$

with L is a upper triangle matrix and D is a diagonal matrix. This decomposition renders the manipulation with A^{-1} more efficient.

Practically simulation is done in the double precision and due to the even-odd preconditioning, the size of matrix A is $8 \cdot N_c^2 \cdot N_\mu^2 \cdot \tilde{N}_\sigma^3 \cdot \tilde{N}_\tau$, for L it is $8 \cdot N_c^2 \cdot N_\mu^2 \cdot \tilde{N}_\sigma^3 \cdot \tilde{N}_\tau$ and for D it is $8 \cdot N_c \cdot N_\mu \cdot \tilde{N}_\sigma^3 \cdot \tilde{N}_\tau$. The \tilde{N} s with hats are the number of points in the spatial/temporal directions on the local lattice, N_c is the number of colors and N_μ is the number of spinors. To save the memory, we do not allocate memory for matrices A , L and D on heap and just evaluate them by using the basic matrices W s when needed. The matrices W s have a size of $16 \cdot N_c^2 \cdot N_\mu \cdot \tilde{N}_\sigma^3 \cdot \tilde{N}_\tau$, thus in this way $25/(25+6) \approx 80\%$ of the original memory consumed by the colver term is reduced.

References

- [1] Samuel C. C. Ting et al., *Experimental Observation of a Heavy Particle J*, Phys. Rev. Lett. **33** (1974) 1404.
- [2] B. Richter et al., *Discovery of a Narrow Resonance in e^+e^- Annihilation*, Phys. Rev. Lett. **33** (1974) 1406.
- [3] By Quarkonium Working Group (N. Brambilla et al.), *Heavy quarkonium physics*, CERN Yellow Report, CERN-2005-005, hep-ph/0412158.
- [4] See a recent review: M. B. Voloshin, *Charmonium*, Prog. Part. Nucl. Phys. **61** (2008) 455, arXiv:0711.4556.
- [5] T. Matsui and H. Satz, *J/ψ Suppression by Quark-Gluon Plasma Formation*, Phys. Lett. **B178** (1986) 416.
- [6] See a recent review: H. Satz, *Colour deconfinement and quarkonium binding*, J. Phys. **G32** (2006) R25, hep-ph/0512217.
- [7] See a recent review: R. Rapp, D. Blaschke and P. Crochet, *Charmonium and bottomonium production in heavy-ion collisions*, arXiv:0807.2470.
- [8] R. Vogt, *Cold Nuclear Matter Effects on J/ψ and Υ Production at the LHC*, Phys. Rev. **C81** (2010) 044903, arXiv:1003.3497.
- [9] M. Le Bellac, *Thermal Field Theory*, Cambridge University Press, 2000, ISBN **0521654777**.
- [10] J. I. Kapusta and C. Gale, *Finite-Temperature Field Theory: Principles and Applications*, Cambridge University Press, 2006, ISBN **0521820820**.
- [11] E. Eichten, K. Gottfried, T. Kinoshita, K. D. Lane and T.-M. Yan, *Charmonium: Comparison with Experiment*, Phys. Rev. **D21** (1980) 203.
- [12] See a recent review, A. Mócsy, *Potential Models for Quarkonia*, Eur. Phys. J. **C61** (2009) 705, arXiv:0811.0337.

- [13] G. Röpke, D. Blaschke and H. Schulz, *Dissociation Kinetics And Momentum Dependent J/ψ Suppression In A Quark-Gluon Plasma*, Phys. Rev. **D38** (1988) 3589.
- [14] F. Karsch, M.T. Mehr and H. Satz, *Color Screening and Deconfinement for Bound States of Heavy Quarks*, Z. Phys. **C37** (1988) 617.
- [15] T. Hashimoto, K. Hirose, T. Kanki and O. Miyamura, *Mass Shifts Of Charmoniums And Electromagnetic Signals*, Z. Phys. **C38** (1988) 251.
- [16] S. Digal, P. Petreczky and H. Satz, *String breaking and quarkonium dissociation at finite temperatures*, Phys. Lett. **B514** (2001) 57, hep-ph/0105234.
- [17] S. Digal, P. Petreczky and H. Satz, *Quarkonium feed down and sequential suppression*, Phys. Rev. **D64** (2001) 094015, hep-ph/0106017.
- [18] C.-Y. Wong, *Heavy quarkonia in quark-gluon plasma*, Phys. Rev. **C72** (2005) 034906, hep-ph/0408020.
- [19] A. Mócsy and P. Petreczky, *Quarkonia correlators above deconfinement*, Phys. Rev. **D73** (2006) 074007, hep-ph/0512156.
- [20] A. Mócsy and P. Petreczky, *Color screening melts quarkonium*, Phys. Rev. Lett. **99** (2007) 211602, arXiv:0706.2183.
- [21] A. Mócsy and P. Petreczky, *Can quarkonia survive deconfinement?*, Phys. Rev. **D77** (2008) 014501, arXiv:0705.2559.
- [22] W.M. Alberico, A. Beraudo, A. De Pace and A. Molinari, *Quarkonia in the deconfined phase: Effective potentials and lattice correlators*, Phys. Rev. **D75** (2007) 074009, hep-ph/0612062.
- [23] W.M. Alberico, A. Beraudo, A. De Pace and A. Molinari, *Potential models and lattice correlators for quarkonia at finite temperature*, Phys. Rev. **D77** (2008) 017502, arXiv:0706.2846.
- [24] O. Kaczmarek and F. Zantow, *Static quark anti-quark interactions in zero and finite temperature QCD. I. Heavy quark free energies, running coupling and quarkonium binding*, Phys. Rev. **D71** (2005) 114510, hep-lat/0503017, *II. Quark anti-quark internal energy and entropy*, hep-lat/**0506019**.
- [25] D. Cabrera and R. Rapp, *T-Matrix Approach to Quarkonium Correlation Functions in the QGP*, Phys. Rev. **D76** (2007) 114506, hep-ph/0611134.
- [26] X. Zhao and R. Rapp, *Charmonium in Medium: From Correlators to Experiment*, arXiv:1008.5328.

- [27] M. Laine, O. Philipsen, P. Romatschke and M. Tassler, *Real-time static potential in hot QCD*, **JHEP** 0703 (2007) 054, hep-ph/0611300.
- [28] M. Laine, O. Philipsen and M. Tassler, *Thermal imaginary part of a real-time static potential from classical lattice gauge theory simulations*, **JHEP** 0709:066,2007, arXiv:0707.2458.
- [29] A. Beraudo, J.-P. Blaizot and C. Ratti, *Real and imaginary-time $Q\bar{Q}$ correlators in a thermal medium*, **Nucl. Phys.** **A806** (2008) 312, arXiv:0712.4394.
- [30] N. Brambilla, J. Ghiglieri, A. Vairo and P. Petreczky, *Static quark-antiquark pairs at finite temperature*, **Phys. Rev.** **D78** (2008) 014017, arXiv:0804.0993.
- [31] A. Rothkopf, T. Hatsuda and S. Sasaki, *Proper heavy-quark potential from a spectral decomposition of the thermal Wilson loop*, **PoS (LAT2009)162**, arXiv:0910.2321.
- [32] A. Dumitru, Y. Guo and M. Strickland, *The Heavy-quark potential in an anisotropic (viscous) plasma*, **Phys. Lett.** **B662** (2008) 37, arXiv:0711.4722.
- [33] A. Dumitru, Y. Guo, A. Mócsy and M. Strickland, *Quarkonium states in an anisotropic QCD plasma*, **Phys. Rev.** **D79** (2009) 054019, arXiv:0901.1998.
- [34] A. Dumitru, Y. Guo and M. Strickland, *The Imaginary part of the static gluon propagator in an anisotropic (viscous) QCD plasma*, **Phys. Rev.** **D79** (2009) 114003, arXiv:0903.4703.
- [35] Y. Burnier, M. Laine and M. Vepsalainen, *Quarkonium dissociation in the presence of a small momentum space anisotropy*, **Phys. Lett.** **B678** (2009) 86, arXiv:0903.3467.
- [36] A. Beraudo, J.-P. Blaizot, P. Faccioli and G. Garberoglio, *A path integral for heavy-quarks in a hot plasma*, **arXiv:1005.1245**.
- [37] T. Umeda, K. Nomura and H. Matsufuru, *Charmonium at finite temperature in quenched lattice QCD*, **Eur. Phys. J.** **C39S1** (2004) 9, hep-lat/0211003.
- [38] M. Asakawa and T. Hatsuda, *J/ψ and η_c in the deconfined plasma from lattice QCD*, **Phys. Rev. Lett.** **92** (2004) 012001, hep-lat/0308034.
- [39] S. Datta, F. Karsch, P. Petreczky and I. Wetzorke, *Behavior of charmonium systems after deconfinement*, **Phys. Rev.** **D69** (2004) 094507, hep-lat/0312037.

- [40] A. Jakovác, P. Petreczky, K. Petrov and A. Velytsky, *Quarkonium correlators and spectral functions at zero and finite temperature*, Phys. Rev. **D75** (2007) 014506, hep-lat/0611017.
- [41] G. Aarts, C. Allton, M. B. Oktay, M. Peardon and J. -I. Skullerud, *Charmonium at high temperature in two-flavor QCD*, Phys. Rev. **D76** (2007) 094513, arXiv:0705.2198.
- [42] H. Iida, T. Doi, N. Ishii, H. Suganuma and K. Tsumura, *Charmonium properties in deconfinement phase in anisotropic lattice QCD*, Phys. Rev. **D74** (2006) 074502, hep-lat/0602008.
- [43] H. Ohno, T. Umeda and K. Kanaya (WHOT-QCD Collaboration), *Search for the Charmonium Dissociation Temperature with Variational Analysis in Lattice QCD*, PoS (**LAT2008**) 203, arXiv:0810.3066.
- [44] See a recent review, A. Bazavov, P. Petreczky and A. Velytsky, *Quarkonium at Finite Temperature*. **arXiv:0904.1748**.
- [45] K. G. Wilson, *Confinement of Quarks*, Phys. Rev. **D10** (1974) 2445.
- [46] I. Montvay and G. Münster, *Quantum Fields on a Lattice*, Cambridge University Press, 1994, **ISBN 0521599172**.
- [47] R. Gupta, *Introduction to lattice QCD*, hep-lat/9807028.
- [48] H. J. Rothe, *Lattice gauge theories: An introduction*, World Sci. Lect. Notes Phys. **74** (2005) 1, **ISBN 9812561684**.
- [49] H. B. Nielsen and M. Ninomiya, *No Go Theorem for Regularizing Chiral Fermions*, Phys. Lett. **B105** (1981) 219.
- [50] J. B. Kogut and L. Susskind, *Hamiltonian Formulation of Wilson's Lattice Gauge Theories*, Phys. Rev. **D11** (1975) 395.
- [51] L. Susskind, *Lattice Fermions*, Phys. Rev. **D16** (1977) 3031.
- [52] By HPQCD Collaboration and UKQCD Collaboration (E. Follana et al.), *Highly improved staggered quarks on the lattice, with applications to charm physics*, Phys. Rev. **D75** (2007) 054502, hep-lat/0610092.
- [53] D. B. Kaplan, *A Method for simulating chiral fermions on the lattice*, Phys. Lett. **B288** (1992) 342, hep-lat/9206013.

- [54] Y. Shamir, *Chiral fermions from lattice boundaries*, Nucl. Phys. **B406** (1993) 90, hep-lat/9303005.
- [55] V. Furman and Y. Shamir, *Axial symmetries in lattice QCD with Kaplan fermions*, Nucl. Phys. **B439** (1995) 54, hep-lat/9405004.
- [56] B. Sheikholeslami and R. Wohlert, *Improved Continuum Limit Lattice Action for QCD with Wilson Fermions*, Nucl. Phys. **B259** (1985) 572.
- [57] K. Symanzik, *Continuum limit and improved action in lattice theories. 1. Principles and ϕ^4 theory*, Nucl. Phys. **B226** (1983) 187, *Continuum limit and improved action in lattice theories. 2. $O(N)$ nonlinear sigma model in perturbation theory*, Nucl. Phys. **B226** (1983) 205.
- [58] M. Lüscher, S. Sint, R. Sommer, P. Weisz, and U. Wolff, *Non-perturbative $\mathcal{O}(a)$ improvement of lattice QCD*, Nucl. Phys. **B491** (1997) 323, hep-lat/9609035.
- [59] M. Bochicchio, L. Maiani, G. Martinelli, G. C. Rossi and M. Testa, *Chiral Symmetry on the Lattice with Wilson Fermions*, Nucl. Phys. **B262** (1985) 331.
- [60] G. M. de Divitiis and R. Petronzio, *Nonperturbative renormalization constants on the lattice from flavor nonsinglet Ward identities*, Phys. Lett. **B419**(1998)311, hep-lat/9710071.
- [61] M. Guagnelli and R. Sommer, *Nonperturbative $\mathcal{O}(a)$ improvement of the vector current*, Nucl. Phys. Proc. **Suppl. 63** (1998) 886, hep-lat/9709088.
- [62] T. van Ritbergen, J. A. M. Vermaseren and S. A. Larin, *The Four loop beta function in quantum chromodynamics*, Phys. Lett. **B400** (1997) 379, hep-ph/9701390.
- [63] S. Ejiri, F. Karsch, E. Laermann, C. Miao, S. Mukherjee, P. Petreczky, C. Schmidt, W. Soeldner and W. Unger, *On the magnetic equation of state in (2+1)-flavor QCD*, Phys. Rev. **D80** (2009) 094505, arXiv:0909.5122.
- [64] By CP-PACS Collaboration (S. Aoki et al.), *Light hadron spectrum and quark masses from quenched lattice QCD*, Phys. Rev. **D67** (2003) 034503, hep-lat/0206009.
- [65] By HPQCD Collaboration and UKQCD Collaboration and MILC Collaboration and Fermilab Lattice Collaboration (C. T. H. Davies et al.), *High precision lattice QCD confronts experiment*, Phys. Rev. **Lett. 92** (2004) 022001, hep-lat/0304004.
- [66] By CP-PACS Collaboration (Y. Nakamura et al.), *Precise determination of $B(K)$ and right quark masses in quenched domain-wall QCD*, Phys. Rev. **D78** (2008) 034502, arXiv:0803.2569.

- [67] M. R. Hestenes and E. Stiefel, *Methods of Conjugate Gradients for Solving Linear Systems*, J. Res. Natl. Bur. **Stand.** **49** (1952) 409.
- [68] H. A. van der Vorst, *BI-CGSTAB: a fast and smoothly converging variant of BI-CG for the solution of nonsymmetric linear systems*, SIAM Sci. and Stat. Comp. **13** (1992) 631.
- [69] T. A. Degrand and P. Rossi, *Conditioning techniques for dynamical fermions*, Comput. Phys. Commun. **60** (1990) 211.
- [70] N. Stanford, PhD thesis, University of Edinburgh, 1994.
- [71] N. Cabibbo and E. Marinari, *A New Method for Updating $SU(N)$ Matrices in Computer Simulations of Gauge Theories*, Phys. Lett. **B119** (1982) 387.
- [72] A. D. Kennedy and B. J. Pendleton, *Improved Heat Bath Method for Monte Carlo Calculations in Lattice Gauge Theories*, Phys. Lett. **B156** (1985) 393.
- [73] S. L. Adler, *An Overrelaxation Method For The Monte Carlo Evaluation Of The Partition Function For Multiquadratic Actions*, Phys. Rev. **D23** (1981) 2901.
- [74] M. Creutz, *Overrelaxation and Monte Carlo Simulation*, Phys. Rev. **D36** (1987) 515.
- [75] J. Shao and D. Tu, *The Jackknife and Bootstrap*, Springer Series in Statistics, 1995, **ISBN 0387945156**.
- [76] R. G. Edwards, U. M. Heller, and T. R. Klassen, *Accurate Scale Determinations for the Wilson Gauge Action*, Nucl. Phys. **B517** (1998) 377, hep-lat/9711003.
- [77] C. R. Allton, *Lattice Monte Carlo data versus perturbation theory*, **hep-lat/9610016**.
- [78] B. Lucini, M. Teper and U. Wenger, *The high temperature phase transition in $SU(N)$ gauge theories*, JHEP **0401** (2004) 061, hep-lat/0307017.
- [79] B. Beinlich, F. Karsch, E. Laermann and A. Peikert, *String tension and thermodynamics with tree level and tadpole improved actions*, Eur. Phys. J. **C6** (1999) 133, hep-lat/9707023.
- [80] S. Capitani, M. Lüscher, R. Sommer and H. Wittig, *Non-perturbative quark mass renormalization in quenched lattice QCD*, Nucl. Phys. **B544** (1999) 669, hep-lat/9810063.

- [81] ALPHA Collaboration, M. Guagnelli, R. Petronzio, J. Rolf, S. Sint, R. Sommer and U. Wolff, *Non-perturbative results for the coefficients b_m and $b_A - b_P$ in $\mathcal{O}(a)$ improved lattice QCD*, Nucl. Phys. **B595** (2001) 44, hep-lat/0009021.
- [82] QCD-TARO Collaboration (S. Choe et al.), *Quenched charmonium spectrum*, JHEP **08** (2003) 022, hep-lat/0307004.
- [83] K. Nakamura et al. (Particle Data Group), *REVIEW OF PARTICLE PHYSICS*, J. Phys. **G 37** (2010) 075021.
- [84] T. van Ritbergen, J. A. M. Vermaseren and S. A. Larin, *The four loop quark mass anomalous dimension and the invariant quark mass*, Phys. Lett. **B405** (1997) 327, hep-ph/9703284.
- [85] K. G. Chetyrkin, *Quark mass anomalous dimension to $\mathcal{O}(\alpha_s^4)$* , Phys. Lett. **B404** (1997) 161, hep-ph/9703278.
- [86] K. G. Chetyrkin, J. H. Kühn and M. Steinhauser, *RunDec: A Mathematica package for running and decoupling of the strong coupling and quark masses*, Comput. Phys. Commun. **133** (2000) 43, hep-ph/0004189.
- [87] E. Laermann and P Schmidt, *Meson Screening Masses at high Temperature in quenched QCD with improved Wilson Quarks*, Eur. Phys. J. **C20** (2001) 541, hep-lat/0103037.
- [88] F. Karsch, H.-T. Ding, A. Francis, O. Kaczmarek and W. Söldner, *Estimating dilepton rates and electric conductivity from vector current correlation functions in quenched QCD*, **Lattice 2010** proceedings.
- [89] A. Francis, H.-T. Ding, F. Karsch, O. Kaczmarek and W. Söldner, *The continuum limit of hadronic correlation functions in the deconfined phase of an $SU(3)$ gauge theory*, **Lattice 2010** proceedings.
- [90] J. Rolf and S. Sint, *A precise determination of the charm quark's mass in quenched QCD*, **JHEP 12** (2002) 007, hep-ph/0209255.
- [91] G. M. de Divitiis, M. Guagnelli, R. Petronzio and N. Tantalo, *Heavy quark masses in the continuum limit of quenched lattice QCD*, Nucl. Phys. **B675** (2003) 309, hep-lat/0305018.
- [92] M. Göckeler et al., *Perturbative renormalisation of bilinear quark and gluon operators*, Nucl. Phys. **Proc. Suppl. 53** (1997) 896, hep-lat/9608033.

- [93] G. P. Lepage and P. B. Mackenzie, *On the Viability of Lattice Perturbation Theory*, Phys. Rev. **D48** (1993) 2250, hep-lat/9209022.
- [94] S. Sint and P. Weisz, *Further results on $\mathcal{O}(a)$ improved lattice QCD to one-loop order of perturbation theory*, Nucl. Phys. **B502** (1997) 251, hep-lat/9704001.
- [95] M. Göckeler et al., *Non-perturbative renormalisation of composite operators in lattice QCD*, Nucl. Phys. **B544** (1999) 699.
- [96] S. Capitani, *Lattice perturbation theory*, Phys. Rept. **382** (2003) 113, hep-lat/0211036.
- [97] T. R. Klassen, *QCD (lattice) potential and coupling: How to accurately interpolate between multiloop QCD and the string picture*, Phys. Rev. **D51** (1995) 5130, hep-lat/9408016, CLNS-94-1294-REV.
- [98] A. Skouroupathis and H. Panagopoulos, *Higher loop renormalization of fermion bilinear operators*, PoS (**Lattice 2007**) 254.
- [99] A. Skouroupathis and H. Panagopoulos, *Two-loop renormalization of scalar and pseudoscalar fermion bilinears on the lattice*, Phys. Rev. **D76** (2007) 094514, arXiv:0707.2906.
- [100] A. Skouroupathis and H. Panagopoulos, *Two-loop renormalization of vector, axial-vector and tensor fermion bilinears on the lattice*, Phys. Rev. **D79** (2009) 094508, arXiv:0811.4264.
- [101] M. Göckeler et al., *Perturbative and Nonperturbative Renormalization in Lattice QCD*, arXiv:**1003.5756**.
- [102] A. Athenodorou, H. Panagopoulos and A. Tsapalis, *The Lattice Free Energy of QCD with Clover Fermions, up to Three-Loops*, Phys. Lett. **B659** (2008) 252, arXiv:0710.3856.
- [103] M. Lüscher, S. Sint, R. Sommer and H. Wittig, *Non-perturbative determination of the axial current normalization constant in $\mathcal{O}(a)$ improved lattice QCD*, Nucl. Phys. **B491** (1997) 344, hep-lat/9611015.
- [104] S. Sint and P. Weisz, *Further one-loop results in $\mathcal{O}(a)$ improved lattice QCD*, Nucl. Phys. B (Procl. Suppl.) **63A-C** (1998) 856, hep-lat/9709096.
- [105] H.-T. Ding, A. Francis, O. Kaczmarek, F. Karsch, H. Satz and W. Söldner, *Charmonium correlation and spectral functions at finite temperature*, **Lattice 2010** proceedings.

- [106] F. Karsch, E. Laermann, P. Petreczky and S. Stickan, *Infinite temperature limit of meson spectral functions calculated on the lattice*, Phys. Rev. **D68** (2003) 014504, hep-lat/0303017.
- [107] F. Karsch and E. Laermann, *Thermodynamics and in-medium hadron properties from lattice QCD*, hep-lat/0305025, in *Quark-Gluon Plasma 3*, R. C. Hwa (ed.) and X.-N. Wang (ed.), ISBN 9812380779, page 1-59.
- [108] E. Braaten, R. D. Pisarski and T.-C. Yuan, *Production Of Soft Dileptons In The Quark - Gluon Plasma*, Phys. Rev. Lett.64 (1990) 2242.
- [109] F. Karsch, E. Laermann, P. Petreczky, S. Stickan and I. Wetzorke, *A Lattice calculation of thermal dilepton rates*, Phys. Lett. **B530** (2002) 147, hep-lat/0110208.
- [110] J.P. Boon and S. Yip, *Molecular Hydrodynamics*, McGraw-Hill, New York, 1980, ISBN 0486669491.
- [111] H. B. Meyer, *The Bulk Channel in Thermal Gauge Theories*, JHEP **1004** (2010) 099, arXiv:1002.3343.
- [112] S. F. Gull and G. J. Daniell, *Image reconstruction from incomplete and noisy data*, Nature**272** (1978) 686.
- [113] E. Laue et al., *Maximum entropy reconstruction of spectra containing antiphase peaks*, J. Magn. Res**63** (1985) 418.
- [114] S. F. Gull, *Developments in maximum entropy data analysis*, proceedings in *Maximum Entropy and Bayesian Methods*, Cambridge 1988, pages 53-71, ISBN 0792302249.
- [115] J. Skilling, *Classic maximum entropy*, proceedings in *Maximum Entropy and Bayesian Methods*, Cambridge 1988, pages 45-52, ISBN 0792302249.
- [116] W. I. F. David, *Extending the power of powder diffraction for structure determination*, Nature**346** (1990) 731.
- [117] M. Jarrell and J. E. Gubernatis, *Bayesian inference and the analytic continuation of imaginary-time quantum Monte Carlo data*, Physics Reports **269** (1996) 133.
- [118] M. Asakawa, T. Hatsuda, Y. Nakahara, *Maximum entropy analysis of the spectral functions in lattice QCD*, Prog. Part. Nucl. Phys. **46** (2001) 459, hep-lat/0011040.
- [119] Y. Nakahara, M. Asakawa and T. Hatsuda, *Hadronic spectral functions in lattice QCD*, Phys. Rev. **D60** (1999) 091503, hep-lat/9905034.

- [120] By CP-PACS Collaboration (T. Yamazaki et al.), *Spectral function and excited states in lattice QCD with maximum entropy method*, Phys. Rev. **D65** (2002) 014501, hep-lat/0105030.
- [121] K. Langfeld, H. Reinhardt and J. Gattnar, *Gluon propagators and quark confinement*, Nucl. Phys. **B621** (2002) 131, hep-ph/0107141.
- [122] H. R. Fiebig, *Spectral density analysis of time correlation functions in lattice QCD using the maximum entropy method*, Phys. Rev. **D65** (2002) 094512, hep-lat/0204004.
- [123] C.R. Allton, J. E. Clowser, S. J. Hands, J. B. Kogut and C. G. Strouthos, *Application of the maximum entropy method to the (2+1)-dimensional four fermion model*, Phys. Rev. **D66** (2002) 094511, hep-lat/0208027.
- [124] K. Sasaki, S. Sasaki and T. Hatsuda, *Spectral analysis of excited nucleons in lattice QCD with maximum entropy method*, Phys. Lett. **B623** (2005) 208, hep-lat/0504020.
- [125] G. Aarts, C. Allton, J. Foley, S. Hands and S. Kim, *Spectral Functions at Small Energies and the Electrical Conductivity in Hot Quenched Lattice QCD*, Phys. Rev. Lett. **99** (2007) 022002, hep-lat/0703008.
- [126] H.-T. Ding, O. Kaczmarek, F. Karsch, H. Satz and W. Söldner, *Charmonium correlators and spectral functions at finite temperature*, PoS (**LAT2009**) 169, arXiv:0910.3098.
- [127] N. Wu, *The Maximum Entropy Method (Springer Series in Information Sciences)*, 1997, **ISBN 3540619658**.
- [128] D. Sivia and J. Skilling, *Data Analysis: A Bayesian Tutorial*, Oxford University Press, 2006, **ISBN 0198568320**.
- [129] M. A. Shifman, A. I. Vainshtein and V. I. Zakharov, *QCD and Resonance Physics: The ρ - ω Mixing*, Nucl. Phys. **B147** (1979) 519.
- [130] T. Hatsuda, E. M. Henley, T. Meissner and G. Krein, *The Off-shell ρ - ω mixing in the QCD sum rules*, Phys. Rev. **C49** (1994) 452, nucl-th/9304021.
- [131] S.-L. Zhu, W. Y. P. Hwang and Z.-S. Yang, *The Ω and $\Sigma^0\Lambda$ transition magnetic moments in QCD sum rules*, Phys. Rev. **D57** (1998) 1527, hep-ph/9802322.
- [132] T. Bayes, *An essay towards solving a problem in the doctrine of chances*, Philosophical Transactions of the Royal Society of London **53** (1763) 370.

- [133] W. Weaver and C. E. Shannon, *The Mathematical Theory of Communication*, University of Illinois Press, 1949, **ISBN 0252725484**.
- [134] E. T. Jaynes, *Information Theory and Statistical Mechanics*, Phys. Rev. **106** (1957) 620.
- [135] E. T. Jaynes, *Information Theory and Statistical Mechanics. II*, Phys. Rev. **108** (1957) 171.
- [136] A. N. Tikhonov, V. Y. Arsenin, *Solutions of Ill-Posed Problems*, Winston, New York, 1977, **ISBN 0470991240**.
- [137] P. C. Hansen, *Regularization Tools: A Matlab package for analysis and solution of discrete ill-posed problems*, Numer. Algo. **46** (2007) 189.
- [138] H. Jeffreys, *Theory of Probability*, Oxford University Press, 1998, **ISBN 0198503687**.
- [139] R. K. Bryan, *Maximum entropy analysis of oversampled data problems*, Eur. Biophys. **J18** (1990) 165.
- [140] I. Wetzorke, *Lattice QCD calculations of hadron spectra and spectral functions in the vacuum and in a thermal heat bath*, PhD Dissertation, Universität Bielefeld, 2001.
- [141] T. Umeda, *A Constant contribution in meson correlators at finite temperature*, Phys. Rev. **D75** (2007) 094502, hep-lat/0701005.
- [142] J. Engels and O. Vogt, *Longitudinal and transverse spectral functions in the three-dimensional $O(4)$ model*, Nucl. Phys. **B832** (2010) 538, arXiv:0911.1939.
- [143] G. Aarts and J. M. Martinez-Resco, *Continuum and lattice meson spectral functions at nonzero momentum and high temperature*, Nucl. Phys. **B726** (2005) 93, hep-lat/0507004.
- [144] P. Petreczky and D. Teaney, *Heavy quark diffusion from the lattice*, Phys. Rev. **D73** (2006) 014508, hep-ph/0507318.
- [145] D. B. Carpenter, C. F. Baillie, *Free Fermion Propagators And Lattice Finite Size Effects*, Nucl. Phys. **B260** (1985) 103.
- [146] D. Forster, *Hydrodynamic Fluctuations, Broken Symmetry, And Correlation Functions (Advanced Books Classics)*, Perseus 1989, **ISBN 0201410494**.

- [147] F. Reif, *Fundamentals of Statistical and Thermal Physics*, (McGraw-Hill Series in Fundamentals of Physics), June 1, 1965, **ISBN 0070518009**.
- [148] G. D. Moore and D. Teaney, *How much do heavy quarks thermalize in a heavy ion collision?*, Phys. Rev. **C71** (2005) 064904, hep-ph/0412346.
- [149] J. Hong and D. Teaney, *Spectral densities for hot QCD plasmas in a leading log approximation*, **arXiv:1003.0699**.
- [150] S. Datta and P. Petreczky, *Zero mode contribution in quarkonium correlators and in-medium properties of heavy quarks* J. Phys. **G35** (2008) 104114, arXiv:0805.1174.
- [151] P. Petreczky, *On temperature dependence of quarkonium correlators*, Eur. Phys. J. **C62** (2009) 85, arXiv:0810.0258.
- [152] S. Datta, F. Karsch, S. Wissel, P. Petreczky and I. Wetzorke, *Charmonia at finite momenta in a deconfined plasma*, hep-lat/0409147.
- [153] G. Aarts, C. Allton, J. Foley, S. Hands and S. Kim, *Spectral functions at non-zero momentum in hot QCD*, PoS (**LAT2006**) 134, hep-lat/0610061.
- [154] G. Aarts, C. Allton, J. Foley, S. Hands and S. Kim, *Meson spectral functions at nonzero momentum in hot QCD*, Nucl. Phys. **A785** (2007) 202, hep-lat/0607012.
- [155] M. B. Oktay and J.-I. Skullerud, *Momentum-dependence of charmonium spectral functions from lattice QCD*, arXiv:1005.1209.
- [156] G. Aarts, C. R. Allton, S. J. Hands, J. Foley and S. Kim, *Longitudinal and transverse meson correlators in the deconfined phase*, **Lattice 2010** proceedings, **arXiv:1007.4897**.
- [157] H.-T. Ding, O. Kaczmarek, F. Karsch and H. Satz, *Charmonium correlators and spectral functions at finite temperature*, PoS **CONFINEMENT8** (2008) 108, arXiv:0901.3023.
- [158] G. D. Moore and J.-M. Robert, *Dileptons, spectral weights, and conductivity in the quark-gluon plasma*, hep-ph/0607172.
- [159] E. Shuryak, *Correlation functions in the QCD vacuum*, Rev. Mod. Phys. **65** (1993) 1.
- [160] W. Florkowski and B. L. Friman, *Spatial dependence of the finite temperature meson correlation function*, Z. Phys. **A347** (1994) 271.

- [161] S. Caron-Huot, M. Laine and G. D. Moore, *A Way to estimate the heavy quark thermalization rate from the lattice*, **JHEP** 0904 (2009) 053, arXiv:0901.1195.
- [162] Y. Burnier, M. Laine, J. Langelage and L. Mether, *Colour-electric spectral function at next-to-leading order*, **arXiv:1006.0867**.

Acknowledgements

This dissertation in its present form would not have been possible without the help I received from many people, to whom I want to express my acknowledgements.

First, I would like to thank my supervisor Prof. Dr. Edwin Laermann for his guidance and encouragement during my PhD study. It is always a pleasure to talk to him. I am especially grateful to my advisor Dr. Olaf Kaczmarek for his patience and mentorship, which led to this interesting result. He also provided me a lot of opportunities to attend schools, workshops and conferences around the world. Their help are invaluable to me.

In addition I want to express my deep gratitude to Prof. Dr. Helmut Satz for introducing me to the charmonium physics and for the constant support. I am also grateful to Prof. Dr. Frithjof Karsch for kind hospitality at BNL and for valuable discussions and suggestions on this project. I thank Prof. Dr. Jürgen Engels for introducing MEM to me and also for interesting discussions on this method. I am grateful to Anthony Francis and Dr. Wolfgang Söldner for fruitful collaboration on this interesting project.

I am thankful to Prof. DaiCui Zhou for kind hospitality during my stay in Wuhan and also encouragement and constant support. I also acknowledge Dr. Damir Bećirević for supervision and kind hospitality for my two-month stay in Orsay.

Concerning the writing of my thesis, I want to thank Anthony Francis and Prof. Dr. David E. Miller for proofreading and constructive discussions.

I would like to thank all my officemates, in particular Wolfgang Unger for discussions of physics and things beyond that. I am very grateful to our secretaries Gudrun Eickmeyer and Susi von Reder, in particular Gudrun: she is always there when I need help. I also want to thank all the members in the high energy physics group for creating such a very friendly atmosphere.

I want to thank my kind neighbor at IBZ, Martin H. Vargas, and my former flatmate, Kai Ristau, for kind help during my earlier days in Bielefeld. I am very grateful to my current flatmate Ulla König for a very comfortable living environment during last two years.

I also want to thank Dr. Cheng Ping, Dr. Guo ZongKuang, Dr. Li Nan, Dr. Miao Chuan, Dr. OuYang ShunXiang, Dr. Xiang WenChang, Zhou Rui and many others for the enjoyable time and generous help during my last three years in Bielefeld.

I am grateful to Dr. Liu Lei, Song YanSheng, Dr. Tang Ying, Dr. Tian HaiJun and Zhang Lie for their friendship and encouragement during last eight years.

最后, 我衷心的感谢我的祖父丁振良, 祖母鲁宇秀, 外祖母廖引兰, 父亲丁元俊, 母亲邓银芬对我无私的关爱及支持, 感谢弟弟丁亨达对我的理解和支持。

丁亨通

二零一零年九月二十七日于比勒费尔德